Quantification of tectonic controls on the distribution and architecture of deep-water facies during the growth of the toe-thrusts region of the Niger Delta

Marco Pizzi

Department of Earth Science & Engineering

Imperial College London

Submitted in fulfilment of the requirements for the award of the degree of

Doctor of Philosophy

September 2019

Declaration of originality

I declare that this thesis is the result of my own PhD research carried out under the supervision of Dr. Michael Mayall, Dr. Lidia Lonergan and Dr. Alexander Whittaker. All published and unpublished material used in this thesis has been appropriately referenced. None of this work has been previously submitted to Imperial College London or any other academic institution for a degree or diploma, or any other qualification.

Marco Pizzi
September 2019

Copyright Declaration

Abstract

Using 3D seismic data, the deep-water fold and thrust belt of the southern lobe of the Niger Delta has been investigated over an area of 4500 km^2 to document, for the first time, the detailed growth history of a thrust array and how it controlled the distribution and architecture, through time, of the coeval deep-water sedimentary systems. Quantification of the growth of each structure has been achieved using line-length balancing and yielded measures of cumulative shortening and strain, and their evolving rates, along and across strike and through time. This has enabled a new model for thrust growth to be proposed and linked to the observed change in stratigraphic architecture. The results show that all thrusts nucleated coevally in the study area as small segments, deforming at low strain rates, which caused the deflection of early leveed channels. The progressive lateral propagation and linkage of the segments, along with an increase in strain rates, caused the spatial restriction of the slope channels, until it induced the deposition of ponded lobes and the alteration of the channel architectures into erosional forms. The later decrease in strain rates and smoothing of the topography linked to the deposition of channelized sheets within shallow-ponded basins. These observations lead to the development of a predictive facies model where the occurrence of a specific facies (the architecture) is explained depending on when and where (along strike) a channel (or flow) interacts with a given fold. The specific location where channels cross structures, in turn, is dictated by how deformation is partitioned between structures across-strike, and by the particular distribution of strain rates along-strike. Distribution and architecture are effectively two linked variables which depend on a set of evolving parameters during the growth of a thrust array; the cumulative strain, strain rates and degree of fault linkage.

Acknowledgments

Contents

List of Figures

List of Tables

1. Introduction and background

1.1 Overview and rationale

In the last two decades the academic community, along with the oil and gas industry have shown great interest in understanding and predicting the depositional characteristics of deep-water turbidite systems developed on topographically complex slopes. This has been driven by the discovery of major hydrocarbon fields in these settings in many locations around the world including the Gulf of Mexico, Nigeria, Angola, Brazil and NW Borneo. Almost all of these locations are found on continental passive margins where thick sedimentary clastic prisms have been deposited on top of either salt (Gulf of Mexico, Angola, Brazil) or shale (Nigeria and NW Borneo) layers (Damuth, 1994; Cohen and McClay, 1996; Prather et al., 1998; Wu and Bally, 2000; Prather, 2003; Ingram et al., 2004; Morley, 2009, 2011; Wu et al., 2015). Over time these layers act as mobile substrates and their deformation is commonly driven by the sediment load itself (or in combination with far-field stresses). This process creates gravitational collapse and extension in the upslope region, resulting in a compressional domain being present further downslope, which leads to the formation of topographic relief on the seabed. Deformation styles at the down dip end of the gravitational system vary upon the substrate present, but typically include the intrusion of salt diapirs and salt walls and/or the development of large deep-water fold and thrust belts (Niger Delta). Sedimentation occurs at the same time as deformation and their interaction produces a variety of basin architectures and complex patterns of sand deposition (Shaw et al., 2004).

In the Niger Delta area, and on other slopes deformed in response to gravity failure, a number of seismic-based studies have been published with the aim of understanding the relationships between growing topography on the seabed and the linked response of turbidite channels and lobes/fans (Prather et al, 1998, 2012a, b; Hooper et al., 2002; Broucke et al., 2004; Morgan, 2004; Gee and Gawthorpe 2006, 2007; Clark and Cartwright 2009, 2011, 2012a, b; Mayall et al. 2010; Deptuck et al., 2012; Hay, 2012; Jones et al., 2012; Oluboyo et al., 2014; Jolly et al., 2016, 2017; Don et al., 2019; amongst others).

The concept of an equilibrium profile has also been used to predict which locations are most likely affected by erosion/incision, bypass or deposition (Pirmez et al., 2000; Ferry et al., 2005). Much work has been then published on the internal architecture and geometry of submarine channels (Mayall and Stewart, 2000; Babonneau et al., 2002; Abreu et al., 2003; Fonnesu,

2003; Deptuck et al., 2003, 2007; Sprague et al., 2005; Mayall et al., 2006; Janocko et al., 2013 amongst many others) and on the development of the architectural-element approach for describing deep-water sedimentary systems (Posamentier and Kolla, 2003).

These studies focused on individual aspects of slope sedimentation ranging from the classification of different channels (Janocko et al., 2013) or deep-water elements, to the relationship between local slope gradient changes and channel incision or deposition, and the external geometry of channel-levee complexes with respect to the timing of growth of structures, however, often highlighting examples of individual channels interacting with topography.

Moreover, most of the above seismic studies have been calibrated in the shallow subsurface within Pleistocene sections where seismic resolution is greater and the slope morphology is almost identical to the present day, therefore aiming to create "shallow seismic analogues" as a means to aid the interpretation of the deeper and most structurally deformed sections.

However, no attempt is found in the literature to take a holistic approach to try and predict the evolving stratigraphic architectures at a regional scale, throughout, and in response to, the long-term history of deformation (>10Myr) of large areas of deep-water slopes deforming over shale layers. Therefore, unlike the salt-withdrawal minibasins of the Gulf of Mexico (Prather et al., 1998), predictive models for the distribution in time and space of reservoir facies in gravity-driven fold and thrust belts have yet to be proposed.

With the use of 3D seismic industry data, in this thesis I quantitatively investigate the relationship between sea-floor deformation and the distribution and architecture of the main deep-water reservoir facies throughout the growth history of the toe-thrust region of the southern lobe of the Niger Delta, over ca. 40 km down slope and 60 km along strike.

1.2 Research Background

1.2.1 Characteristics of deep-water sedimentation

In deep-water areas most of the deposition of clastic materials is by sediment gravity flows (Middleton and Hampton, 1973) along with hemipelagic sedimentation. The processes comprise a spectrum of flow types ranging from cohesive debris flows to non-cohesive turbidity currents and several classification schemes have been proposed to address the wide range of observed deposits (Pickering et al., 1986; Nemec, 1990; Ghibaudo, 1992; Mulder and Alexander 2001; Haughton et al., 2009; Talling et al., 2012; Peakall and Sumner, 2015). The deposits resulting from these flows are varied, however, this PhD work is mainly concerned

with those derived from turbidity currents and to a lesser extent with mass-transport deposits, which collectively include slumps, slides and debris flows. A turbidity current is a "*flow induced by the action of gravity upon a (fluidal) turbid mixture of fluid and (suspended) sediment, by virtue of the density difference between the mixture and the ambient fluid*" in which sediment suspension is due to turbulence (Kneller and Buckee, 2000). The deposits of these currents were first described in outcrop by Bouma (1962) who recognized a transition from planar, to ripple laminated and finer beds, deposited from a single event and characteristic of a low-density turbidity flow. Later, higher concentration turbidity flows were recognized to deposit sand and gravel (Lowe, 1979, 1982).

However, because of the seismic-based nature of this PhD work and the lack of well control, deep-water facies are here described in terms of depositional or architectural elements (Posamentier and Kolla, 2003), which are the basic mappable components of both modern and ancient turbidite systems (Mutti and Normark, 1991). The 'architectural-element' approach provides a systematic means for describing sedimentary systems, taking into consideration their lithofacies assemblages (inferred from seismic appearance) and internal and external geometries. The architecture of deep-water systems is often predictable and when understood it can be used to improve reservoir production performance (Hampton et al., 2006, Mayall et al., 2006). Depositional elements, and the way they are arranged vertically and laterally, can vary through space and time in response to changes in sand-to-mud ratio, flow discharge, relative sea-level and slope topography (Posamentier and Kolla, 2003). Moreover, they show a hierarchy from the deposit of a single sediment gravity flow (bed) to the accumulated deposits that comprise entire slope or basin floor successions (Cullis et al., 2018 for a review). The main depositional elements found in deep-water areas comprise channels, levees, frontal splays, lobes and sheets, mass-transport deposits and hemipelagic drapes (Mutti and Normark, 1987, 1991, Posamentier and Kolla, 2003).

1.2.1.1 Channels and sheets

Channel belts are the main depositional element studied in this work, and their associated internal architecture, evolution of the fill, levees, sinuosity, initiation, and response to topography have been extensively addressed by many authors (Clark et al., 1992; Babonneau et al., 2002; Mayall and O'Byrne, 2002; Navarre et al., 2002; Skene et al., 2002; Abreu, 2003, Fonnesu 2003, Deptuck et al. 2003; Beaubouef, 2004; Huyghe et al., 2004; Sullivan et al, 2004; Sprague et al., 2005; Fildani et al., 2006; Mayall et al., 2006; Deptuck et al. 2007; Henio and Davies, 2007; Wynn et al, 2007; Cross et al., 2009; Catteral et al., 2010; Mayall et al, 2010;

McHargue et al., 2011; Sylvester et al, 2011; Maier et al, 2012; Alpak et al., 2013; Fildani et al., 2013; Janocko et al., 2013, Gamboa and Alves, 2015; Jobe et al., 2016; Jolly et al., 2016, 2017; Sylvester and Covault, 2016; Deptuck and Sylvester, 2017; Hassen et al., 2017; Niyazi et al., 2018; Zhang et al., 2018; Zhao et al., 2019; amongst others). The turbidite channels imaged in this work are large systems that can be up to 3 km wide and 300 m deep. These large systems have been proven to represent important hydrocarbon reservoirs, however, they also comprise smaller-scale, higher-frequency channel fills that exhibit a hierarchical order. This adds complexity to the internal facies distribution and authors have tried to model their internal architectures with the use of high-resolution seismic datasets, core and well data, and outcrop analogues (Figure 1-1; Mayall and O'Byrne, 2002; Navarre et al., 2002; Abreu, 2003; Deptuck et al. 2003; Gardner et al., 2003; Beaubouef, 2004; Sprague et al., 2005: Mayall et al., 2006; Porter et al., 2006; Cross et al., 2009; Alpak et al., 2013; Cullis et al., 2018). Biostratigraphic data indicate that the large channel systems generally imaged in 3D seismic data, as those in this work, correlate to third-order sequences, while the smaller-scale channels represent fourth and fifth order scales (Mayall et al., 2006; Zhang et al., 2018).
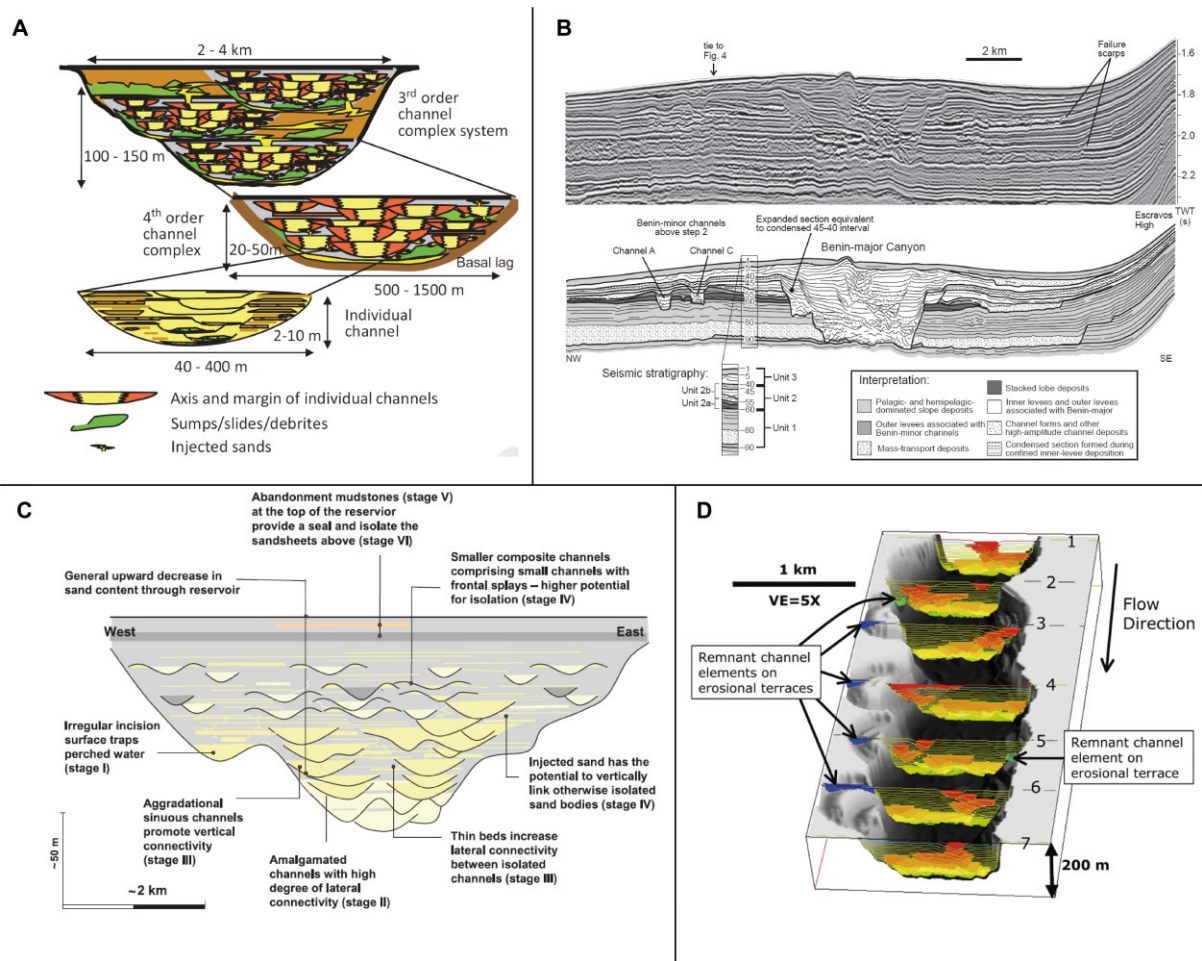
Figure 1-1: Different models of the internal architectures of large 3rd-order channels, showing the complex distribution of reservoir facies. (A) from Jones et al., 2012; (B) from Deptuck et al., 2012; (C) from Cross et al., 2009; (D) from McHargue et al., 2011.

Along with channel complexes, other important hydrocarbon reservoirs in deep-water settings are represented by sheets, fan or lobe deposits. These are deposited at the down-dip end of submarine channels of any scale as a result of decreased levee height and confinement that occurs when there is a marked reduction in channel gradient and flow deceleration (Posamentier and Kolla, 2003). For this reason, they can be found on the low-gradient basin floors of topographically unconfined slopes (Babonneau et al., 2002; Bouma, 2004), ponded within intraslope minibasins (Prather et al., 1998; Doughty-Jones et al., 2017), and as transient fans along the flatter intervals of stepped slopes (Adeogba et al., 2005). Alternatively, high-amplitude sheet-like deposits can be found at the base of channel-levee systems, interpreted to form in response to levee avulsion and temporary loss of confinement ("HARPS"; Pirmez et al., 1997; Piper and Normark, 2001; Deptuck and Sylvester, 2017). Similarly to the channel complexes, they show an internal hierarchical order and consist of smaller distributary channel complexes, which has led many authors to document their internal architectures and dimensions according the environment of deposition (Gervais et al., 2006; Deptuck et al., 2008;

Saller 2008; Prelat et al., 2009, 2010; Prather et al., 2012; Doughty-Jones et al., 2017; Jobe et al., 2017; Spychala et al., 2017). At the present, a widely used hierarchical scheme is that of Prelat et al. (2010) who recognized that the larger lobe complexes consist of smaller lobes, lobe elements and beds (Figure 1-2).

As previously discussed, the way that depositional elements are arranged vertically and laterally can vary in space and time and the resulting basin architecture can be complex and difficult to predict. This is even more complex if the interval analysed comprise slope successions several km thick, over an area of thousands of km^2, and deposited over > 10 Myr, during the growth of a fold and thrust belt; an issue that has not been addressed yet in the literature in a comprehensive way. Therefore, given the exploration significance of submarine channels and lobes, this PhD work is not concerned with their internal architectures, but with the distribution of these third-order depositional elements and the way their external architecture and morphology has evolved, at the scales stated above, in response to the growth history of a deep-water fold and thrust belt.
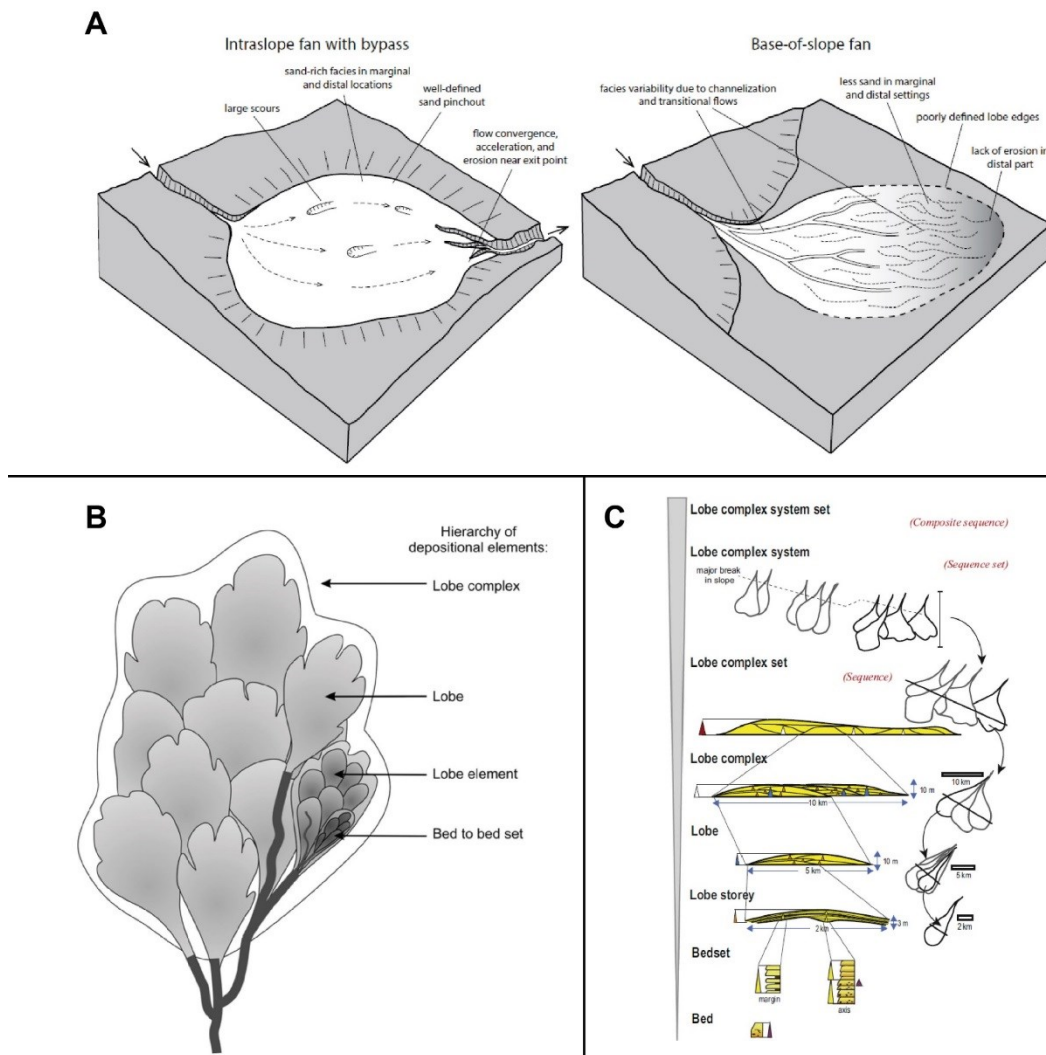
Figure 1-2: A) Difference between intraslope and base-of-slope fans (from Jobe et al., 2017). B, C), internal hierarchy of lobe deposits. B) from Prelat et al., 2010; C) from Sprague et al., 2005.

1.2.2 Deep-water fold and thrust belts and slope topography

Deep-water fold and thrust belts are a common feature of many submarine environments both along active and passive margins (Morley et al., 2011). On passive margins, they form when thick sedimentary sequences are deposited on top of either salt or shale (weak detachments), which trigger the deformation of the entire slope system by the processes of gravity gliding and/or spreading (Morley and Guerin, 1996; Rowan et al., 2004; Peel, 2014). Deformation is accommodated by upslope extension and downslope contraction, however, in a variety of styles where the development of arrays of folds and thrusts is the most common, particularly above shale substrates (Damuth, 1994). The growth of these thrusts and folds, and other structures such as salt diapirs and walls, deforms and creates topography on the seabed, which changes from a graded (undeformed) profile to an above-grade state (Prather et al., 1998; Figure 1-3).

Above salt detachments, when the rates of substrate deformation outpace those of sedimentation (as in the Gulf of Mexico), the intrusion of salt diapirs creates fully enclosed, intra-slope minibasins and the slope profile is termed "ponded above grade" (Prather et al., 1998). Shale-based substrates (e.g. Niger Delta) are argued to have lower mobility and are unable to create fully-enclosed ponded accommodation space, resulting in a "stepped above grade slope profile" (Prather, 2003; Figure 1-4), but values for deformation rates are not provided. However, Steffens et al. (2003), who made a comparative bathymetric analysis of four siliciclastic continental margins (Gulf of Mexico, Angola, Nigeria and NW Borneo) reported that at present-day, in the Niger Delta, ponded accommodation is, indeed, areally small and restricted to the lower slope between strike-oriented active toe-thrust folds, whereas healed slope accommodation is uniformly thin on the upper and middle slope. Healed-slope accommodation space, as defined by Steffens et al. (2003), "*is the space between the top of ponded accommodation and below a 3D convex hull fit to the rugose seafloor topography*". On shale-based stepped slopes this type of accommodation space is strike-oriented and elongated, and common processes include the deflection of submarine channels around topographic highs. Prather (2000, 2003) states that when ponded accommodation space is not present "*the sand content of the entire slope system can drop, because there is less accommodation to capture sandy gravity flow deposits*", and, therefore, it becomes crucial to have an accurate model to predict sand distribution on such shale-based slopes.
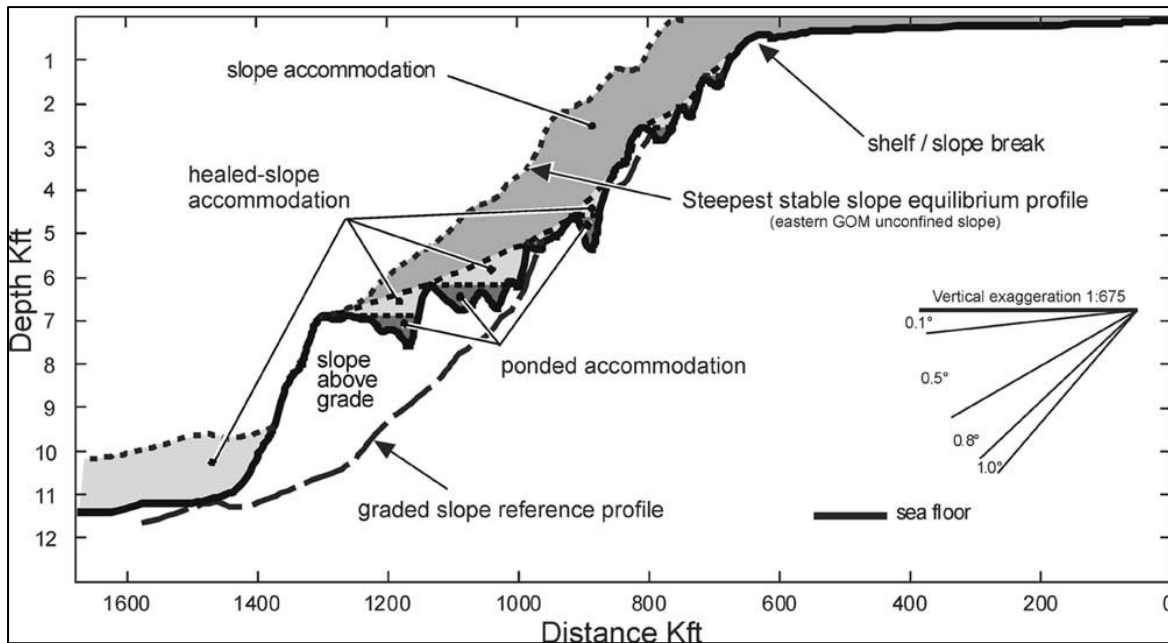
Figure 1-3: Slope profile from the central Gulf of Mexico showing distribution of different types of accommodation spaces. From Prather, 2003.
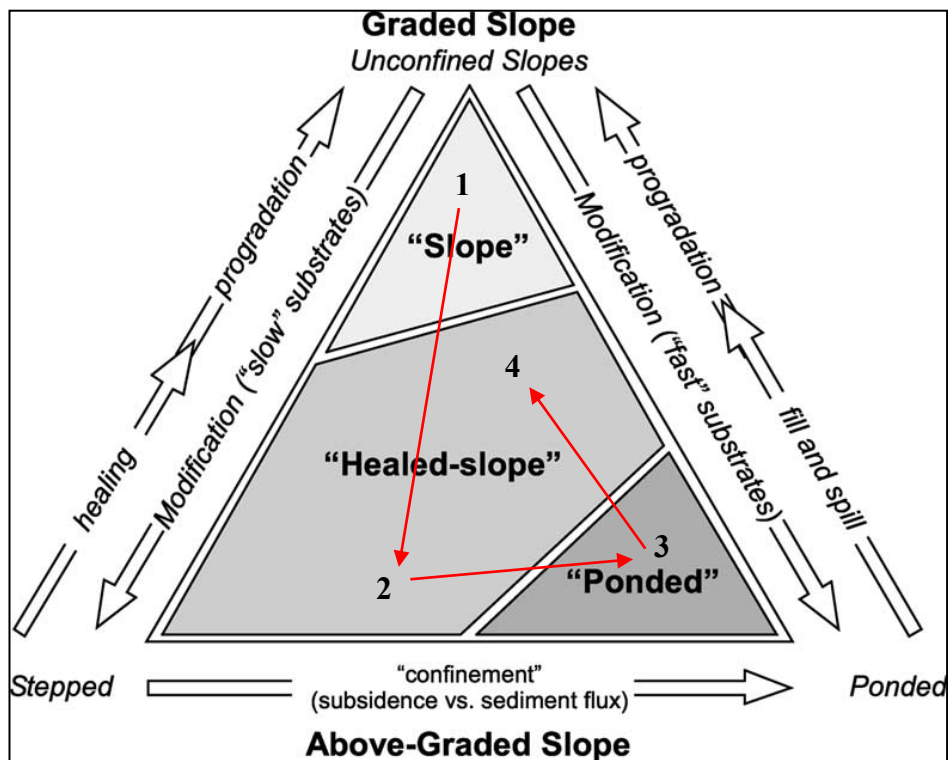
Figure 1-4: Ternary diagram showing key slope processes controlling types of accommodation space present on different slopes. Predicted evolution of the studied toe-thrust region is also plotted from time 1 to 4. Modified from Prather, 2003.

The first step to achieve an accurate prediction requires good constraints on the temporal and spatial variations in structural activity. The growth of folds, in both terrestrial and submarine environments, is generally expressed and tracked by identification of growth sequences, which

9

can give indication of the folding style and the relative rates of uplift and sedimentation; (Suppe et al., 1992; Burbank and Verges, 1994; Burbank et al., 1996; Verges et al., 1996; Rowan, 1997; Salvini and Storti; 2002; Shaw et al., 1999, 2004; Corredor et al., 2005; Morley and Leong, 2008; Morley, 2009; Clark and Cartwright, 2012a, b; Eichelberger et al., 2015; Figure 1-5). Growth sequences are characterized by stratal thinning or onlap onto the fold crest and thickening into both fold limbs.
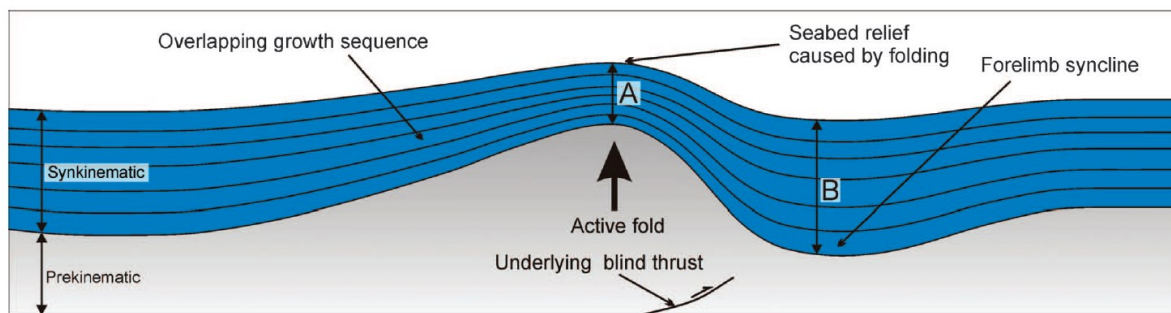
Figure 1-5: Example of overlapping growth sequence showing stratal thinning over fold crest. B-A represents the cumulative fold uplift occurred during the deposition of the syn-kinematic sequence. Note that the top of the pre-kinematic sequence is placed at the first occurrence of visible growth strata. From Clark and Cartwright, 2012.

By tracking the first clear occurrence of onlap relationships, Kreuger and Grant (2011), reconstructed how the intensity of deformation changed along strike and through time in the toe-thrusts of the Niger Delta, using a qualitative approach.

Recently, authors have started to address the along and across strike structural variations of folds and thrusts (Higgins et al., 2009, Bergen and Shaw, 2010; Clark and Cartwright, 2012a, b; Totake et al., 2018) and how that might affect deep-water sedimentation (Mayall et al., 2010; Clark and Cartwright, 2012a, b; Jolly et al., 2016). To date, only two studies have attempted to add a time perspective to the growth of thrust-folds (Jolly et al., 2016; Don et al., 2019), however, only Jolly et al. (2016) have done it quantitatively. Because growth packages developed in deep-water settings contain channel-levee complexes and other deep-water facies (Morley and Leong, 2008; Morley, 2009; Clark and Cartwright, 2012a, b), and given the sensitivity of the channel systems to growing topography (Mayall et al., 2010), Don et al. (2019) have used patterns of distribution of channels in the Niger Delta to model and document that thrust-folds grow by both lateral propagation and with constant length, or a combination of the two. However, the continued use of growth packages as only indicators of tectonic activity limits the analysis to a qualitative assessment and assumes that any deeper stratigraphic section present below the base of the growth packages is purely pre-kinematic. Jolly et al. (2016), using line-length balancing, have instead proved that the start of tectonic activity in the Niger Delta can be placed below the base of the clear growth strata and that the growth of folds

followed periods of low and high strain rates. It follows that deep-water sedimentary systems interacting with early growing fold and thrusts might have been overlooked, yet they would respond to any subtle topography (Mayall et al., 2010), such that comparisons of the architecture and distribution of these early systems with those developed within the shallower growth packages cannot be made nor predicted.

Therefore, one of the aims of this PhD work is to significantly expand the work done by Jolly et al. (2016) and to fully quantify and reconstruct the growth of folds and thrusts both along and across-strike and through time to create a robust structural framework to be linked to the changing stratigraphic architecture.

1.2.3 Interaction between deep-water sedimentation and growing seabed topography

Original models for clastic deposition in deep water environments date from the early 1970s (Normark, 1970; Mutti and Ricci Lucchi, 1972; Walker, 1978). These models were applicable to topographically unconfined settings where the slope region was not affected by deformation. The deep-water environment was divided into an upper fan located between the shelf and upper slope characterized by a deeply incising feeder canyon that connected the shelf staging area to the slope (fan valley), which transited downslope into a mid-fan environment comprising leveed channels, and a lower fan on the basin plain where the deposition of low-leveed distributary complexes and sheet sands/depositional lobes occurred (Bouma, 2004; Figure 1-6). The variability of these systems was argued to reflect their grain size (mud or sand rich) and the type of feeder system (point versus linear source; Reading and Richards, 1994). Example of these systems are represented by the Congo/Zaire deep-sea fan (Babonneau et al., 2002; Savoye et al., 2009). However, it has been later recognized that on passive margins affected by gravity tectonics (Damuth, 1994; Rowan et al., 2004), the creation of seabed topography on the slope can fundamentally alter the architecture, distribution and stacking of the deep-water elements at a range of scale; from the fill of individual channels (Mayall et al., 2010) to the large scale arrangement of the entire turbidite system (Sprague et al., 2005; Figure 1-7).
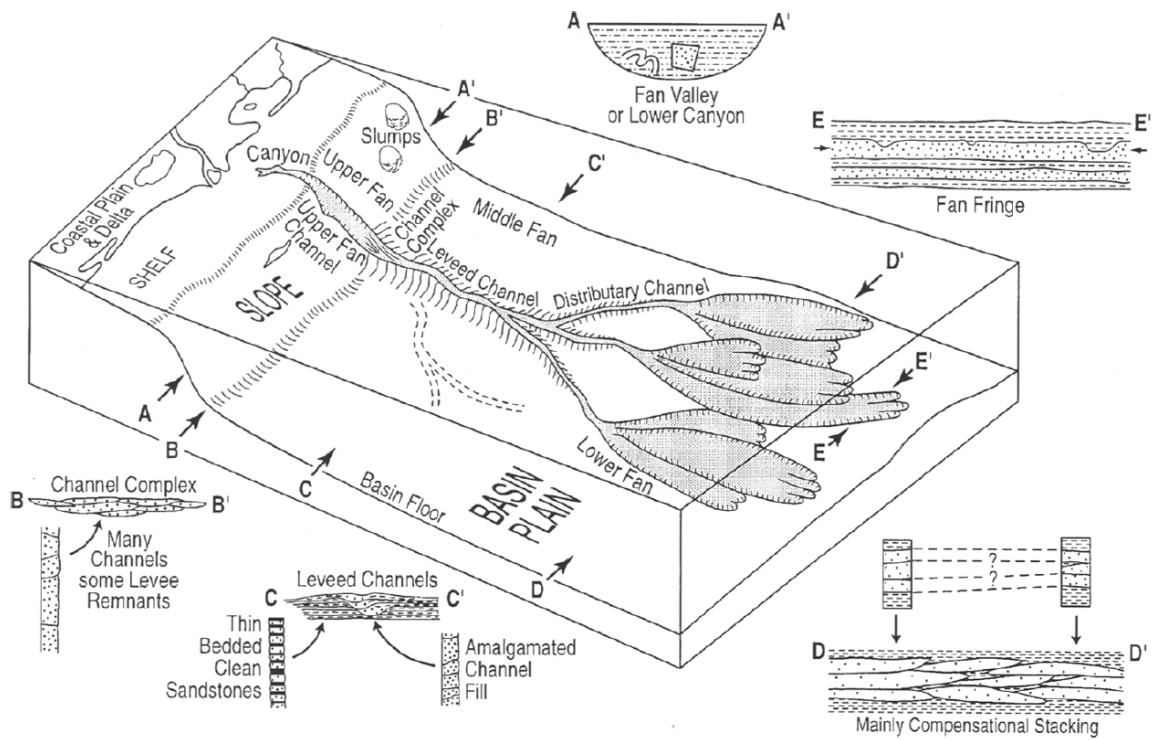
Figure 1-6: Model of topographically-unconfined fine-grained turbidite systems. From Bouma, 2004.
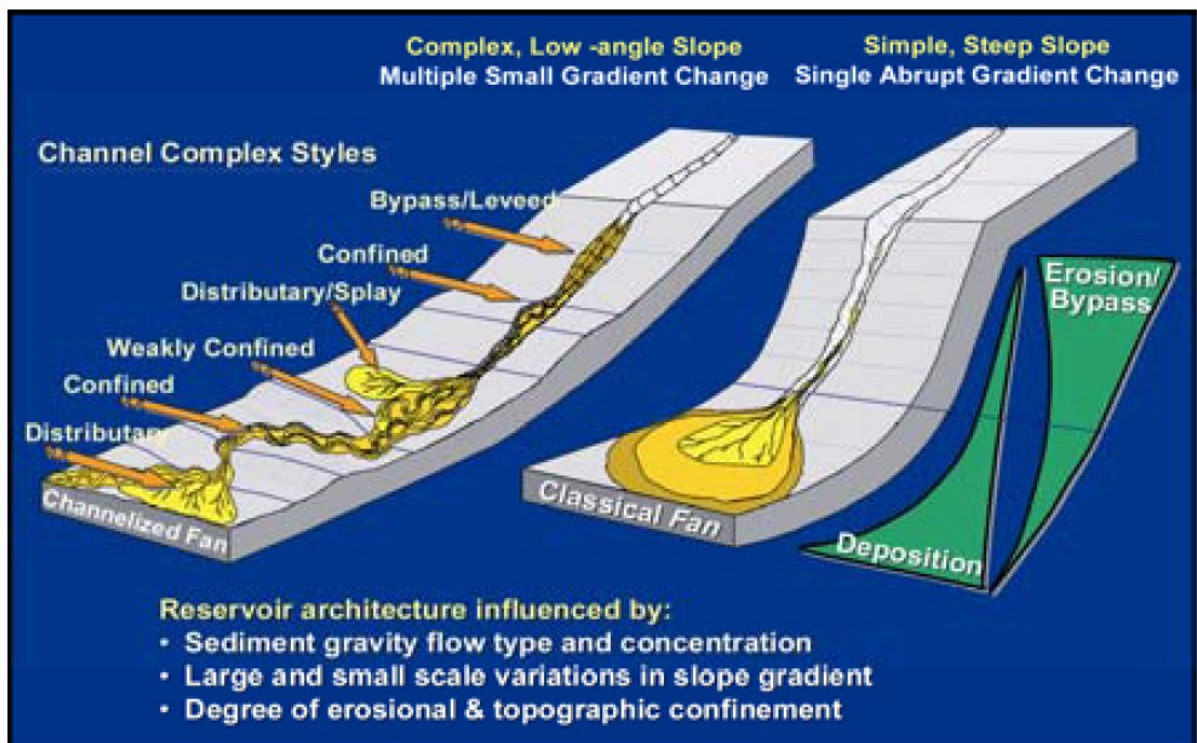
Figure 1-7: Comparison between simple and topographically-complex slopes. Note how sedimentary architecture changes down slope in response to variations in slope gradient. From Sprague et al., 2005.

The interaction between deep-water sedimentation and seafloor topography was originally addressed in the Gulf of Mexico (GOM) with seismic-based studies with the work of Winker (1996) and Prather et al. (1998). The latter recognized that deep-water sequences in the GOM consisted of two main assemblages which reflected the fill and subsequent spill over the barrier created by salt diapirs and walls. While the deeper ponded facies assemblage consisted of sand-prone beds, deposited in intraslope minibasins and blocked against pre-existing, static barriers, the shallower facies assemblage consisted of shale-prone units which reflected the bypass of flows towards deeper and more distal minibasins.

Subsequent work, conducted in the Alps by Sinclair and Tomasso (2002), integrated the seismic evidence with outcrop data to better characterize the fill of these confined turbidite basins. They suggested that while flows were totally trapped in the deeper parts of the salt-withdrawal minibasins, the sand-to-mud ratio of the flows increased upwards as the more dilute part of the flow escaped over the confining topography.

The effect of topography on turbidite sequences/flows, however, is not exclusively expressed as complete confinement within enclosed minibasins. In fact, many other studies, particularly on the west African margin, Mediterranean and Borneo (Hooper et al., 2002; Fonnesu, 2003; Shaw et al. 2004; Smith 2004; Adeogba et al., 2005; Gee and Gawthorpe, 2006 and 2007; Morley and Leong, 2008; Clark and Cartwright, 2009, 2011, 2012a, b; Callec et al., 2010; Mayall et al., 2010; Prather et al., 2003 and 2012; Hay, 2012; Oluboyo et al., 2014; Jolly et al., 2016 and 2017; Don et al., 2019), experimental studies (Ge et al., 2017, 2018; Howlett et al., 2019) and outcrop studies (Haughton, 2000; Hodgson and Haughton, 2004) have documented and modelled flows deflected and diverted by growing topography on the seabed without the need for complete containment or, at most, with temporary containment (e.g. transient fans; Adeogba et al., 2005). In this case submarine channels can be directly connected across different sub-basins through a network of tortuous corridors (Smith, 2004; Figure 1-8), a scenario that is particularly characteristic of topography induced by the growth of buried (or partially buried) thrust-sheets that form large deep-water fold and thrust belts (e.g. Niger Delta, Borneo, Barbados accretionary prism).
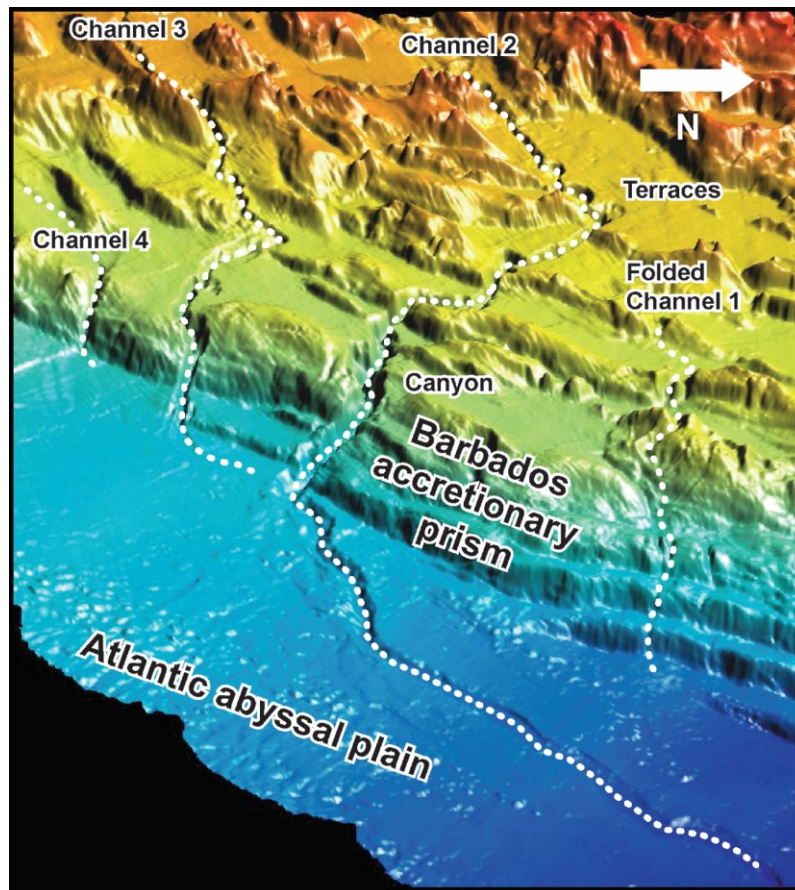
Figure 1-8: Bathymetry of the Barbados prism showing seabed channels deflected around slope irregularities but connected and converging within the abyssal plain. From Callec et al., 2010.

Along these topographically complex slopes sedimentation may interact with topography in the form of channels showing variations in sinuosity, in their aggradational or erosional character and asymmetry of the overbank deposits (Clark and Cartwright, 2009, 2011, 2012a, b). Alternatively, deposition can take place as an original phase of lobe deposition which is then followed and eroded by a bypass channel (Fonnesu, 2003; Adeogba et al., 2005; Hay, 2012). Effectively these different types of interaction depend upon variation in accommodation space, the relative rates of deformation versus sedimentation as well as variation in the slope profile. For example, Clark and Cartwright (2011) suggest that localised increase in accommodation space within the synclines between subsequent folds results in channel aggradation and increase in sinuosity over time, whereas increased erosion and a decrease in sinuosity is observed when channels cross over the fold crests where accommodation space locally decreases (Clark and Cartwright, 2011 and 2012). The same responses of channels to deformation were previously suggested by Pirmez et al. (2000) and Ferry et al. (2005) with the concept of an equilibrium profile as erosion and deposition are the main processes through which slope channels adjust their longitudinal profile when it is perturbed by modification of the slope profile (Pirmez et al., 2000). Along an idealized sigmoidal-shaped slope profile,

induced by tectonics, the convex segments (increased slope) will experience erosion and channels will decrease sinuosity whereas levees and sinuosity will be both well-developed along concave reaches of the slope where gradient decreases (Ferry et al., 2005; Figure 1-9).
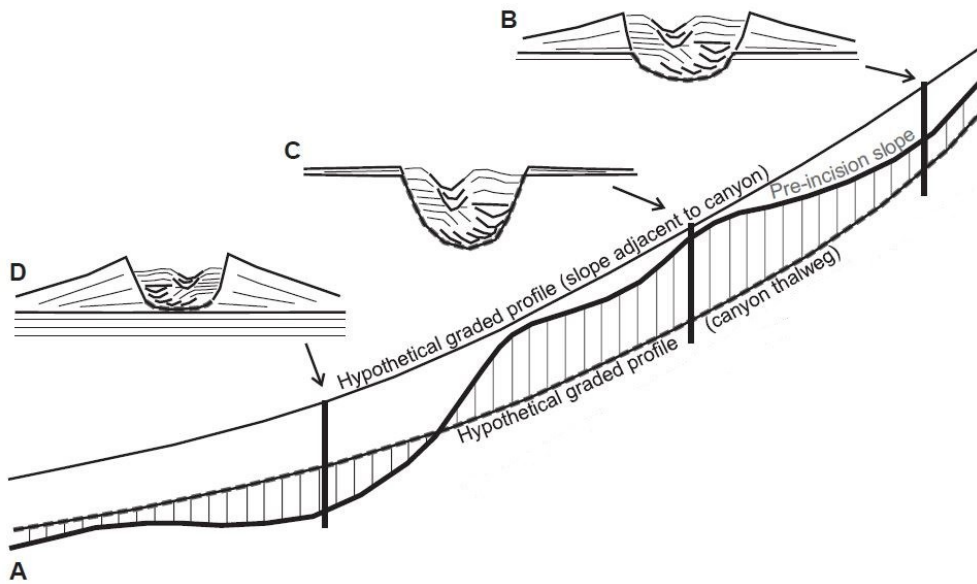
Figure 1-9: Development of different external channel architectures in response to pre-incision slope morphology with respect to hypothetical graded profiles. From Deptuck et al., 2012.

In effect, most of the previous studies addressed how sedimentary systems respond to topography along what Prather (2003) defines as a stepped above-grade slope to emphasize the fact that the slope has a terraced topography characterized by steeper and flatter intervals. As previously mentioned, along these slopes the common stratigraphic evolution may comprise an initial phase of lobe deposition (perched aprons or transient fans) along the flatter intervals of the stepped slope, which results in the smoothing of the topography and leads to the subsequent phase of sediment bypass within channels as the slope irregularities are healed (Fonnesu, 2003; Adeogba et al., 2005; Prather et al., 2003 and 2012; Deptuck et al., 2012; Hay, 2012; Figure 1-10).
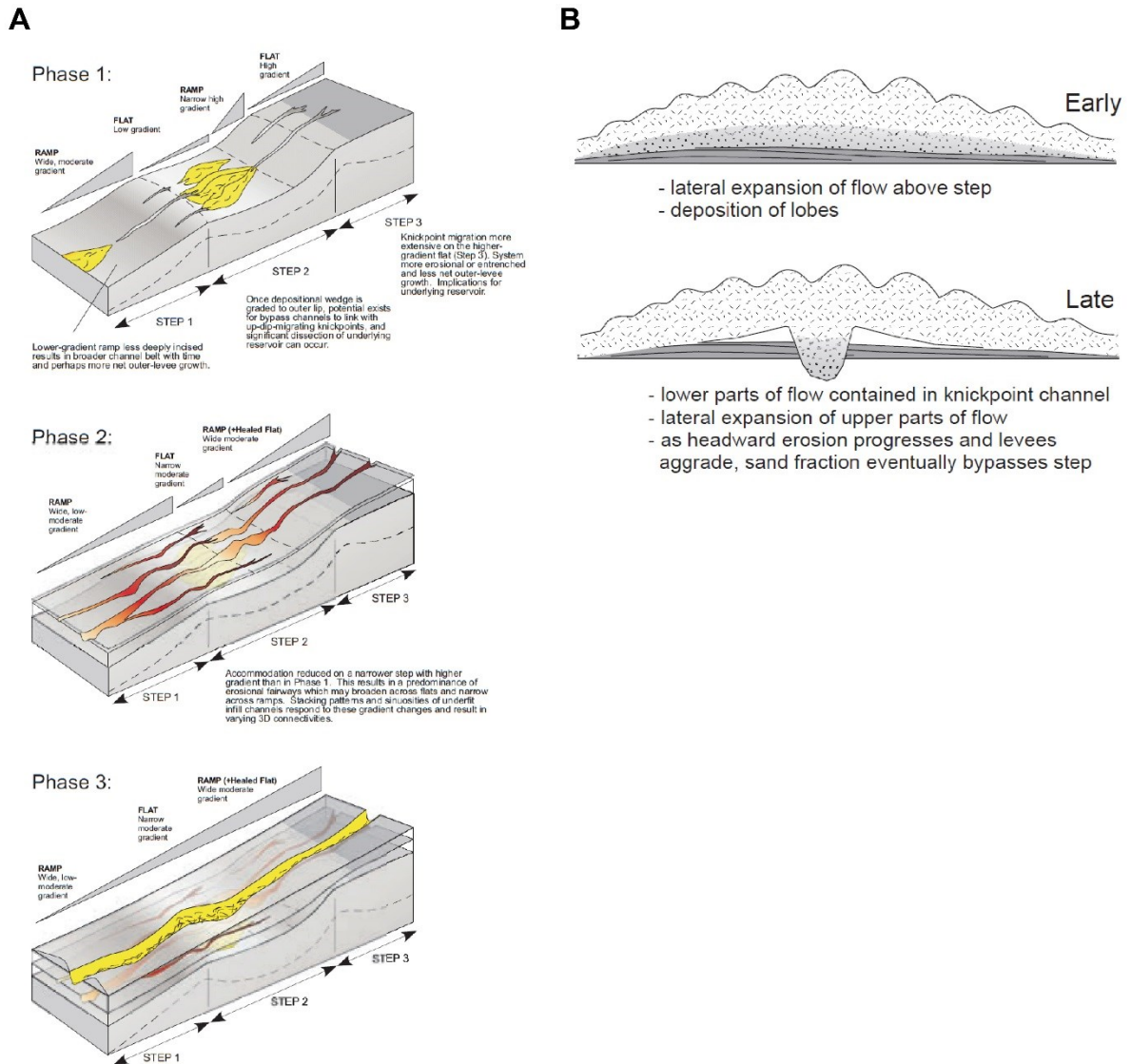
Figure 1-10: A) Sequence of lobe deposition on the flatter intervals of a stepped slope, followed by erosion and bypass channels as the slope irregularities are healed. From Hay, 2012. B) Same sequence of events and resulting deposits seen on strike section. From Deptuck et al., 2012.

Larger-scale interactions between submarine channels and topography along stepped slopes are also expressed as avulsions and large diversions around the emergent fold even in conditions of little relief (Kolla, 2007; Clark and Cartwright, 2009, 2011, 2012a, b; Cross et al., 2009; Mayall et al., 2010; Jolly et al., 2016; Don et al., 2019; amongst others). In fact, it has been shown that structural variations along the strike of thrust-folds can lead to the focal points of uplift to vary both temporally and spatially (Clark and Cartwright, 2012) and force the channels to cross folds at the position of recent strain minima (Jolly et al., 2016). Some authors have highlighted that while slope channels can exhibit topographic response by way of confinement, diversions, deflection and blocking (Clark and Cartwright, 2009), there are no examples of channels cross-cutting structures (Georgiopoulou and Cartwright, 2013). However, Mayall et al. (2010) suggest that channels with low erosive power can be deflected

16

by subtle topography, but those with high erosive power can keep pace with the growing structure and cut across it (Mayall et al., 2010; Jolly et al., 2017). In general, Mayall et al. 2010 propose that the size, shape and orientation of the structures, the relative timings of growth and channel initiation and development, and the erosive power of the channel will all affect the observed sedimentary response. Another key issue to address is whether the observed relief of a fold reflects the maximum length and displacement of that fold or simply the portion that is emergent after sediment burial (Jolly et al., 2016) and where the channel is located relatively along its strike.

Despite this large amount of work which has significantly advanced our knowledge on the interactions between sedimentation and structurally-driven topography, it is mostly concerned with seabed or shallow sub seabed examples, within Quaternary sections, where the slope profile did not undergo major alteration and, therefore, has allowed authors to assess directly how sedimentary systems respond to topography. This implicitly means that, in order to study and predict sediment-structure interactions we either have to assume little or no deformation or we require detailed knowledge of the deformation history. Because the deformation history generally is the main unknown, to model the filling history of thick and long-term deformed sequences, authors have developed static models where different amounts of pre-existing topography on the seabed affects and are progressively filled and healed by sediments (Prather et al., 1998; Hay, 2012). The different amounts of existing topography may reflect the difference between stepped and ponded slopes; this depends on the rate at which the seafloor deform through time, where "slow" versus "fast" deformation is suggested to characterize the two, respectively (Prather, 2003); however, values for deformation rates have never been provided. Moreover, owing to the fact that both deformation and sedimentation rates likely change over time (Jolly et al., 2016), slope regions may have significantly altered their profile, over several Myr, and we are unable to reconstruct or assess this effect without constraining deformation rates first. As a direct result of the inability of restoring past seabed topography within older, more deformed, sections and the unknown evolution of deformation rates, predictive models for the overall stratigraphic evolution of thick (several km) slope successions above shale detachments have not been provided as yet. Jones et al. (2012) were the first to attempt to quantify and reconstruct the growth of folds and later Jolly et al. (2016) quantified the growth history of four folds in the toe-thrust region of the Niger Delta along and across strike and through time and demonstrated the importance of ascertaining deformation rates to better understand how channels interact with folds. This PhD work significantly expands the work done by Jolly et al. (2016) to eleven thrust-folds on the lower slope of the Niger Delta

over a much larger area (4500 km^2), aiming to fully constrain the deformation history of the area to then provide a predictive model that explains the architecture and distribution of deep-water sedimentary systems through time and space.

1.3 Geological setting of the Niger Delta

The Niger Delta is located at the southern, oceanward portion of the Benue Trough (Figure 1-11). This is a NE-SW folded rift basin that runs across Nigeria and formed during the Lower Cretaceous opening of the Equatorial Atlantic. The first clastic deposits date to the Early Eocene and, over approximately 55 Ma, nearly 12 km of sediments have been deposited in its thickest parts. From a lithostratigraphic perspective, its fill has been historically divided into three diachronous formations: The Benin, Agbada and Akata Formations. The Benin Formation is deposition in a delta-top environment; The Agbada Formation deposition in a delta-front environment; and the Akata Formation represents pro-delta facies. However, both the Agbada and Akata Formations are also present further offshore and, as such, there they consist of basinal and slope shales, and deep-water turbidite sands and mass-wasting deposits, respectively. The entire sedimentary fill has been divided into eleven third-order cycles consisting of strata bounded by maximum flooding surfaces contained within transgressive shales, which define regional marker horizons, and create regular alternations of sands and shales (see Short and Stauble, 1967; Evamy, 1978; Knox and Omatsola, 1989, Stacher, 1995, Reijers et al., 1997; Reijers, 2011 for additional information).
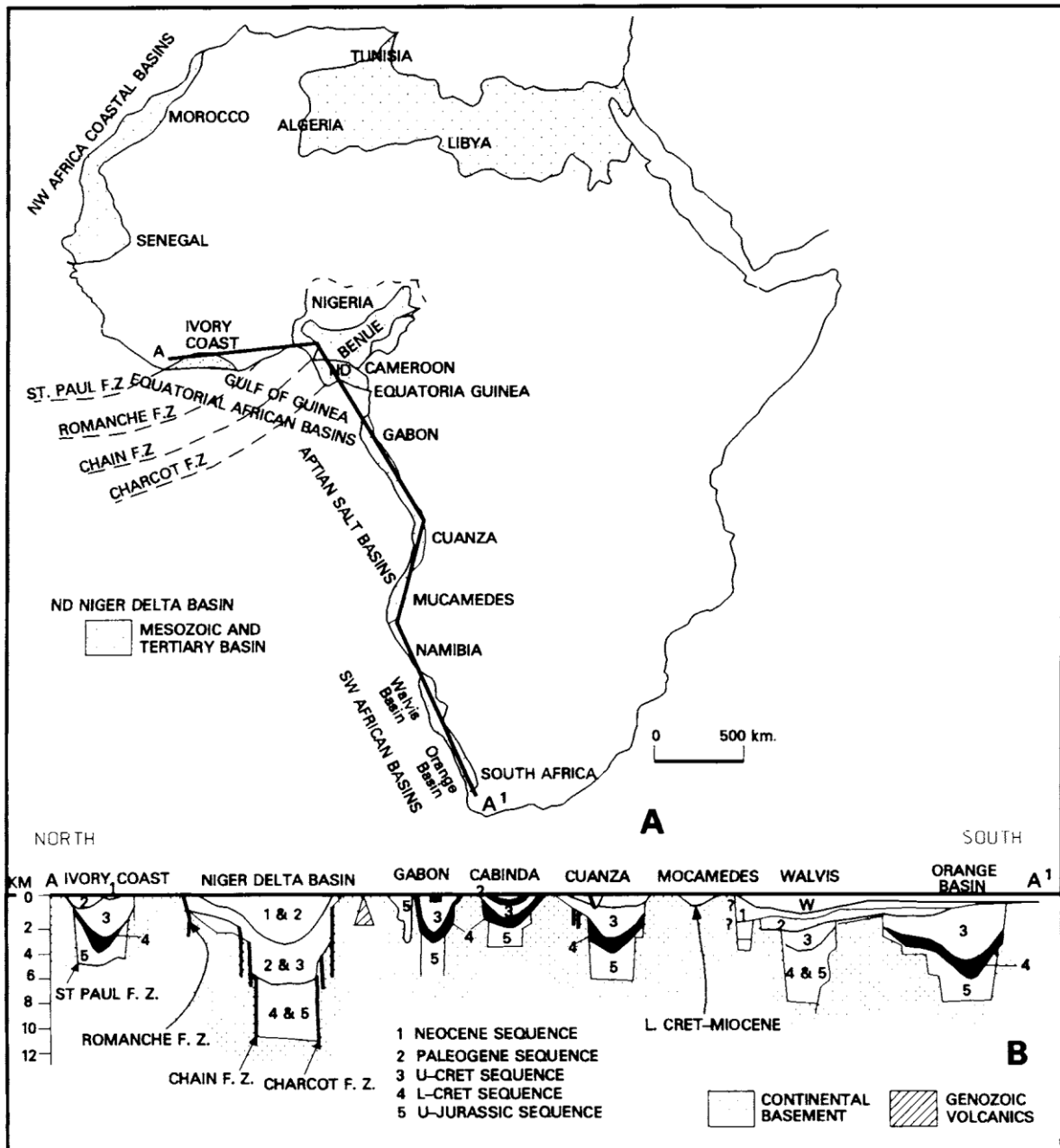
Figure 1-11: Regional setting of the Niger Delta basin. From Reijers et al., 1997 (after Emery et al., 1975; Dingle, 1982)

Since the Miocene the delta has deformed due to gravity tectonics (Damuth, 1994) that created a linked extensional-compressional system affecting the up dip and down dip regions, respectively. The gravity collapse occurred through multiple detachment levels present within the weak, overpressured shales of the Akata Formation (Bilotti and Shaw, 2005; Briggs et al., 2006; Cobbold et al., 2009), while the Agbada Formation is the main deforming unit. The deformation in the extensional domain has been accommodated by the development of regional and counter-regional normal listric faults in the delta-top area which have created a series of depobelts, younger in a seaward direction (Rouby et al., 2011). The up slope extension was

19

compensated by a variety of down dip compressional structures that affected both the Agbada formation and the shallower levels of the Akata shales. The styles are represented by fault-bend folds and shear fault-bend folds, fault-propagation folds, faulted detachment folds, front and back thrusts and mud diapirs. Corredor et al. (2005) divided this gravity systems into five structural domains, after the original subdivision of Damuth (1994), shown in Figure 1-12:

1. An extensional zone beneath the continental shelf;
2. A mud-diapir zone (Morley and Guerin, 1996);
3. An inner fold and thrust belt;
4. A transitional domain with large detachment folds;
5. An outer fold and thrust belt (focus of this study).

The outward radial gravity spreading of the Delta has produced two contractional toe-thrusts lobes (this study focuses on the southern lobe), separated by the Charcot fracture zone, and segmented by oblique extensional tear faults that accommodate lateral contractional gradients (Wu and McClay, 2015).

The delta has prograded through time at variable rates (Reijers, 2011) starting at 2 km/Ma from the Late Eocene to Middle Oligocene. Progradation rates reached the apex during the Miocene (16-22 km/Ma; see also Wiener et al., 2010) and decreased in the Pliocene (13-17 km/Ma). This was followed by a retrogradation/aggradation of the delta in response to a decreased sediment supply that Jermannaud et al. (2010) attribute to the aridification of West Africa during the Pleistocene. This progradation resulted in the coeval seaward migration of the linked gravity system, such that the earliest thrust-folds of the contractional domain are today found below the extensional upper slope (Hooper et al., 2002). Since the deformation in gravity systems is driven by sediment supply (Rowan et al., 2004), Rouby et al. (2011) and Jolly et al. (2016) documented a recent (ca. 4 Ma) decrease in deformation rate in the extensional and outer contractional domain in the Eastern Niger Delta, respectively, and linked it to the decreased sediment supply during the Pleistocene. On the other hand, in both the transitional domain and outer fold and thrust belt, Kreuger and Grant (2011), Jolly et al. (2016) and Sun and Liu (2017) document that deformation started between 15 and 9 Ma, however, with the period of main deformation after 9 Ma (Kreuger and Grant, 2011; Jolly et al., 2016). During the Pliocene, Reijers (2011) also documents the occurrence of "*catastrophic gravity events*" that the author relates to the coeval activity along the Cameroon volcanic line, and which resulted in high sedimentation rates.
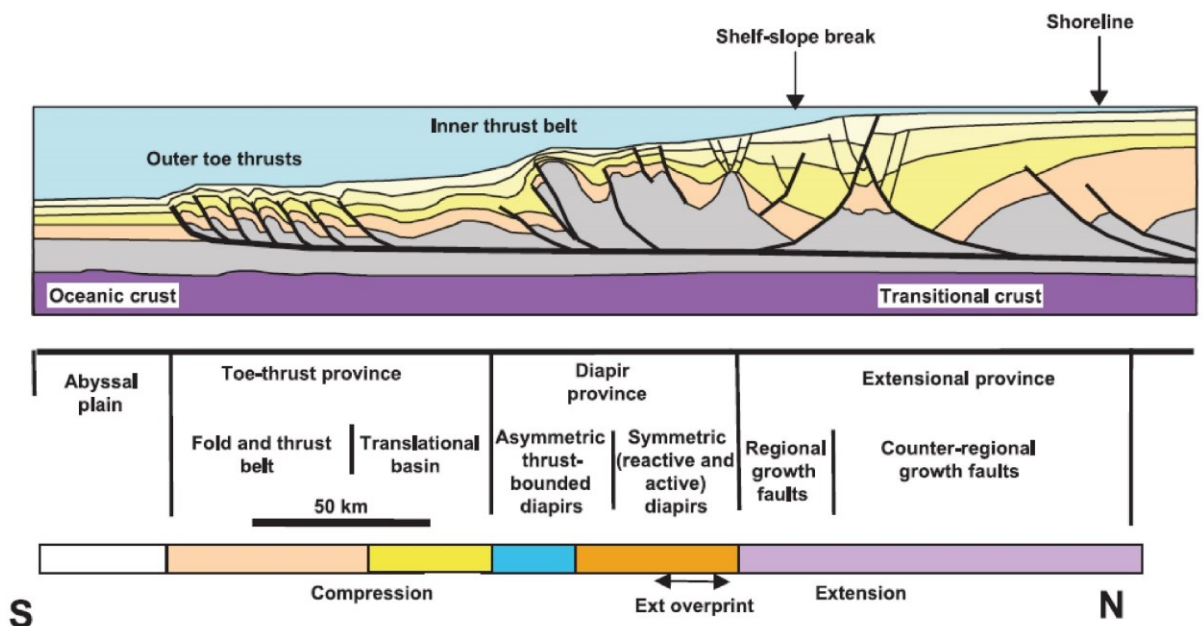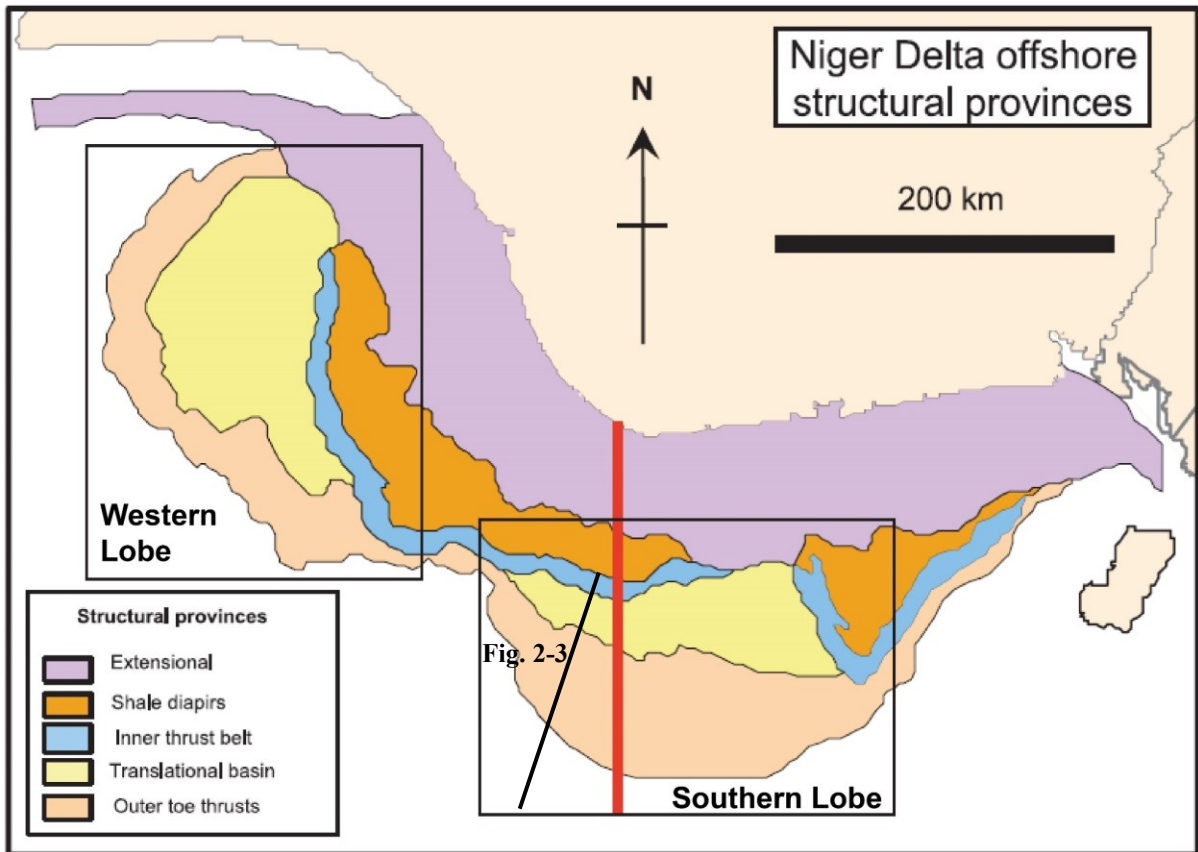
Figure 1-12: Structural zones of the offshore of the Niger Delta region. Modified from Krueger and Grant, 2011.

The Niger Delta has been modelled as a critical taper wedge (Bilotti and Shaw, 2005). Its anomalous low taper and surface slope is thought to result from the overpressures generated in the basal detachment, as also documented by Morley (2007) for NW Borneo fold and thrust belt. Additionally, the widespread occurrence of back-thrusts is a consequence of the low taper where the maximum compressive stress is subhorizontal (Bilotti and Shaw, 2005). The large

transitional domain which separate the inner and outer fold belts results from the stable sliding of a wedge where the taper is built by sediments, rather than deformation (Bilotti and Shaw, 2005). Finally, Corredor et al. (2005), using the geometry of growth stratal patterns and section restorations, document that thrusts in the outer fold belt developed with break-forward and break-backward propagation as well as coeval thrusting.

The interaction of deep-water turbidites with the growth of thrust-folds meant that reservoir facies could have been later folded and trapped into structural anticlines, however, potential for mixed and stratigraphic traps has also to be assessed. To this end, reconstructing the detailed spatial and temporal growth of structures is crucial to assess the relative timings of deposition and deformation and to unravel the dominant facies architecture and trap style throughout the growth history of the outer fold belt.

1.4 Aims, objectives

The goal of this thesis is to quantitatively investigate the interaction and relationships between the growth of a deep-water fold and thrust belt and the coeval sedimentation to predict the distribution and architecture of deep-water facies through time and space. To achieve this, the workflow has been developed to answer three main aims and questions, which are, in turn, divided in a series of intermediate objectives. The main aims are:

Aim 1: Reconstruct, quantitatively, the growth of an interacting fold and thrust array through time and space;

Aim 2: Assessing the evolution of the overall stratigraphic architecture both in terms of basin configuration and geometry, and occurrence, architecture and distribution of deep-water facies;

Aim 3: Integrating the structural and stratigraphic information to assess their mutual relationships and to derive a predictive model for the distribution and architecture of deep-water facies in time and space.

The **first** aim was addressed through the following intermediate objectives:

1.1 The regional seismic-stratigraphic mapping of the key age horizons and the structural mapping of the entire fault array within the study area over 4500 km^2;

1.2 Selection of seventeen dip profiles to cover the entire strike length of the study area. Therefore, shortening and strain were measured, through line-length balancing, to

reconstruct the individual growth of each thrust-fold, along each of the seventeen dip profiles;

1.3 The growth of the thrust-array was reconstructed, for the first time, through assessing how strain and shortening varied both along and across-strike, and through time.

The **second** aim was divided in the following objectives:

2.1 Subdividing the larger study area into four areas to analyse independently the depositional characteristics of individual receiving basins/depocenters;

2.2 Identifying and classifying the facies present within each stratigraphic interval (e.g. different types of submarine channels and lobes/sheets). Hence, identifying predictable patterns in the vertical change and transition in facies architectures through time; and comparing the occurrence of specific facies types between the four areas;

2.3 Creating a series of isopach maps for each stratigraphic interval to assess the broad evolution of the geometry and configuration of the receiving basins, qualitatively. Subsequently, sediment accumulation rate maps were derived to assess if and how accumulation rates changed over time and to link these to deformation rates, qualitatively;

2.4 Mapping the spatial distribution of sedimentary systems, hence the routing system, and assess how it changed through time.

The **third** aim focuses on the integration of the structural and stratigraphic analysis, and has been divided as follows:

3.1 Assessing to what extent the vertical change in seismic facies is linked and dictated by the structural evolution of the fault array;

3.2 Coupling the distribution of sedimentary systems with that of strain rates on a series of time slices to understand how structures have controlled the drainage network, including the number of pathways at each time interval and the specific locations where channels cross faults;

3.3 Developing a predictive model to explain the location, timing of occurrence and architecture of sedimentary facies and their relationship to how faults interact in 3D.

1.5 Thesis Outline and Structure

This thesis consists of a methods chapter, four research chapters, a discussion, and a conclusion. The content of chapters 3, 5, 6 and 7 provides stand-alone contributions to the literature. The methods chapter is meant to be a brief overview of the techniques employed in this PhD project, however, further details on the methodologies used is provided within each research chapter. Each research chapter comprises an introduction and methods sections, a results section, a summary/discussion and conclusions. The final thesis discussion brings together and synthesizes the results of the individual research chapters to fulfil the aims and objectives stated in **aim 3**, however, each of the research chapters partially contributes to meet those objectives.

Chapter 2 presents the 3D seismic dataset used for the stratigraphic and structural interpretation and the sources for dating the key stratigraphic horizons. The chapter also lists, and briefly describes, the techniques used in all the subsequent chapters and, when needed, will reference the appropriate result chapter for more details.

Chapter 3 focuses exclusively on the structural evolution of the study area (**aim 1**). In this chapter I investigate and quantify, through line-length balancing, how thrust-folds, both as individual entities and as part of an array, growth and interact with time. This strain analysis forms the basic framework for all the subsequent stratigraphic and facies analysis to assess and quantify the structural impact on deep-water sedimentation. Here, I will present strain-distance plots along the strike of each thrust-fold and how strain was accumulated with time as well as a sequence of map-views to show how strain rates were distributed during each time interval. This chapter forms a stand-alone study as it documents, for the first time, the sequence of thrusts nucleation, propagation and linkage in 3D, which has allowed me to develop a new general model for thrust growth. This work is in final preparation for publishing in the Journal of Structural Geology as: Pizzi, M., Lonergan, L., Whittaker, A. C., Mayall, M., *Growth of a thrust fault array in space and time: an example from the deep-water Niger Delta.*

Chapter 4 focuses on seismic facies analysis. Here, seismic sections are used in conjunction with RMS amplitude extractions to inspect and classify the range of different facies architectures present in the study area with the aim of identifying patterns in their vertical evolution (**objectives 2.1 and 2.2**) and to start to assess their link to structural development (**partially objective 3.1**). Implications for hydrocarbon prospectivity are also discussed. This chapter does not form a stand-alone paper, but it was needed to synthetize the large variability in deep-water facies and elements.

Chapter 5 focuses on the evolution of the stratigraphic architecture and how the geometry of the receiving basins changed over time (**objective 2.3**). This chapter, additionally, integrates the results of chapter 3 and 4 with the mapping of the distribution of the routing systems through time (**objective 2.4**). The mapped sedimentary systems are coupled with strain data to continue to investigate the tectonic forcing on the location and architecture of deep-water facies (**partial aim 3**). In particular, this chapter demonstrates the close link between the progressive growth of a fault array and the response of the sedimentary systems both in terms of modifications of the drainage network and the occurrence of specific facies types.

In **Chapter 6** I use the same data presented in chapter 5 and I conduct a further detailed statistical analysis with the specific objective of demonstrating the structural control on facies distribution in a more quantitative way (**objectives 3.1 and 3.2**). This chapter is written and should be read as a stand-alone paper to be summited to *Geology*.

In **Chapter 7** I synthetize the key research findings in an overarching discussion, which allows me to present a new model to predict sediments architectures and distributions during the growth of gravity-driven fold and thrust belts (**aim 3**). Finally, **Chapter 8** summarizes the main conclusions of the PhD work to highlight how it advanced our understanding of deep-water sedimentation on deforming slopes.

2. Data and methodology

2.1 Data and sources

A time-migrated 3D seismic reflection dataset provided by Petroleum Geo-Services (PGS) was used for the study. The dataset used covered the OPL (Oil Prospecting Licence) blocks 245 and 256 (Figure 2-1) in the deep-water of the Niger Delta and represents a total area of approximately 4500 km^2. The 3D seismic data volume was processed to near zero-phase and is displayed using Society of Exploration Geophysicists (SEG)-normal polarity. The data were migrated using Kirchhoff prestack migration and bending ray post-stack migration to generate a 12.5 m by 12.5 m grid with a 4 ms twtt sampling interval. The data were originally provided every four in-lines and cross-lines, giving a bin size of 50 m, which corresponds to the maximum horizontal resolution. Based on a frequency content of 35 Hz and average seismic velocities ranging from 1800 m/s (Plio-Pleistocene) to 4000 m/s (late Oligocene – early Miocene), the vertical seismic resolution (limit of separability) is estimated to range from 13 to 30 m, respectively. In July 2018 PGS provided the full seismic volume with 12.5 metre separation between each inline and crossline (Figure 2-2).

The seismic-stratigraphic and structural interpretation were first conducted on the lower resolution 3D volume following the principle of seismic-stratigraphy (e.g. Mitchum et al., 1977) by mapping the main unconformities (i.e. erosional truncations and onlap) as well as the regional marker horizons. In particular, the interpretation was guided by a confidential interpreted tie-line that Shell provided between two nearby wells and passing through OPL 256. The interpretation on the tie-line was calibrated with biostratigraphic data available to Shell and showed five key dated horizons (23.2, 15, 12.8, 9.5 and 7.4 Ma horizons). Therefore, the interpretation on this study originally followed these dated horizons with the addition of the 3.7 Ma horizon which was mapped mid-way between the 7.4 Ma and the seabed, hence, assuming a constant sedimentation rate during that interval. Subsequently this interpretation was checked and integrated with the ages in Krueger and Grant (2011) who showed a regional seismic line (Figure 2-3) passing entirely within the study area. This regional cross-section broadly confirmed the interpretation provided by Shell and included two more age horizons, which were also included in this study (5.5 and 6.5 Ma). These authors stated that they have used available well biostratigraphy, therefore, being able to date stratigraphy from the Oligocene to Holocene. All the mapped marker horizons were originally identified based on prominent characteristics and were then assigned the nearest age. The horizons up to and

included 7.4 Ma are all comprised within the lower stratigraphic section which only shows subtle thickness changes and sub-horizontal stratigraphy, therefore, generally assumed to be pre-kinematic. These horizons can all be identified by their marked high-amplitude, thick seismic wavelet and semi-continuous lateral extent, and were mapped as positive polarity (peaks; positive reflection coefficient). These horizons do not show evident erosional truncations, however, angular unconformities, and resulting thickening/thinning of stratigraphy, can be observed on the regional scale. The main issues associated with mapping these lower horizons are listed below:

- they are faulted by all the eleven thrust-faults which makes difficult their correlation across;
- they may pass laterally into dim reflections;
- they show thickness variations across fault blocks as the wedge stratigraphy thins in a seaward direction;
- on time-migrated data, velocity artefacts may alter the actual thickness of the units making problematic their precise correlation across faults.

The upper marker horizons (6.5 to 3.7 Ma) are generally easier to map regionally and are fully contained within the shallower growth stratigraphy. They are identified based on similar seismic appearance (polarity; amplitude) as the lower horizons, however, they bound clear, discrete growth packages and are associated with more evident erosional truncation surfaces and thickness changes. Moreover, they can be traced for longer distances as they are less affected by faulting, which allowed me to map them over the crest of folds into the next fault block with higher degree of confidence.
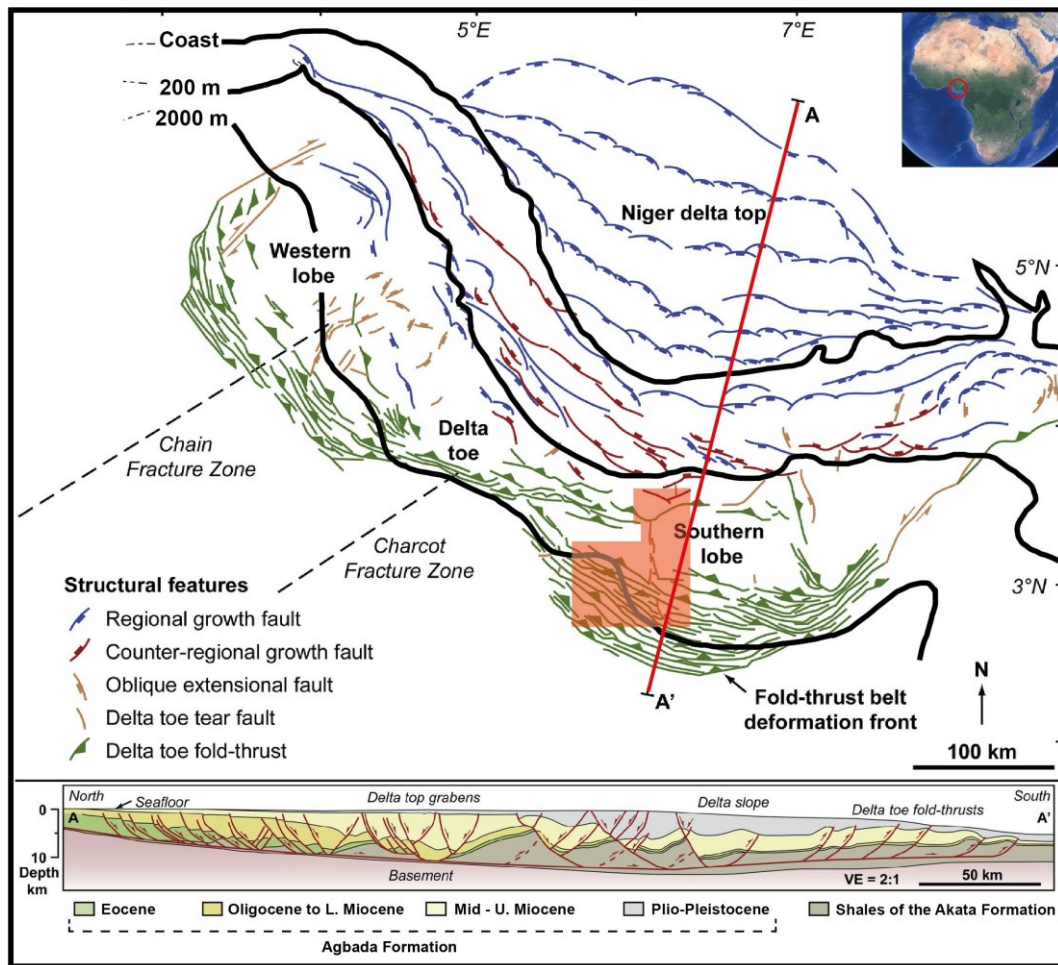
Figure 2-1: Structural map of the Niger Delta showing the up-dip extensional domain and the down-dip contractional zone (modified from Wu et al., 2015). The orange polygon is the extent and location of the 3D seismic cube used in this work.

To perform an accurate stratigraphic and structural interpretation and strain analysis (chapter 3), the 3D seismic volume was depth converted. Because of the lack of well data, the velocity-depth relationships were first derived from a published seismic section passing across the toe-thrusts of the Niger Delta which showed an overlay of the depth variation in interval velocity (Morgan, 2003; Figure 2-4). The depth-conversion (further described in chapter 3) was performed using the $V_0 - K$ relationship (Marsden, 1992; Smallwood, 2002) which assumes a linear velocity increase with depth, which was applied to the interval between the seabed and the base of the Agbada Formation; this assumption was confirmed by the velocity-depth variation shown by Morgan (2003) within the Agbada Formation. The most important variable in this method is the gradient, K, which is the rate of velocity increase with depth. Using the relationship between TWTT (two-way traveltime) and interval velocity shown by Morgan (2003), I calculated the depths and plotted these against the increment in velocity (Figure 2-5). This was repeated for seven locations along the seismic profile and yielded an average $K \approx 0.6$ s^{-1}. In July 2017 PGS provided root-mean-square (RMS) velocities along the easternmost inline

28

on OPL block 256. I converted these RMS velocities into interval velocities using the Dix equation:

$$V_{int} = [(t_2 V_{RMS2}^2 - t_1 V_{RMS1}^2) / (t_2 - t_1)]^{1/2},$$

Where, V_{int} = interval velocity, t_1 = traveltime to the first reflector, t_2 = traveltime to the second reflector, V_{RMS1} = root-mean-square velocity to the first reflector, V_{RMS2} = root-mean-square velocity to the second reflector. These confirmed the choice of the gradient, K, at 0.6 s^{-1}.
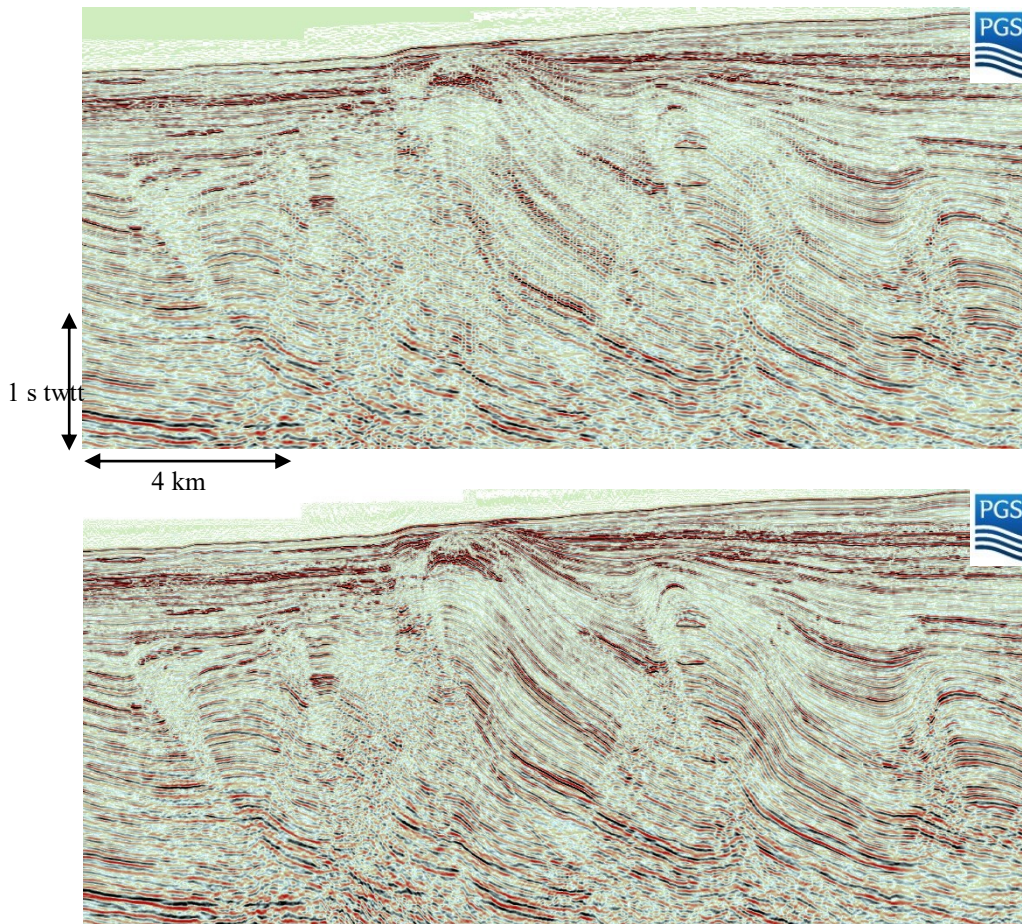
Figure 2-2: Examples of the same arbitrary seismic profile from the lower resolution seismic volume (above) versus the higher resolution volume (below).
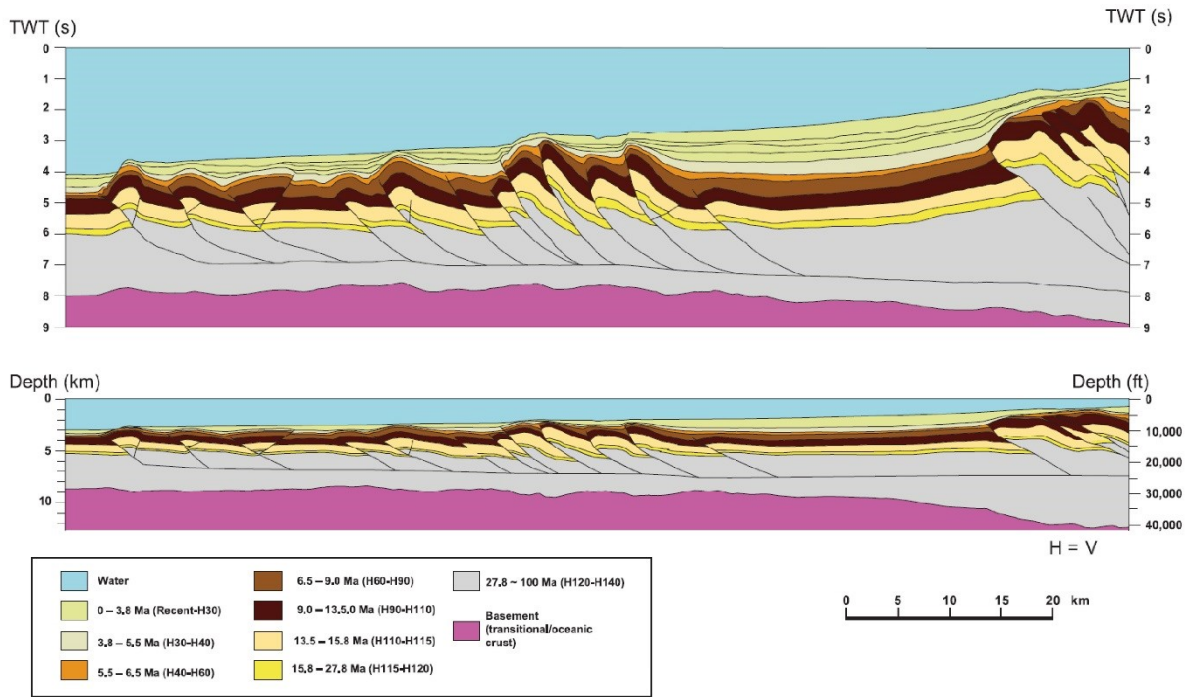
Figure 2-3: Time and depth sections of the outer fold and thrust belt of the southern lobe of the Niger Delta (location in Figure 1-12), showing the main stratigraphic sequences and age of the bounding horizons. This cross-section is fully imaged in the dataset used for the current study. From Krueger and Grant, 2011.
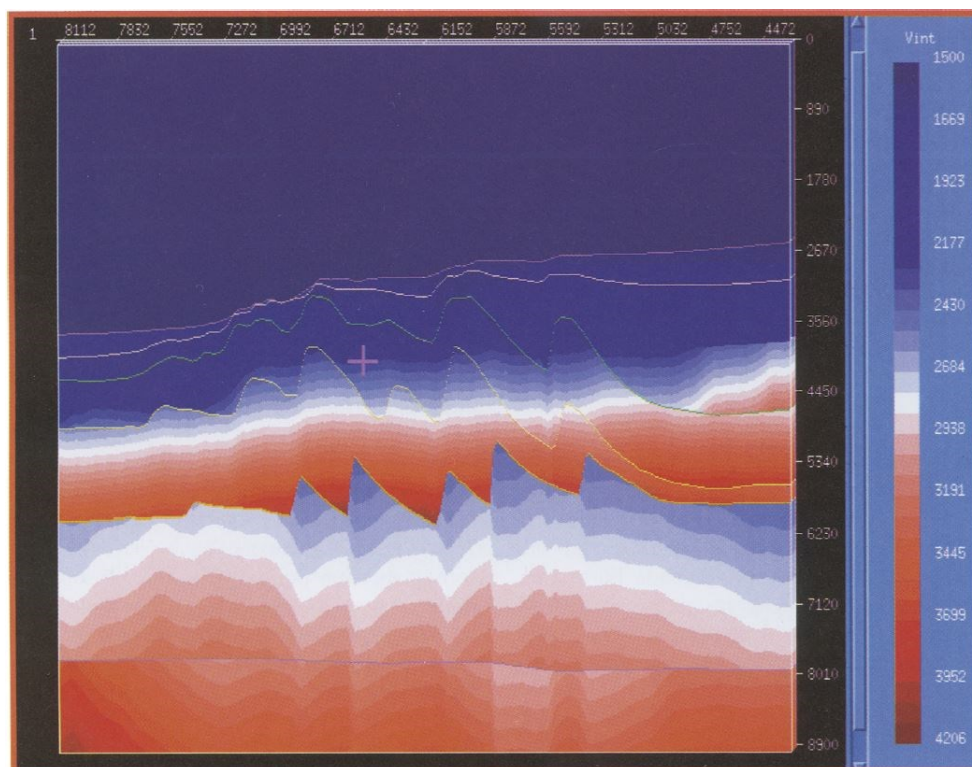
Figure 2-4: 2-D velocity model showing variation in interval velocity with depth. The velocity appears to increase almost linearly with depth, following the broad morphology of the seabed, while structures seem to have a minor effect on velocity. Note the reduction in seismic velocity below the base of the Agbada Formation, indicating high pore-fluid pressure within the Akata shales. From Morgan, 2003.
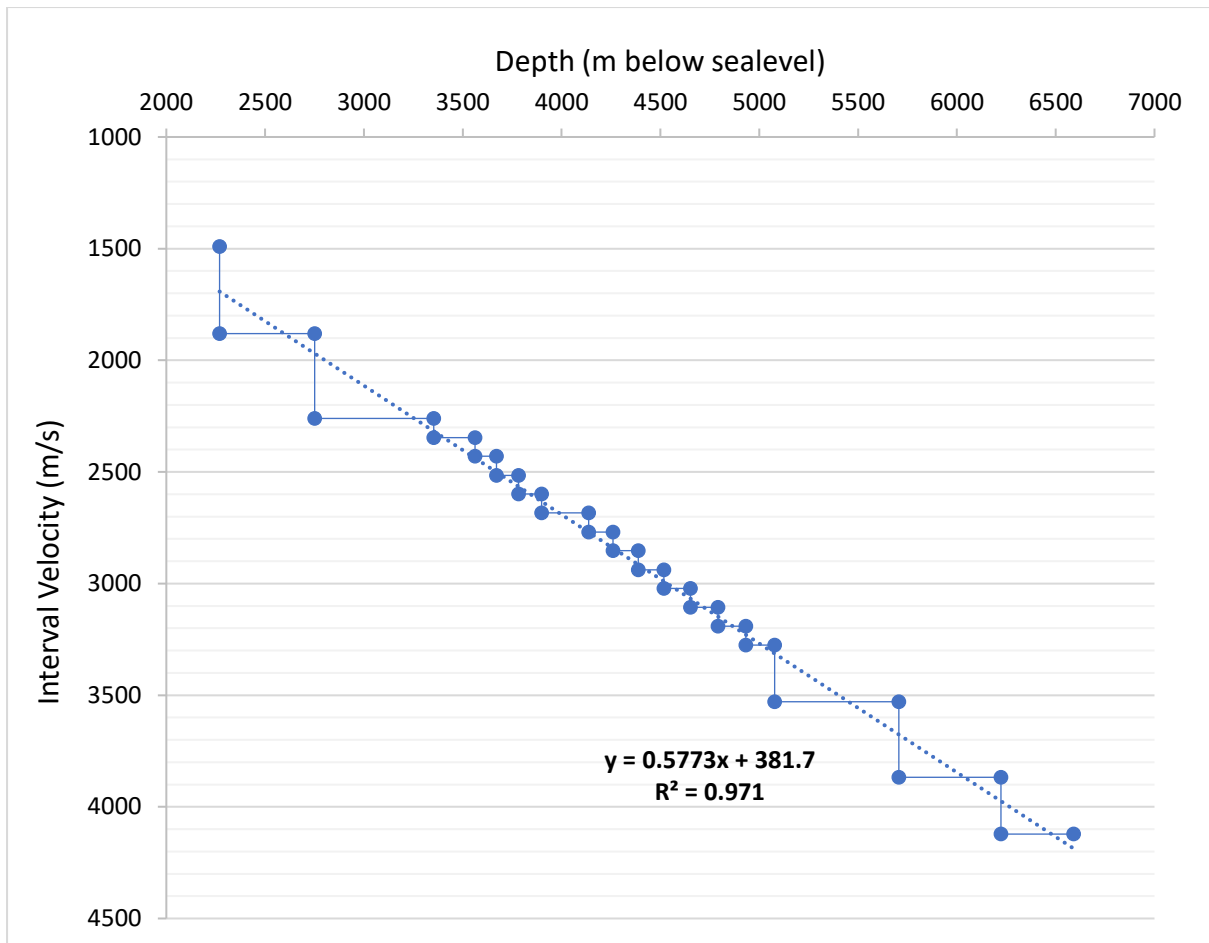
Figure 2-5: Examples of velocity-depth relationship derived from any 1-D location along the profile shown in Figure 2-4. The value 0.5773 s^{-1} ≈ 0.6 s^{-1} and is the gradient, K, used in the velocity modelling in this study.

2.2 Methodology

Once depth-converted, the seismic interpretation of the 3D volume has been carried out using Landmark DecisionSpace® on a grid of inlines and crosslines, whose number was variable depending on the geological complexity (tighter grid for complex geology). A sequence of horizon editing stages then followed the mapping, which included 3D auto-tracking, de-spiking, interpolation and smoothing. The stratigraphic interpretation across the fold belt underwent an iterative process where interpreted sections were subsequently imported into StructureSolver™ and sequentially restored to validate or modify the interpretation (Figure 2-6). The restoration algorithm used by the software is very similar to that described in Nunns (1991), and has the following characteristics:

- Length is conserved along the reference horizon.
- The internal parts of fault blocks are restored using vertical shear.
- A constant amount of slip is removed along each fault, equal to the slip of the reference horizon across that fault

This simple method is suited for an interactive seismic interpretation environment where the main aim is checking interpretations across faults for seismic correlation and structural balance, however, StructureSolver™ restored sections are not decompacted. Where there is a substantial compaction gradient with depth, the restored thicknesses of beds near the top of the restored section will not be representative of their true thicknesses at the time of deposition of the reference horizon. However, analysis presented in Nunns (1991) showed that the relative restored structural relationships across faults will be fairly accurate provided that there are not rapid changes in compaction gradient either vertically or horizontally.

Seismic interpretation across faults was additionally checked with the use of RMS amplitude maps extracted along and between the mapped horizons. RMS (root-mean-square) amplitude computes the square root of the sum of squared amplitudes divided by the number of samples within the specified window used (yields the reflection intensity); these maps were computed on the higher resolution seismic volume. RMS extractions are a powerful tool for imaging buried depositional systems as they provide unambiguous evidence for the presence of sinuous channel forms and other features that are not often apparent on vertical seismic profiles (see chapter 5 for further detail). It follows that if slope channels can be imaged on the same RMS amplitude extraction along a pre-kinematic, faulted horizon, it indicates that the stratigraphic interpretation across the faults is accurate and reliable, at least within the window used for the

amplitude extraction. Seismic interpretation in this study was continuously adjusted and informed by structural restorations (see above) until this condition was satisfied, within a 100 m vertical window.
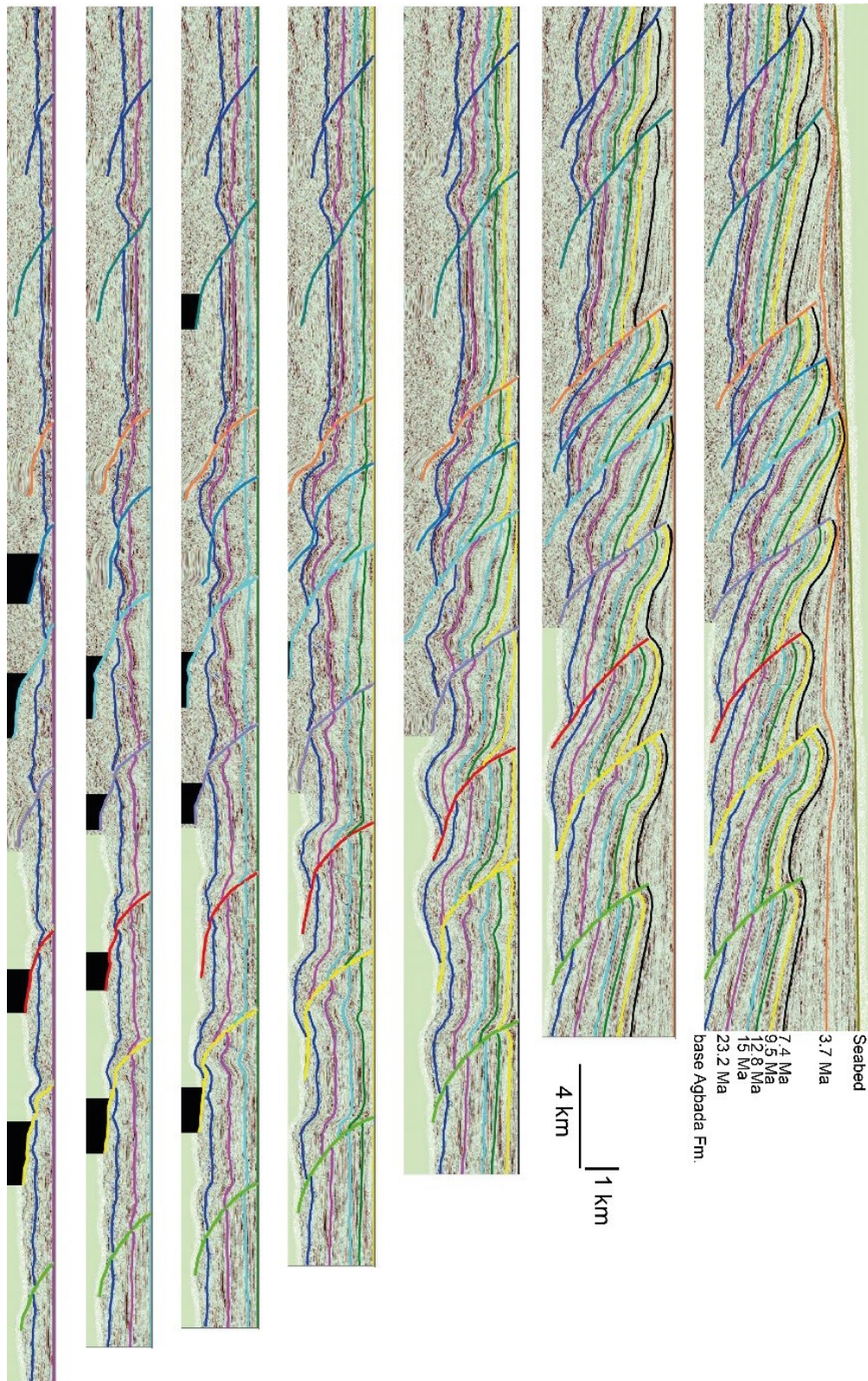
Figure 2-6: Example of interactive restoration used during the stratigraphic interpretation with the aim of aiding the correlation of horizons across faults and check for structural balance (after depth-conversion).

Once the stratigraphic and structural interpretation across the outer fold and thrust belt was complete, the work continued with the aim of defining the deformation field over the Miocene-present interval (**aim 1**). This has been achieved with the use of line-length balancing (Dahlstrom, 1969), building on the methodology described by Jolly et al. (2016). A full description of the methodology used in provided in chapter 3; however, this had the main aim of reconstructing the growth history of each individual thrust-fold in the area, along-strike, across-strike and through time. During this step, shortening and strain have been measured and quantified to show their temporal and spatial variations. Jolly et al. (2016) originally applied this methodology to four thrust-fold structures within OPL Block 256 which they labelled A, B, C and D. With the exception of fold C, which is outside the study area of this work, folds A, B and D are again analysed here along with additional eight structures which I label altogether 11 to 22 (see chapter 3). Folds A, B and D of Jolly et al. (2016) correspond to structures 11, 13 and 17 in this work, respectively. Moreover, Jolly et al. (2016, 2017) investigated the geomorphic response to deformation of the submarine channels on the present-day seabed and how the current state of deformation controlled their location and were, therefore, particularly interested on the distribution of strain rates within the last 3.7 Ma, at the end of the growth history of the fold and thrust belt. Conversely, this work aims to understand how sedimentary architectures have changed (or have been altered) and the distribution controlled by deformation throughout the growth history of the fold belt, since its start. Additionally, this work aims to provide a new model for the structural evolution of gravity-driven fold and thrust belts to help explain the sedimentary responses, which was not provided by Jolly et al. (2016, 2017).

Strain is a non-dimensional measure of deformation, here usually shown as the percentage contraction of a horizon from an original undeformed state to its final deformed (faulted and/or folded) state. Strain is derived after and from the measure of shortening, which is the absolute reduction in line-length (in metres) that a horizon(s) has undergone during deformation (see chapter 3). The eleven thrust-folds analysed in this study show high variability in the amount of deformation (and size) they have accumulated through time, both across and along the strike of the same thrust-fault, and the correlation between strain and shortening along each measured fault is non-univocal as it is dependent upon the width of the window over which the measure is taken. In order to relatively compare the results between faults of different size, a correction was applied to all the measures of strain and shortening as if they were all taken from a window of a fixed length of 7 km (see chapter 3). Therefore, by measuring both strain and shortening

across the fold belt, I have been able to derive a direct, univocal correlation between the two, which is shown in Figure 2-7.This shows how shortening and strain are related along a specific 2D section along the strike of the largest thrust-fault in the study area (fault 13; see chapter 3), where the largest cumulative strain is recorded across the entire fold and thrust-belt. The correlation shown is considered representative for the dataset as a whole for both low and high values, and any shortening value quoted in this work has been calculated with this relationship.
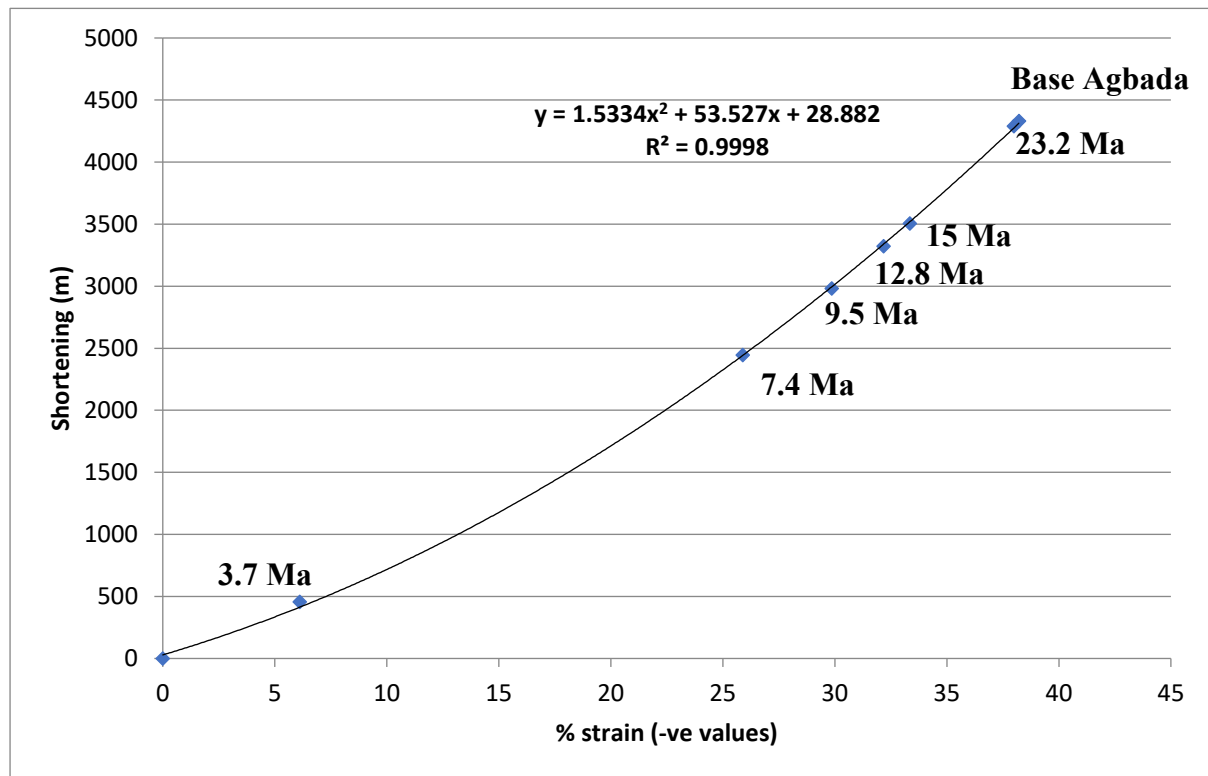
Figure 2-7: Shortening (y axis) as function of strain (x axis) taken from the 2D section where the largest cumulative strain is recorded across the entire fold belt. The curve is constructed by plotting the amount of strain and shortening accumulated by each marker horizon used in this work along that specific section (from the base of Agbada Formation to the seabed). Note that, as expected, the older horizons have been shortened more than the younger ones.

Erosion due to either slumping or channel incision is common on the crest of the folds and leads to the removal of substantial parts of stratigraphy (Figure 3-3). For any horizon truncated by a scarp we measure the length by projecting the horizon over the structure while maintaining the overall shape of the structure. Similarly, where recent channels have incised across a growing fold, we also extrapolated the stratigraphic horizon over the growing structure(s). This method allows us to estimate the likely strain accumulated by the horizon assuming it had not been affected by slumping or channel incision.

The structural analysis, and the reconstructed growth history, have been subsequently integrated with a series of isopach maps for each time-interval (measured along the local normal of the surface, i.e. perpendicularly to the horizon) and sediment-accumulation rate maps

in order to better characterize the deformation field (**aim 1** and **aim 2**). These maps are presented and discussed in chapter 5.

The evolution of the stratigraphic architecture is assessed by classifying the range of depositional/architectural elements (Posamentier and Kolla, 2003) present in the study area (**aim 2**). This classification is fully addressed in chapter 4 and it is mostly concerned with the external geometry of the third-order channel systems and how they changed through time and space. Particular attention has been given to the distribution of constructional and/or erosional slope channels and lobes as differentiated by Broucke et al. (2004). They defined an "*erosion/construction ratio (E/C ratio) corresponding to the depth of erosion of the channel axis versus the height of the levees. The E/C ratio of an erosive channel complex will be over 2, below 1 for a constructive channel-levee complex and equal to 0 for depositional lobes*" (Broucke et al., 2004; Figure 2-8). Moreover, RMS amplitude maps have been systematically extracted from each time-interval to map the spatial distribution through time of the different sedimentary systems. These maps are shown and discussed in chapter 5.
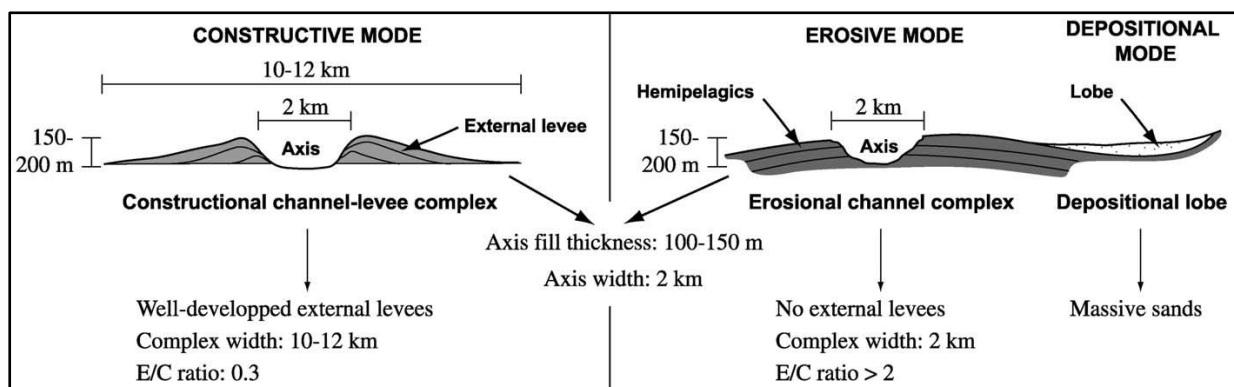
Figure 2-8: Examples of constructional, leveed-confined channel complexes versus erosional channel complexes and lobes. This main distinction has guided the classification of the seismic facies in this study. Modified from Broucke et al., 2004.

Finally, the distribution of the different architectural types has been integrated with the structural-stratigraphic evolution of the area to understand and predict how deformation has controlled the spatial and temporal variability of the sedimentary systems (**aim 3**). These data are presented and discussed in chapters 5, 6 and 7.

3. Growth of a thrust fault array in space and time: an example from the deep-water Niger Delta

This chapter is presented in paper form – due to be submitted to the
Journal of Structural Geology

3.1 Introduction

The evolution and growth of thrust belts have historically been investigated by field work in mountain belts, the construction of 2D cross-sections, and the analysis of limited, mostly 2D seismic reflection data. The linking of kinematic predictions of geometrical and analogue models of fault-related folding to both synkinematic strata in outcrop (e.g. Poblet and Hardy 1995, Ford et al 1997; Poblet et al 2004) and on sub-surface seismic reflection data (e.g Suppe et al. 1992; Gonzalez-Mieres & Suppe, 2006; Hughes & Shaw 2015) has provided further valuable insight into a quantitative understanding of fault and fold growth in thrust belts. The study of the deformation of the ground surface via mainly geomorphic methods has proved very useful in constraining recent deformation rates (e.g. Lavé & Avouac 2000; Daëron et al. 2007; Simoes et al. 2007; Hughes et al. 2018). However, while important in providing insight on style and rate of thrusting, these studies typically provide a two-dimensional, transport-parallel view of the growth of thrust systems. Yet, in common with other fault types, thrust faults lengthen in the strike direction and link with increasing displacement (e.g. Elliott 1976; King and Yielding; 1984, Fermor, 1999; Hatcher, 2004; Davis et al., 2005; Bergen & Shaw, 2010) highlighting the need to understand thrust development, both in transport parallel and transport perpendicular directions for a more complete three-dimensional understanding of thrust evolution.

Surface growth of emergent folds has been increasingly addressed by studies of combined structural, geomorphic and chronological analyses of deformed geomorphic surfaces (e.g. Jackson et al. 1996; Delcaillau et al. 1998, Keller et al. 1999; Davis et al. 2005; Li et al. 2013; Hughes et al., 2018) and these provide insight to at least one component of 3D thrust fault growth. However, descriptions of the full growth in space and time of thrust systems are still very rare. We seek to address this gap in understanding in this paper, by quantifying the strain both parallel and perpendicular to transport direction, through time, of a linked thrust system.

The expansion of hydrocarbon exploration and production into deep-water passive margin settings within the last two decades has provided us with new 3D seismic reflection datasets imaging deep-water fold and thrust belts, affording the opportunity for truely three-dimensional studies of thrust and fold growth (e.g. Morley 2009; Higgins et al. 2009; Bergen & Shaw 2010; Jolly et al 2016; 2017; Totake et al 2017: Yarbuh et al. 2018). The power of these datasets is not just that they afford 3-D coverage of the stratal geometries, which is impossible in field-based studies, but that they also preserve a greater record of the full deformation field because the folds and thrusts are not subject to erosion as occurs in mountain belts. Here we use a large 3D seismic reflection survey to investigate the growth through space and time of an extensive fold and thrust array in the outer fold and thrust belt of the Niger Delta (Figure 2-1) allowing us to propose a new model for thrust growth and linkage for deep-water fold and thrust belts.

Much of the early research on thrust belts concentrated on understanding the geometry and sequence of thrusting. One of the main arguments addressed by early workers was whether thrusts formed in a foreland, or basinward -propagating sequence or the reverse (overstep sequence; break-backward) (e.g. Bally et al., 1966; Dahlstrom, 1970; Milici, 1975). In the piggyback model, thrusts form in-sequence, where a younger thrust forms in the undeformed footwall of the older thrust. The mechanism proposed was footwall collapse by increasing tectonic load and elevated pore pressure. (Boyer and Elliot, 1982; Butler, 1982, 1987; Elliot, 1983). Thus, thrusts become progressively inactive with time and are carried passively on the back of new thrusts that develop in the footwall areas. Older thrusts achieve higher structural relief and the propagation of thrusts is recorded by the development of piggyback basins above moving thrust sheets (Ori and Friend 1984). A different model (e.g. Peach et al., 1907; Milici, 1975; Butler, 1982, 1987) proposes that successive thrusts develop in the hangingwall of older structures and hence propagate toward the hinterland or landward, in a 'break-back' sequence. However, for this to happen, a sole thrust has to quickly propagate out into the foreland, be pinned at the toe, allowing new thrusts to then propagate landward. At the same time many workers have recognized that while the growth of fold and thrusts belts appears to be largely dominated by foreland or basinward propagation, "out-of-sequence", break-back and synchronous thrusting is a common characteristic giving rise to complex thrust geometries (e.g. Searle, 1985; Morley, 1988; Boyer, 1992; Shaw et al., 1999; Corredor et al 2005).

Both analogue sandbox models (e.g. Colletta et al. 1991; Storti and McClay, 1995; Storti et al. 1997, Wu and McClay, 2011) and numerical simulations (e.g. Hoth et al. 2006, Simpson, 2006; Yamada et al 2006, Buiter et al. 2006;) show that in the earliest phases of thrust belt

development thrusts tend to develop by forward-propagation. However, recent more sophisticated numerical, and analogue models incorporating changes in the surface slope of a thrust wedge with variable amounts of syn-tectonic erosion and deposition generate more complex sequences of thrust activity (Simpson, 2006, Stockmal et al., 2007; Wu & McClay 2011; Fillon et al, 2012). Additionally, the nature of the décollement has long been known to affect both the style and sequence of a propagating thrust belt, where weak salt and overpressured shale detachments favour near synchronous forward- and backward-propagation of thrusts and larger spacing between thrust-fold pop-ups (e.g. Burbridge and Braun, 2002; Costa & Vendeville, 2002; Dean et al. 2015). On a weak detachment, the frontal tip of the deformation reaches the foreland pinch-out of the décollement horizon very quickly, effectively pining the thrust-belt tip and allowing deformation to be accommodated by shortening within the entire wedge, with new thrusts/folds forming between older ones (Costa & Vendeville, 2002).

Unlike orogenic belts, or accretionary prisms, the majority of fold belts developed on passive margins are controlled by gravitational instability rather than far-field plate convergence forces and deformation only occurs when the gravity potential is sufficient to overcome both the resistance to slip along the basal detachment and the internal strength of the overburden (Rowan et al., 2004; Morley et al 2011). Although Rowan et al. (2004) suggest that for gravity-driven deep-water fold and thrust belts, shale detached structures should develop in a forward propagating sequence, Wu & Bally (2000) and Corredor et al (2005) have documented out-of-sequence thrusting in the gravity-driven system of the Niger Delta. Both the Niger Delta and Brunei fold and thrust belts forming on a weak shale detachment have very low tapers in comparison to other fold and thrust belts (Bilotti and Shaw ,2005 and Morley 2007). Morley (2007) has predicted that for such fold and thrust belts a broad belt of synchronously active folds and thrusts, or out of sequence thrusting is likely to be required to maintain the critical taper and allow the deforming wedge to propagate.

In this study we address the problem of thrust propagation and 3D geometrical evolution by reconstructing the 4D evolution of an area within the deep-water fold and thrust belt of the Niger Delta (Figure 2-1). Our aim is to show how thrusts grow and propagate through time and space both as individual entities and as a part of an array (i.e. a fold and thrust belt).

3.2 Background

3.2.1   Fault growth

Since the pioneering work of Scholtz (1982), Muraoka & Kamata (1983), Walsh and Watterson (1988), Cowie & Scholz (1992) and Peacock & Sanderson (1991) there has been an enormous increase in our knowledge of how faults grow, propagate and scale. It is generally accepted that fault displacement (D) and length (L) are related by the following power-law:

$$D = \gamma L^n \tag{1}$$

Where γ is an expression of fault displacement at unit length which depends on rock properties. When $n=1$, γ is simply the ratio D/L, which, regardless of its value, indicates self-similarity (i.e. the relationships between D and L are constant as the fault grows). However, when $n \neq 1$, the relationship becomes scale-dependent and growth is not self-similar. Authors generally agree on $n=1$, but a range of values have been proposed from 0.5 to 2. Values for γ generally range from 10^{-3} to 10^{-1} (kim & Sanderson, 2005). However, this body of work has predominantly focussed on normal fault systems, and in comparison, there has been substantially less investigation of whether thrust systems behave in a similar manner. While we might expect that they should, thrust faults frequently have an additional characteristic of being kinematically linked through a basal detachment, or other internal detachments within the thrust wedge. Early work on thrusts tended to focus on the final state of thrust-systems, when fully connected (e.g. Boyer & Elliot, 1982; Diegel, 1986), and while useful for understanding thrust geometries they provide little insight into how thrusts grow and link in three-dimensions. Nonetheless since the 1960s there have been a number of papers published which indicate that thrust faults link and grow in a similar manner to that observed, and modelled, for normal fault systems.

Dahlstrom (1969) schematically showed displacement being transferred along strike between thrusts, and Price & Mountjoy (1970) described the stratigraphic separation of an individual fault decreasing and being taken up proportionately across adjacent or nearby thrusts. These observations were supported by work on modern earthquakes. King and Yielding's (1984) study of the 1980 El Asnam Algerian earthquake showed that the vertical component of the displacement along the three rupture segments of the fault to increase towards a central maximum and decrease towards the thrust tips. Analogue models of two interacting thrusts (Gardner & Spang, 1973) and a full thrust array (Liu & Dixon 1991) produced similar displacement patterns in plan view. In terms of fault scaling, Elliot (1976) showed that for

thrusts in the Canadian Rockies the maximum displacement in the central part of a thrust scaled with its mapped length, and his data are included in the global compilation of Cowie & Scholz (1992).

More recently displacement-distance data for thrust systems in mountain belts (Fermor, 1999; Hatcher, 2004; Davis et al 2005; Mazzoli et al. 2005; Amos et al. 2010; Watkins et al. 2017) and in subsurface 3D seismic reflection datasets (Higgins et al 2009; Bergen & Shaw 2010; Jolly et al 2016, 2017; Totake et al 2018) show that thrust faults display many of the growth and linkage characteristics of other fault systems, at least in their along-strike (transport perpendicular) evolution. They are mostly segmented, where each segment displays a maximum displacement towards its centre, with displacement decreasing in the direction of segment/thrust propagation. The segments can be hard-, or soft-linked via relay systems, the equivalent of transfer zones in the older thrust literature (e.g. Nicol et al. 2002).

However, far less understood are the effects of mutual interaction between several, parallel thrusts, in the transport parallel direction, and what implications this might have on the distribution of strain and shortening at the scale of an entire fold and thrust belt. Bergen and Shaw (2010) begin to address this as they recognised that the effect of thrust faults being linked along a basal detachment had not been previously considered in growth analysis of thrust arrays. If a thrust is physically linked to other faults by movements along the basal detachment, they are effectively hard linked. Bergen and Shaw (2010) define this type of behaviour as 'detachment linkage', and they propose a model for the displacement –distance profiles that might be observed in adjacent (in the transport direction) thrusts in the array. If the faults are detachment-linked and there is no change in overall shortening rate, any displacement accrued on a new fault growing in a break-forward sequence must be balanced by displacement loss on an older structure behind it. So, multiple maxima might develop on the 'older fault' to balance the displacement accommodated by the 'younger fault' (Figure 3-1).
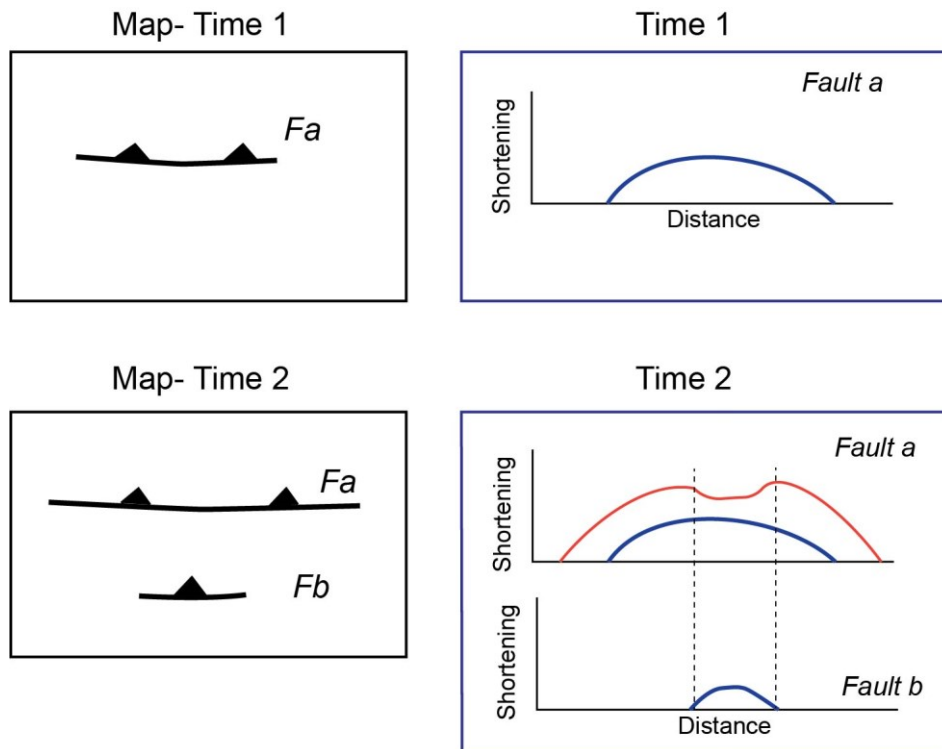
Figure 3-1: Model for detachment linkage, as proposed by Bergen and Shaw (2010). At time 1 fault "Fa" grows in a self-similar manner. At time 2, the growth of younger thrusts (fault "Fb"), either in the footwall or hangingwall of the older structure, accommodates part of the deformation, particularly where the two structures overlap. This process causes the displacement-distance plot of fault "a" at time 2 to be asymmetric as some of the displacement is transferred and balanced by the new thrust.

In this study we significantly expand the initial work done by Jolly et al. (2016) to almost the entire outer fold and thrust belt of the Niger Delta over an area of ~60 km along strike and 40 km in the transport parallel direction (Figure 2-1, Figure 3-2 and Figure 3-3). We use 3D seismic data to quantify the growth and interaction of eleven fold-thrust structures both in time and space where shortening and strain can be well constrained. We measure the shortening and strain accumulated by the thrusts, and associated fault propagation folds, and, by doing so, we quantify and characterise:

1. The sequence of thrust-fault growth;
2. How thrusts accrued lateral extent and strain with time;
3. How thrusts interacted in both the along and across-strike directions (with time).

Subsequently, we interpret our results in light of the current understanding of thrust growth mechanisms, and we propose a new model for the growth of a thrust fault array through time.
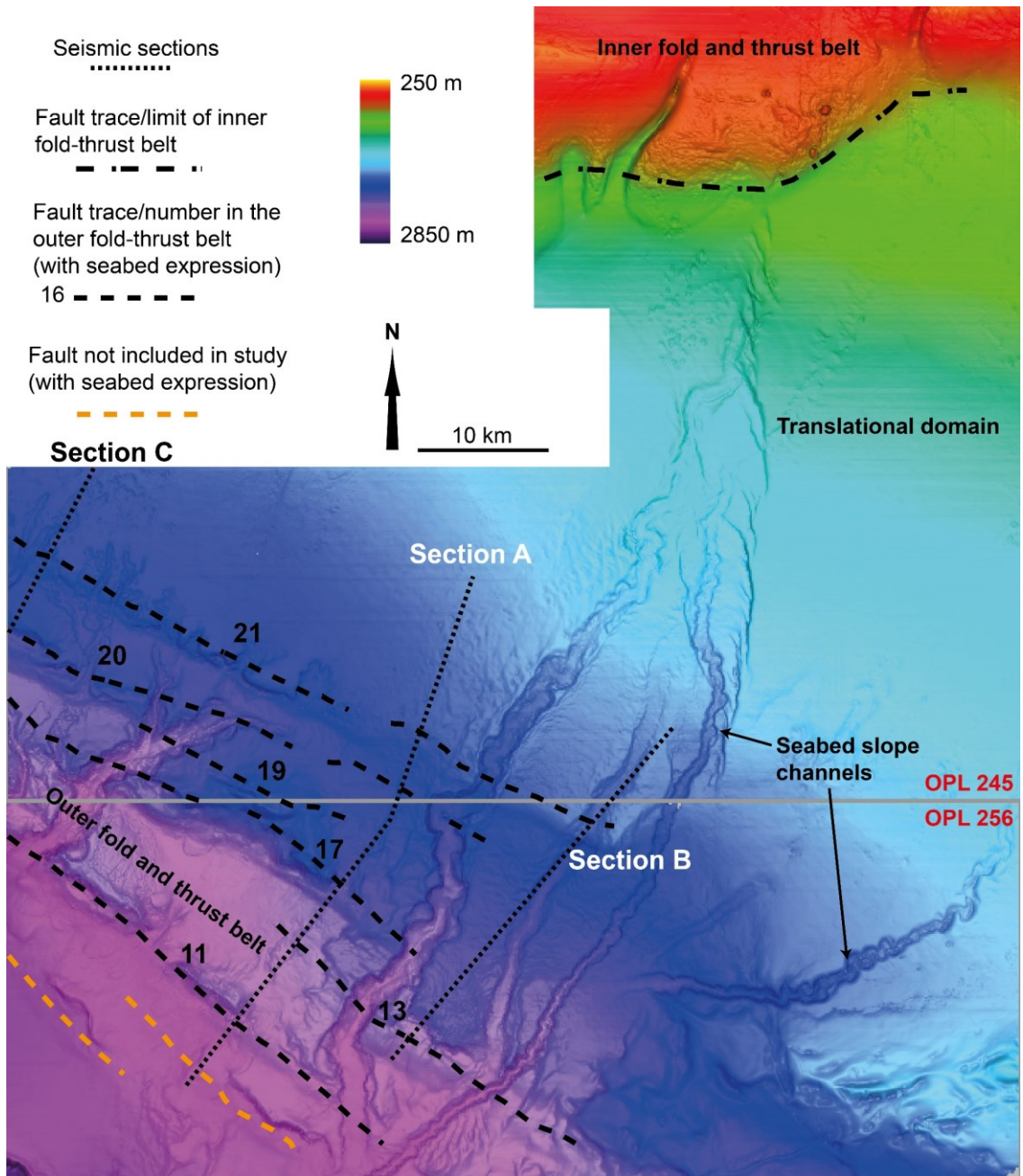
Figure 3-2: Seismic-derived seabed bathymetry across the study area. The seismic cube extends from the inner fold and thrust belt to the outer fold and thrust belt. Dashed black lines represent the trace of thrust-faults at depth that have been most recently active (past 3.7 Ma), causing deformation of the seabed. Seabed channels are seen to interact with active structures and are discussed by Jolly et al. (2016, 2017).
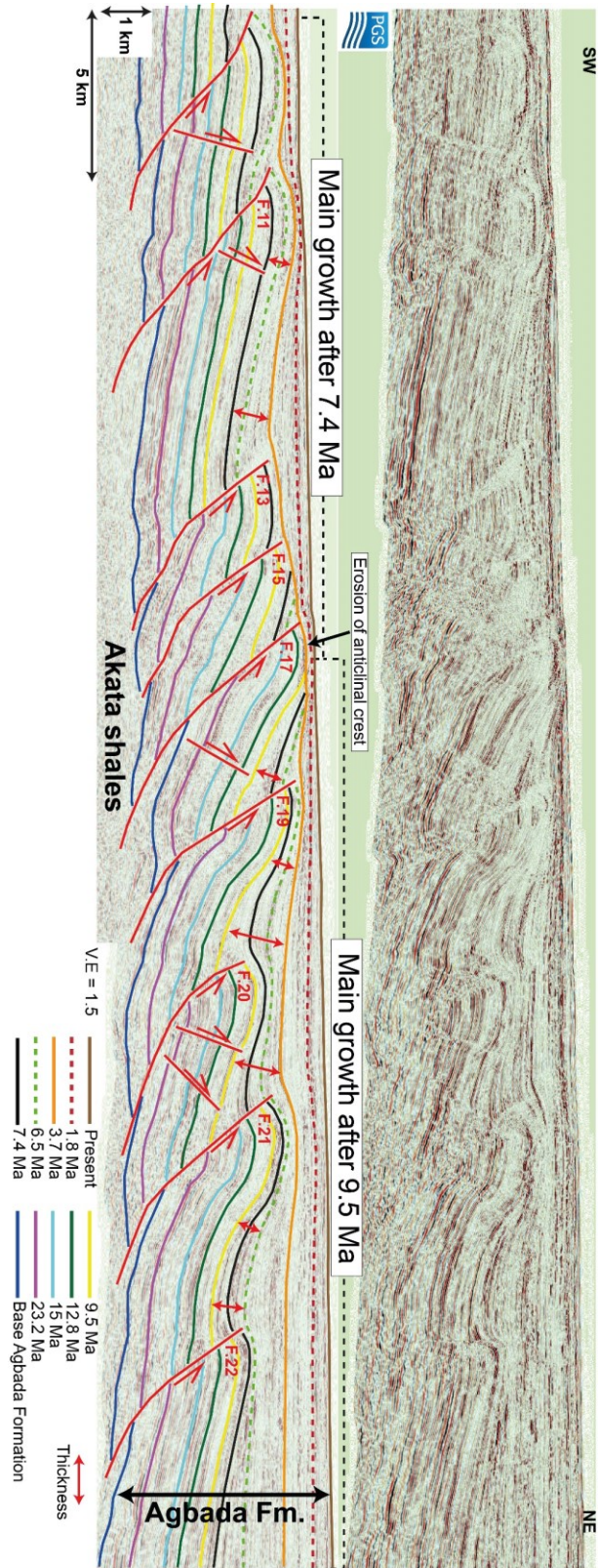
Figure 3-3: Uninterpreted and interpreted seismic section A (located on Figure 3-2 and Figure 3-4). Age horizons 1.8 and 6.5 Ma (dashed red and green lines) are for illustrative purposes only and were not included in the structural analysis. Note that the fold belt is divided into two domains, separated by a region of high structural relief at its centre (see fig. 5), where the anticlinal crest of fault 17 is eroded by seabed channels. Inboard of fault 17, the main growth occurred after 9.5 Ma (see the growth strata after the yellow horizon), while further basinward the main growth occurred after 7.4 Ma (see the growth strata after the black horizon) indicating a general forward propagation of contractional front at 7.4 Ma. The base of the Agbada Formation (blue horizon) is dated at ~ 30 Ma, and the thickness of the sediments accumulated after 9.5 Ma represent half of

44

the Agbada formation (suggesting increase in accumulation rate). Total shortening along this section is approximately 15 km (26%).

3.3 Structural setting

Deposition of the Niger Delta (Figure 2-1) began during the Early Eocene and, since then 12 km of sediments have accumulated (Evamy et al., 1978; Doust and Omatsola, 1990; Damuth, 1994). This thick sedimentary section is generally divided into three diachronous formations, which from the base to top are the Akata, Agbada and Benin Formations (Doust and Omatsola, 1990). They comprise marine shales, deltaic and fluvial deposits respectively (Doust & Omatsola, 1990). However, in offshore slope regions and basin floor, the Agbada Formation consists of slope deep-water channel-levee systems, sheet sands, mass-transport deposits (MTD) and hemi-pelagic mudstones and the Benin Formation is absent (Figure 2-1). Within the study area, the base of the Agbada Formation is dated at approximately 30 Ma (Krueger and Grant, 2011).

The Niger Delta is currently deforming above the overpressured Akata shales which act as a décollement layer, while the Agbada Formation is the deforming unit (Figure 2-1). Major tectonic zones dominated by extensional tectonics on landward up-dip areas of the delta and thrusting and folding towards the delta toe have long been recognised (Evamy et al., 1978; Knox and Omatsola, 1989; Doust and Omatsola, 1990; Damuth, 1994). This structural style is attributed to gravitational collapse of the advancing delta above the under-compacted weak shales of the Akata Formation (Morgan, 2003; Bilotti and Shaw, 2005; Briggs et al, 2006; Rouby et al, 2011). Early work identified an intermediate area between the up-dip listric growth faults and the down-dip fold and thrust belt, dominated by shale diapirism (Morley and Guerin, 1996; Cohen and McClay, 1996, Wu and Bally, 2000).Subsequently, Corredor et al. (2005) further subdivided the down-dip contractional zone into an inner and outer fold and thrust belt, separated by a translational zone characterized by broad detachment folds.

The extensional-compressional zones have migrated basinward with time, in tandem with over more than 300 km of slope progradation since the Late Eocene (Short and Stauble, 1967; Evamy et al., 1978). The result of this process is the presence of a paleo-fold belt beneath the upper slope, which is today deformed by the normal faults of the extensional domain (Hooper et al., 2002). In the late Miocene-Pliocene interval Wiener et al. (2010) also reported a significant increase in shelf-margin deposition coeval with a significant basinward progradation of the contractional front.

The deformation in the contractional domain of the outer fold and thrust belt started at ~ 15 Ma (Jolly et al., 2016) with peak activity concentrated between ~9 and 3.5 Ma (Krueger and Grant, 2011; Jolly et al., 2016; Sun and Liu, 2018), and is mostly expressed as fault-propagation folds and faulted detachment folds detaching on the Akata shales, which itself in places is internally deformed (Corredor et al., 2005; Bilotti and Shaw, 2005; Briggs et al., 2006; Cobbold et al., 2009). 2D section restorations suggest a complex growth history of the outer fold and thrust belt with both break-forward, break-backward, coeval and out-of-sequence thrusting (Corredor et al., 2005; Wiener et al., 2010; Krueger and Grant, 2011). Additionally, Krueger and Grant (2011) suggested that the along-strike evolution of thrust-faults consist of an initial stage when faults rapidly gained most of their strike-length, later followed by increase in fault slip and structural relief. At local scale, Higgins et al. (2009) published the first data on the along-strike linkage of a single, isolated thrust-related anticline in the deep-water Niger Delta and argued that strain transfer is the main mechanism through which initially separated folds coalesce into single structural culminations. The work by Jolly et al (2016, 2017) corroborate these results and show segment growth and linkage through time for four structures in the outer fold and thrust belt since 15 Ma.

3.4 Data and Methodology

3.4.1 Seismic dataset and interpretation

The 3-D seismic data volume (Figure 2-1, Figure 3-2) was processed to near zero-phase and is displayed using Society of Exploration Geophysicists (SEG)-normal polarity. The data were migrated using Kirchhoff prestack migration and bending ray poststack migration to generate a 12.5 m by 12.5 m grid with a 4 ms Twtt sampling interval. The data were provided every four in-lines and cross-lines, giving a bin size of 50 m, which corresponds to the maximum horizontal resolution. Based on a frequency content of 35 Hz and average seismic velocities ranging from 1800 m/s (Plio-Pleistocene) to 4000 m/s (late Oligocene – early Miocene), the vertical seismic resolution (limit of separability) is estimated to range from 13 to 30 m, respectively.

Eight key horizons (from the seabed to the base of the Agbada Formation; Figure 3-3) were interpreted throughout the dataset, and 17 closely-spaced profiles perpendicular to the structural trend were selected for detailed structural analysis (Figure 3-4). The horizons were calibrated with age data provided by Shell from an unpublished well in the block covered by the seismic data and from published data in Krueger and Grant (2011); the same age scheme is

used in Jolly et al. (2016). In the study area the fold belt consists of 11 fault-propagation folds (structures 11 to 22; Figure 3-4) striking north-west to south-east, and they can be traced along strike for approximately 60 km. The across-strike distance from the most inboard structure (fault 22) to the most outboard one (fault 11) is approximately 35 km, however it is noted that the total amount of shortening varies along the strike of the fold belt as does the spacing between the thrusts (Figure 3-5). The two most outboard thrusts of the fold belt are not fully imaged on our dataset and are not included in the study.
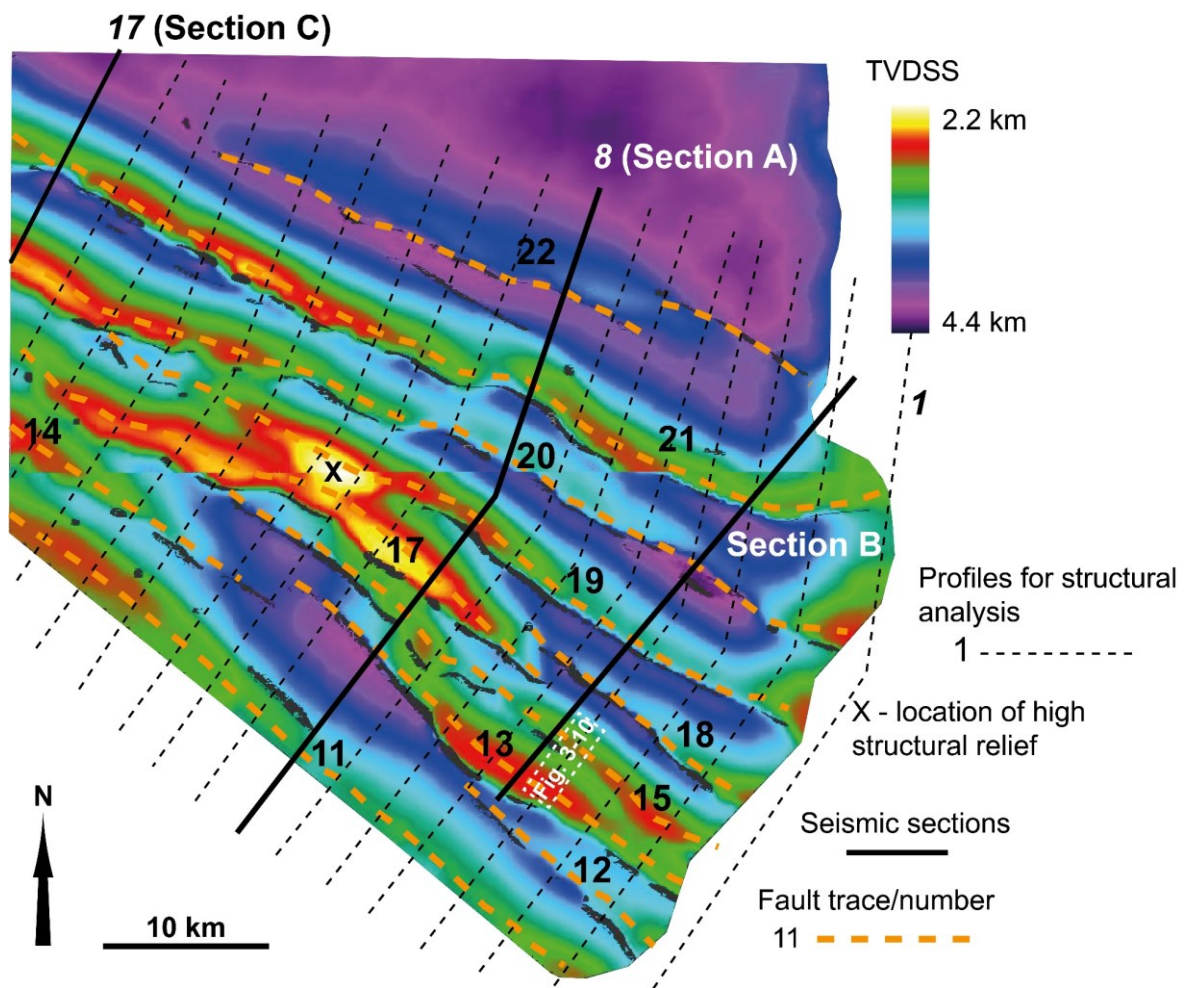
Figure 3-4: Depth-structure map of the 9.5 Ma horizon (yellow horizon in Figure 3-3 near base of syn-kinematic section). Dashed orange lines are the trace of the 11 thrust-faults at depth. Dashed black lines are the 17 profiles used for the structural analysis. Section B (Figure 3-5) is an arbitrary line. Note the variable present-day structural relief of the thrusts both along and across-strike (due to fault linkage and interaction). Location "X" is the region with highest structural relief in the area (note this location is at centre of the fold belt).
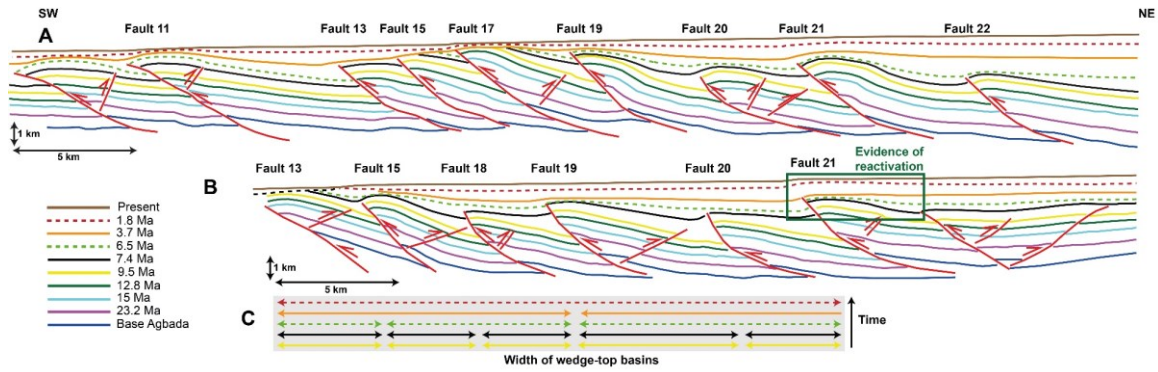
Figure 3-5: Comparison between sections A and B with no vertical exaggeration (sections located on Figure 3-4). The sections are pinned at Fault 21 and are approximately 10 - 15 km apart along-strike. Note how the amount of shortening between faults 21 and 13 has changed over a short distance. Along section B, fault 21 can be observed to have been reactivated out-of-sequence very recently. Growth strata show that it was active at least between 7.4 and 3.7 Ma, inactive between 3.7 and the inferred 1.8 Ma event, and then active again to the present day. C shows the width of the wedge-top basins through time along section B. Note the progressive broadening of the wedge top basins with time for section B, indicating widening of the spacing between simultaneously active thrusts and cessation of activity on intermediate structures.

3.4.2   Depth conversion

Depth conversion is required to accurately calculate the shortening of folded and faulted strata. Previous work in the same area (Jolly et al., 2016, 2017) used an average seismic velocity for depth conversion, but to match the known increase in velocity with depth as documented by Morgan (2003), depth conversion was treated more accurately. In particular, it was found that to correlate horizons across-strike between all the structures of the outer fold belt, a more robust velocity model was required to restore the geometries of the sedimentary packages and to aid interpretation in deeper sections, where the thicknesses of units can be under-estimated, depending upon the thickness of the overburden. The Agbada Formation was depth converted using a linear velocity function with depth, the V_0, K relationship (Marsden, 1992), which is based on the following relation:

$$V_z = V_0 + K*Z, \qquad\qquad\qquad (2)$$

where V_0 is the initial velocity, and K is the velocity gradient within the analysis interval. Two horizons, the seabed and the base of Agbada Formation, were regionally mapped and gridded in 3D and input into the velocity model to constrain the velocity function within the Agbada Formation. In our model an initial velocity, V_0, of 1490 ms^{-1} was assigned to time-structure map of the seabed (the reference surface; Figure 3-2) and a gradient, K, of 0.6 s^{-1} described the linear change in velocity with depth within the Agbada Formation. The gradient was derived from a velocity section published in Morgan (2003), which has a very similar structural style to that in the study area. RMS velocities were also provided by PGS for one inline in the seismic volume and were included in the analysis in order to find an average value that could be applied

to the entire Agbada Formation. The results of the velocity modelling (Figure 3-6) were consistent with Morgan (2003) and Kreuger and Grant (2011), both in terms of maximum velocity and depth (TVDSS) reached at the base of the Agbada Formation. Similar values of initial velocity and velocity gradient were used by Totake et al. (2017) in one of their models to depth covert a fault-propagation fold in the deep-water of Niger Delta. The water column, and therefore the seabed, was depth converted for a constant velocity of 1490 ms^{-1}, while the Akata shales were converted for a constant velocity of 2700 ms^{-1} to model the strong velocity decrease due to overpressure (Morgan, 2003; Figure 3-6). The choice of the gradient, K_z, is the major uncertainty; plausible values of gradients could range from 0.5 to 0.7 s^{-1}. Tests on the variability of measured total strain (see section 3.4.3) were made on seismic sections converted for different gradients within that range and showed that errors fell within 5%, so a K_z value of 0.6 s^{-1} was deemed appropriate.
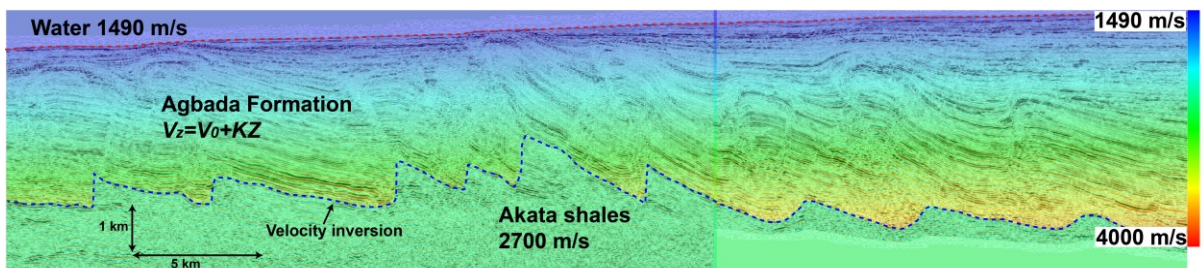
Figure 3-6: Results of velocity modelling overlain on seismic section A. The Agbada Formation was depth-converted using a linear velocity function with depth , while the Akata shales have a constant velocity of 2700 ms^{-1}. In its thickest part the Agbada Formation has seismic velocities of 4000 ms^{-1}. A sharp velocity inversion occurs at the boundary between the Agbada and Akata Formations due to overpressure developed within the Akata shales.

3.4.3   Strain analysis

Previous work on thrust displacement and linkage has tended to measure fault displacement or heave (Elliot, 1976; Mazzoli et al 2005; Davis et al 2005; Bergen & Shaw 2010). However, as also carried out by Higgins et al (2009); Jolly et al. (2016, 2017); Watkins et al (2017) and Totake et al (2017) we prefer to measure the total shortening and strain as this includes both fault displacement as well as fault-related folding. We specifically do this as we are interested in the strain through time, and in the younger syn-kinematic strata the strain is mostly expressed by folding. Strain was measured by line-length balancing (Dahlstrom, 1969), using the same methodology as that described by Jolly et al (2016) on 17 dip sections spaced at approximately 3 km intervals across the study area (Figure 3-4), and of lengths from 30 to 50 km. The

potential limitations of the approach are discussed further in Jolly et al. (2016). Strain (Figure 3-7a) was calculated using the following formula:

$$e = (L_f - L_o)/L_o \qquad (3)$$

Where L_f is the present-day length of the measured section and L_o is the original length of the horizon. For horizons which are only faulted:

$$L_o = P_1 + P_2 \qquad (4)$$

Whereas for folded horizons:

$$L_o = S \qquad (5)$$

Measures of strain were preferred to shortening to make them independent of the absolute value of shortening of structures, which is related to the size of the structure, and to compare the results relatively. However, in order to quantify the strain, we first measured shortening, therefore we are able to present both results. By deliberately changing the position of the stratigraphic horizons by up to 200 m (accounting for the possible inaccuracy of the stratigraphic correlation and depth conversion), we assess that the measurement errors may be up to 10-15% of total strain.
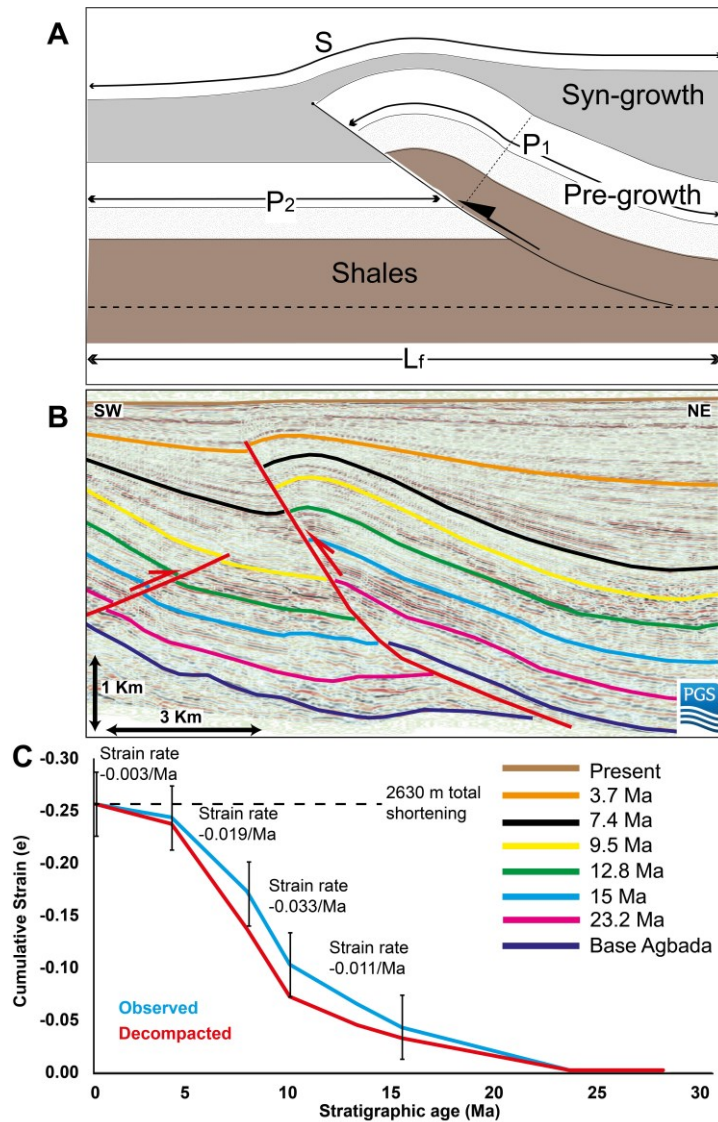
Figure 3-7: A) Methodology used for measuring strain based on line-length balancing. L_f= the present day length of the section while the original bed length is defined as L_0. L_0 for pre-growth horizons = P_1 + P_2 and L_0 for syn-growth strata = S. B) Seismic section C (Fault 21 along profile 17; see Figure 3-4); horizons used for strain measurements are labelled. C) Cumulative strain through time for both the observed and decompacted section (see text for explanation); note that uncertainty due to decompaction falls within 12% of the total cumulative strain (i.e. within the measurement error).

Values of strain were then obtained for each of the eight mapped horizons and, from these, cumulative strain curves were reconstructed to show the incremental growth of a structure (Figure 3-7b, Figure 3-7c). Reconstructing the cumulative strain curve relies on the assumption that, in absence of tectonic activity, the difference in strain between two subsequent horizons should be zero; in other words, the amount of displacement on any pre-kinematic horizon is the same. Conversely, a difference in the amount of strain accumulated by two subsequent horizons (i.e. the interval strain) indicates structural activity. The cumulative strain curve was then calculated as the summed difference in strain recorded between adjacent stratigraphic layers. Using the biostratigraphically dated ages for the mapped horizons, the interval strains

51

were divided by the time to obtain average interval strain rates (Figure 3-7c). This was done for 17 dip sections and the 11 faults in the study forming a database of 122 individual cumulative strain profiles. Consequently, we are able to view the variation in strain along the length of each structure as strain-distance diagrams (Figure 3-8b) as is routinely done for extensional fault systems (i.e., displacement-distance plot). We have also compared the difference between measuring the heave and total shortening for one structure (fault 21; Figure 3-8c), and it can be seen that heave accounts for up to 80% of the total shortening, but the curves are broadly similar which is in agreement with results of previous authors (Higgins et al. 2009 and Totake et al. 2017).
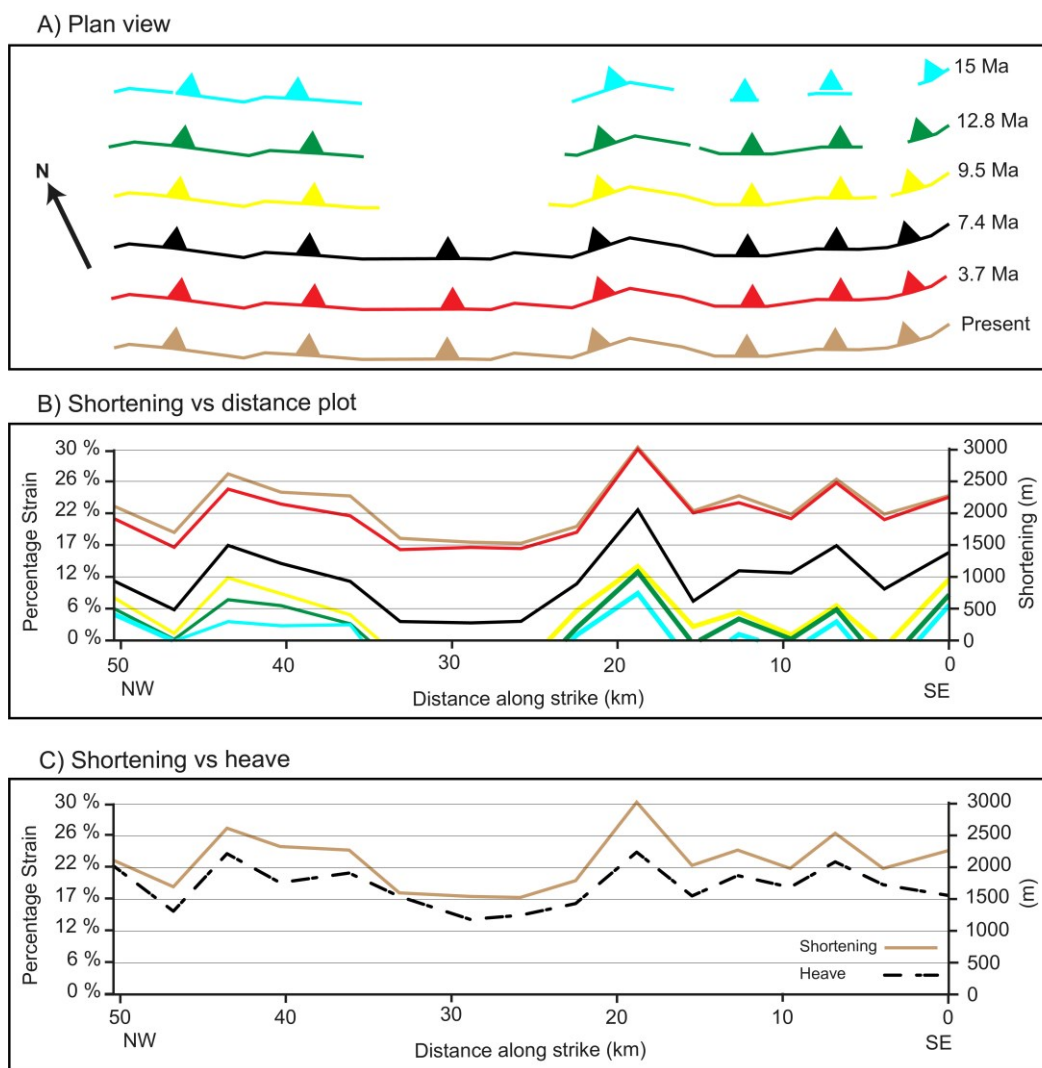
Figure 3-8: Growth history of fault 21 in map view (A) and as a strain-distance plot (B). Note that at 15 Ma the thrust-fault consisted of several isolated fault segments that progressively propagated laterally and linked. Fault linkage is complete by 7.4 Ma and subsequently the fault grew by accruing strain and shortening with fixed strike-length. (C) Comparison of total shortening versus thrust displacement, measured as heave, for fault 21.

Line-length balancing ideally requires the present-day sections (i.e. the final lengths, L_f) to be pinned away from structures at the point where strata become horizontal. However, within the study area, thrusts are often imbricated and closely spaced, requiring the shortening and strain to be measured over varying final lengths. Tests were then made to assess the sensitivity of the strain measured, if different final lengths had been used. These tests showed, as anticipated, that the strain (but not the shortening) measured was very sensitive to the choice of final length; in general, for a given percentage decrease in the final section length, the total cumulative percentage strain would increase by approximately the same amount.

Because of this approximate inverse relationship, to compare our strain values robustly between structures, we decided to normalise our measures of strain, e, to a fixed final length, L_n, of 7 km, which corresponds to the minimum length required to enclose the largest structure within the dataset. Consequently normalised strain, $e_n = (L_f / L_n)e$. The scaling is functionally equivalent to measuring the strain across each individual fold-thrust with a fixed line length of 7 km if the total shortening in each time line is relatively insensitive to increasing line length and the ratio of L_f / L_n is similar to the ratio of the original line lengths. Consequently, the cumulative strain measured on the largest structure in the domain is considered to be the highest and other smaller structures in the area are scaled relatively with respect to this. Normalised strain, $e_{n,}$ additionally allow us to overcome the issue of having multiple, specific relationships between strain and shortening for each thrust-fold and measured profile (which would make the comparison unreliable), therefore, it yields an univocal conversion between the two, which is the same for the 122 measured profiles (i.e the entire fold belt). All the values of strain and shortening quoted in this work are the normalised versions and we have used these measurements to assess their variation along the strike of each thrust-fold (Figure 3-8 and section 3.5.1), through time for both individual structures and the entire array (Figure 3-7 and section 3.5.2), and versus fault length to address how the displacement-length relationships have changed over time and to compare it to global datasets (section 3.5.3).

To this end, faults within the study area have a present-day maximum length of approximately 60 km. Of the eleven thrust-folds, eight have been used for the displacement-length analysis as three faults are only partially present within the study area. Seven of the eight faults also extend partially beyond the area analysed, however, not all outside the 3D seismic data coverage. For 5 faults we have verified that only 25% of their length is not included in the analysis, therefore, our results in section 3.5.3 remain largely unaltered.

3.4.4 Compaction

As we reconstruct the growth history of structures by measuring the present-day length of older horizons, we acknowledge that this measured length could be different if we consider that, at the time of their deposition, beds were uncompacted or less compacted than they are today. However, compaction will mainly impact the analysis of the synkinematic strata and can be considered negligible in the pre-growth section where beds were at least partially compacted prior to the start of deformation (Eichelberger et al., 2015). We tested the effects of compaction on one dip section along the strike of fault 21 (Figure 3-7b) by backstripping the sedimentary column (through time) on twelve 1D locations spaced 1 km across the structure, but we did not restore the horizontal shortening (i.e. equivalent to flattening each horizon). We used a surface porosity of 60% and a porosity-depth coefficient of 0.5 km^{-1}, typical values for shales (Sclater and Christie, 1980). As expected, the results show that, when decompacted, the older horizons had accumulated less shortening than we measure today (Figure 3-7c), and because the present-day cumulative strain does not change (present-day sediments are not buried), this slightly modifies the reconstructed interval strain rates (the slope changes). The results also show that the maximum error is approximately 30% between the measured and de-compacted cumulative strain at the 9.5 Ma horizon (Figure 3-7c). However, it should be noted that the absolute value of the error equals 3% of strain, which is still a negligible value in a structure that accumulated 25% of strain throughout its entire growth history. This is also the maximum possible error because we assumed a stratigraphy consisting entirely of shales; the presence of sandstones would reduce the compaction. Additionally, when plotting this decompacted curve against the aggregate of the 122 uncompacted individual profiles, we assess that the error due to compaction falls within our 10-15% measurement error. For normal faults neglecting the compaction for syn-kinematic strata has been shown to decrease displacement by up to 15% (Taylor et al; 2008).

In summary we estimate the potential errors in the methodology to be similar to that discussed by Jolly et al. (2016), but we have improved on the earlier work by using a more robust depth conversion and addressing the potential effects of compaction.

3.5 Observations and Results

The seabed deepens towards the south-west to depths of almost 3 km and has a step-like geometry due to the presence of six elongated ridges perpendicular to the slope (Figure 3-2). These ridges represent the surface expression of faults and associated folds 21, 20, 19, 17, 13

and 11, which have been recently (less than 3.7 Ma) deformed and uplifted. The 11 thrusts verge towards the south-west, and back-thrusts are only locally present showing small displacements. On section A (Figure 3-3) the total net shortening is approximately 15 km, corresponding to 26% of the original length. The 11 thrusts are variably spaced, ranging from 2.5 to 8 km. The core of the fold belt comprises four closely-spaced, imbricated thrusts (13, 15, 17, 19; Figure 3-5) and shows the highest structural relief in the area (Figure 3-4); in this central part horizon 9.5 Ma is elevated approximately 2 km above its regional level, and the crests of the three folds are eroded by modern seabed slope channels (Jolly et al, 2016, 2017; Figure 3-3, Figure 3-5). This elevated area divides the fold belt into two domains; an inboard zone where, based on the occurrence of growth strata, deformation started at approximately 9.5 Ma, and an outboard zone where deformation started not later than 7.4 Ma (Figure 3-3). Growth strata form wedge-shaped sequences that thin or onlap onto the backlimb of the thrusts forming narrow thrust-top basins. The basins broaden with time, because some of the thrusts, such as Faults 18 and 20, become inactive with time (Figure 3-5c).

3.5.1   Strain distribution in space

When structures are analysed individually their strain-distance profiles show variability both in profile shape and maximum attained strain, as illustrated by fault 21 (Figure 3-8). This type of strain profile is typical of structures that have grown by segment linkage. The cumulative strain-distance profiles for each major structure are presented in Figure 3-9a, allowing the thrusts to be compared. The maximum total cumulative strain within the data set is recorded by fault 13 with a value of -0.38 (38%). The profile shapes show a range of geometries with a general decrease in total cumulative strain from the centre of the structure towards the lateral fault terminations, as is seen for normal faults; however, many profiles also show asymmetries, multiple maxima/minima and steep displacement gradients (fault 13) which reflect the extent to which faults interact. Two or more isolated strain maxima are often seen (e.g. faults 22, 21). Some of the strain-distance profiles shown in Figure 3-9a can be tied to the relevant seismic sections along the strike of the main faults, which are provided in chapter 7. This allows the measured strain profiles to be compared with the (actual) depth-section along strike. Fault 22 is shown in Figure 7-1 and Figure 7-5; fault 21 in Figure 7-6; fault 20 in Figure 7-9; fault 16 in Figure 7-13.
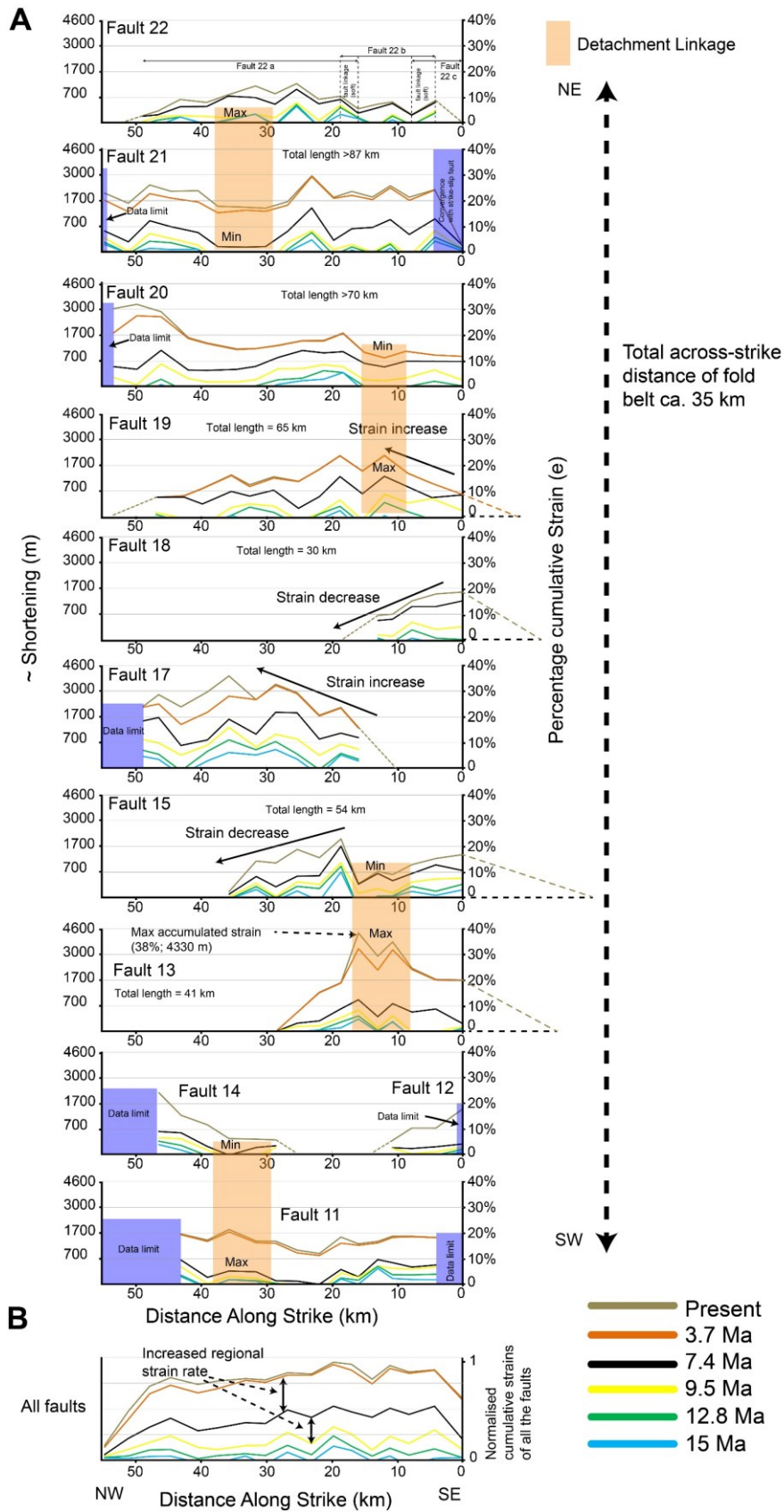
Figure 3-9: A) Strain-distance plots for the 11 thrust-faults in the study area. Each plot also shows how strain was accumulated through time (between 15 Ma and the present day). Asymmetric profiles for individual structures are the result of different types of interaction and strain transfer between faults. In general the faults grow by initial lateral propagation (15 to 7.4 Ma) followed by strain accumulation, without significant fault trace lengthening (7.4 Ma to present). The orange boxes are regions where strain maxima are compensated by a strain minimum on an adjacent inboard thrust, indicating detachment linkage. B) Aggregate strain-distance plot for all the 11 thrust-faults showing that the thrust array has accummulated a near uniform total strain at the present day, indicating full kinematic linkage across the array.

56

Interactions between faults segments had a major role in controlling the observed strain-distance profile shapes. Three main types of interactions can be identified in the data set. The most common type is that also observed in normal fault systems, where initially separate fault segments that are broadly co-aligned, propagate toward one another until the fault tips can interact and link. This leads to persistent strain-minima throughout the growth history of the fault. A clear example is shown by the three segments of fault 22 (a, b and c; Figure 3-9a), and fault 21 (Figure 3-8b). When the strain distribution through time is examined for fault 21 (Figure 3-8) it can be observed that the fault has indeed grown by the growth and linkage of individual segments. The second interaction type is by soft-linkage where faults are not physically connected but are linked through the interaction of their stress fields. In the study area this is commonly observed where strain on one fault is seen to progressively decrease and is transferred to the next fault, either in the hangingwall or footwall as seen for example between faults 18 and 17 (Figure 3-9a). The third type is observed where a strain minima occurs in the centre of a fault and is balanced by strain maxima at the same along-strike distance of the next fault down-dip across-strike. This type of interaction is particularly evident between faults 21 and 22, 20 and 19, 13 and 15, and 14 and 11. It would appear to be an example of detachment-linkage as defined by Bergen and Shaw (2010) and shown in Figure 3-1, where the thrusts become hard-linked during growth parallel to transport direction along a regional detachment level.

The variability in profile shape is reduced when the 11 individual strain-distance diagrams are summed together, as if they described an imaginary single fault plane at the down-dip end of the fold belt. The resulting strain-distance diagram shows a smooth, quasi-elliptical profile (Figure 3-9b) and demonstrates that in both the transport-parallel and perpendicular directions of this part of the thrust belt, all the faults are contributing to the accumulated strain. Where a fault further landward in the array may have accumulated less displacement, this is balanced by a greater cumulative shortening on a seaward adjacent fault. This suggests that all thrusts in the fault array are kinematically either soft, or hard linked, to accommodate displacement along the common underlying detachment, and strain was efficiently transferred across the structures in a coherent and distributed fashion, particularly after 9.5 Ma. At this scale there are no obvious displacement deficits.

3.5.2   Strain distribution through time

Temporal changes in strain rate are clearly illustrated in the cumulative strain profile through time for fault 21 (Figure 3-7c). It shows that the present-day total cumulative strain for this structure has been achieved by periods of low and high strain rates (the slope of the curve). Strain rates are seen to be relatively low between 15 and 9.5 Ma and then from 3.7 Ma to present-day, while, between 9.5 and 3.7 Ma, rates increase. During this period the highest recorded strain rate for this section is -0.033/Ma, which equals 3.3%/Ma, while the recorded total cumulative strain is -0.26 (26%). This result reveals that for this fault tectonic activity started before 9.5 Ma with the intervals between 15 and 9.5 Ma are seen to have accumulated less than 10% cumulative strain.

However, when the same fault is examined in plan view (Figure 3-8a, b) we can extract even more information from our analyses. At 15 Ma 5 short thrust faults existed in the place of fault 21; by 9.5 Ma significant lateral growth had occurred and there were only 3 separate segments. At 7.4 Ma all segments had hard-linked to form a single through-going fault, which continued to shorten until the slow-down in strain rates after 3.7 Ma.

As a way of examining the variation in strain through time for the entire data set, all individual profiles were summed to create the normalized curve shown in Figure 3-10a; which also improves the "signal-to-noise" ratio for all the measurements. The normalized curve shows the same trend as that for the single section through fault 21 confirming that the 15 Ma horizon represents the top of the pre-kinematic section in a regional context. The normalized curve also confirms the "low-high-low" strain rate pattern and suggests this is consistent for the entire outer fold belt evolution rather than representing behaviour of individual faults. When these data are plotted for each of the seventeen transects (Figure 3-11) it can be shown that the strain accumulated between 9.5 and 3.7 Ma (shown in yellow and black) accounts for up to 70-75% of the total cumulative strain recorded today.
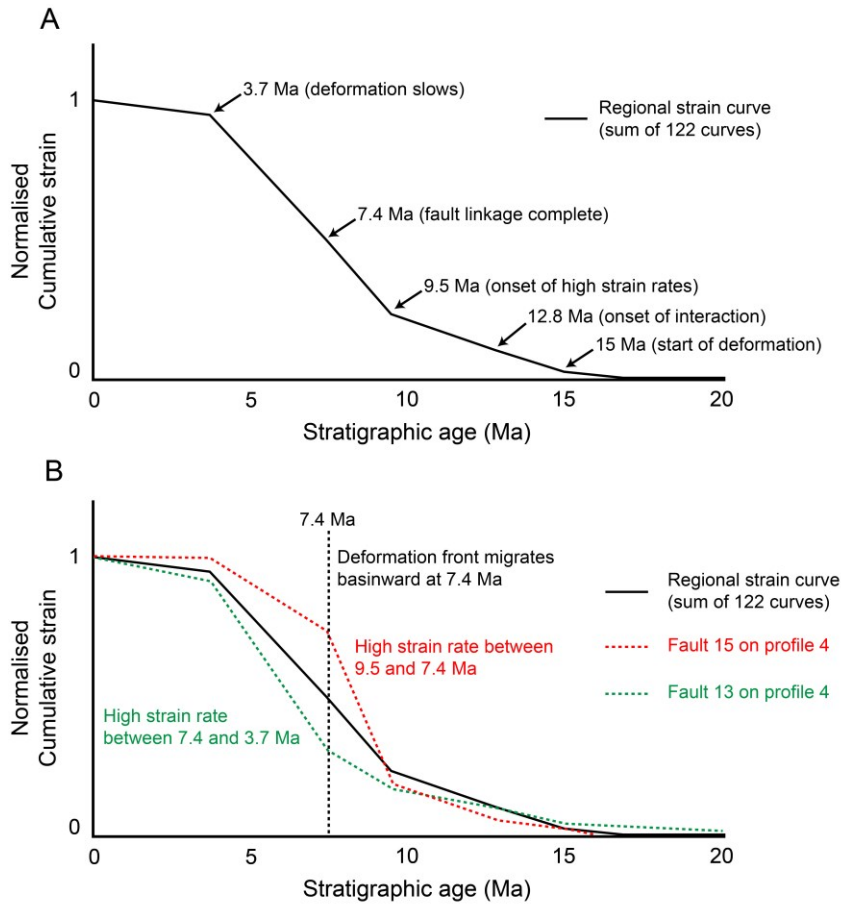
Figure 3-10: (A) Normalised cumulative strain through time for the entire fold and thrust belt. The curve is constructed as the sum of the 122 individual measurement profiles and demonstrates the variation in strain rate through time. The results indicate that tectonic activity started at 15 Ma, a phase of rapid growth took place between 9.5 and 3.7 Ma, and thereafter growth slowed. (B) Comparison between the normalized variation in regional strain rate through time (sold line) and that measured for faults 15 and 13 on profile 4 (see Figure 3-4 for location). The migration of the deformation basinward at 7.4 Ma, is evident from this graph, where strain was transferred from fault 15 (more inboard) to fault 13.
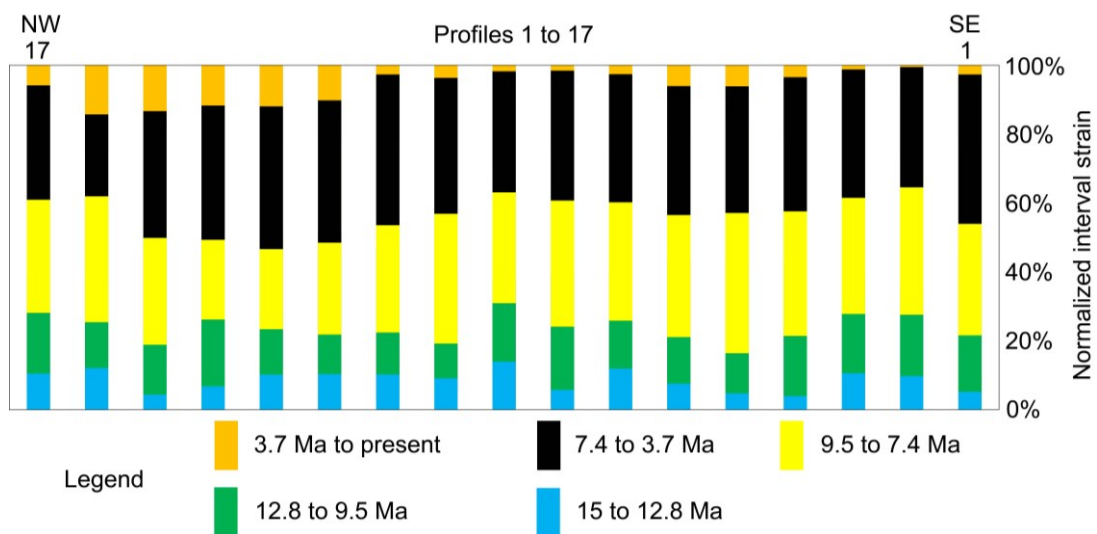
Figure 3-11: Normalized interval strains accumulated by all the thrust-faults on the 17 profiles used for the structural analysis, plotted by time interval, per profile. Note that the strain accumulated between 9.5 and 3.7 Ma (black and yellow bars) accounts for up to 75% of the total cumulative strain.

The data can also be analysed as a series of 'time slices' to investigate the growth history of the thrust fault array through time and space in detail. In Figure 3-12 and Figure 3-13 the fault trace intersections for each horizon are plotted for a depth of 5 km beneath sea-level, providing a template of fault segments through time. The total cumulative strain, and interval strain rate is then colour-coded as a percentage and plotted on fault segment maps for the relevant time, or time interval. This allows us to spatially examine the changes in strain and strain rate throughout the fault network through time. This analysis reveals that at 15 Ma the majority of the faults were small individual segments that had not yet linked. At this time faults 22, 17 and 11 exhibit some lateral continuity (Figure 3-12). On average, fault segments had accumulated 1 to 5 % of the total shortening and only a few localised areas were shortened up to 10% (light green). By 12.8 Ma faults had propagated laterally and partially linked, but the amount of cumulative strain did not exceed 10%, with the highest values concentrated on the most laterally extensive faults (22 and 17). By 9.5 Ma faults had continued to laterally propagate and link, particularly faults 22, 21 and 17. Faults to the front of the array were generally less linked. The average amount of accumulated strain had increased, with more areas showing up to 10 or 15% (dark green). Lateral fault propagation and linkage is complete by 7.4 Ma. At this time the outer fold belt showed two distinct domains; a zone inboard of fault 17 where faults had accumulated between 15 and 25% of strain, and an outboard zone where strain was still as low as 5 to 10% (Figure 3-12). By 3.7 Ma the cumulative strain in the outboard zone also increased up to 20-25%, and fault 17, which marks the boundary between the two domains, accumulated up to 30% of strain. The present-day configuration shows cumulative strains variably distributed, with three main faults (21, 17 and 13) showing the highest values (between 25 and 35%). The absolute highest value of cumulative strain (38%) is measured on fault 13 along profile 6 (Figure 3-12).

Maps of cumulative strain are static, instantaneous "snapshots" of the amount of strain that faults had accumulated by a given time and as such they do not provide information on which faults or fault segments were most active during a specific time interval. Interval strain rate maps are presented in Figure 3-13 to overcome this issue. These data also provide information on the relative accumulation rates of growth packages. As the dips are progressively reduced upward within a growth package (bounded by two surfaces), the line-length of the upper bounding surface will be small compared to that of the lower bounding surface. This would result in a large strain difference (i.e. large interval strain) so that high values of interval strain rates correlate to thicker growth strata sequences. It follows that in the absence of growth strata

(i.e. absence of tectonic activity) the line-length of two subsequent horizons would be approximately the same, and the interval strains and strain rates would be zero or very small.

Results in Figure 3-13 show that in the intervals between 15 to 12.8 Ma and from 12.8 to 9.5 Ma almost all the structures were active simultaneously, regardless of their location within the fold belt. Strain rates were very low, mostly 1%/Ma, increasing locally to 2 and 3% /Ma. In the interval from 9.5 to 7.4 Ma strain rates rapidly increased up to 5%/Ma. At this time deformation was localized on the most proximal structures, inboard of fault 17. From 7.4 to 3.7 Ma results show that the deformation front propagated basinward and the strain rates increased to values of 6 and 7%/Ma in both the inboard and outboard domains (Figure 3-10b). During this time, the most inboard fault (22) decreased to background values of 2%/Ma as it was the first structure to be "abandoned" by the migrating deformation front. During the last interval, from 3.7 Ma to present day, strain rates decreased across the entire fold belt to 1 to 3%/Ma and the majority of the faults stopped moving. Tectonic activity only continued along the three main fault zones (or segments; 21, 17-13, 11). Both the cumulative strain and interval strain maps (Figure 3-12, Figure 3-13) show that the individual thrust faults underwent an initial period of lateral propagation (15 to 7.4 Ma) and established their trace-length, followed by a period dominated by strain increase with little fault lengthening (7.4 Ma to present).
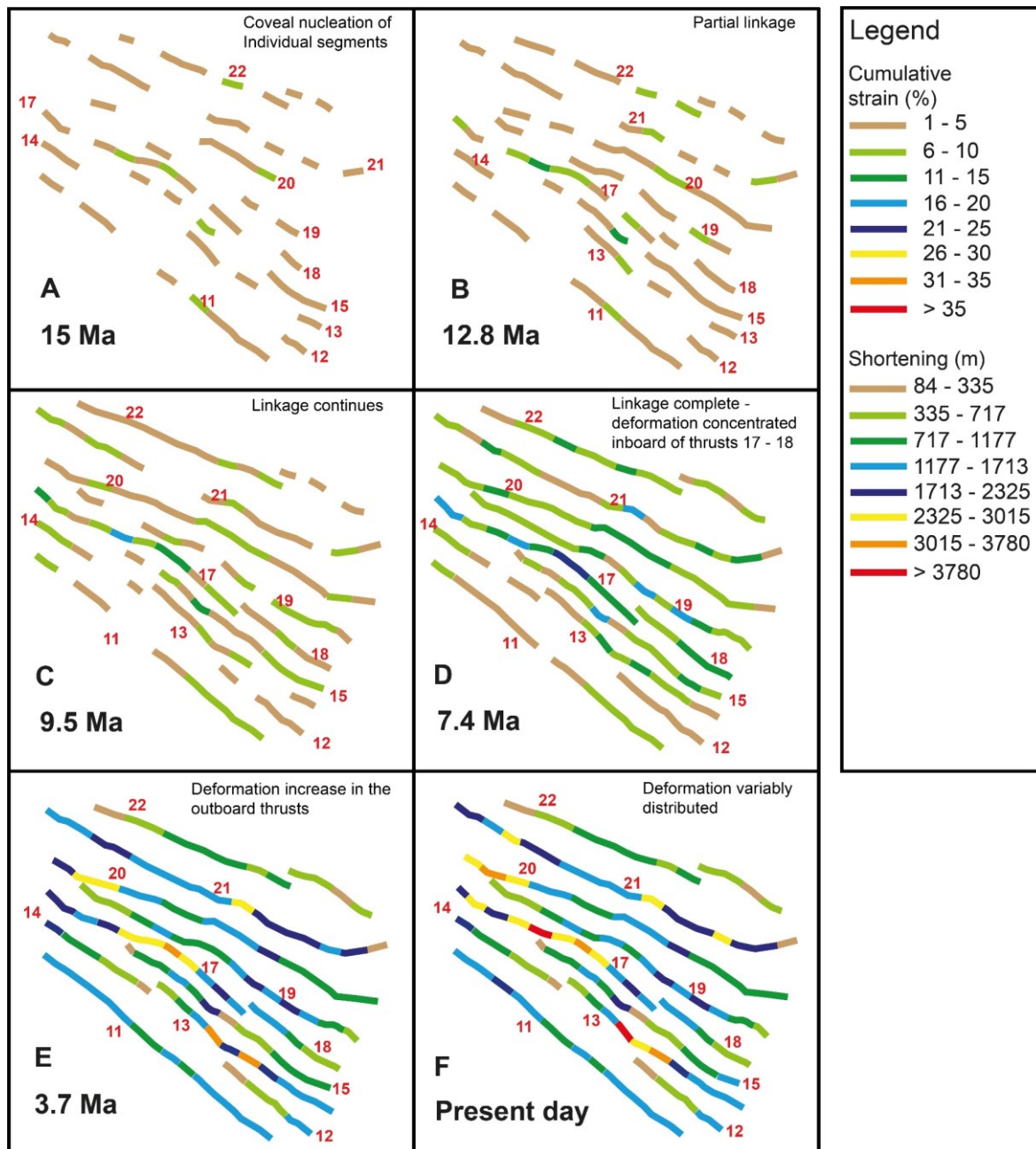
Figure 3-12: Maps of the cumulative strain for structures through time. All thrusts had initiated as short segments by 15 Ma; they then grew by lateral linkage until ~7.4Ma (maps A to C), by which time most of the segments were linked (except faults 14 and 11 at the front of the array). Most faults had reached maximum total shortening by 3.7 Ma, except for short segments of faults 20, 19 17,13 and 11.
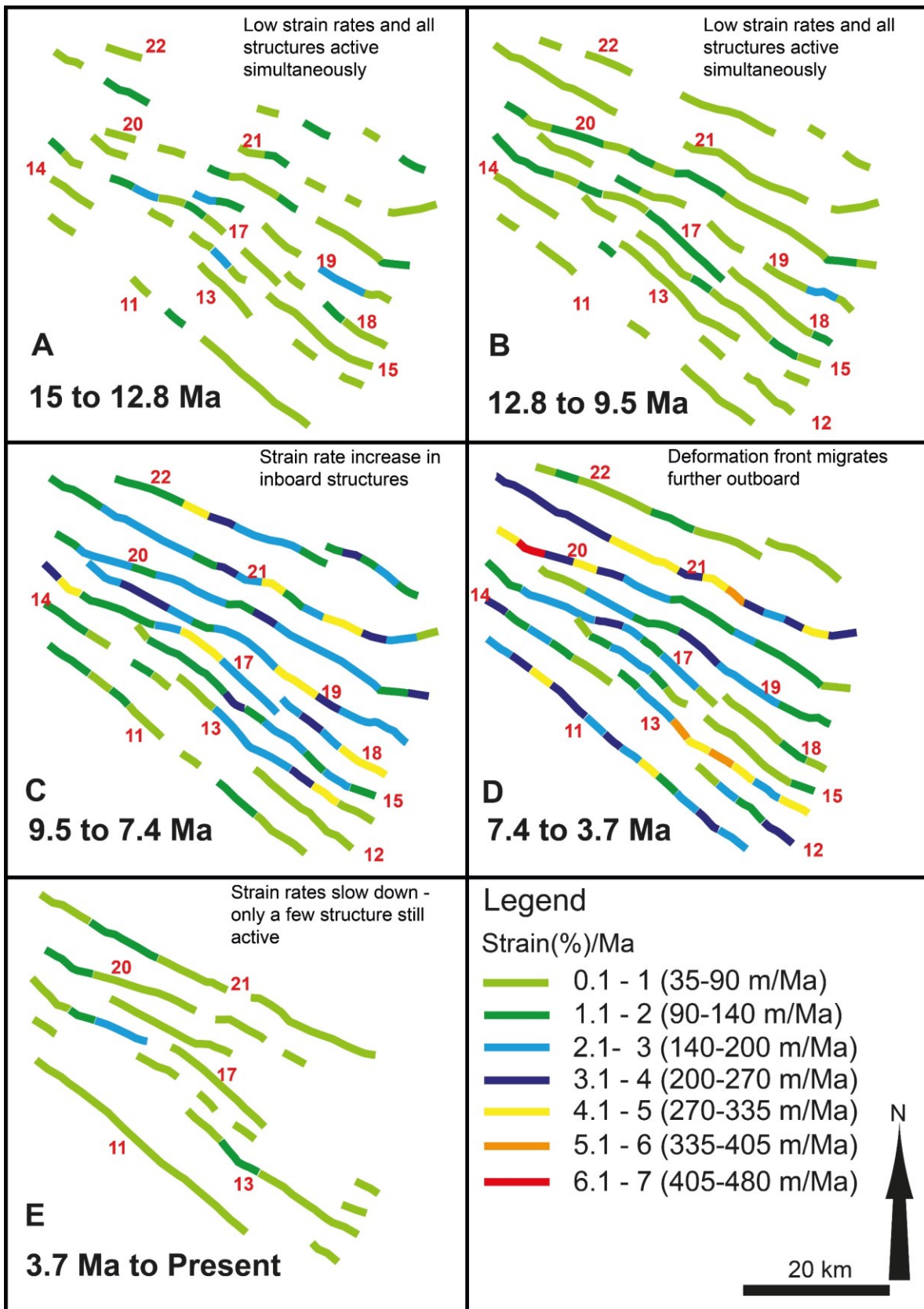
Figure 3-13: Maps of the interval strain rates through time. Low strain rates dominated between 15 and 9.5 Ma (Maps A and B). Strain rates increased notably between 9-5 and 3.7 Ma to values above 200m/Ma, however the more inboard thrusts reach higher strain rates between 9.5 to 7.4 Ma and the more outboard thrusts between 7.4 to 3.7 Ma. In the past 3.7 Ma the strain rate has decreased significantly (<150m/Ma) and many thrusts have ceased to grow. Low regional strain rates allowed continued growth on a few thrusts, while the majority stopped growing.

3.5.3   Strain versus fault length

We also plot the maximum shortening versus maximum fault length for the majority of the faults in the dataset (Figure 3-14). We omit faults 12, 14 and 18 that are only partially present in the mapped area. For comparison we also include data points for seven faults from the Niger Delta analysed by Bergen and Shaw (2010) and the fact that our data align with the previous work, gives further confidence in the robustness of our results and validates our use of line-length balancing. In contrast to most previous analysis of this sort presented for normal faults or thrust faults (e.g. Bergen and Shaw 2010) our data allow us to plot the data through time so we can assess the effect of 'maturity' of fault on these types of analyses. In the normal fault literature (e.g. Cartwright et al., 1995) it has been proposed that at early stages of fault formation, before the segments link, a data point should plot below the global trend line for all faults on a maximum displacement versus maximum fault length graph. As the fault segments link, a data point should move more upward vertically on the graph with a greater increase in displacement for less increase in maximum length. In general, our data show that independent of fault segment maturity, the data plot in the same space as similar data reported by Bergen and Shaw (2010) and can be fitted with a very similar linear or power-law trends. So, in a general sense the juvenile fault segments appear to behave largely as do the mature thrusts. However, when we calculate the average fault segment length and maximum shortening for each time interval (filled black circles on Figure 3-14) a different behaviour emerges. For the early stages of fault growth when the segments are largely unlinked (15-9.5 Ma) the data plot on or below the average linear trend through the entire data set. At 7.4 Ma the average segment length increases substantially with maximum shortening remaining below the trend line, but at 3.7 Ma there is a significant increase in shortening, for a smaller increase in length and the data point moves above the trend line. Between 3.7 Ma and the present day the average maximum fault length does not change while the shortening increases. So, a line linking the average points describes an exponential shape (Figure 3-14b). In Figure 3-15 we show the individual data points for three faults, 22, 19 and 13 respectively. The data show convincingly that this behaviour is not an averaging effect and that for each of these three faults by 9.5 Ma the fault segments had largely linked and in fact it is from 7.4 Ma the faults had reached their maximum length, but they continued to accumulate shortening. All the other faults in the dataset behave in the same way, and this result is entirely consistent with the results in Figure 3-12 and Figure 3-13. The data will be biased by the fact that some of the faults extend out of the study area (Figure 3-9a) and we try to assess the affect that this might have by showing a maximum, estimated, present-day fault length calculated by extending the fault length as mapped outside

of the area of detailed measurements (Figure 3-9a). Extending the fault lengths in this way suggests that the results would be largely unchanged.
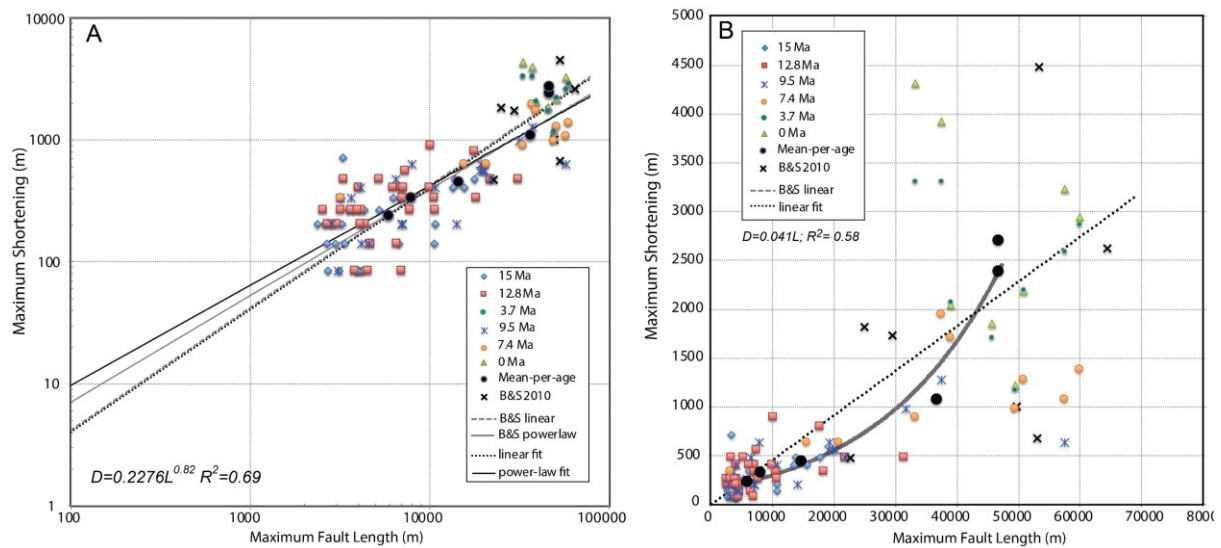
Figure 3-14: Power-law (A) and linear (B) scaling relationships between maximum fault length and maximum shortening for all the faults in the dataset through time and comparison with results from Bergen and Shaw (2010). Although a linear relationship between maximum shortening and length can be assumed for both juvenile and mature faults, average values (black dots), computed at separate times, show a somewhat exponential curve where initially faults accrue length and subsequently shorten at almost fixed length, producing higher D/L ratios than juvenile segments.
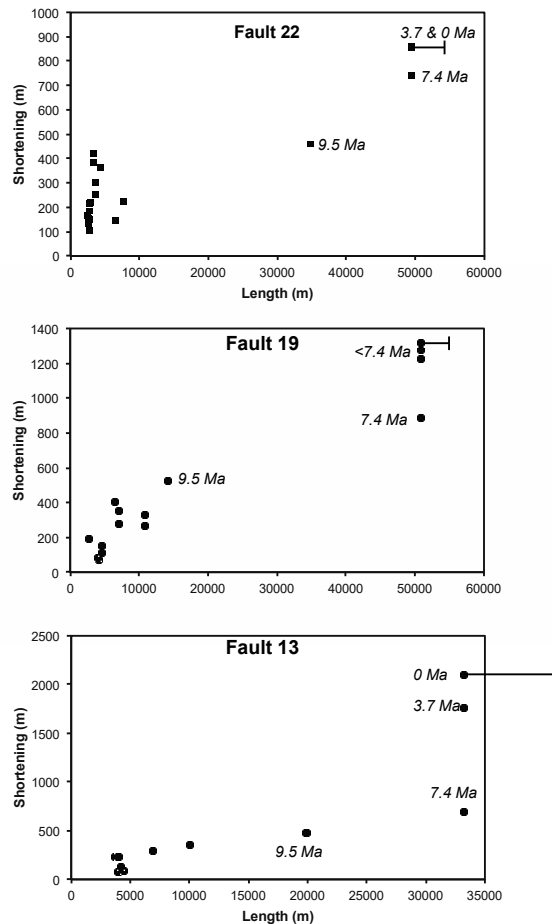
Figure 3-15: Examples of shortening versus length variation through time for three faults in the dataset. All the faults show an initial period of lateral propagation followed by a period of shortening increase at reduced rates of lengthening (or nearly constant length). This proves that the average growth history of all the faults in the dataset (black dots on Figure 3-14) does not result from an averaging effect.

3.6 Discussion

3.6.1 Growth model for thrust-faults

The results of our mapping and 'backstripping' of shortening through time show that fault segments occur distributed throughout the study area over a 40 km across strike distance from the earliest time that we can document their occurrence (15 Ma) (Figure 3-12). Consequently there is no clear evidence of the thrust fault array growing in a piggyback style, but we do observe a wave of deformation that moves from the back to the front of the array, where the maximum strain rate is reached within the 9.5-7.4 Ma interval on the more inboard structures and moves forward to reach the frontal thrusts in the array by 7.4 to 3.7 Ma (Figure 3-10b, Figure 3-13). When the final thrust-fault strike lengths are plotted versus maximum shortening, we get comparable results to those of Bergen and Shaw (2010) for other thrusts in the Niger Delta, indicating that our results are robust and representative. Bergen and Shaw (2010) also reported data from thrusts within the Sichuan and Magdalena Basins, and all three datasets

66

showed very similar power-law, displacement-length relationships. From this we can infer that our results are likely also to be applicable to other thrust arrays.

The second important observation is that for the first half of the deformation history, over a period of c.7-8 Ma, the majority of the faults in the array increase in strike length by segment linkage, where faults growing independently, but broadly colinear, eventually merge. Thereafter the faults accrue shortening without significant increase in fault strike length, and their strain versus distance profiles preserve local minima recording sites of earlier fault linkage (Figure 3-9a, Figure 3-12, Figure 3-15). We observe this not only on the shortening profiles of individual faults (Figure 3-9a), and on the cumulative and interval strain maps (Figure 3-12, Figure 3-13), but also when we plot data for individual faults on maximum shortening (D) versus maximum length (L) graphs for the same fault at different points through time Figure 3-15). These graphs show particularly clearly that an individual fault moves horizontally in D-L space, indicating a dominance of growth by linkage, until c.7.4 Ma and thereafter they move vertically, accruing shortening, but without substantial increase in the fault strike length.

We also know, that at least at the present day, the thrusts in the array are all linked to a detachment level in the Akata shales, so in the terms of Bergen and Shaw (2010) they are detachment linked, and a pertinent question for understanding the growth of a thrust array in three-dimensions is when this detachment linkage occurred. Using the prediction of Bergen and Shaw (2010) that when thrusts are linked along a basal detachment, any displacement that accrues on an outboard thrust should be balanced by displacement loss on inboard structure behind it, we see examples of such behaviour on faults 20 and 19, 15 and 13 and 14 and 11. The discrepancy is most marked in the later stages of fault growth, post 7.4 Ma and this might suggest that by this time there is significant, or complete displacement linkage across the outer fold and thrust belt. As shown in Figure 3-14 and Figure 3-15, this is also when there is a change in mode from increase in fault strike length by segment linkage, to continued shortening on near-constant length thrusts. If the thrusts are hard-linked both laterally and across strike, then this would favour such a pattern of displacement accumulation. The faults are effectively pinned at their lower tips, and linked along strike, so growth is expressed as an increase in shortening. We present a summary of this model for thrust fault growth in Figure 3-16 for one representative thrust in the array. The phase of growth dominated by along strike segment linkage is shown by idealised shortening versus length profiles for two faults segments that increase in length until they are fully linked 7.4 Ma. The linkage location will be recorded by areas of strain minima as per Figure 3-9, but we do not show the linkage-related minima on

Figure 3-16 for clarity. Thereafter the thrust still accumulates strain but does not grow appreciably in strike length. The signal of detachment linkage is shown by a local shortening minimum which we predict is most likely to have occurred from between 9.5 to 7.4 Ma when the segments are largely linked laterally (Figure 3-16a). How this growth would appear on a maximum shortening versus maximum fault length graph is shown on Figure 3-16b, where one can observe that for at least half of the fault's history, growth was dominated by lateral linkage. For this example of a deep-water fold and thrust belt, fault growth by lateral linkage is the dominant mode of thrust fault growth for about 50% of the fault array history. Subsequently strain accumulates by increasing shortening, with more evidence for direct feedback, and hard-linkage along the detachment, where an increase in shortening in a more frontal thrust may be kinematically compensated by less shortening in a more landward thrust, as indicated by the dashed local minimum in Figure 3-16a.
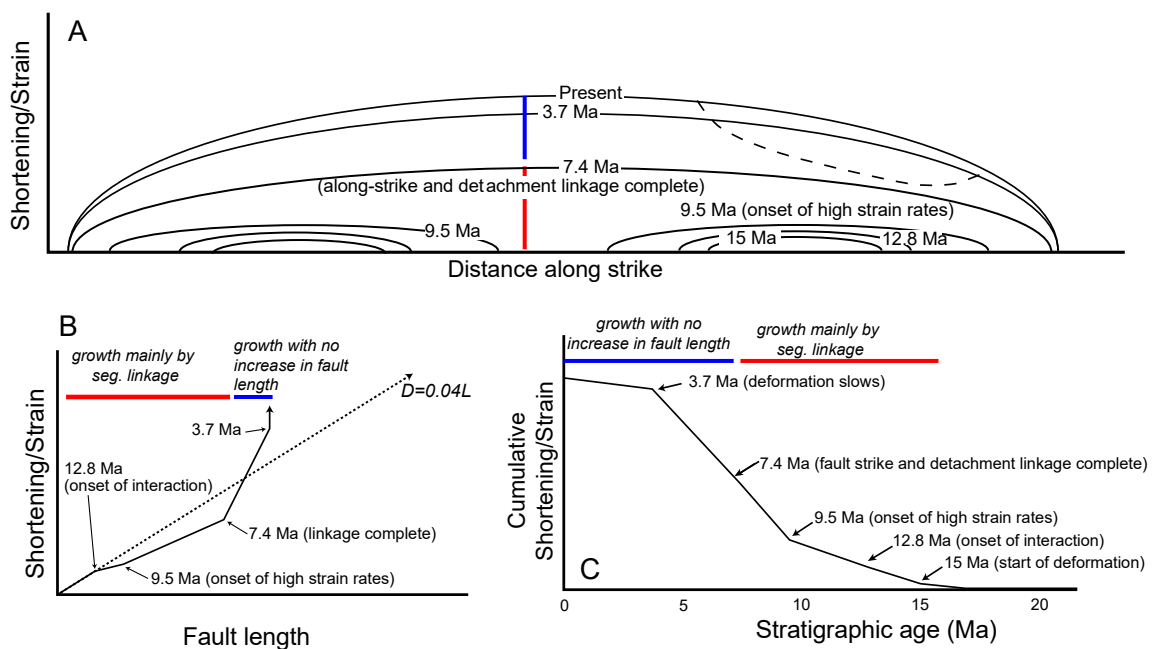
Figure 3-16: (A) Summary model for thrust-fault growth. For the first half of the growth history the fault segments grow by increasing length (red bar), thereafter when the faults are linked both along and across strike (detachment linkage), the fault continues to shorten but does not grow significantly in strike length (blue bar). The dashed line illustrates the potential shortening deficit that can occur between neighbouring faults across strike when hard-linked though a basal detachment. The corresponding evolution of maximum fault length versus displacement through time is shown in (B). As the fault segments grows laterally it will move to the right in D/L space and once linkage is complete, both along and across strike it moves above the best fit D/L line, as it shortens with minimum increase in segment length. (C) The cumulative strain rate curve through time shows that linkage timing is not a function of strain rate variations.

An implication of this model is that the thrust faults do not form within the Akata detachment level and propagate upwards, but that they must nucleate within the deforming sedimentary succession (Agbada Formation) and propagate in all directions near simultaneously. Indeed Figure 3-12 shows that by 15 Ma, small short isolated thrusts are present throughout the main

part of the deforming Abgada Formation, distributed over a 40 km distance across strike and have started to displace the prekinematic stratigraphy older than 15 Ma. One test of the model would obviously be to elucidate where the thrusts nucleated. Data on thrust fault initiation location is rare, and there have been many different ideas over time, with earlier work tending to assume that faults emerge from the low-angle detachment and ramp upward to higher stratigraphic levels, and then others using field and seismic reflection observations suggesting that thrusts nucleate within a stratigraphic package and propagate both upward and downwards (see Feral et al 2016, Marshak et al 2019 for recent reviews). A suite of discrete-element numerical models by Hardy et al (2009) showed that many of the faults did not develop at the basal detachment and propagate upwards, but rather initiated within the cover. Recent particle-image velocimetry analysis of a sandbox model by Marshak et al (2019) shows fore-thrust ramps initiating in the middle of the deforming layers, with the fault then growing both up and down-dip until it reaches the detachment. The model of thrust growth that we propose is consistent with these recent modelling results.

In summary, within the external boundary conditions imposed on the outer fold and thrust belt of the Niger Delta, where the deformation is driven by gravitational processes, and the strain rate starts slow, builds up and then slows down again (Figure 3-16c), short faults start to grow at ~15 Ma distributed throughout the area and nucleating within the pre-kinematic sedimentary succession. Our strain rate through time data (Figure 3-13) demonstrates that the entire sedimentary wedge over distances of 10s km in both along and across strike directions deforms at a similar time, albeit with strain rates varying on individual structures, and across the belt. As displacement on the thrusts and fold growth continues the thrusts increase in length by fault linkage, for about 50% of their history and thereafter grow mainly by increasing shortening. We postulate that the transition in mode of growth corresponds with when the majority of the thrusts are hard-linked across strike along the detachment. Hence to fully understand thrust growth in deep-water systems the full 4-D deformation field should be documented, and systems have to be considered to link not only along strike, but also across strike via the detachment, as also proposed by Totake et al. (2018) based on their analysis of two parallel thrust-fold anticlines in the Borneo deep-water fold and thrust belt. Such a model provides an explanation for the development of asymmetric displacement profiles, low displacement-length ratios (strike linkage), and local minima, corresponding with local maxima for adjacent structures across strike (detachment linkage) as predicted by Bergen and Shaw (2010).

How does the growth of thrust faults compare to normal fault growth models? There are two end-member models that have tended to dominate the literature on normal fault growth models (see review in Rotevatn et al. 2019). The first, and earliest is that fault growth occurs via an increase in fault length synchronously with displacement, (e.g. Walsh and Watterson, 1998; Cartwright et al. 1995 amongst many others). The second model proposes that faults reach their near final lengths early in their history with early linkage and then they mainly grow by increasing displacement, the 'constant length' model (Walsh et al 2002, Nicol et al. 2005 amongst others). Our new data agrees with the results reported by previous authors for thrust systems, where thrust faults display many of the growth and linkage characteristics of normal fault systems, at least in their along-strike direction, but previous workers did not give any indication of the time frame over which the linkage occurs (Fermor, 1999; Hatcher, 2004; Davis et al 2005; Mazzoli et al. 2005; Amos et al. 2010; Watkins et al. 2017; Higgins et al 2009; Bergen & Shaw 2010; Jolly et al 2016, 2017; Totake et al 2018). However, our new results have allowed us to detect a switch in mode from fault growth being dominated by segment linkage in the first half of its history to shortening with near constant thrust strike-length later, and thus we observe elements of the 'constant-length' normal fault model in the second half of the thrust wedge's history. While there are clearly some similarities with normal fault growth models, there is one important difference. The proponents of the 'constant-length normal fault model', say it is the *dominant* mode of fault growth and that linkage occurs early in the fault history (e.g. Walsh et al. 2002), but it is not always clear how to establish exactly what 'early' means. Quantitative data with age constraints, such as that presented by Nicol et al (2005) in the offshore Taranaki Basin, New Zealand for recent faults active within the last ~4 Ma, show that the fault tips remained approximately stationary for at least the last 3.2 Ma; these data would support the constant-length model for normal faults. The recent review by Rotevatn et al (2019) acknowledges that the duration of the initial phase of normal fault growth by segment linkage remains uncertain. Their summary of previous work done on real faults with age data and experimental faults generated in analogue models suggests that the majority of normal faults have established their near-final lengths within ~20-30% of their slip history (Rotevatn et al. 2019). We do not observe the same behaviour for our comprehensive analysis of the thrust array in the Niger Delta. Instead growth and increase in fault strike linkage dominates 50% of the lifetime of fault growth. Of course, our data are censored in the sense that we do not know when the fold-belt will stop growing, so this percentage may well reduce with time. However, the most recent internal strain rate map (Figure 3-13E) showing that fewer

faults are now active, and the notable reduction in strain rate observed in the last ~4 Ma (Figure 3-10, Figure 3-11) indicate that growth is slowing significantly.

Regardless of when the thrust array finally arrests, 7-8 Ma of growth dominated by segment linkage is a significant length of time. Given that thrust systems ultimately link in the third dimension along a basal detachment and linkage needs to be examined both along and across strike, it is not surprising that there are significant differences between how normal faults and thrust arrays grow and evolve, and we suggest that it may not be appropriate to expect the same models to apply in both modes of deformation.

3.6.2 Strain variation through time

In deep-water fold and thrust belts forming on shale detachments such as the Niger Delta, it is well accepted that the gravity- deformation is driven by sediment loading. The deformation will not begin until the amount of overpressure can overcome the critical yield stress of the shale, and this only occurs once a large thickness of overburden sediments has been deposited rapidly enough to raise fluid pressures (Rowan et al. 2004), which Krueger and Grant (2011) estimate to be when the Akata formation was buried to a depth of ~4 km for the Niger Delta fold and thrust belt. The deformation is manifest as broadly coeval up-dip extension and down-dip shortening. It therefore follows that the rate of sediment loading affects the rate of both extension and shortening in the fold and thrust belt.

Our new data supports the results of Jolly et al. (2016) who demonstrated a varying strain rate through time for 4 structures within the outer fold and thrust belt. Over a much larger area, than the previous study (4500 km^2), we show that in the past 15 Myr the strain rates were initially slow (average strain rates <200m/Ma), then increased between 9.5-3.7 Ma (200-400m/Ma) and have decreased substantially in the last ~ 4 Ma to < 150 m/Ma (Figure 3-10, Figure 3-11, Figure 3-13); when the strain is summed across all thrusts studied, up to 75% of the total strain accumulated between 9.5-3.7 Ma (Figure 3-11). Analysis of thrust faults from both lobes of the Niger Delta by Krueger and Grant (2011) also led them to conclude that many of the thrusts have ceased activity since the end of the Pliocene, and they too identify a main phase of thrust activity between ~9 and 3.85 Ma.

Our data documents that the thrusts started growing from ~15 Ma and this contrasts with the only two other studies with biostratigraphic data to allow dating of the deformation. Restoring a series of regional cross-sections, Wiener et al. (2010) deduced that the thrusts started to grow at 9.3 Ma. Kreuger and Grant (2011), using growth strata geometries, produced a series of

comprehensive thrust growth activity maps for both the lobes of the Niger Delta and showed that the main activity on the thrusts also started from ~9 Ma. Three thrusts that they describe in more detail show the main interval of growth to be between 9 Ma and 3.85 Ma. We suspect that the differences in approaches in deducing deformation timing is responsible for this discrepancy. Our method of analysing strain has allowed us to identify bed length changes that occurred earlier than observed by purely identifying the most obvious growth strata, and by close inspection of the seismic data we have identified subtle stratal thinning towards the crests of structures in the 12.8 to 9.5 Ma interval. However, all approaches agree that the main phase of growth was between ~9-3.7 Ma. Wiener et al (2012) have suggested that substantially increased shelf-margin deposition in the late Miocene to Pliocene was responsible for the increase in deformation rates. We agree that this would appear to be a very plausible explanation. Thereafter the deformation rate notably slowed, and Rouby et al. (2011) and Jolly et al. (2016) have proposed that the reduction in deformation rates in the upslope extensional and downslope contractional domains in the last 4 Ma is a response to decrease in sedimentation rate caused by a reduction in sediment supply to the delta top during the Plio-Pleistocene interval (Jermannaud et al., 2010).

The other significant result of our work is that at any time interval the activity was not focussed on the most frontal thrust but distributed throughout the thrust array, showing many faults moving synchronously with no obvious piggy-back or break-back propagation of the thrusts (Figure 3-13 and Figure 3-14). Previous work on the Niger Delta fold and thrust belt (Wu and Bally, 2000; Corredor et al., 2005; Krueger and Grant, 2011; Wiener et al., 2010) also document complex, out-of-sequence and synchronous sequences of thrusting. That said, we do observe a basinward propagation of the main phase of fault growth (Figure 3-3), with thrusts to the NE of Fault 19 (Figure 3-3, Figure 3-4) growing most rapidly between 9.5 and 7.4 Ma, and the more basinward thrusts growing faster after 7.4 Ma (Figure 3-10B; Figure 3-13C and D).

Considering the evolution of the Niger Delta in the context of critical wedge theory (e.g. Rowan et al. 2004; Bilotti and Shaw, 2005; Morley 2007) allows some further insight into potential controls on the synchronous and complex evolution of thrust growth that we document. The Niger Delta and other deep-water fold and thrust belts, such as that offshore northwestern Borneo have very low critical tapers (<4°) and surface dips of <2.5° (Bilotti and Shaw, 2005; Morley 2007). Such low taper values imply that they must have very weak basal detachments, with pore-fluid pressures near lithostatic to enable the wedge to propagate. In contrast to

subaerial wedges in active tectonic setting, where the main processes that acts to lower the taper is erosion of the hinterland, in deep-water fold and thrust belts the wedge is generally subject to net deposition (Morley 2007); erosion is rare and is mostly limited to submarine slumping at the delta front or on structural highs. The addition of sediment to the shelf margin by building up the delta (i.e. the back of the wedge), will increase the upper slope dip which in turn will drive extensional deformation at the back of the wedge as it aims to lower its slope and return to equilibrium. In turn the increased extensional deformation will drive the down-dip contraction. Conversely, increasing sedimentation over the entire wedge lowers the surface slope, and the development of a broad belt of synchronously active fold and thrusts, which may include out-of-sequence thrusts, would be an effective way of elevating the back of the wedge and maintaining critical taper as predicted by Morley (2007).

Numerical and analogue wedge models of emergent fold and thrust belts that include the effects of erosion in the hinterland and re-deposition in the foreland, have shown that complex sequences of thrusting may occur as the wedge responds to perturbations in the critical taper (e.g. Stockmal et al., 2007; Wu & McClay, 2011). Analogue models of a critically tapered Coloumb wedge show that erosion in the hinterland and re-deposition in the foreland tends to reduce the taper, and consequently internal deformation of the hinterland is needed to increase the surface slope, through reactivation and out-of-sequence thrusting (Wu and McClay 2011). The numerical models of Stockmal et al. (2007) and Fillon et al (2012) show that feedback between parameters such as syn-tectonic sedimentation, erosion, strength and number of detachment levels control how the wedge at a large scale behaves, and how in turn structural styles within the wedge adjust. The experiments of Stockmal et al (2007) show many examples of older formed thrusts continuing to move behind the active front, and new thrusts forming in out-of-sequence geometries. Hence results of numerical models for sub-aerial wedges would support the prediction that for submarine wedges lowering surface slopes by increasing sediment supply to the entire wedge will promote synchronous thrusting with thrusts having long histories, some of which may be out-of-sequence or be reactivated to help build and maintain the critical wedge taper.

Variation in detachment strength through time and space may be an additional factor that affects the sequence of thrust growth. If, for example, locally the Akata shale dewaters, the detachment will strengthen and that may promote out-of-sequence motion on thrusts (Wu and Bally 2000; Rowan et al. 2004). Using a simple pore-pressure evolution model, Kreuger and Grant (2011) show how excess pore-fluid pressure transfer can help explain the localization of

out-of-sequence thrust growth during the evolution of a single structure. However, from the work of Bilotti and Shaw (2005) we know that the Akata shale must be currently very weak across the entire width of the fold and thrust belt to maintain the very low taper of the wedge; likewise the anomalously low seismic velocities of 2700 m/s for the Akata formation in our study area (Figure 3-6) also supports the fact that over large areas the Akata detachment has high pore-fluid pressures. We therefore favour the critical taper model, as opposed to appealing to local strengthening of the detachment, due to pore-pressure release, as a more plausible explanation for why near synchronous movement of thrusts over a broad swathe of the outer fold and thrust belt is observed.

Lastly, the thinning and pinching out of the detachment layer may also exert some control on thrust growth timing, as effectively the point at which it dies out will pin the front of the wedge. As shown in the sandbox models of Costa and Vendeville (2002), where they model a very weak viscous detachment, the frontal tip of the fold and thrust belt reaches the pinch-out position of the detachment early and forces the shortening to be accommodated over the entire length of the system. Very little data exists on the distalmost part of the fold and thrust belt and thickness of the Akata shales. Regional sections drawn from seismic data interpret Akata shales thinning to thicknesses of c. 0.5 sec Twtt over distances of 100 km (Haack et al, 2000; Wu & Bally, 2000; Morgan, 2004; Wiener et al. 2010). One seismic line across the southern lobe in Wu and Bally (2005) does show the Akata thinning to less than 200ms Twtt within 20 km of the outermost thrust of the fold belt, which would suggest that the detachment does not extend much beyond the present day thrust front. The fact that our data show that all thrusts start to form contemporaneously within the resolution of our data, provides support for the early propagation of the thrust front to the outboard limit of the over-pressured, weak Ataka shale detachment, and that this may be an additional control, that will affect taper dip, and hence the timing of thrusting.

In summary, we suggest that the first-order control on the growth of the fold belt is the variation in regional strain-rate driven by sediment supply to the delta. This contributes to surface slope changes through time and in terms of maintaining the low critical taper of the fold and thrust belt of the Niger Delta, wedge mechanics theory would predict a broad swathe of near-synchronously active fold and thrusts. Rapid migration of the deformation front to the oceanward pinch-out of the weak detachment will also promote the accommodation of shortening throughout the deforming wedge, and also act to change the surface dip of the wedge.

3.7 Conclusions

The detailed analysis of 3D seismic data, in combination with age data, has allowed us to 'backstrip' the growth history of an extensive array of thrust-related folds in the toe-thrust region of the southern lobe of the Niger Delta over along and across-strike distances of 10s of km. Using these results, we propose a new model for how thrusts grow and link both along and across strike through time, where linkage along the underlying detachment plays an important role. All faults nucleated at a similar time, by ~15 Ma, most likely within the pre-kinematic strata, and for the first 50% of their history (~ 7-8 Ma) grew predominantly by lateral strike-linkage, but also extending both upwards to interact with syn-kinematic strata and downward towards the underlying detachment. Thereafter the thrusts and related folds continued to shorten, without significant increase in strike length. This is evident from both the maps of shortening through time and plotting the D_{max} v L_{max} relationship for individual thrusts through time. Local shortening minima, corresponding with local maxima for adjacent structures across strike are interpreted as evidence for linkage along the detachment. We propose that the change in mode from along-strike linkage, to continued growth by increasing shortening corresponds with when the majority of the thrusts are hard-linked across strike along the detachment. There are thus some similarities with growth models for normal fault systems, but also significant differences. Given that many thrust systems ultimately link in the third dimension along a basal detachment and linkage needs to be examined both along and across strike, this is perhaps not a surprising result and we suggest that it may not be appropriate to expect the same models to apply in both modes of deformation.

Additionally, the quantification of shortening and strain rates through time shows that the majority of the thrusts were active broadly contemporaneously, but that the strain rate has varied through time. In the past 15 Myr the strain rates were initially slow (average strain rates <200m/Ma), then increased between 9.5-3.7 Ma (200-400m/Ma) and have decreased substantially in the last ~ 4 Ma to < 150 m/Ma, with many of the thrusts becoming inactive. When the strain is summed across all thrusts studied, up to 75% of the total strain occurred between 9.5-3.7 Ma. At a large scale, a pulse of higher strain prograded basinward between 7.4 and 3.7 Ma. Despite the variation in strain rates through time our results show that when the total strain is summed for the 11 faults studied, strain was efficiently transferred across the structures in a coherent and distributed fashion, with no obvious displacement deficits.

We propose that variation in sediment supply to the delta front and slope was the dominant control on the strain variation through time. A high shelf-margin deposition rate in the late Miocene to Pliocene led to the increased strain rates measured through this time interval. Reduction in sediment supply to the delta in the last ~4 Ma is thought to be responsible for the recent reduction of strain rates. In turn, variations in sediment supply, in addition to the down-dip pinching out of the Ataka shale detachment, contribute to changing the surface slope of the wedge through time. Because sedimentation acts to lower the surface slope, in a critical taper wedge model the wedge will respond by shortening over a wide area to build up the surface slope. Therefore, application of critical wedge mechanics to deep-water fold and thrust belts can help explain why over large areas, a broad swathe of synchronous thrust and fold growth can occur, as observed for the outer fold and thrust belt of the Niger Delta.

4. Classification and evolution of seismic facies and depositional elements

4.1 Introduction

The main aim of the following four chapters (4 to 7) is to investigate the relationships between the growth of the gravity-driven fold and thrust belt (previously quantified in chapter 3) and the distribution in space and time of the main deep-water facies, including their architecture. To achieve this, the first step in understanding the stratigraphic evolution of the sedimentary systems within the study area and their areal distribution with respect to the location and amounts of strain attained by the different controlling thrusts, is to conduct a systematic classification of the dominant seismic facies observed in the data set. In this chapter, I describe the seismic facies observed vertically within each stratigraphic interval according to a set of parameters (see below) in order to assign them to distinct categories. Subsequently, I overview the evolution of these seismic facies through time and in space, addressing the different sub-basins in the study area in terms of timing of occurrence of a specific facies type in a proximal to distal transect. In subsequent chapters, the vertical change in seismic facies will be further interpreted and discussed with the integration of isopach and strain data which will provide regional constraints on the basin evolution.

The stratigraphic interval analysed here starts from the base of the Agbada Formation (ca 30 Ma), but specifically focusses on the interval between the 15 Ma horizon, regionally corresponding to the start of the deformation, to the 3.7 Ma horizon, a time which marks the end of the main tectonic pulses and the start of low strain rates which persist until the present day (see chapter 3). This interval was divided into 6 units (15-12.8, 12.8-9.5, 9.5-7.4, 7.4-6.5, 6.5-5.5, 5.5-3.7 Ma), and for each unit the dominant seismic facies and their associations were extracted in order to construct a vertical evolutionary model for the outer fold and thrust belt.

It is important to note that the interval between 7.4 and 3.7 Ma has been further subdivided from chapter 3 into three units with the addition of the 6.5 and 5.5 Ma horizons. These two age horizons have been correlated from Krueger and Grant (2011) who showed a regional seismic line passing entirely within our dataset. These authors state that they have used available well biostratigraphy, therefore, being able to date stratigraphy from the Oligocene to Holocene.

The seismic facies classification adopted here follows the basic principles of seismic-stratigraphy and seismic-geomorphology (Prather et al., 1998; Posamentier and Kolla, 2003, Cartwright and Huuse, 2005).

The scheme developed here is not based on any pre-existing classification model as it is developed specifically for the studied area; however, I suggest that similarities can be noted with other basins worldwide. The seismic facies were classified based on their cross-sectional external and internal geometry and architecture, plan view form, character and seismic amplitude of internal reflections, dimensions and relationship with underlying stratigraphy (erosional or concordant) and type of interaction they exhibit with the structures (e.g. major/minor deflections etc.). The result of the initial analysis yielded 4 main seismic facies types: channel forms, lobe forms, mass-transport complexes and background slope sediments. A second-pass screening, aimed to highlight the variability of channel forms (Janocko et al., 2013) and lobe forms, yielded 5 types of submarine channels and 3 types of lobate elements. In the following sections a full description of each facies type will be provided while a summary is presented in Table 4-1.

Table 4-1: Summary of facies types observed in the dataset.

Seismic Facies	Description	Width	Depth/Height	Sinuosity - type	E/C ratio	Interval of occurrence
Leveed channels	Consists of a channel axis and gull-wing shaped levees on side . Channels axis show high amplitude internal reflections; levees have low to moderate amplitude.	Channel axis: up to 2 km Levees: up to 4 km Overall: up to 10 km	Up to 200 m. Highly aggradational channels are up to 350 m	Sinuosity ranges between 1.2 to 1.4. It appears to be induced by tectonics or seafloor topography as there are no signs of lateral migration or stacking. Evidence of sharp bends and cut-offs.	0.4 - 0.6. 0.3 - 0.4 (highly aggradational)	Dominant between 12.8 and 7.4 Ma. Highly aggradational occur between 9.5 and 6.5 Ma.
Erosional channels	Channels axis confined within a deep erosional surface. Repeated cycles of downcutting and deposition and presence of terraces. Complex internal architecture with low to high amplitude reflectors from continuous to chaotic.	3 to 5 km	Up to 200 m	Sinuosity ranges between 1.4 to 1.7. It appears to result from lateral migration and/or stacking. Lateral accretion packages often visible	1.5 - 2.5	Dominant between 7.4 to 5.5 Ma
Low-relief channel-levees	Consist of low amplitude (mud-filled) channel axis and high amplitude levees or wings. Occasionally levees are missing.	Channel axis: up to 1 km Levees: up to 1.5 km Overall: up to 4 km	Up to 100 m	Linear to slightly sinuous (1.1-1.2). Sinuosity due to seabed topography with evidence of sharp bends.	Approximately 1 +/- 0.2	They occur just before 7.4 Ma until 6.5 Ma but never dominant.
Linear channels	Lack the typical U or V shaped geometry of channelized bodies, but appear as slightly elongated high amplitude features where top and base amplitude responses increase and dim simultaneously.	Up to 1 km	Up to 50 m (one seismic loop)	Linear to slightly sinuous (1.1-1.2). Sinuosity likely due to seabed topography with evidence of sharp bends. no evidence of lateral migration or stacking due to limited seismic resolution.	N/A	They occur between 15 and 12.8 Ma and partly in the 12.8 to 9.5 Ma interval.
Channelized sheets	Vertically stacked high amplitude, semi-continuous reflectors dissected by numerous small low amplitude u-shaped channels.	Channels: up to 200 m Individual sheets: up to 3 km Sequence: 10s of km	Channels: up to 50 m Individual sheets: up to 50 m Sequence: up to 250 m	Channels linear to moderately sinuous (up to 1.5). Sinuosity due to seabed topography with evidence of sharp bends.. No LAPs visible.	N/A	Dominant between 5.5 and 3.7 Ma
Unconfined lobe complexes	Laterally extensive and generally continuous high amplitude reflectors, with either tabular or wavy geometry. Internally organized in a hierarchy of progressively smaller lobes.	Lobe complex: 15 km Lobe: up to 3 km Lobe element: < 1 km	Lobe complex: up to 250 m Lobe: up to 50-100 m Lobe element: up to 50 m	N/A	N/A	Dominant from base of Agbada Fm. until 15 Ma and partly from 15 to 12.8 Ma
ponded lobes	Laterally extensive high amplitude reflectors, with tabular geometry. They lack internal organization and hierarchy. Plan-view geometry controlled by shape of depocentre.	Between 10 - 20 km	Up to 100 m	N/A	N/A	Frequent between 7.4 to 6.5 Ma. Occasional between 12.8 to 7.4 Ma and from 6.5 to 5.5 Ma
Crevasse splays	High amplitude continuous reflectors, with mounded geometry and variable plan-view shape. Typically found on the outher bend of leveed channels.	Up to 2 km	Up to 50 m	N/A	N/A	Occasionally found between 12.8 and 7.4 Ma associated with channel-levee complexes.
MTCs	Characterized by low to moderate seismic amplitudes, highly chaotic in character. The basal surface is typically erosional, while the upper surface is generally smoother and mounded.	Up to several km	Up to 200-300 m	N/A	N/A	Frequent between 5.5 to 3.7 Ma. Occasional between 9.5 to 7.4 Ma and from 6.5 to 5.5 Ma
Hemipelagic deposits	Consist of low to moderate amplitude packages, almost internally transparent that generally drape and smooth older topography. They have variable lateral topography. They have variable lateral continuity, but some packages can be correlated for tens of kilometres.	Basin scale	N/A	N/A	N/A	Continuous background deposition. Dominant between 6.5 to 5.5 Ma.

79

4.2 Channel forms

4.2.1 Leveed channel complexes

This category of submarine channels dominates the stratigraphic intervals between 12.8 and 7.4 Ma. On seismic sections they are formed by two main building blocks; a channel axis and levees each side of it (Figure 4-1). The channel axis can be up to 2 km wide and 200 m deep, containing high amplitude reflections from chaotic to sub parallel. The larger channel axis fill likely consists of smaller scale channel fills which are unresolvable due to the seismic resolution limitation (Deptuck et al., 2003; Zhang et al., 2018). However, it is occasionally possible to recognize late stage channel fills 500 to 700 m wide and 100 m deep (Figure 4-1).
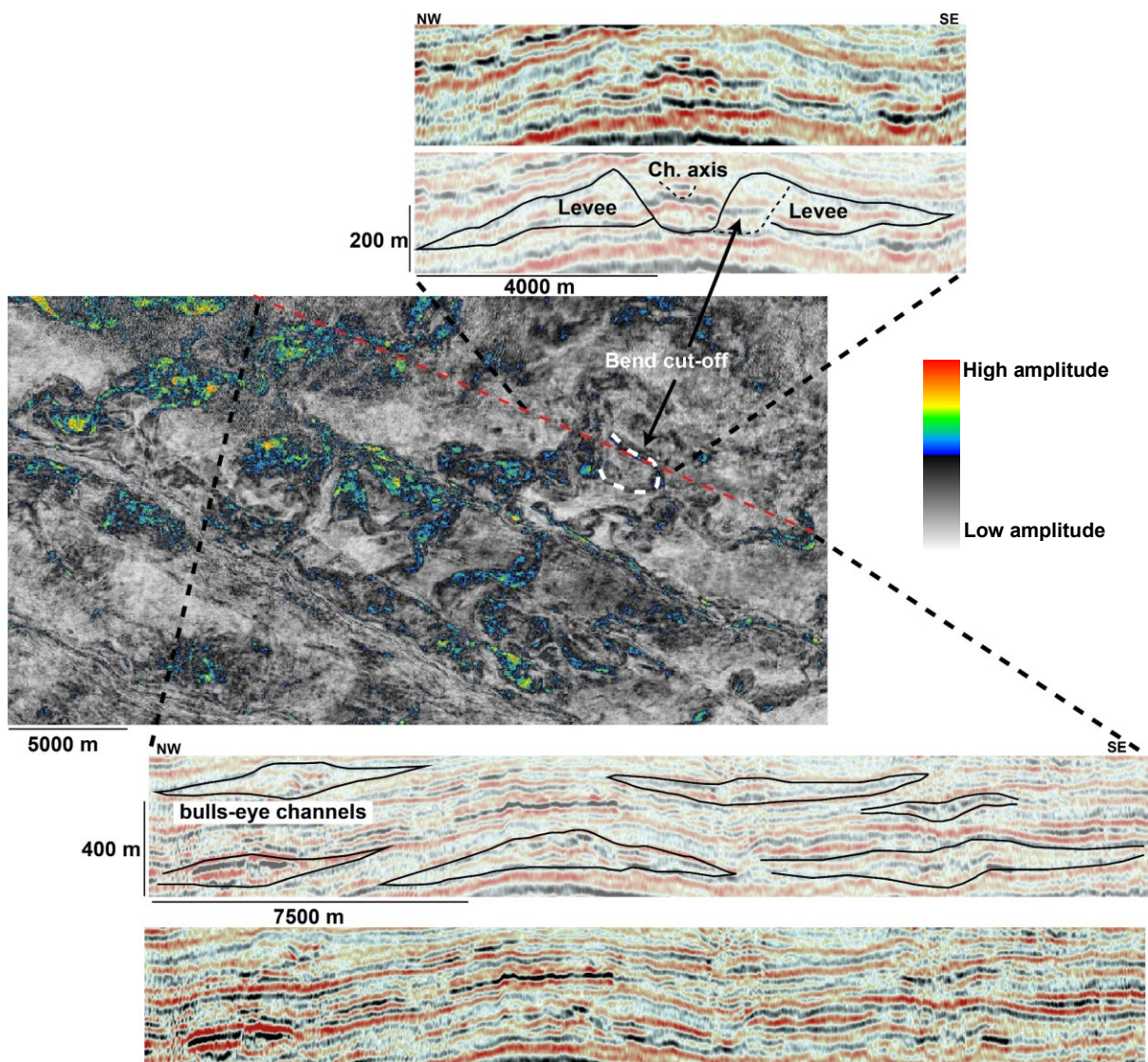
Figure 4-1: (Top) Typical leveed-channel consisting of a sandy, high amplitude axis and low-amplitude wing-shaped levees each side of it. The discontinuous high amplitude reflection within the channel axis result from the stacking of smaller scale channel fills. (Centre) RMS amplitude map showing high amplitude and sinuous character of leveed-channels. (Bottom) Seismic section of the interval between 12.8 and 9.5 Ma showing multiple channel-levees compensationally stacked and some bull-eye channels due to differential compaction between sandy fill and muddy levees.

Levees can be observed in the seismic data as wing-shaped bodies that thin away from the channel axis with low to moderate seismic amplitudes. Each levee body can reach 4 km in length such that the entire leveed channel can be up to 10 km in width. The height of the levee crests is approximately the same as the depth of the channel axis, meaning that most of the flows were levee-confined and the channel complex aggraded with time. The contact between leveed channels and underlying stratigraphy generally is not erosional, however angular unconformities can sometimes be seen as levee deposits downlap onto earlier sediments. Occasionally the channel axis thalweg shows some degree of erosion as it truncates underlying stratigraphy to a lower level with respect to the base of the adjacent levees (Figure 4-2). Their net aggradational architecture can be expressed by a ratio of erosion to construction (E/C ratio) ranging between 0.4 and 0.6 (see chapter 2) and can also appear as bulls-eye shaped when sandy axis fills promote prominent convex-up compaction (Mayall et al., 2006; Figure 4-1). In areas where multiple leveed channels are present, they are often seen to stack in a compensational manner such that subsequent bodies fill the topographic lows and smooth the topography created in response to the external mounded geometry of earlier deposits (Straub et al 2009; Figure 4-1). This generally results in the building up of very thick sequences (700 m or more) of widely-distributed leveed channels. In RMS maps they appear as high amplitude belts with sinuosity of 1.2 to 1.4 and often show sharp bends or diversions as well as meander bend cut-offs (Figure 4-1). Their sinuosity does not appear to be associated with either lateral accretion or stacking, thus suggesting they did not originate as linear features that evolved into sinuous forms with time. Therefore, it is likely they were originally sinuous, developing in response to pre-existing topography on the seabed, which may be responsible for the observed sharp bends which are noticeable in the RMS images (Figure 4-1).
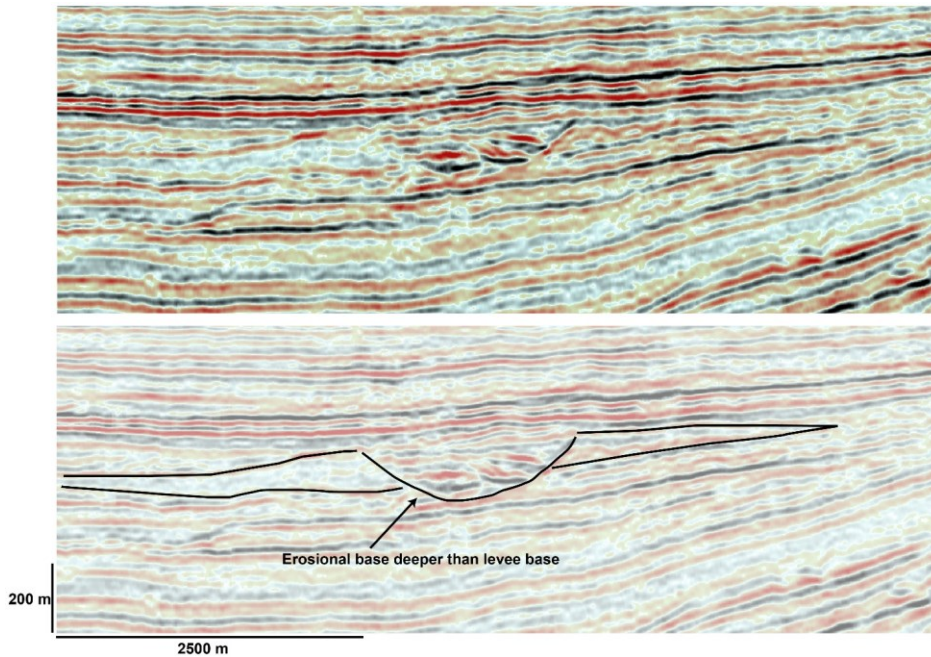
Figure 4-2: Uniterpreted (top) and interpreted (bottom) leveed-channel with mixed aggradational-erosional character as thalweg erosional surface incide deeper than the base of adjacent levees.

A sub-category of leveed channels is here differentiated, mainly based on their highly aggradation architecture with an E/C ratio of 0.3-0.4. These form some of the largest depositional elements in the study area (Figure 4-3). Only a few examples of this type exist in the data set, however when they occur, they can reach thickness of > 350 m, with an extent of several km in width. They are generally found to the side of growing folds and composed of low to moderate amplitude levees and chaotic high-amplitude axis fills. They consist of repeated cut and fill cycles where 5 or more successive leveed channel complexes partially erode previous deposits in a net aggradational and laterally off-stacking sense. As they aggrade, they also migrate away from the growing folds such that subsequent channels do not completely erode previous deposits (Figure 4-3). The result of this process is that the channel axis fills of the various growth stages become connected and amalgamated. In the same way as for the leveed facies type, the axis fill of each channel complex would likely be composed of smaller scale fills 500 m wide and 100 m deep.

The levees of these complexes are asymmetric, with those closer to the fold smaller than those further away from the fold. In RMS maps, they show clear evidence of diversion/deflection and tectonic interaction as they follow the contours of the controlling folds (Figure 4-3).
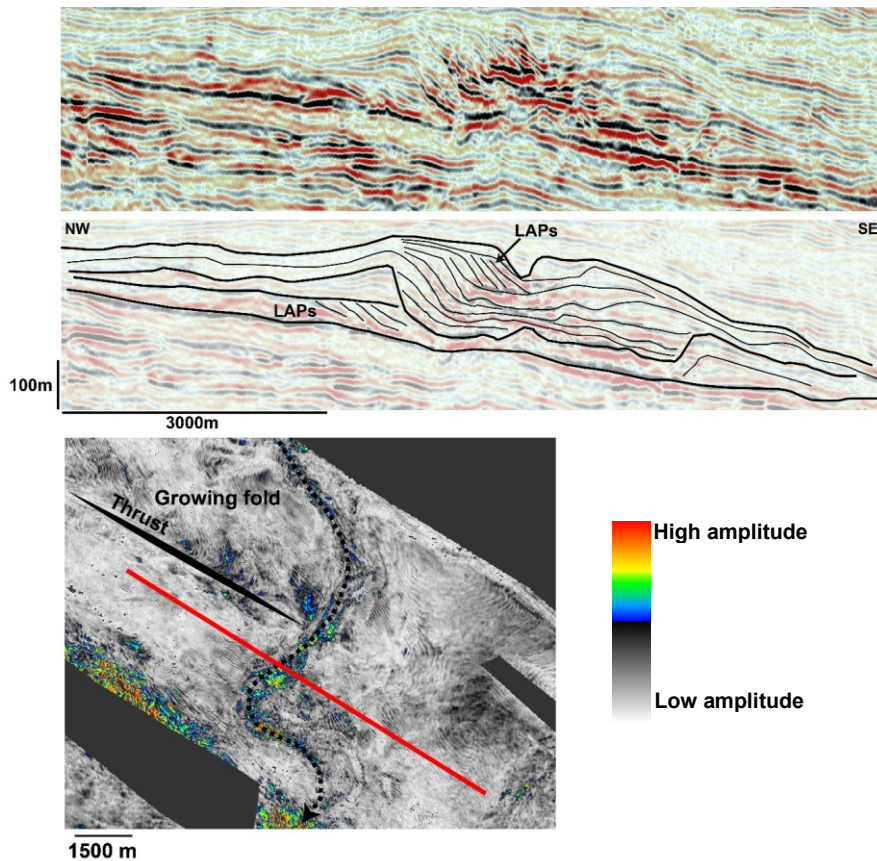
Figure 4-3: Uniterpreted and interpreted highly aggradational leveed-channel. It consists of a series of verically stacked channel complexes in a net aggradational and laterally off-stacking sense, each marked by an internal erosional surface (thin black lines). The chaotic high amplitude reflections represent the sandy axis of each successive cut and fill stage, partially eroded by subsequent channels. In this example the aggradational complex is juxtaposed on an earlier meandering channel belt with evident lateral accretion packages. In RMS amplitude it is visible that this complex is diverted around growing topography.

4.2.2 Erosional channels

These channels predominantly occur above the 7.4 Ma horizon and dominate the stratigraphic intervals until 5.5 Ma in the inner domain, and 3.7 Ma in the outboard domain. In effect, these channels are fully contained within the clear growth packages that develop after the 7.4 Ma horizon (see chapter 3). They constitute the most variable systems in the region in terms of facies or facies associations contained within them and have received much attention in the past as they could represent stand-alone developments in deep-water (Mayall and O'Byrne, 2002; Abreu et al., 2003). Within the study area they have average depth or thickness of 200 m, they are between 3 and 5 km wide and are the most sinuous systems, resulting from lateral accretion or stacking as they respond to growing topography (1.4-1.7 or more; Figure 4-4). The most prominent feature of these systems is the deep erosional surface that confine their fill such that they are sometimes referred to as valley-fill complexes (Janocko et al., 2013). The E/C ratio for these channels ranges between 1.5 and 2.5. Additionally, their fill generally shows multiple cycles of repeated downcutting and deposition leading to the formation of terraces and resulting in a very complex internal architecture. The seismic facies observed within them

range from low to moderate to high amplitude reflectors which could either be tabular and continuous or chaotic. Generally, the base of the larger erosional container as well as the base of any internal erosional phase is marked by very high amplitude reflectors moderately continuous, while the middle part of the fill shows low or moderate amplitudes from continuous to very chaotic. The top part of the fill is commonly marked by a high amplitude flat reflector that caps the entire channel width. Other examples instead show their fill to consist almost exclusively of high amplitude sub-parallel reflectors.
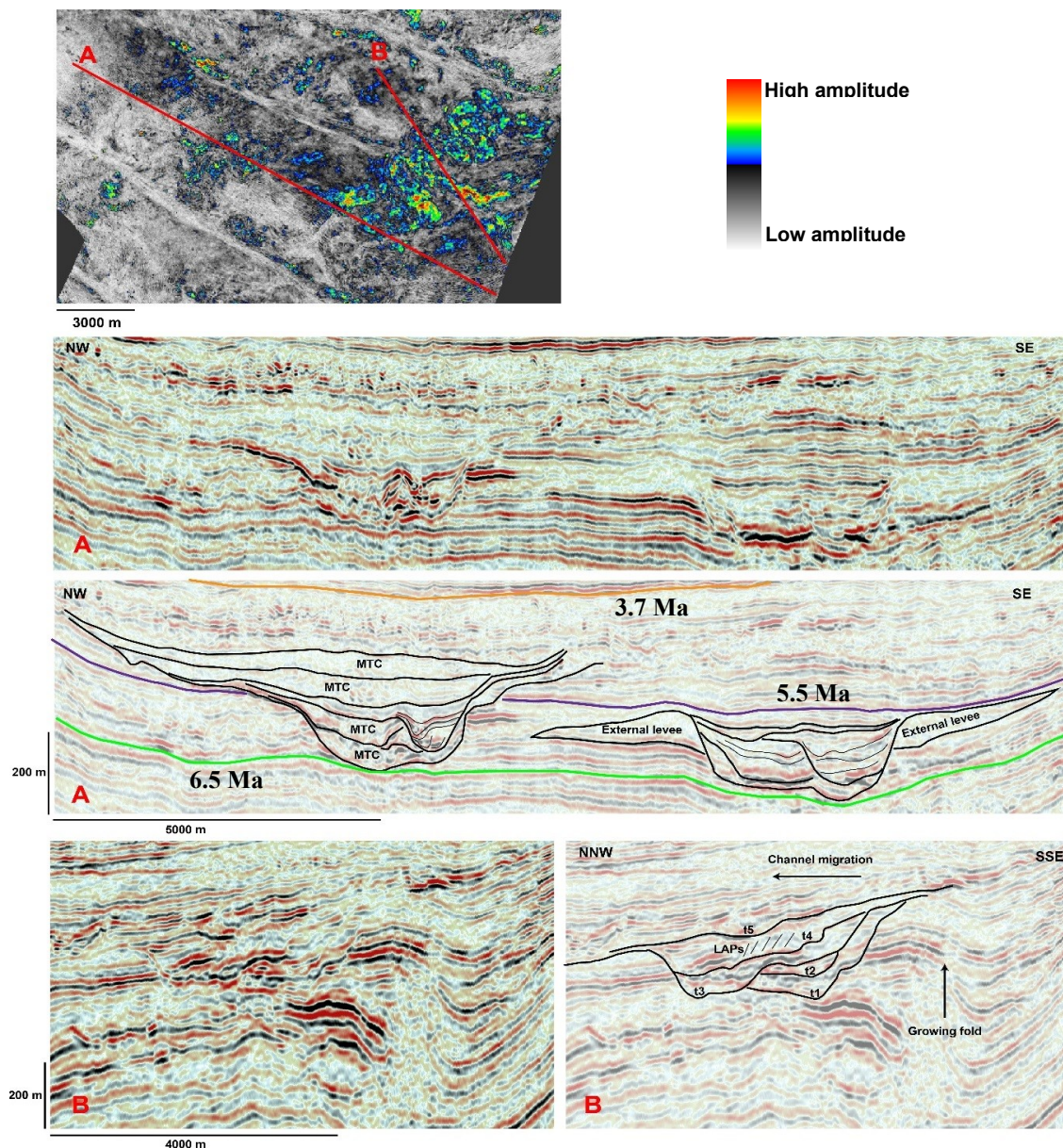
Figure 4-4: Uniterpreted and interpreted erosional channels from area 3 (see Figure 4-15). Here they occur after the 6.5 Ma horizon (green line), while purple and orange lines represent the 5.5 and 3.7 Ma horizon, respectively. A) The channel to the right is older and shows external levees. Internally it consists of multiple cut and fill cycles with discontinuous, moderate to high amplitude reflectors of individual channel-fills. The channel to the left is younger and completely erosionally-confined. It is mostly filled with caothic reflectors likely representing mass-transport deposits. B) Erosional channel complex showing lateral stacking and migration in response to growing topography.

4.2.3 Low-relief channel-levees

This type of facies only occurs at specific horizons, particularly occurring between the 9.5 and 7.4 Ma horizons, which represent the times of the two main deformation phases. They are occasionally found above this until 5.5 Ma is reached. Despite the presence of levees, they are fundamentally different form the leveed channels based on three main characteristic differences: Firstly, these channels show high-amplitude levees and low-amplitude fills (opposite to leveed channels); second, they are linear to slightly sinuous (1.1-1.2); third, they have much smaller dimensions than the leveed facies association which are typically 2 km wide and 200 m deep. (Figure 4-5 and Figure 4-6).

Here the low-relief channel facies have channel axes that are generally not wider than 1 km and not deeper than 100 m. Similarly, the levees dimensions do not exceed 1.5 km in length; consequently, including both axis and levees the total width is up to 3-4 km.

These channels can either show a flat base with wing-shaped levees or a combination of both erosion and aggradation or complete lack of levees, effectively leaving a U or V shaped scour. For these reasons the E/C ratio is around 1 +/- 0.2.

Additionally, those channels showing some degree of erosion tend be associated with, and truncate, underlying sheet-like high amplitude reflectors (Figure 4-5 and Figure 4-6). These channels are often seen to modify their aspect ratio and shape from leveed/aggradational to erosional downstream along their route over relatively short distances (3-4 km; Figure 4-7). Additionally, while in RMS amplitude maps they generally have smooth, low sinuosity paths, they can suddenly show sharp (sinuous) bends and associated width variation (Figure 4-7). These changes are likely to be driven by the effect of underlying topography (Pirmez et al., 2000; Ferry et al., 2005 and others). In fact, topography is also considered the main control on their sinuosity as there is no evidence for lateral accretion/stacking, therefore, suggesting an original sinuous form.
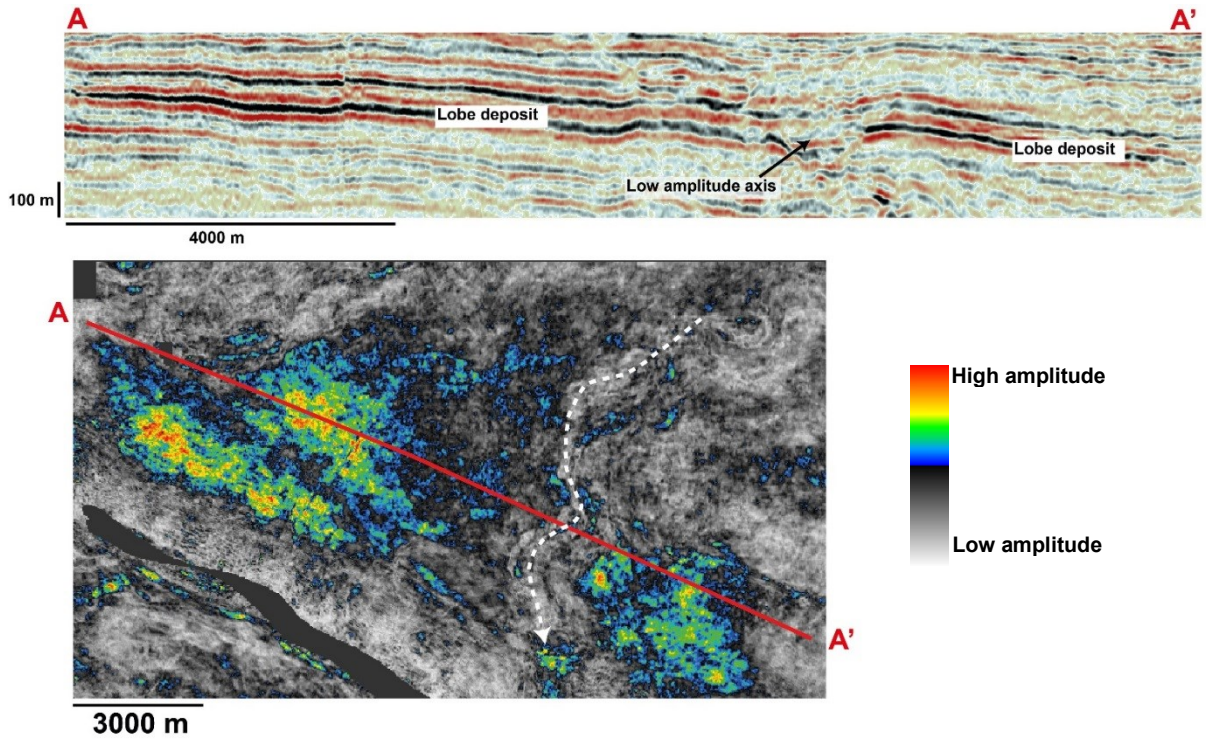
Figure 4-5: Low-relief channels showing low-amplitude channel axis (white dotted line on bottom figure) cutting high-amplitude, sandy lobe deposits.
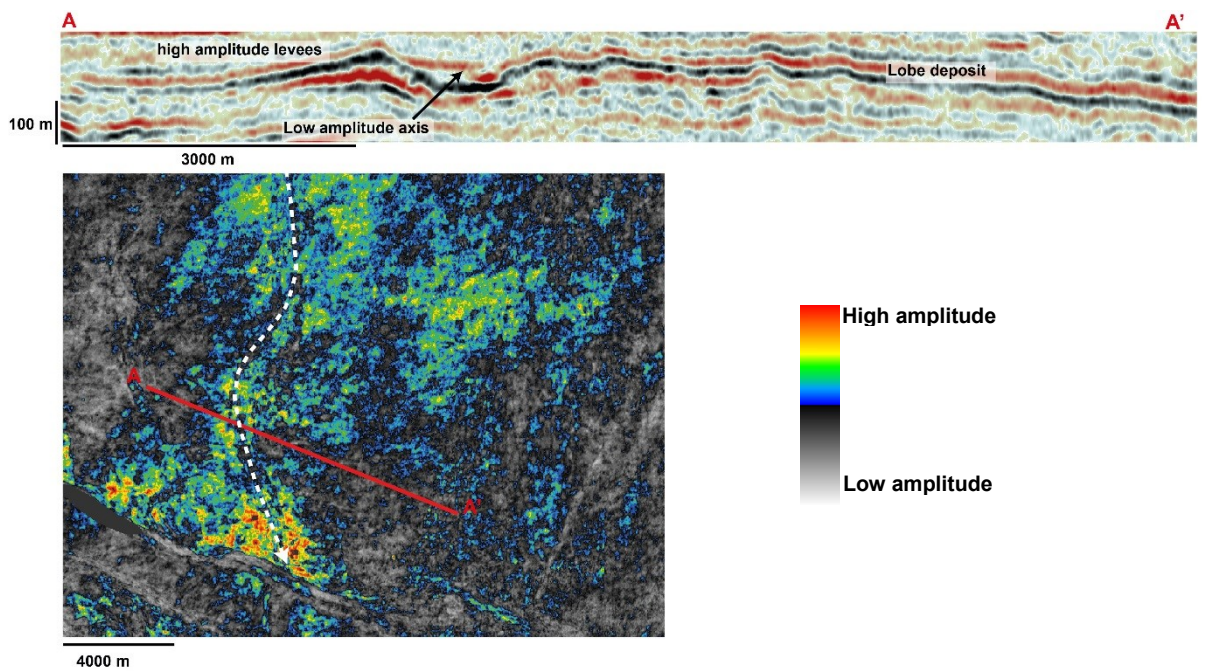
Figure 4-6: Low-relief channel-levess showing low-amplitude channel axis (white dotted line on bottom figure) cutting high-amplitude, sandy lobe deposits.
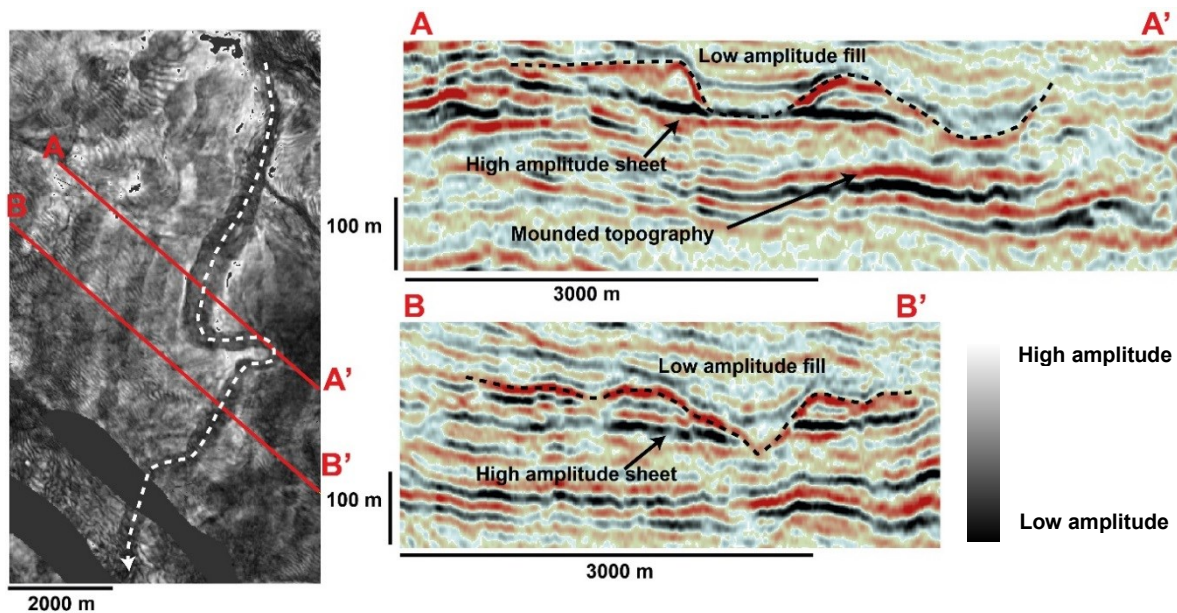
Figure 4-7: Low-relief channel levee showing (A) well-defined levees and flat base and (B) v-shaped erosional character. Note that the channel axis is low-amplitude and mud-filled, while levees have high amplitude. Also note the sharp bend the channel takes mid-way through its course caused by the mounded topography of an underlying crevasse splay (A).

4.2.4 Linear channels

Linear channels represent the smallest channel elements in the study area and are exclusively present in the deepest stratigraphic sections between 15 and 12.8 Ma and partly in the 12.8 to 9.5 Ma interval. On seismic profiles they appear as high amplitude reflections approximately 1 km wide and 50 m thick (Figure 4-8). Given the depth at which they are found, where the vertical seismic resolution is approximately 30 m, they are effectively expressed as one seismic loop, and therefore close to tuning thickness. As a result, the expected U or V shaped geometry of channelized bodies is not often seen, but rather they appear as slightly elongated features with lateral edges defined by abrupt changes in amplitude. Although they can locally show some degree of sinuosity, on a regional scale they are nearly straight and linear systems that cut across the entire region, evenly spaced from each other. These channels do not show a great degree of deflection or diversion, and only occasionally have sharp bends, however on a regional scale they appear to gently converge in a south-west, basinward direction (see following chapter 5). The low seismic resolution at this depth does not allow an assessment of their internal architecture (lateral/vertical stacking or migration), however, similarly to the leveed channels and the small-relief channel levees they are likely originally sinuous forms. Therefore, pre-existing topography is considered the main control on their sinuosity/course.
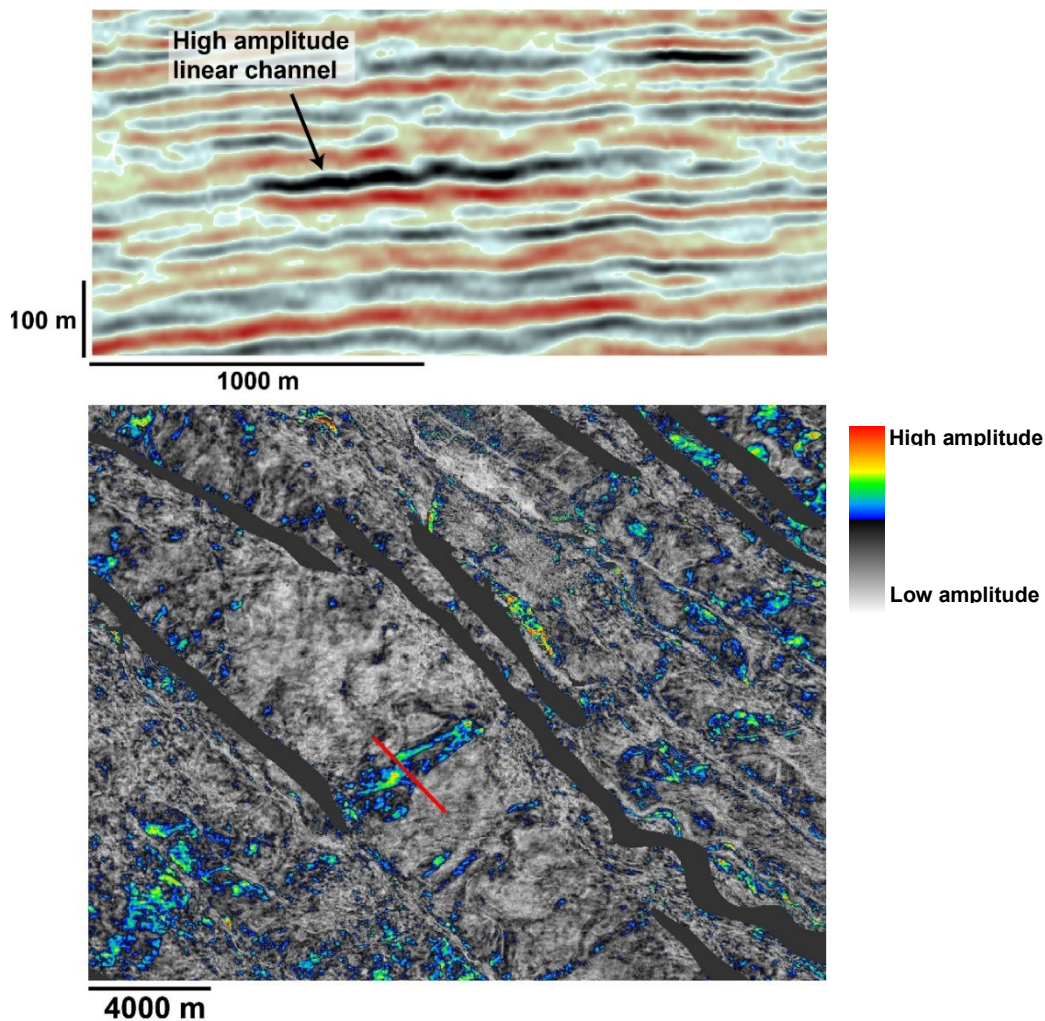
Figure 4-8: (Top) Seismic section showing high amplitude response from a typical linear channel. (Bottom) RMS amplitude extraction linear character of these channels.

4.2.5 Channelized sheets (or weakly-confined systems)

This facies type starts to occur below the 5.5 Ma horizon, particularly in the inboard domain, and dominates the sedimentation style until the 3.7 Ma horizon. It is contained within the upper parts of the growth packages, where strata become progressively shallower in dip, becoming sub-horizontal. This marks the time during which sedimentation rates started to exceed deformation rates and partially healed the topographic expression of the growing folds. A striking difference from the facies previously described is that the channelized sheets are not discrete features such as the erosionally or leveed confined channels that only exist at specific locations. Rather, they are regionally distributed and widespread systems at this time covering most of the seabed area. In seismic cross-sections this facies appears as a series of 1) compensationally stacked high amplitude, sub-horizontal and semi-continuous reflectors (sheets), dissected by 2) numerous small erosional u-shaped channels (Figure 4-9). In their

thickest parts, the stacking of these systems can generate sequences 250 m thick, however, although these packages largely overlap the growing folds, closer to the fold limbs or above the fold crests they become substantially thinner and show an externally convergent geometry. This is reflected by internal pinch outs of some of the high amplitude reflectors, causing the overall thickness to decrease by 50-60 m.

Both channels and sheets are up to 50 m deep, however, channels are 200 m wide, while sheets can be up to 3 km wide. RMS amplitude maps through these facies confirm they consist of broad areas of high amplitude, elongated to sub-circular in shape, densely cut by a network of small sinuous, mutually-eroding channel elements. The channels generally show low amplitudes, but while they are widely spaced in the centre of the basin away from the folds, they progressively converge as they approach the folds eventually exploiting one single location (entry/exit point) to cross them. Channel sinuosity is likely induced by topography (Figure 4-9) as there are no visible lateral accretion packages or lateral stacking of multiple channels.

Due to the limitations on data resolution, the sheets appear as single-cycle seismic events that lack sub-seismic variability or architecture.
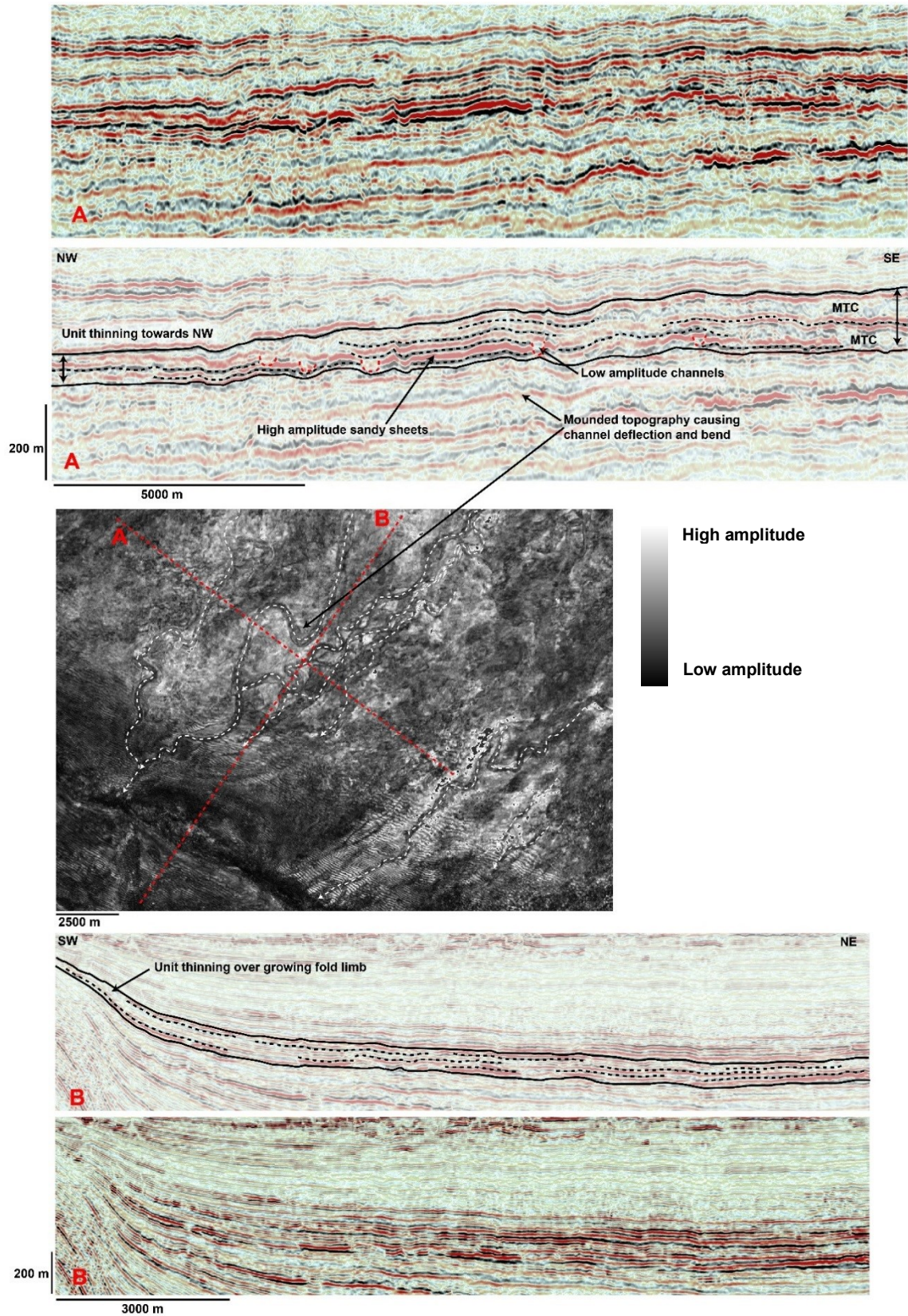
Figure 4-9: Channelized sheets showing discontinuous and patchy high-amplitude reflectors, broken by low-amplitude, muddy channels. In RMS amplitude maps they appear as high-amplitude sheets incised by a network of small sinuous, mutually-eroding channel elements that converge because of topographic confinement in the distal part of the basin towards a single entry/exit point.

4.3 Lobate forms

With this category I include a range of deposits (depositional lobes) resulting from unconfined flows when turbidity currents exit channel confinement and lose competence or capacity to carry some or all of their load, which can occur in different sub-settings or environments (frontal or crevasse splays, transient vs terminal fans, and ponded lobes and sheets). Within the study area lobes are a recurrent depositional element, and therefore not characteristic of a specific time interval. However, an evolution between different types of lobes can be seen to occur and correlate with given stratigraphic intervals. In seismic sections all lobes have the common characteristic of appearing as laterally extensive and generally continuous high amplitude reflectors, with either tabular or wavy geometry.

4.3.1   Unconfined lobe complexes

Unconfined lobe complexes are found before the start of deformation at 15 Ma and during the first interval until 12.8 Ma when deformation rates were very low (see chapter 3). These complexes form sequences a few hundred meters thick of compensationally stacked individual lobes where subtle thinning and amplitude decrease is observed towards the lateral terminations of the individual reflectors (Figure 4-10). Often the high amplitude lobes are vertically separated by thinner and internally chaotic/transparent low amplitude reflectors. This potentially is the result of lobe deposition switching, in association with feeder channel avulsion and/or topographic build-up of a lobe mound, forcing subsequent lobes to be deposited within relative topographic lows at each successive time interval (Doughty-Jones et al., 2017; Burgess et al., 2019). In seismic amplitude maps lobe complexes show to be internally organized in a hierarchy of progressively smaller features distributed in a compensational manner, with generally higher amplitudes in the centre of a lobe that dim towards the lateral fringes or distal parts. In map-view the unconfined lobe complexes have a radial or divergent shape away from the main feeder channel, which contrast with channelized sheets that diverge in the proximal part of the basin to then converge because of topographic confinement in the distal part of the basin. In fact, these systems are generally thought to occur on very low gradient slopes and basin floors, where topographic confinement is thought to be minimum (Gervais et al., 2006, Deptuck et al., 2008, Deptuck and Sylvester, 2017).

While the overall lobe complexes may have diameters in the order of 10-15 km, they consist of discrete patches of high amplitude (lobes), either separated from each other or partially overlapping, with diameters of 2.5 to 3 km. These, in turn, consist of even smaller lobate

features (lobe elements) hundreds of meters wide. Due to recent technological advances in seismic imaging, achieving meter-scale resolution, it has been possible to recognize that these systems, in fact, consist of a distributary network of erosional channels responsible for the distribution of the sediment load within the lobe complex environment (Doughty-Jones et al, 2017). These channels, however, are usually not deeper than 10 m and therefore not clearly resolvable due to seismic resolution limitations, especially at the depth at which they are found in this study.
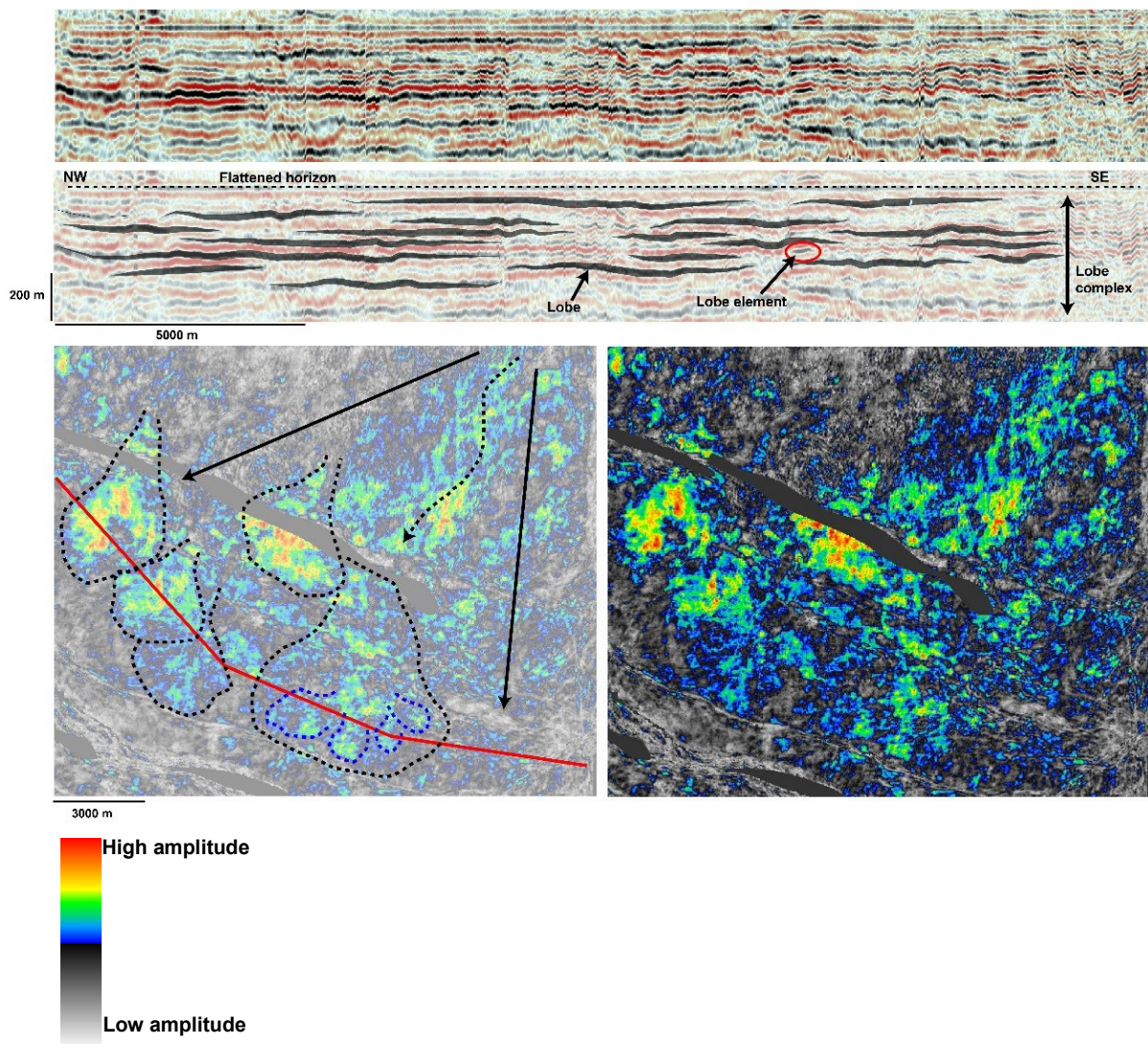
Figure 4-10: Unconfined lobe complexes consisitng of aggradational and compensationally stacked lobes separated by low-amplitide mudstone interbeds. In RMS maps the lobe complex is seen to diverge away from the feeder channel and consist of multiple lobes, each appearing as a high amplitude sub-circular patch. Smaller lobe elements can be also observed (blue dotted lines).

4.3.2 Ponded lobes

After the deposition of the largely unconfined lobe complexes, other types of lobes are observed to occur at various stratigraphic intervals and in different parts of the evolving sub-basins as increased strain rates and deformation progressively segment the lower slope. In particular they occur immediately above the 7.4 Ma horizon which marks the start of a period of very high strain rates lasting until 3.7 Ma. However, they are also locally present between 12.8 and 9.5 Ma. In seismic section, these lobes appear as laterally extensive reflectors 80-90 metres thick (one seismic loop), at times vertically stacked, but are substantially different from the unconfined facies as they do not show signs of compensational stacking, and visibly onlap the back limb of growing folds (Figure 4-11). The lack of compensation and their "single-event" character, where high amplitudes can be laterally followed for kms, is expressed in RMS maps as isolated patches of high amplitude a few kms wide, sub-circular to elongate in shape. Their shape follows that of the surrounding, confining basin and the amplitudes are generally high in the centre and dim towards the lobe margins.   However, these lobes are not clearly organized in a hierarchical manner, but rather are almost structure less with few resolvable internal elements. Occasionally, feeder channels can be imaged as small and sinuous features of discontinuous high amplitudes. Commonly, these lobes are found at the base of sequences that culminate with the occurrence of erosional channels that sometimes erode the lobe itself. The lack of compensation and internal architecture along with their variable plan-view shape and the pinching-out against growing folds suggest that the architecture of these lobes is strongly influenced by the local slope topography and configuration of the receiving basins. In fact, high-resolution seismic imagery has shown that deep-water lobe morphology is largely dependent on basin floor bathymetry (Gervais et al., 2006; Hay, 2012; Doughty-Jones et al., 2017). For these reasons, these facies type are classified as ponded lobes where sediments are deposited from unconfined gravity flows (not confined within erosional valleys or levees) but confined by topography. Ponded lobes have been extensively investigated in both completely enclosed basins as the salt-withdrawal mini-basins in the Gulf of Mexico (Booth et al., 2003; Prather et al., 1998, 2012b; Prather, 2003) and the stepped slopes in West Africa (Adeogba et al., 2005; Hay 2012, Prather et al., 2012a; Jobe et al., 2017; Doughty-Jones et al., 2017), where ponding occurs temporarily, later followed by systems bypass as both depositional and erosional processes progressively smooth the tectonically-driven topography. Lobes deposited in the original flat areas of a stepped slope are commonly referred to as transient fans (Adeogba et al., 2005, Hay, 2012).

The occurrence of ponded lobes followed by erosional channels indicates that, subsequent to each deformation phases, ponded accommodation space was first created and then healed by the deposition of the lobes themselves. At present, the slope morphology in the Niger Delta is classified as a stepped above-grade slope, where ponded accommodation space (Prather et al., 1998; Prather, 2003) is present in the lower slope and is associated with the strike-oriented topography created by the actively deforming toe-thrusts ridges, while healed slope accommodation is uniformly thin on the upper and middle slope (Steffens et al., 2003); this pattern of ponding-healing has likely been a common motif of deposition throughout the growth history of the outer fold belt.
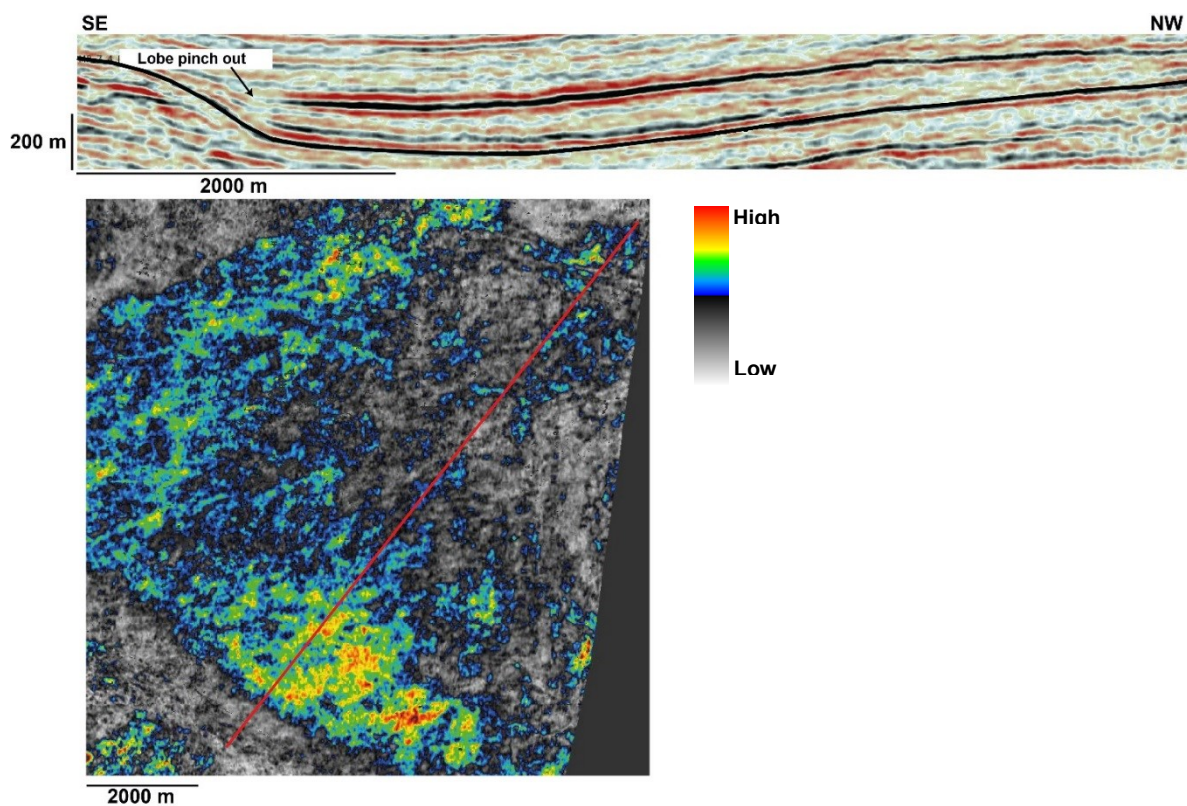
Figure 4-11: Ponded lobes appear as high amplitude single-seismic-loop reflections which abruptly terminate against topographic barriers as growing folds. In RMS maps they show similar character as the individual lobes of a lobe complex.

4.3.3 Crevasse splays

More ephemeral types of lobe are found where channel levees are breached, commonly along outer channel bends, where flow momentum results in an increased tendency for flows to overtop or breach the adjacent levee (Posamentier and Kolla, 2003). In this circumstance distributary-channel complexes can form, of considerably smaller dimensions than basin-floor complexes or transient fans, in the overbank areas of channel-levee complexes. For these

reasons, in the present study, they are almost exclusively found in the interval between 12.8 and 9.5 Ma, when leveed-channels were the dominant depositional elements in the area.

4.4 Mass-Transport Deposits (MTDs)

MTDs is a collective term to represent a range of deposits derived from large submarine landslides including slumps, slides and debris flows and, as such, their composition is generally muddy. In seismic amplitude maps they typically appear speckled or mottled and, because of their erosional character, they typically leave striations and grooves on the seabed (Figure 4-12). MTDs in the study area are internally characterized by low to moderate seismic amplitudes, generally chaotic to transparent in character, but they are generally well defined "stand-alone" units because of the strong acoustic impedance contrast occurring at both the top and base surfaces (Figure 4-12). The basal surface is typically erosional, while the upper surface is generally smoother and mounded. This facies mainly occurs at two distinct stratigraphic levels. Its first occurrence is immediately above the 9.5 Ma horizon and then it becomes one of the dominant facies between 5.5 and 3.7 Ma. The main difference between the two intervals is the size of the deposits. The lower units are smaller and localised, and they appear to be encased in the stratigraphy, generally sitting beneath channel-levee systems. The upper units are regionally widespread (many km in length and width) and are often vertically stacked to form sequences hundreds of meters thick. The upper MTDs are typically interbedded with the mixed slope channels and channelized lobes of the weakly confined systems. In outcrop they often appear as mud-dominated chaotic and contorted facies with meter-scale dispersed clasts of varying origin, where the original stratigraphy can be completely disrupted by folding, faulting and shearing. Outcrop studies on the evolution of deep-water systems report that MTDs occur during the late stages of filling of the deep-water accommodation space as they tend to equilibrate the regional slope profile, especially during time of significant sedimentation rate and slope progradation, or in response to faulting (Romans et al., 2011; Burgreen and Graham, 2014; Others).
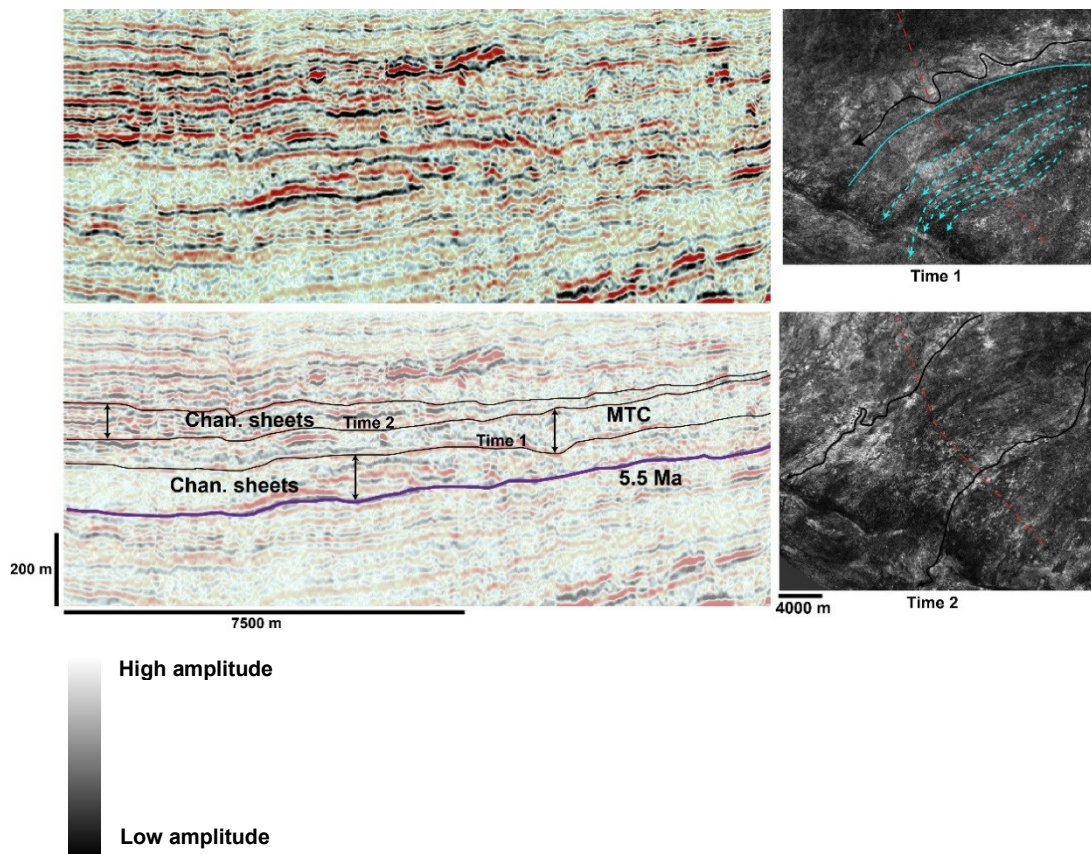
Figure 4-12: Uninterpreted and interpreted seismic sections showing a typical mass-transport deposit with a sharp erosional base and internal chaotic and low amplitude character. Note that channelized sheets and MTD are compensationally stacked. In RMS maps MTDs can be recognised by their mottled character and a set of erosional grooves and striations (light blue dotted lines). Also note that that at Time 2 subsequent channelized sheets are offset by the topography created by the underlying MTD (visible a Time 1).

4.5 Background slope deposits

The background slope deposits consist of low to moderate amplitude packages, almost internally transparent that generally drape and smooth older topography (Figure 4-13). They have variable lateral continuity, but some packages can be correlated for tens of kilometres. These deposits represent the periods of coarse sediment starvation and therefore mainly comprise mud and shale. They are deposited via both muddy-turbidity currents and suspension fall-out from delta-fed plumes. Slope deposits may incorporate condensed sections deposited during period of rising sea level (HST), when deep-water areas become disconnected from shelf sediment staging areas, as shallow water depositional systems retrogress towards land and sediment delivery to the slope is strongly reduced. In the Niger Delta, eleven of these transgressive-regressive cycles are recognised regionally (Reijers et al., 1997; Reijers, 2011), but the lack of well control hinders our ability to readily identify these condensed packages.
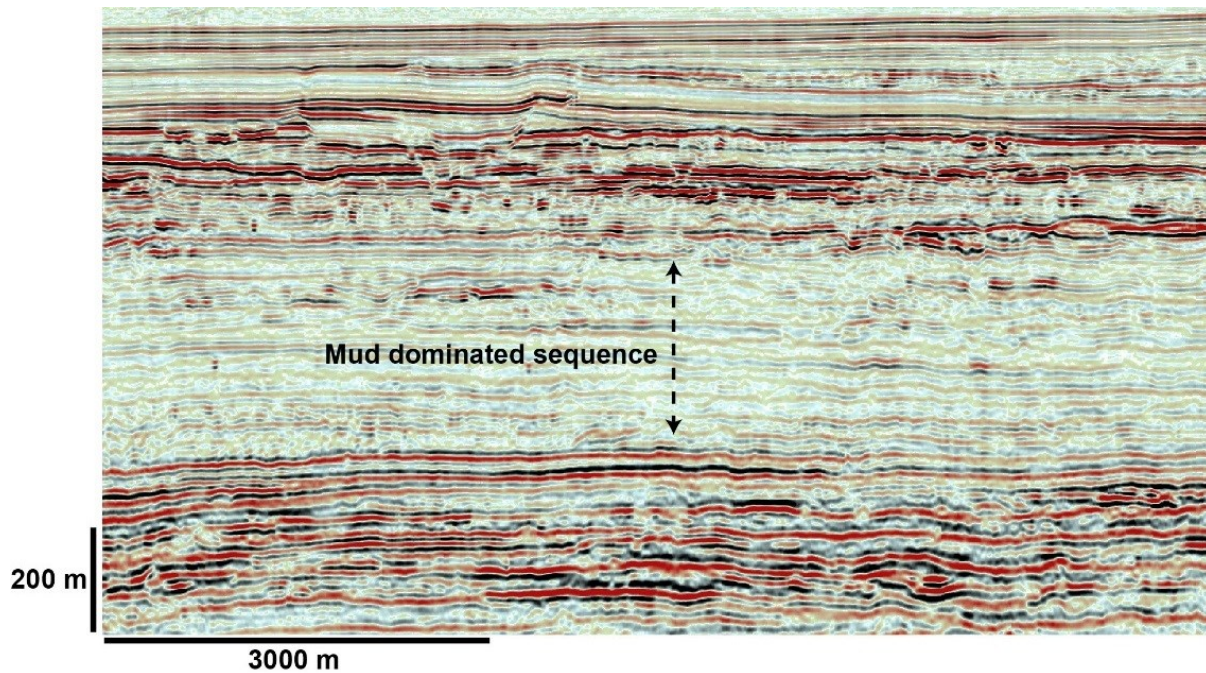
Figure 4-13: background slope deposits consisting of low to moderate amplitude packages with variable lateral continuity.

4.6 Implications for reservoir potential

4.6.1 Leveed channel complexes

From a reservoir perspective the high-amplitude reflection character of their fill is interpreted to record the presence of sand filling the channels (Posamentier and Kolla, 2003) and may contain thin-bedded, coarse-grained basal lag deposits due to the bypass of flows (Sprague et al., 2005). The highly aggradational leveed channels may form better reservoirs because of their vertical stacking which results in the amalgamation of subsequent channel fills, therefore, increasing both the potential capacity and the connectivity.

However, the overbank/levee areas associated with these systems are interpreted to consist of thin bedded, fine grained sediments interbedded with sand and silt. In the overbank area, therefore, reservoirs are considered to have a lower net to gross and lower quality (Sprague et al., 2005).

4.6.2 Erosional channels

Well logs through these systems has allowed some authors to develop models or schema to predict the general vertical evolution of the channel fill (Abreu et al., 2003; Mayall and O'Byrne, 2002; Mayall et al., 2006). Mayall et al., (2006) suggested that 4 main facies types can be recognised in these erosionally confined systems; these from the bottom upwards consist

of basal lags sitting above the erosional surface and comprising mud-clast conglomerates, slump/debris flow complexes, stacked channel sands formed by both low- and high-density turbidity currents and finally sinuous and narrow channel-levee deposits that cap the overall channel system fill which can show a set of inclined sand bodies which have been referred to as lateral accretion packages (Abreu et al., 2003). However, as observed in this study, this four-fold sequence is not always fully developed. Other facies generally associated with these systems are external levees that only confine the upper part of the fill, while most of it is erosionally confined. External levees show their typical wing-shaped morphology that thins away from the channel. They have very low amplitude to transparent character, however, their base is marked by a sharp high amplitude reflector which can be used to estimate that extent of the overlying levee.

4.6.3 Low-relief channel-levees

These type of channels have received much attention in the past in terms of viability as exploration targets. Mayall and O'Byrne (2002) reveal that well logs through the levees of these systems show massive blocky sands as well as injected sands, slumps and mud-clast conglomerates, particularly towards the channel margins. Other observed facies associations are represented by cleaner sands at the base of the levees becoming more interbedded with muds upwards (Mayall and O'Byrne, 2002). Fonnesu (2003) also reported that the levee deposits of similar channels of the West Africa continental slope constitute a very thin-bedded heterolithic reservoir with possible connectivity problems related to syndepositional instability, while the low amplitude (muddy) axis fill represents the major permeability barrier.

Generally accepted models for the development of these channels can be grouped in three scenarios; (1) they could represent prograding channel-lobe systems where a phase of lobe deposition is later followed by a phase of channel incision and bypass (Fonnesu, 2003; O'Byrne et al., 2004; Adeogba et al., 2005; Deptuck et al., 2012; Hay, 2012; Prather et al., 2012); (2) the presence of a mud-filled channel could be genetically unrelated to the underlying lobe or sheets. However, this seems unpersuasive as the low-relief channel levees always occur associated with high amplitude sheets; (3) Alternatively, the high amplitude sheets may result from the merging of successive lateral splays along channels edges, and, as the levees gain elevation, only the muddy parts of flows overtop the channel (Mayall, 2007; personal communication).

4.6.4 Linear channels

The general decrease in width, depth, cross-sectional area, and levee height associated with these systems has been previously considered the result of decreasing discharge towards the distal parts of fan systems (Pirmez and Imran 2003; Spinewine et al. 2011; Skene et al. 2002). As these channels occur in the deeper stratigraphic sections, it is plausible that they record deposition in a distal fan setting, at times where the slope had not prograded yet. Moreover, their general bright appearance could be related to the spill of coarser fraction of the flow over smaller levees in distal setting, as suggested by Hiscott (1997).

4.6.5 Channelized sheets

These deposits may be analogous to the type of sheeted or layered systems that have been described in the Carboniferous Ross Sandstone Formation, Ireland, which consists of stacked turbiditic sandstones and mudstones deposited in a channelized basin-floor fan setting (Sullivan et al. 2004). These authors recognize a transitional zone between the proximal and medial locations of the fan where they report the occurrence of compensationally stacked "weakly confined channels", meaning that the sand bodies have high aspect ratios, being 1000 m wide and 10-15 m deep. These could represent an equivalent of the high amplitude sheets usually encountered in seismic data, and outcrop data show these high aspect ratio channels (or sheets) to be composed of highly amalgamated sandy axis, becoming progressively layered towards the margins (Sullivan et al. 2004).

Nevertheless, weakly confined systems have been recognised in variety of tectonic settings including salt-withdrawal minibasins and fold belts associated with continental margin-scale extensional and compressional systems (Moody et al, 2012) and also record the progressive decrease in topographic confinement associated with broad low-relief mini-basins, tens of kms across (Sprague et al., 2005, Moody et al., 2012 Sullivan et al., 2004). In this case, weak topographic confinement is expressed by channels elements that diverge in the up-dip parts of intraslope minibasins and converge in the downdip parts, as is also observed in the present study. Therefore, the channelized sheets in this study likely represent deposition in broad low-relief minibasins, within which sheets are organized in a compensational manner. Additionally, weak topographic confinement also mean that channels are able to eventually bypass the minibasin and reach the exit point. This is likely indicated by occurrence of numerous mud-filled "bypass" channels.

Weakly confined systems form important hydrocarbon reservoirs, and, in the Niger Delta, a typical example of these systems has been exploited at the Bonga Field (Chapin et al., 2002).

At Bonga well penetrations and core data suggest that broad areas of high amplitude (sheets) correspond to massive sandy turbidite channel axes, which are interrupted by dim (mud-filled) shoestring-like channels liable for the erosion of parts of the sandy component and the decrease in connectivity of the sheets. Additionally, two main reservoir type have been identified in the example from the Bonga Field; loosely amalgamated systems and highly amalgamated systems. The first one consists of relatively discontinuous seismic loops, abrupt thickness changes, sinuous map patterns and a high proportion of thinly laminated intervals of sands and muds found within either margin and/or overbank areas (Chapin et al., 2002). The second type have more consistent seismic loops as well as broader areas of high amplitude and blocky sands with few thin-bedded intervals mostly found within channel axis (Chapin et al., 2002). Effectively, the high amplitude character of the laterally extensive reflections may result from the amalgamation and lateral stacking of numerous sandy channel fills which create pseudo-sheet stacks.

4.6.6 Unconfined lobe complexes

From a reservoir perspective these systems have high to very high net-to-gross and high lateral continuity but poor vertical connectivity due to laterally extensive mudstone interbeds deposited when the locus of lobe deposition switches in response to their autocyclicity (Sprague et al., 2005; Prelat et al., 2009; Burgreen et al., 2014).

4.6.7 Ponded lobes

Ponded lobes often represent an important exploration target for their high sand content, but because of the lack of well data it is not possible to comment on the sand content and internal architecture of ponded lobes in this study. Outcrop studies from the Karoo basin, South Africa, indicate that the type of lithofacies present will vary from the thick-bedded sands of the lobe axis to the thin-bedded siltstone deposits of the distal fringe, passing through medium-bedded sands and hybrids beds (Spychala et al., 2017). However, a recent seismic study of a Pleistocene submarine fan in the western Niger Delta (Jobe et al., 2017) reveal that lobes deposited in intraslope settings do not show significant downslope trends in sand presence or grain size and that they may consist of more sand-rich facies near lobe edges than predicted by traditional models (Jobe et al., 2017). The reason for this is attributed to the ability of flows to bypass large volumes of mud as well as fine-grained sands of the T_b and T_c intervals, leaving very coarse-grained and thick-bedded sands within the intraslope basin (Jobe et al., 2017).

4.7 Vertical evolution of facies association

Deep-water fans show great variability in terms of overall size, bulk composition and architecture, reflecting: the volume and composition of the terrestrial material delivered to the systems; the overall margin physiography and tectonic setting (passive vs active margins); and the frequency and nature of triggering mechanisms for sediment-gravity flows. Despite this variability, original conceptual models of the evolution of deep-water deposits along continental slopes suggest that sediment gravity-flows are commonly confined within erosional canyons on the upper slope, passing downslope to being levee-confined to unconfined distributive systems on the basin floor, primarily controlled by seafloor gradient (Mutti and Ricci Lucchi, 1972; Mutti and Normark, 1987, 1991; Babonneau et al., 2002; Sprague et al., 2005). In fact, many studies show this evolution to be mostly driven by changes in slope gradient, with shallower slopes (on the lower slope and basin floor) favoring flow deceleration and decreased confinement (Pirmez et al., 2000, Ferry et al., 2005, Deptuck et al., 2008). In an idealized scenario, therefore, the natural progradation of a delta-fed slope in a tectonically-quiescent region should be recorded by the deposition of basin-floor fans at the base, consisting of unconfined distributive systems, followed by levee-channeled middle fan deposits, terminating with upper fan slope canyons (Babonneau et al., 2002). However, processes active on the fan itself or within the substrate above which the fan sits greatly impact fan architecture, such that "*for a given basin and for a particular set of extra-basinal and shelf edge controls, sediment gravity flow interaction with changing sea floor gradient exerts the strongest control on depositional style and reservoir architecture*" (Sprague et al., 2005). These concepts, applied to the study of the sequences developed on above-grade slopes, may help to explain the sudden change in depositional architecture resulting from irregular slope topography in tectonically active regions.

In the present study, the vertical evolution and change in depositional architecture that we observe differ from what would be predicted by traditional facies models. Since the start of deposition of the delta in the Eocene, the study area has been in a lower slope environment and, at present, the water depth ranges between 1500-3000m. Despite this, in the time interval between 15 and 3.7 Ma we see a distinct vertical change from unconfined lobe complexes at the base, followed by leveed-confined channels passing upward to ponded lobes and erosionally-confined channels, terminating with widespread channelized sheets (Figure 4-14). Given this complex evolution between contrasting styles of deep-water sediment architecture, we propose that tectonic processes had a profound influence on how the stratigraphic

architecture in the toe-thrusts region of the Niger Delta changed over time. While further detailed evidence and mechanisms by which the change occurs will be shown and discussed in the following chapters, clear support for a strong tectonic control on depositional style is deduced by comparing the timing of occurrence of specific facies types in different sub-basins with the overall propagation of the deformation front at the scale of the entire fold belt (as discussed in chapter 3). To this end, we sub-divided the outer fold and thrust belt into four areas (Figure 4-15), 1 being the most proximal and 4 the most distal, and, for each area, we summarize the presence and the lateral and vertical variability in facies type in an idealized stratigraphic column (1D). Area 1 is the largest sub-basin and represents the most inboard part of the fold belt. It is bounded by the seismic data limit to the north, a tear fault to the east and thrust 21 to the south and it incorporates thrust 22. Areas 2 and 3 represent the core of the fold belt and are bounded by thrust 21 to north and by the structural lineament of thrusts 13, 15 and 17 to the south. Internally, these areas incorporate thrusts 20, 19 and 18. Areas 2 and 3 have been separated due the presence of the central structural culmination of thrusts 19 and 17 (location "x" on Figure 4-15), which interrupts the lateral continuity between the two basins and has impacted the stratigraphic evolution since 15 Ma. Because of the more complete stratigraphic sequence in Area 3, this is considered as the reference stratigraphic record in the core of the fold belt while Area 2 is a lateral variation for which causes will be later discussed. Area 4 is the most distal part of the fold belt and is bounded by the structural lineament of thrusts 13, 15 and 17 to the north and thrust 11 to the south. Internally, it incorporates thrusts 12 and 14. Additionally, while areas 1, 2 and 3 are all part of the larger inner domain of the fold belt, area 4 coincides with the outer domain (see chapter 3; Figure 3-3). In chapter 3 we showed that the inner and outer domains of the fold belt progressively deformed at different times; after the start of deformation at 15 Ma, the inner domain started to deform at high strain rates since 9.5 Ma, while at 7.4 Ma the deformation front propagated basinward and impacted the outer domain. Our analysis suggests that the timing of occurrence or change between facies types in each area (1 to 4) correlates to, and is dictated by the timing of the start, increase and migration of deformation in the fold belt.

Figure 4-14: Dip seismic section through Area 1 (location on Figure 4-15) showing the typical vertical sequence of seismic facies observed in every sub-basin. Note that, while the vertical change is the same for each area, the timing of occurrence of facies types is for area 1 only. See fig. Figure 4-16 for relative timings for other areas.

103
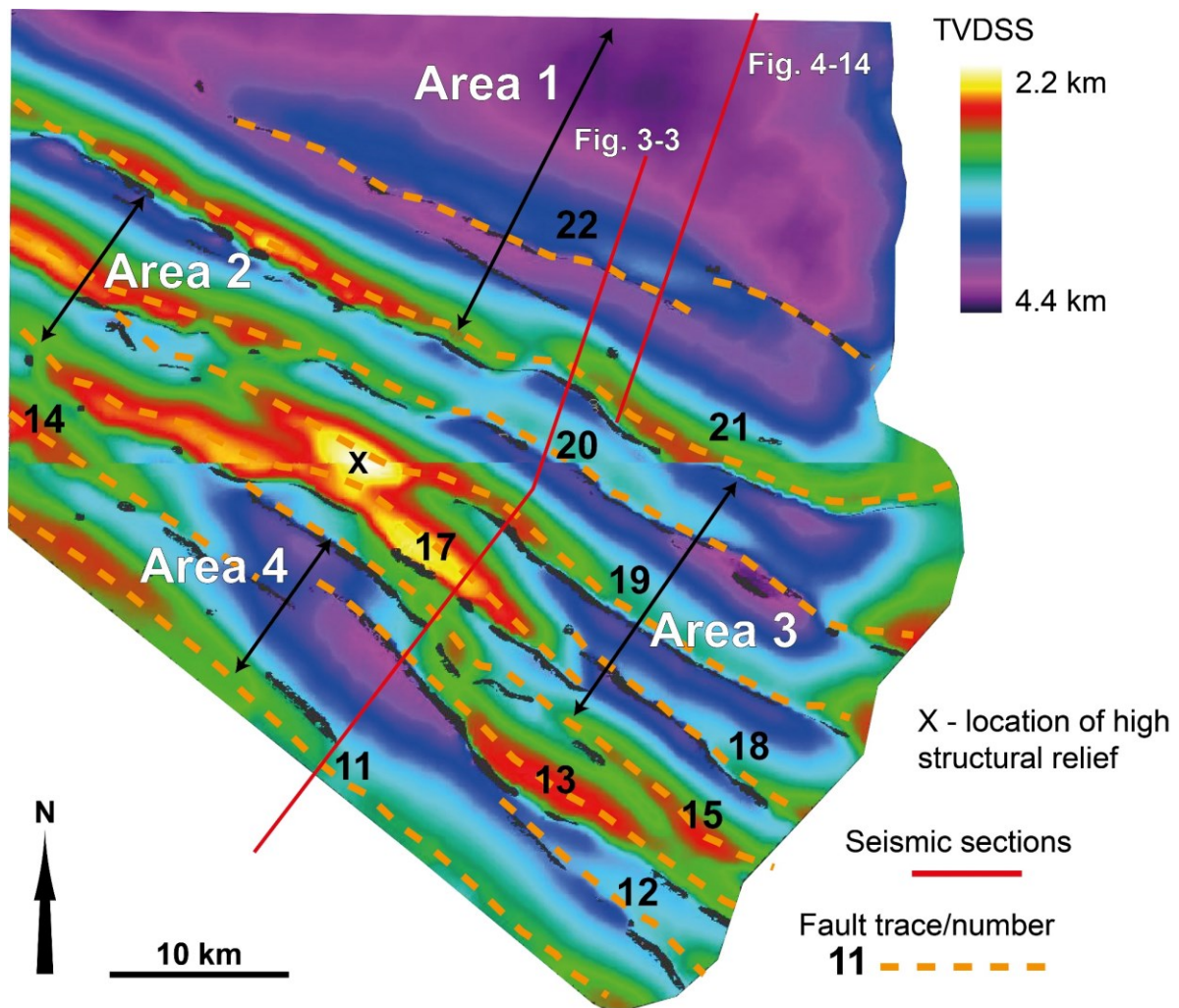
Figure 4-15: Depth-structure map of the 9.5 Ma horizon (yellow horizon in Figure 4-14 and Figure 3-3) defining the extent of the four areas analysed in this study.

Figure 4-16 summarizes this tectono-stratigraphic evidence and shows that prior to the start of deformation (30 to 15 Ma) unconfined lobes complexes were widespread throughout the entire study area. As the deformation regionally started at 15 Ma, unconfined lobes complexes became restricted to area 1, while the more distal areas 3 and 4 developed a network of small linear channels and leveed channels. Leveed-channels persisted until 7.4 Ma in both the inner and outer domains, but after 9.5 Ma also local MTDs and ponded lobes occurred, particularly in the proximal areas 1 and 3. In area 1 ponded lobes became the dominant facies immediately after 7.4 Ma, passing upwards to erosional channels. These erosional channels developed in areas 3 and 4 only after 6.5 Ma (see also Figure 4-4). The same diachronous occurrence can be observed between area 1 (between 6.5 and 5.5 Ma) and areas 3 and 4 (after 5.5 Ma) for the deposition of the weakly confined systems (channelized sheets) along with the emplacement of large MTDs.
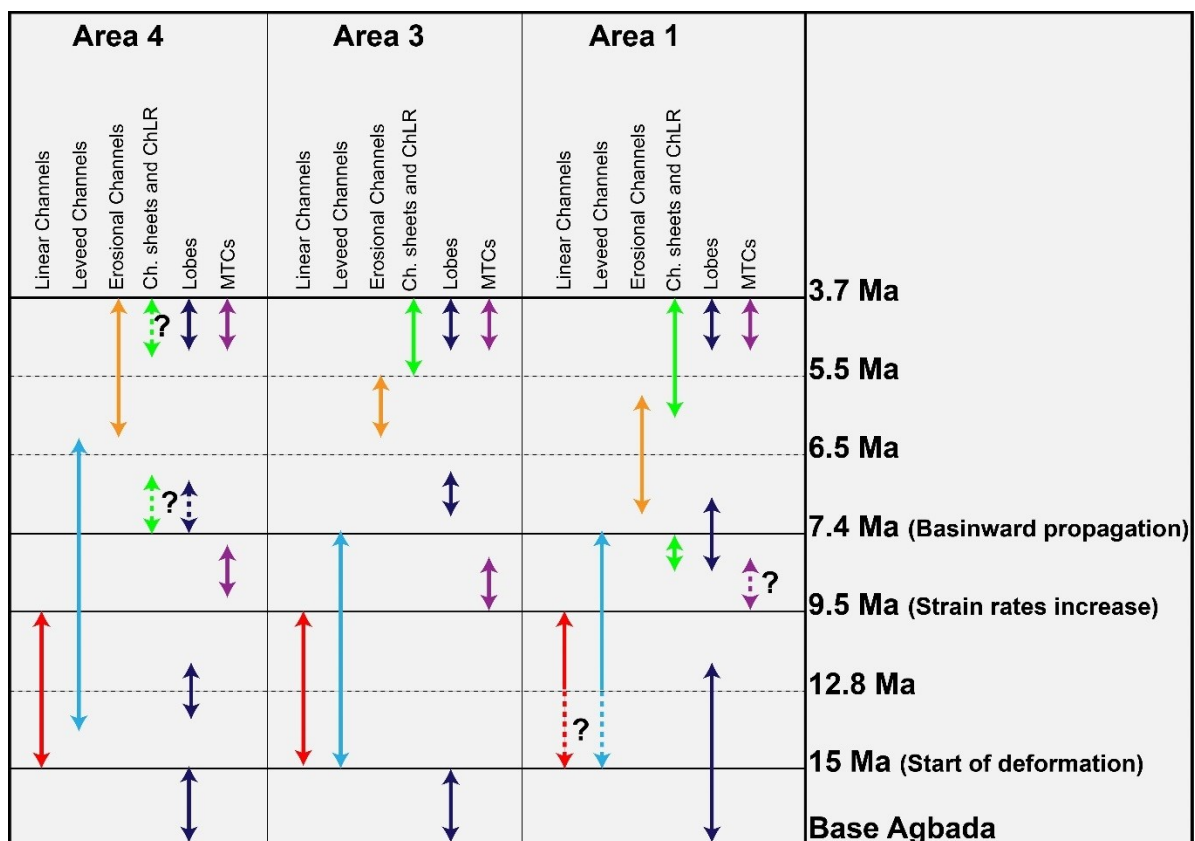
Figure 4-16: Diagram showing relative timing of occurrence of each facies type by area. Area 1=proximal and Area 4=distal. Deformation started at 15 Ma. Particularly note the time-transgressive occurrence of the erosional channels (orange arrows) and the weakly confined systems (green arrows) between Area 1 and Areas 3, 4, which follows the propagation of the deformation front (7.4 Ma). Question mark and dotted lines = uncertain occurrence of facies.

Although these results do not show how the changes in depositional style happen in a mechanistic sense, or in response to which specific driving factor, (see chapter 5 and 7), they do occur at 15, 9.5 and 7.4 Ma which corresponds to main tectonic phases during the progressive deformation in this part of the Niger Delta. Therefore, we deduce that tectonics must have had an impact on or contributed to the stratigraphic evolution of the area.

A similar vertical evolution in architecture has been observed in the Magallanes Basin, Chile, a deep-water succession deposited within a foreland basin that formed to the east of the proto-Andean orogenic belt during the latest Jurassic to Early Cretaceous (Romans et al., 2011; Beaubouef, 2004; Pemberton et al., 2016). This particular field example has been chosen as both thickness (4000 m) and duration of the basin filling (20 Myr) are of a similar magnitude as the present study area in the Niger Delta. In the Magallanes Basin, three formations record an evolution from unconfined or weakly confined turbidite systems (Punta Barrosa Fm.), passing upwards to slope valleys and channel-levee complexes (Cerro Toro Fm), terminating with sandstone-rich successions of variable architecture and MTDs (Tres Pasos Fm.). The latter is interpreted as a progradational slope system dominated by failure and channels interacting

with complex topography depositing sand in minibasins. Romans et al. (2011) suggest this evolution is mainly related to changes in basin configuration subsequent to the emplacement and propagation of thrust sheets and destruction of accommodation as a result of progressive basin filling.

Similar processes are believed to have controlled the evolution of the lower slope of the Niger Delta and in the following chapters we will explore in more details how tectonics has impacted both flow pathways and the distribution of the deep-water elements and will propose a mechanism by which it can alter their architecture through time.

5. Evolution of basin configuration and its impact on the distribution and architecture of deep-water systems

5.1 Introduction

The aim of this chapter is to explore in detail the tectono-stratigraphic evolution of the lower slope of the Niger Delta and show how the evolving basin configuration influenced both the distribution and the architecture of deep-water systems. This work builds on the previous understanding of the vertical change in facies associations which is diachronous between the four areas identified in the previous chapter (Figure 4-14 and Figure 4-16) as well as on the tectonic evolution of the slope discussed in chapter 3. Here the focus is on the 6 units, defined in chapter 4, that develop from the start of deformation (15 Ma) to 3.7 Ma when strain rates slowed down regionally (see chapter 3), which have been labelled U1 to U6 from top to bottom. For each unit isopach maps and sediment accumulation rate maps are presented. This allows me to reconstruct how the basin geometry evolved, by tracking how the accommodation space migrated through time. These maps are integrated and compared with structural measurements (chapter 3) including both the cumulative strain and interval strain rate maps, which are also shown for the intervals between 7.4-6.5, 6.5-5.5, 5.5-3.7 Ma. In fact, in comparison with chapter 3, additional interval strain rates have been obtained between 7.4 and 3.7 Ma, but exclusively for faults 22, 21, 20 and 19 (coinciding with areas 1, 2 and 3; the inner domain). This was due to a thicker wedge of sediments present in the inner domain which allowed analysis in greater detail. However, in the distal area 4 the thinner stratigraphy did not permit further subdivision and, as such, strain rates are averaged between 7.4 and 3.7 Ma.

RMS seismic amplitudes are extracted from each unit, through multiple isoproportional slices providing high level of detail even within a single unit. Seismic facies are interpreted from the RMS extractions (and seismic sections) using the classification described in Table 4-1 and show the spatial distribution and character of the sedimentary systems and how they evolved with time. The RMS extractions proved the existence of a large number of slope channels throughout the growth history of the fold belt. In order to make the discussion easy to follow, many of the channels were labelled, however their numbering does not represent a chronological order of formation.

For each unit, schematic "palaeogeography" maps, interpreted from the RMS extractions, are overlain onto the strain and isopach maps to evaluate the relationships between the structures

(strain rates) and the distribution and architecture of deep-water sedimentary systems. It is important to note that often, within a single unit, two or more intervals (times) have been defined that show sedimentary systems changing flow directions at a scale presumably smaller than 0.5 Ma and inside our age constraints. These intermediate times have been labelled following the numbering of the units that contain them with the addition of suffixes as "a, b" and so on from the oldest to the youngest. These maps were overlain onto the isopach and strain maps of the larger unit within which they are contained.

First, I will discuss the interpretation of isopach and RMS amplitude maps and derive accumulation rates; then I will discuss the caveats of using strain rate maps to assess the structural impact on the distribution of sedimentary systems. In section 5.2 each unit (from bottom to top) will be characterized in terms of their sediment thickness distribution, structural constraints and distribution and architecture of deep-water facies contained within it. Finally, in section 5.3 the tectono-stratigraphic evolution of the study area will be discussed, and how this has impacted the distribution and architecture of sedimentary systems, as well as its potential link to the variation in sediment supply from the delta top.

5.1.1   Isopach maps: interpretation and limitations

As previously mentioned, the evolution of the basin geometry is partly interpreted from the isopach maps. These maps show how the thickness is distributed within each unit and, therefore, allow us to visually assess where the main depocenters and accommodation space were located at each time. The palaeo basin physiography is, therefore, reconstructed from the sedimentary record with the assumption that the growth of thrust-folds limits the availability of accommodation space on their crest (causing thin sequences), while it favours the deposition of thicker sequences away from it (e.g. growth strata). This also means that any sedimentary system active at any time will preferentially exploit the areas away from the growing folds and will be incorporated within the thicker intervals.

For these reasons, isopach maps do not strictly represent the palaeoseabed topography, but show which fold-thrust structures were mostly active during each time interval and what thickness changes they caused from fold limb to crest. The amount of topography being created by each thrust-fold can be approximated by the rate of sediment thickness decrease (m/Km) from fold limb to crest.

However, one of the difficulties when interpreting isopach maps is understanding to what extent a thickness change represents the effect of a tectonic forcing as opposed to either

depositional or erosional processes occurring within the basin (e.g. the deposition of a thick MTD or a thick levee sequence). It is clear that during periods of high strain rates, such as those developed after 9.5 Ma, the fast growth of folds will most likely imply a tectonic forcing on the distribution of thickness (and sedimentary systems), but this is not so obvious when strain rates are very low. In fact, when strain or shortening rates drop below the average sedimentation rate for the same interval, then, autocyclic processes might also be expected to play a role in determining how thickness and depositional bodies are distributed within the unit. This is further complicated when the intervals analysed lie in the deeper parts of the stratigraphy, within the section that is commonly considered "pre-kinematic". The units deposited at the earliest stages of tectonic activity will have undergone the longest post-depositional deformation, along with compaction that altered their original geometry, making unambiguous conclusions about the palaeo basin geometry challenging. Finally, within the faulted intervals, sudden thickness variations across faults might result from the inability of the interpretation software to allow the interpretation of overlapping horizons in a contractional setting (see chapter 2) thus linking bits of stratigraphy that were not originally contiguous. This issue is more pronounced the larger the fault heave. Among the 6 units studied here, units 6 and 5, the two oldest, appear to be most affected by the issues discussed above, therefore the structural configuration of the study area at those times is mostly interpreted from the integration of the cumulative and strain rate maps presented in chapter 3.

5.1.2   Sediment accumulation rate maps and compaction

Isopach maps have the additional limitation of not being directly comparable between subsequent units because their absolute thickness is a direct result of the time over which sediments accumulated. Therefore, in basin analysis, a further step is to normalize the isopachs to make them comparable, by dividing them by the duration of the relative stratigraphic intervals. In effect, this process produces sediment accumulation rate maps which allows a direct assessment of how the sediment supply changed over time and facilitate arguments aiming to relate sedimentation and deformation (see section 5.3.3). Both isopach and accumulation rate maps ideally require the stratigraphic column to be decompacted in order to yield more accurate values of thickness and/or sediment supply, but, in this study, they have been presented un-decompacted for the following reasons:

1. This work only uses isopachs as a qualitative integration of the structural measurements to analyse the broad geometric evolution of the fold and thrust belt, but it is not concerned with the absolute values of thickness.
2. This study primarily focuses on how sedimentary systems respond to structural deformation as derived from the strain measurements rather than isopachs.
3. Isopachs are not used to deduce absolute values of fold uplift or to relate it to channel incision.
4. Curves of changing accumulation rates through time are calculated from the isopachs to compare them with the evolution of strain rates, relatively (section 5.3.3).

To test this simplification, a single, 1D column at the location of thickest stratigraphy in the study area was decompacted, using the same methodology described in chapter 3 (Figure 5-1). The choice of the thickest location allows one to assess the maximum potential error. Results show that both the observed and decompacted stratigraphy produce a pattern of increasing-decreasing accumulation rates over the past 15 Ma. Since we are interested in these relative variations rather than the absolute values (section 5.3.3), this approach is considered to be appropriate.
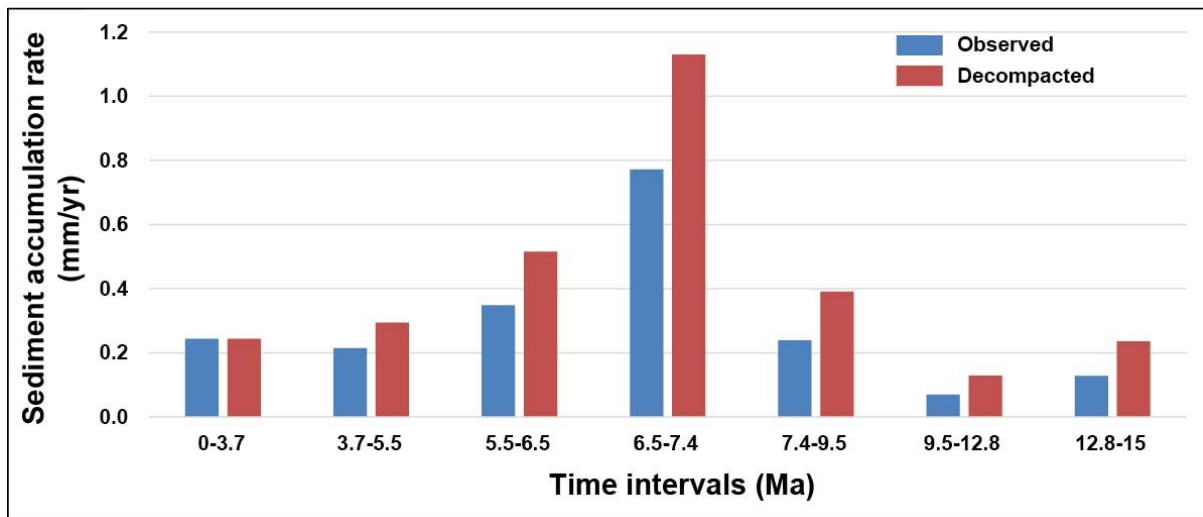
Figure 5-1: Max sediment accumulation rates in the study area from 15 Ma to present-day, extracted from a 1D location of thickest stratigraphy in area 1. In blue, observed values while in red are the decompacted values for an original surface porosity of 60%. Note that both observed and decompacted trends follow the same pattern of increasing-decreasing accumulation rates that matches the observed variation in strain rates through time.

5.1.3   Seismic amplitude maps: interpretation and limitations

RMS amplitude extractions were calculated for all the 6 stratigraphic units with the aim of mapping the distribution of the sedimentary systems through time with respect to the thrust-

fold structures. By converting both the peaks and troughs of the seismic wavelet into positive amplitude values they provide a measure of the reflection strength and intensity and are able to pick even subtle amplitude variations within what could be, otherwise, considered a homogeneous high amplitude reflector. However, the accuracy of RMS amplitude maps depends on three main factors: 1) the size of the window over which they are extracted; 2) the accuracy of the stratigraphic interpretation (which they follow) and 3) the vertical seismic resolution at the extraction depth. Therefore, following a general upward increase in seismic resolution in the study area (from 30 to 18 m approximately) and accuracy of stratigraphic correlation across structures, RMS maps extracted from the shallower levels are inevitably more precise than those extracted deeper in the stratigraphy. Additionally, from the RMS maps alone, it was only possible to distinguish between the main facies types (e.g. channel vs. lobe forms; chapter 4), while the specific architecture of each facies type (e.g. leveed vs. erosional channels) was established from the seismic sections shown in chapter 4. However, for simplicity of discussion, in this chapter, only the dominant facies types within each unit are discussed. Additional vertical seismic profiles, and more complex facies associations, will be shown in Chapter 7, where they will be compared and integrated with the strain-distance plots of the eleven thrust-folds. The imaged submarine channels were not always tracked entirely across the study area, either because of the degraded seismic quality in the highly deformed regions or due to the erosion of substantial portions of stratigraphy over the crests of anticlines. These issues are especially pronounced in the centre of the fold belt and, as a result, channels were mapped with high degree of confidence in both the inner and outer domain, but often without a direct link between the two because of the gaps in the core of the fold belt. In these circumstances, a tentative correlation between submarine channels in the inner and outer domain was established based on the stratigraphic level where they were found.

5.1.4   Integrating strain maps with the distribution of sedimentary systems

As discussed previously, one of the aims of this chapter is to demonstrate that the structures controlled the distribution of the sedimentary systems, and this is achieved with the use of strain rate maps. These maps show how deformation rates were spatially distributed through time (chapter 3) and, therefore, allow us to quantitatively assess which faults or fault segments were mostly active during each time interval and also to identify the zones of lower/lowest deformation. One prediction to test, therefore, would be that slope channels exploit these zones of low deformation to cross faults, and it is, indeed, anticipated that this is the outcome of

following analysis. However, there are a few exceptions where slope channels will be seen to cross faults for higher strain rates, which do not necessarily represent the lowest value along the strike of a given fault or lower in absolute terms. The reason for this derives from a number of factors which are here discussed:

1. The strain rates presented in the maps are divided into eight categories which comprise a range of values (e.g. 0.1 to 1 %/Ma), therefore, although a given (or two adjacent) fault segment is assigned to a category, the strain rate may still vary along it within that range and the channels respond accordingly.

2. The strain rates are averaged between our age data (stratigraphic intervals), but could have varied within that interval. Nonetheless, multiple "times" are often observed where channels at different levels within the same unit respond to deformation at a higher scale than the resolution of our analysis.

3. The distribution of strain rates on the most inboard structures dictate what directions/diversion channels must take and, therefore, influence where the channels will cross the down dip structures. Occasionally, channels are forced to exploit higher strain rates in absolute terms.

4. Strain rates are proxies for developing topography, but their maps do not account for the deformation that has been already accumulated (the cumulative strain). Therefore, a location of relative higher strain rates may still have a lower total cumulative strain than the surrounding areas.

5. In a few cases, very large and thick depositional bodies (e.g. levees) may widen the distance between the top and base horizons and alter the relative change in line-length from base to top. This may result in an overestimation of the strain rates.

However, this variability is fully addressed in chapter 6 where the distribution of the channel crossing points (and their relative values of strain rate) are systematically recorded and compared statistically with the evolution of strain rates through time. Moreover, in chapter 7 channel location and architecture will be further discussed with the integration of cumulative strain data. Therefore, the results and conclusions presented here are deemed reliable.

5.2 Tectono-stratigraphic development of the lower slope

5.2.1 Unit 6 (15 to 12.8 Ma)

5.2.1.1 Isopach and accumulation rate maps

The isopach map for this interval (Figure 5-2a) shows an average unit thickness of 240 m and a general trend of decreasing thickness from the NE to the SW. Specifically, the thickness varies from a maximum of approximately 450 m in the NW of area 1 to 250-300 m in the NE of area 1 and in area 3 to a minimum of 180 m in area 4 and beyond. Due to the high degree of deformation that has occurred in area 2, both the interpretation and the resulting thickness distribution are considered unreliable in area 2 and will not be discussed further.

Localized, short-wavelength variations are visible across the region, many of which create thickening and thinning trends which are elongated in a NE to SW direction (Figure 5-2a). These features are caused by the presence of submarine channels either within this unit (thicker) or eroding into this unit from the unit above or creating topography from the unit below (thinner).

The thickness distribution within this interval does not clearly show the impact of tectonic activity as no clear thickening is observed on the backlimb of folds. The isopach is therefore interpreted to represent the seaward thinning of a distal delta wedge. However, given the limitations associated with the deeper isopach, discussed in section 5.1.1, the influence of tectonic activity cannot be completely ruled out on this basis. Therefore, the results of the structural analysis need to be integrated to better understand the degree of deformation undergoing during this time interval.

The sediment accumulation rate map (Figure 5-2b) reveals an average 0.11 mm/yr during this interval (triangle in Figure 5-2b), ranging from 0.06 mm/yr to the S and SE to 0.22 mm/yr to the N-NW.
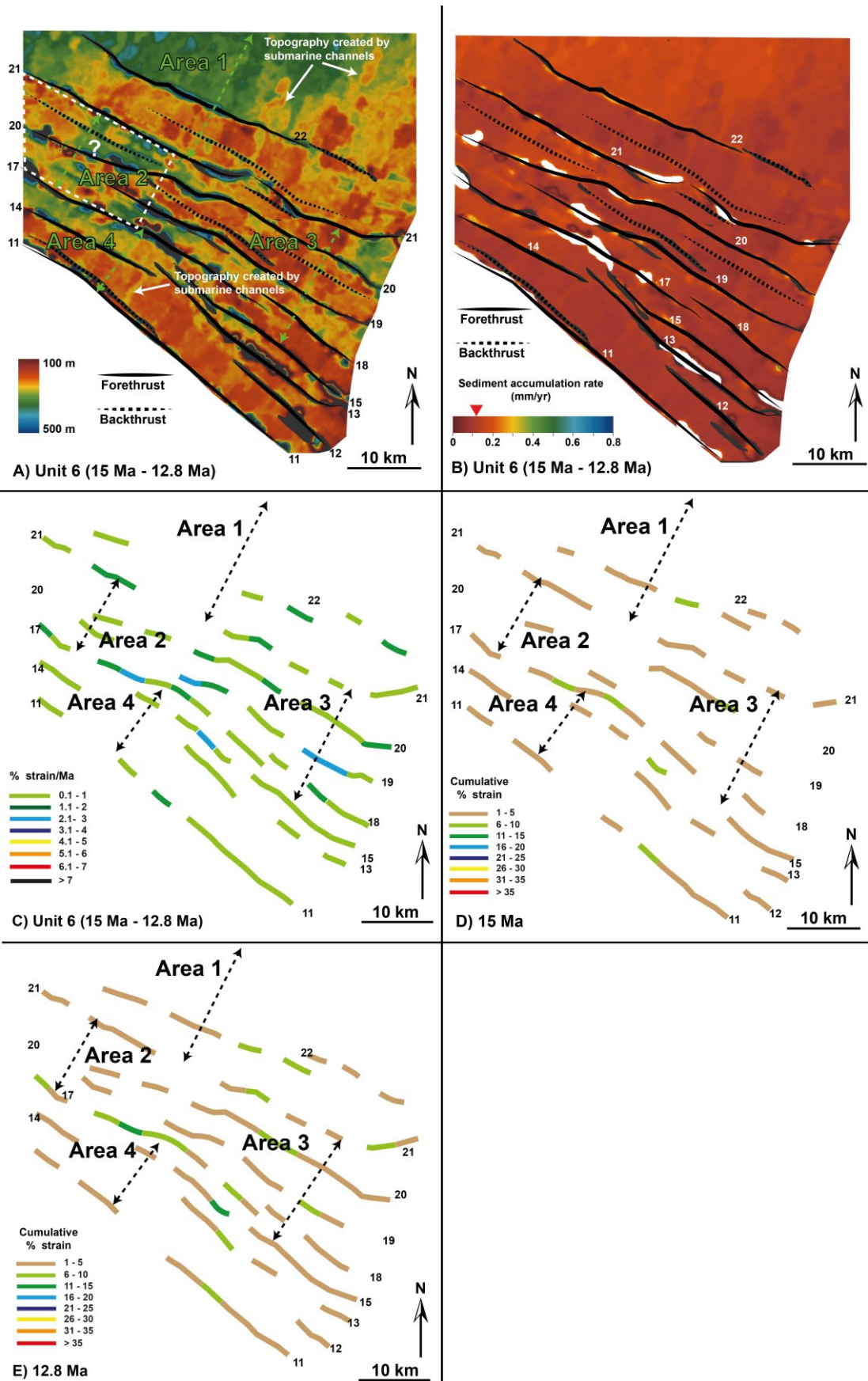
Figure 5-2: Characterization of unit 6. A) Isopach map. B) Sediment accumulation rate map. C) Distribution of strain rates between 15 and 12.8 Ma. D) Distribution of cumulative strain at 15 Ma. E) Distribution of cumulative strain at 12.8 Ma.

114

5.2.1.2   Structural analysis

Unit 6 is bounded by the 15 Ma horizon below and by 12.8 Ma horizon at the top, therefore the deformation activity of this interval is described by the interval strain rate map between the two surfaces (Figure 5-2c). Strain rates for this interval were generally low across all the faults (up to 1%/Ma; Figure 5-2c) with the central portions of the fault arrays shortening at higher rates of 2%/Ma and exceptionally up to 3%/Ma along faults 19, 17 and 15 (Figure 5-2c).The strain analysis from chapter 3 shows that the deformation started at 15 Ma and that, at this time, the faults in the area initially developed as individual segments. A few faults (e.g. 22, 20, 17, 11; Figure 5-2d) appear more laterally continuous and their segments partially linked. In general, the fault segments had accumulated between 1 to 5 % of the total shortening (brown colours, Figure 5-2d), with the exception of a small number of segments that accumulated between 6 to 10 % of shortening along the strike of the more laterally continuous faults (green colours). By 12.8 Ma (Figure 5-2e) the fault segments across all the fault arrays had laterally propagated and started to link into longer segments. Cumulative strain across the region was still typically in the order of 1 to 5 %; however, more segments accumulated 6 to 10 % of shortening and two faults (17, 15) had segments shortened by 11 to 15%.

5.2.1.3   Seismic facies and structural impact

Attribute maps extracted from three levels within the unit (times 6a to 6c from oldest to youngest) show that seismic facies within this interval primarily consist of linear channels in areas 1, 3 and 4 (Figure 4-8) and unconfined lobe complexes (Figure 4-10) only present in area 1, inboard of fault 21 (Figure 5-3a-d). As discussed previously, area 2 is difficult to interpret reliably and is not discussed further.

The lower two amplitude maps (Figure 5-3a, b) show the presence of a large area of high seismic amplitudes inboard of fault 21 (and 22) to the SE of area 1. On a seismic section this area consists of high amplitude continuous reflectors, as thick as single seismic loops (ca. 80 m), while, in map view, the reflectors form sub-circular features. These features are interpreted as a large lobe complex in chapter 4 (LC1; Figure 5-3d; Figure 4-10) where individual lobes and lobe elements can be also distinguished. The complex is up to 16 km long and 11 km wide and at least 4 individual sub-circular lobes can be identified with a consistent diameter of 2.5-3 km. Each lobe is composed of 4 to 5 smaller lobe elements, 300 to 800 m in diameter.

The upper amplitude map (Figure 5-3c) shows a similar scenario, where an interpreted second lobe complex (LC2) is present inboard of fault 21 (and 22) to the NW of area 1. The dimensions

of the lobe complex are approximately 14 km x 17 km, which appears to be composed of several lobes and lobe elements of comparable size to LC1.

The influence of structures on the location of LC1 is inferred from the fact that fault 21 limits its southern extent (Figure 5-3d). However, the internal architecture of the lobe complex, as seen in seismic section, appears controlled by compensational stacking of the lobes (Figure 4-10). The location of LC2 is also influenced by structures (Figure 5-3d): for example, the strain rate map for this interval (Figure 5-4) shows that the lateral extent of LC2 is dictated by the space between two active segments of fault 22, whereas its southern, basinward limit is influenced by the location and activity of fault 21, as also seen for LC1. Therefore, the strain rate map suggests that rates of deformation in the order of 1 to 2 %/Ma were enough to control the distribution of the lobe complexes.

In addition to the lobe complexes, the attribute maps (Figure 5-3) reveal the presence of widespread linear channels, as previously described in detail in chapter 4. These are present to the south-east of fault 21, in areas 3 and 4, as well as on top of LC1 and LC2 in area 1. On a regional scale, these channels flow downslope without showing major deflections (Figure 5-3d and Figure 5-4). However, evidence for structural control is suggested by their convergence towards the centre of fault 11, which, at that time, was inactive along most of its strike length (Figure 5-4). In several instances, the channels were deflected either to the side or between fault segments for strain rates as low as 1%/Ma (Figure 5-4), as well as towards the oversteps in map view.
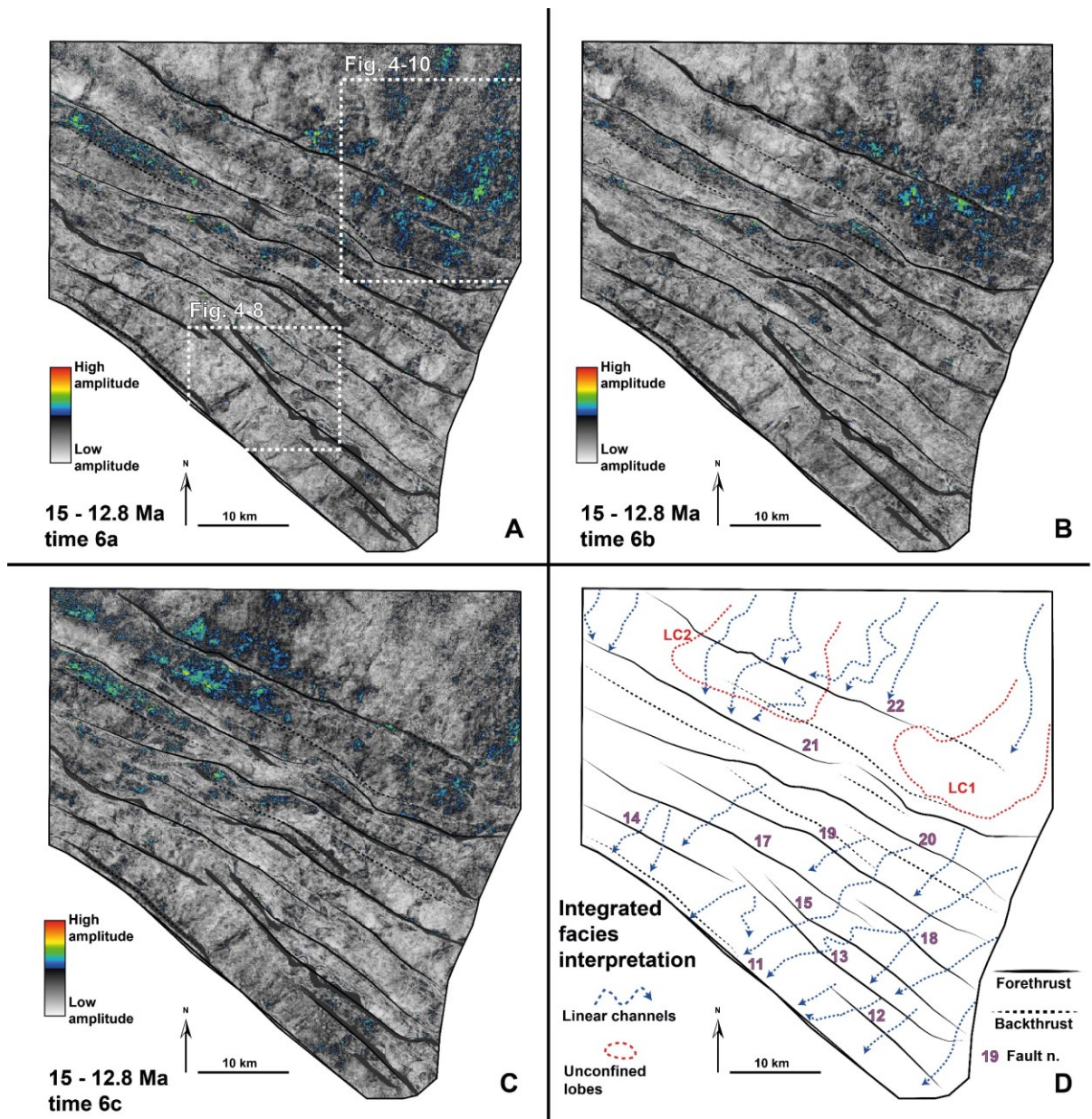
Figure 5-3: A, B and C are RMS amplitude extractions from three isoproportional slices within the 15 to 12.8 Ma interval. In D the resulting integrated interpretation shows the distribution and type of seismic facies present during this time.
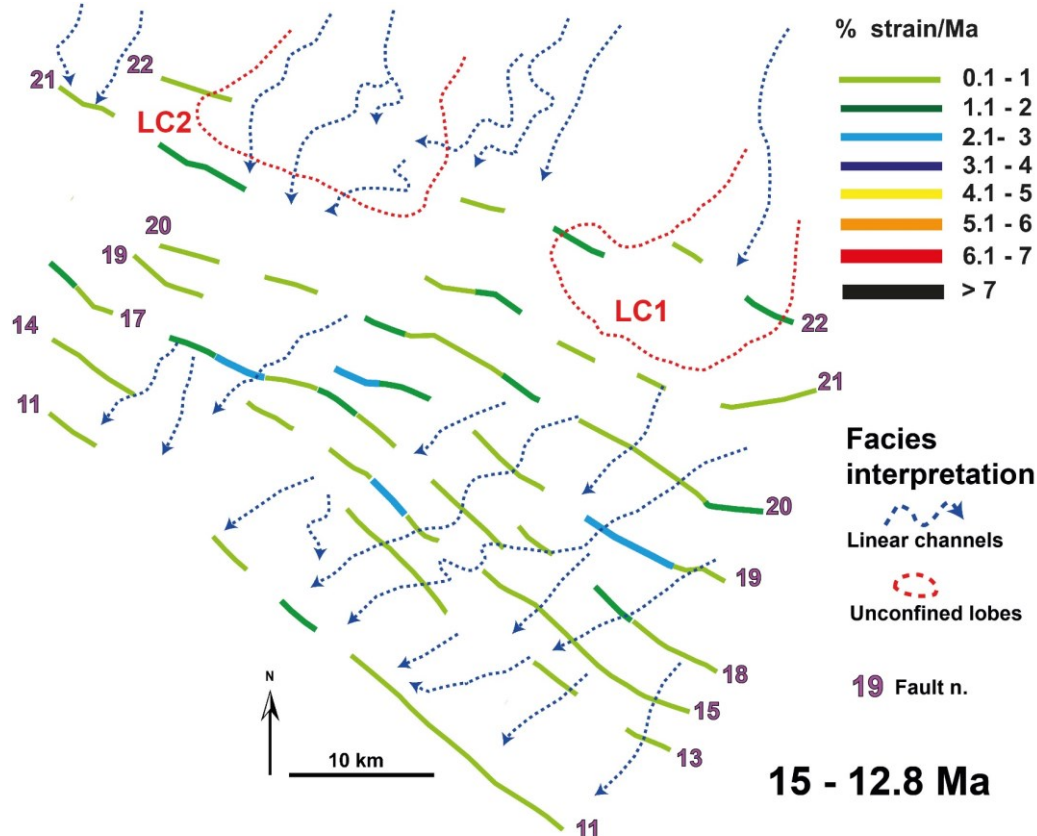
Figure 5-4: Facies interpretaion for the interval 15 to 12.8 Ma shown in Figure 5-3d overlaid onto the strain rate map for the same interval shown in Figure 5-2c. Note that sedimentary systems are widely distributed across the study area. Also note that slope channels at this time already interact with faults as they exploit areas with lower strain rates along the strike of each fault.

5.2.2 Unit 5 (12.8 to 9.5 Ma)

5.2.2.1 Isopach and accumulation rate maps

The isopach map (Figure 5-5a) of this unit shows that thickness is approximately 280-300 m in area 1 and thinner (150-200 m) in areas 3, 4. On a regional scale this unit appears to broadly compensate the thickness distribution of the underlying unit 6. For examples, the relatively thin stratigraphy in areas 1 and 4 of unit 6, correspond to relatively thicker sequences in unit 5 (Figure 5-2a and Figure 5-5a), although this does not appear to occur for area 3. In the same way as for Unit 6, localized, short-wavelength thick and thin areas are caused by the presence of submarine channels either within this unit (thickenings) or eroding into this unit from the unit above or creating topography from the unit below (thinnings) (Figure 5-5a). The sediment accumulation rate map (Figure 5-5b) reveals an average 0.06 mm/yr during this interval, ranging from 0.03 mm/yr in area 4 to 0.12 mm/yr in area 1. This accumulation rate is approximately half of that during unit 6, which has resulted in a substantially thinner unit.

It is again difficult to establish, from the isopach map alone, the degree of tectonic activity occurring at this time. However, the results of the structural analysis, summarized in the following section, aid to unravel the amount of deformation in this interval.
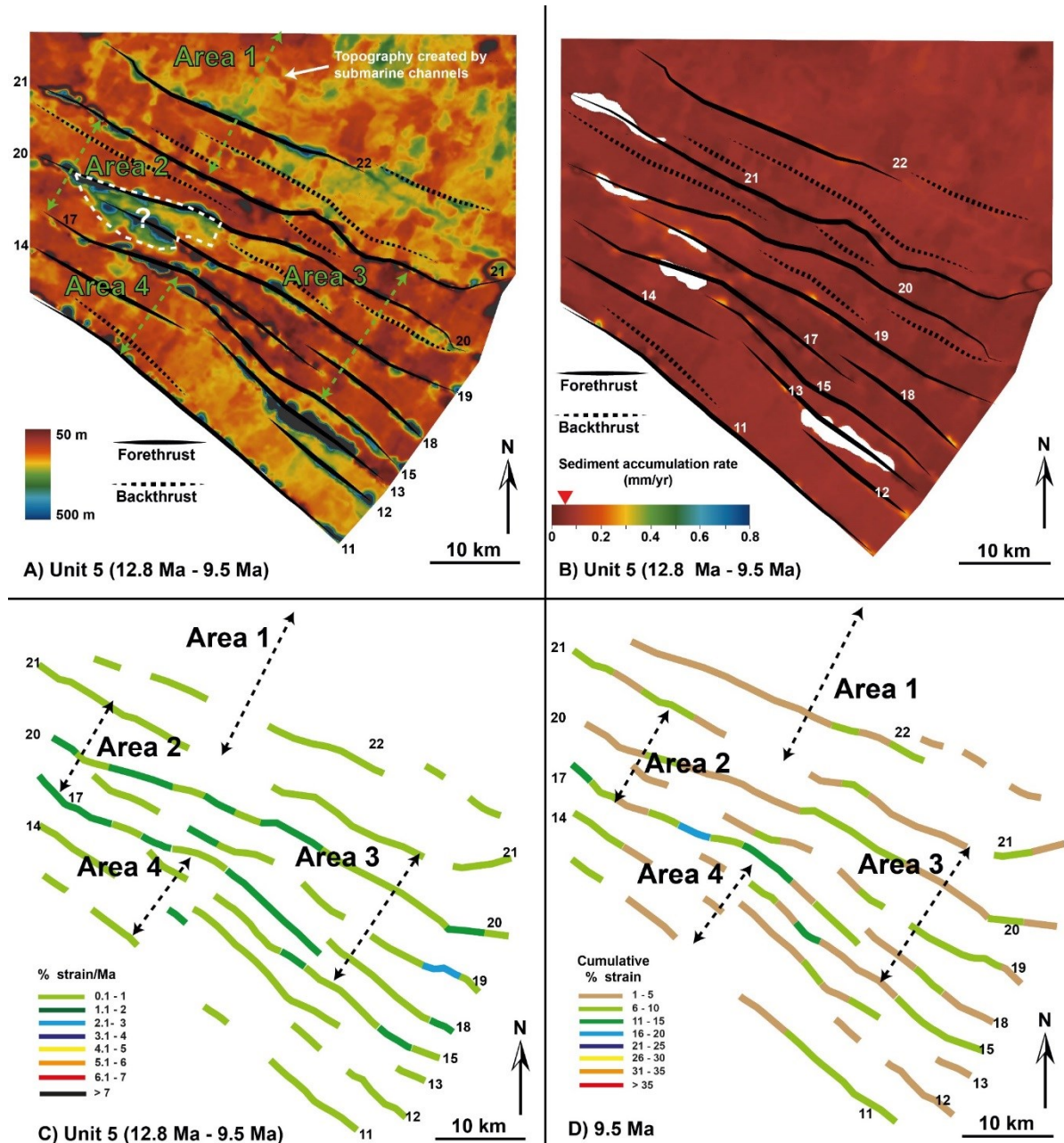
Figure 5-5: Characterization of unit 5. A) Isopach map. B) Sediment accumulation rate map. C) Distribution of strain rates between 12.8 and 9.5 Ma. D) Distribution of cumulative strain at 9.5 Ma.

5.2.2.2 Structural analysis

Unit 5 is bounded by the 12.8 Ma horizon and by the 9.5 Ma horizon at the top. The strain rate map for this interval (Figure 5-5c) shows that all the faults in the area were active at low strain

rates (up to 1%/Ma), while a few segments along the strike of faults 17 and 20, in the centre of the fold-thrust belt, deformed at 2%/Ma. During this interval many of the faults had continued to propagate laterally and link (Figure 5-5d). By 9.5 Ma, the faults in the core of the fold belt (20, 17, 18, 15) had almost fully linked along their entire strike length, while, away from this central area, faults 22 and 21 in area 1 and faults 11, 12, 13, 14 in area 4 still had unlinked segments. By 9.5 Ma, a number of fault segments had cumulative strain in the order or 6 to10 %, particularly in the core of the fold belt. Along the strike of fault 17 one segment had already shortened by up to 20 %.

5.2.2.3   <u>Seismic facies and structural impact</u>

The attribute map shows that this interval is dominated by channel forms, with occasional small lobate forms (Figure 5-6). Significantly, sedimentary systems continued to be widespread across the region for along-strike distances of more than 40 km. The channels entered the study area from the north-east of area 1 and crossed it along two main pathways. One set of channels (12-5, 7, 8) with low sinuosity and classified as linear channels flowed south-west (towards areas 3 and 4), while another set of more sinuous leveed-channels (12-1, 2, 3, 4; Figure 4-1) flowed in a more westerly direction (area 2; Figure 5-6 and Figure 5-7). The leveed channels terminated with the deposition of lobes in the vicinity of the north-west termination of fault 20, whereas, the linear channels crossed the region with unaltered architecture, although they could not be confidently traced in all parts of the fold belt.

The structural influence on the channels location is evident from the overlay of their spatial distribution with the strain rate map of the interval (Figure 5-7). For example, upon entering the study area, the two sets of channels were diverted around the active segments of fault 22 shortening at 1%/Ma (Figure 5-7), predominantly exploiting the inactive zones along the strike of this fault and passing through strain minima between unlinked segments (Figure 5-7). This early diversion caused the leveed channels to flow west, terminating with the deposition of lobes up-dip of segments of fault 20 and 17 that were deforming at greater strain rates (2%/Ma). The greater strain rates along faults 20 and 17 also diverted the linear channels to the south and south-east, where they exploited areas of lower strain rate (1%/Ma) along the strike of the faults. The linear channels also exploited relay zones between faults, where faults overstep, as between faults 17 and 18 (Figure 5-7).
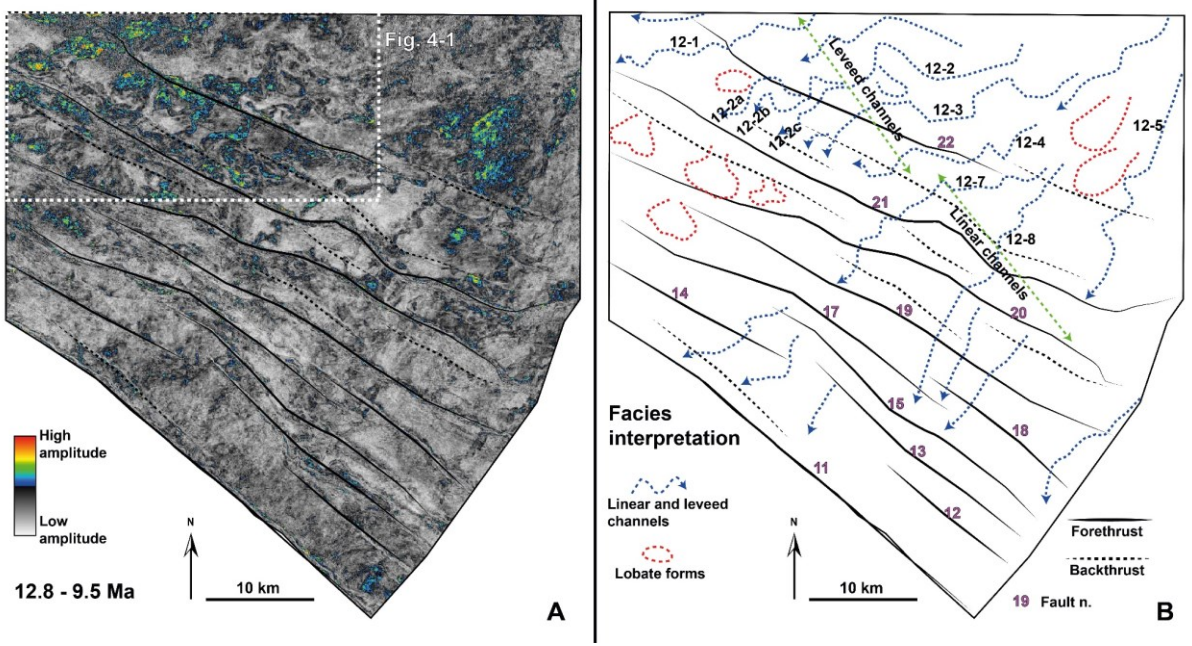
Figure 5-6: A is the RMS amplitude extraction for the 12.8 to 9.5 Ma interval. In B the resulting interpretation that shows the distribution and type of seismic facies present during this time.
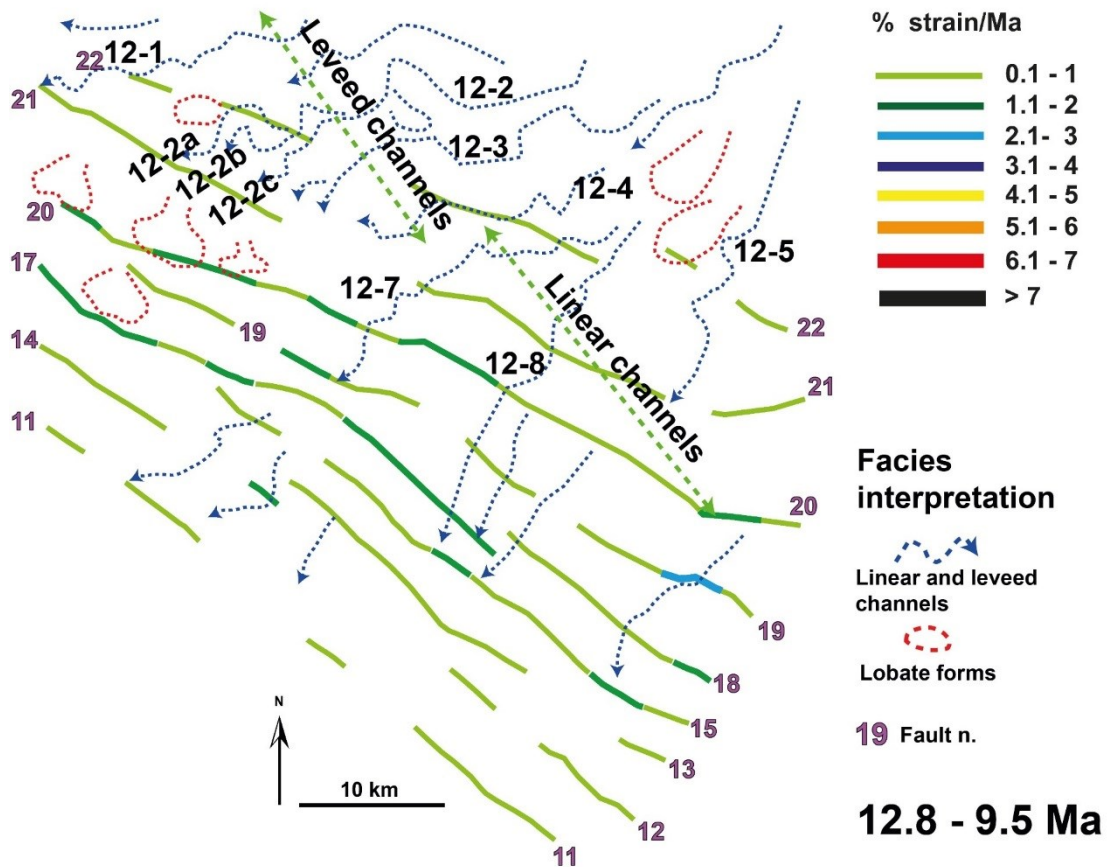
Figure 5-7: Facies interpretaion for the interval 12.8 to 9.5 Ma shown in Figure 5-6b overlaid onto the strain rate map for the same interval shown in Figure 5-5c. Note that sedimentary systems are still widely distributed across the study area. Also note that slope channels continue to interact with faults as they exploit areas with lower strain rates along the strike of each fault.

5.2.3   Unit 4 (9.5 to 7.4 Ma)

5.2.3.1   Isopach and accumulation rate maps

Unit 4 records a period of major change in the basin configuration as the thickness of sediment varies markedly across the study area compared to the preceding time intervals (Figure 5-8a). The eastern portion of area 1 shows a north-east to south-west trending zone where thickness reaches values of more than 700 m, while, towards the north-west of area 1, thickness progressively decreases to 400-500 m, culminating in a minimum of 350 m in the central-located part of the hangingwall of fault 22 (Figure 5-8a). Other thickness minima in the order of 350-400 m are also found on the hangingwall side of fault 21, in its central location, and to the south-east, on the hangingwall of the back-thrust formed along fault 22 (Figure 5-8a). In the central part of the fold belt (areas 2 and 3), thickness minima of 100-150 m are present along strike of most of the faults, including 20, 19, 18, 17, 15, and 13 (Figure 5-8a). The thickness in area 4 ranges from 300 and 400 m, being greatest in the central portion and minimum to the north-west and south-east terminations, on the back limbs of faults 11, 12, and 14.

Sediment accumulation rates in this interval (Figure 5-8b) were up to 3 times greater than the underlying unit 5. Inboard of fault 21, in area 1, rates reached 0.3 mm/yr, decreasing to 0.06 mm/yr in the core of the fold belt, where sediment thickness is at a regional minimum.
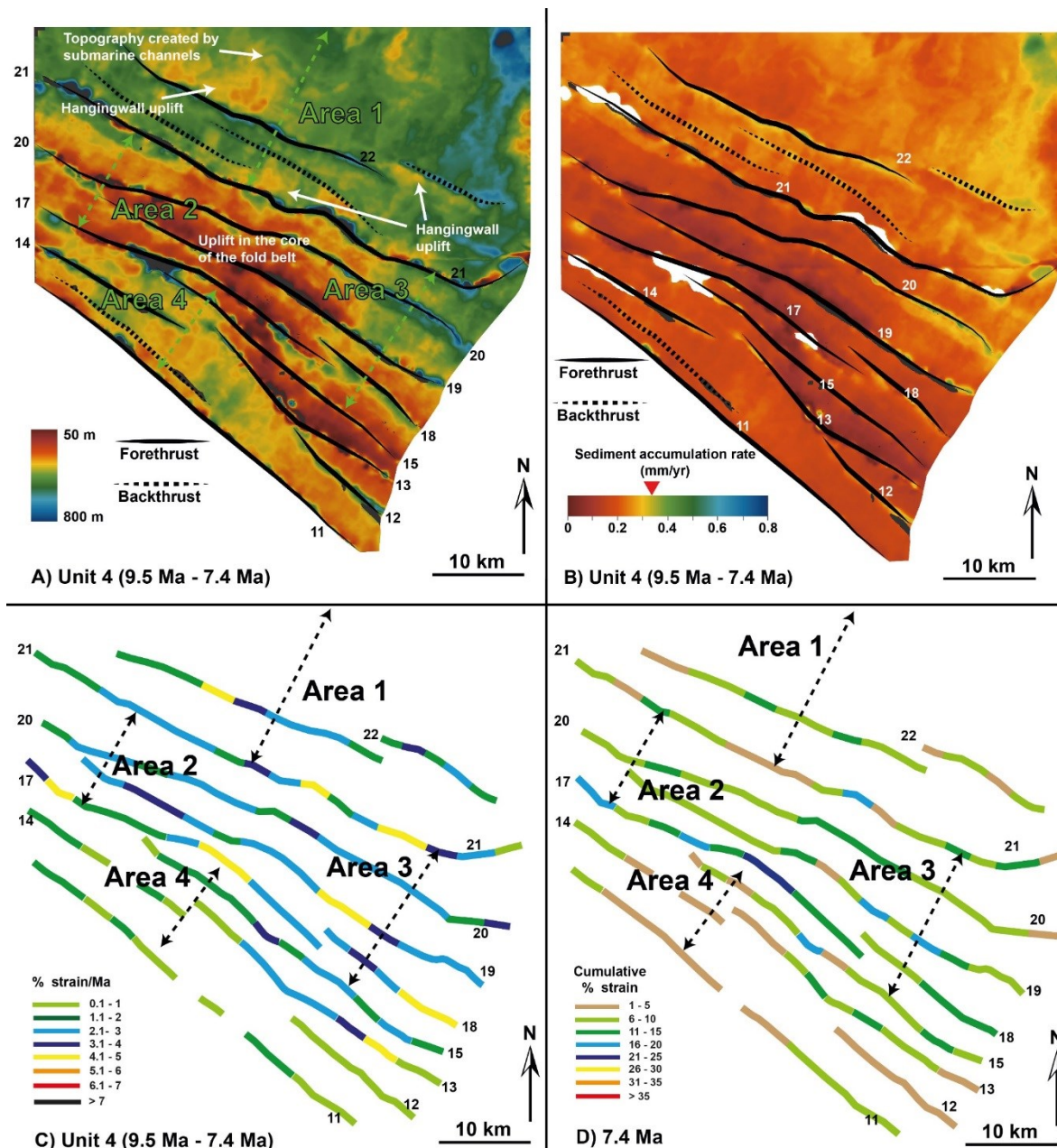
Figure 5-8: Characterization of unit 4. A) Isopach map. B) Sediment accumulation rate map. C) Distribution of strain rates between 9.5 and 7.4 Ma. D) Distribution of cumulative strain at 7.4 Ma.

5.2.3.2   Structural analysis

Unit 4 is bounded by the 9.5 Ma horizon below and by the 7.4 Ma horizon at the top. As discussed in chapter 3, this period records a marked increase in regional strain rates (Figure 5-8c). In the inner domain of the fold belt (areas 1, 2 and 3) all the faults reached background deformation rates up to 3%/Ma and, along their strike, many segments shortened by 4 to 5%/Ma. However, at this time, area 4, the outer domain of the study area, was still deforming at lower strain rates (up to 1 and 2 %/Ma) as the deformation front had not propagated fully into this area (Figure 5-8c). By 7.4 Ma (Figure 5-8d), all the faults in the inner domain had fully linked, although their cumulative strain was generally not higher than 10-15 %. Only a

few segments along the strike of faults 21, 19 and 17 reached a total shortening of 20-25%. By contrast, faults 14 and 11, in the outer domain (area 4), had not fully linked and their cumulative strain did not exceed 5-10%.

5.2.3.3   Seismic facies and structural impact

Two RMS extraction maps (Figure 5-9a, b) show that this interval remained dominated by leveed-channel complexes (Figure 5-9c, d). To a lesser extent, lobate forms and low-relief channel levees are also observed (channel 9-6 in Figure 5-9d; see also Figure 4-6). Notably, the areal distribution of the sedimentary systems become more focused with respect to the underlying unit 5 during this interval. Moreover, while sedimentary systems originally (time 4a) flowed in a similar direction to unit 5 (Figure 5-6), they subsequently (time 4b; Figure 5-9d) entered the study area from the N and flowed to the S or SW, indicating that tectonic activity during this interval caused a change in flow direction with time (Figure 5-9d).

In fact, the influence of tectonic activity on the distribution of the sedimentary systems is again evident from the overlay of the channels' locations with respect to the isopach map (Figure 5-10a, b). This shows that submarine channels established their course where thicker sequences could accumulate (green and blue) and avoided (i.e. were diverted from) the areas which now display relatively thinner sediment thicknesses (yellow and brown) due to the growth of fold-thrusts, particularly on the hangingwall of fault 22, as well as on the large uplifted area present in centre of the fold belt (Figure 5-10).

For example, at time 4a (Figure 5-10a) a leveed channel (9-1) is deflected to the west of the study area by the combined effect of faults 22 and 20 and terminates with the deposition of a lobe on backlimb of fault 20, where the sediment thickness is highly reduced. In Figure 5-11a it is shown that channel 9-1 is evidently deflected to the north-west of fault 22 avoiding the areas of greater strain rates in the centre of the fault (up to 4-5%/Ma) and exploited zones of lower strain rates (2%/Ma). The deposition of the lobe, therefore occurred up-dip of fault segments deforming between 2-3%/Ma. Similarly, channels 9-3 and 9-7 were both deflected away from the zones of greater strain rates along fault 22 and 21 (Figure 5-11a).

At time 4b (Figure 5-10b and Figure 5-11b), to the east of area 1, a large channel levee complex (9-8) originally flowed in a N-S direction, being diverted to the eastern tip points of the back-thrust of fault 22 and fault 21, avoiding their faster deforming segments (3-4%/Ma; Figure 5-11b). Further downslope, it was deflected towards the south-west, exploiting successive relay zones between faults 18, 17, 15 and 13 that progressively stepped down towards area 4. As the

channel 9-8 entered area 4, lobate forms were deposited in its central portion, presumably in response to a break in slope at the entry point of area 4. Subsequently, the channel continued its course beyond the limit of the study area passing through an inactive zone of fault 11 that, at this time, was still segmented (Figure 5-11b).

In the centre of area 1, a large sheet-like deposit is present up dip of segments of fault 22, which was deforming at strain rates of 4%/Ma (Figure 5-10b and Figure 5-11b). The deposit is cut by a north-south trending low-relief channel levee (9-6; see also Figure 4-6). This channel is clearly diverted towards the relay zone between the frontal and back thrusts of fault 22, where the strain rates are at the lowest (2%/Ma; Figure 5-11b). Channel 9-6 appears to terminate with the deposition of another lobate form, further to the south, on the back of fault 21.

To the west of area 1, two leveed channels (9-4 and 9-5) are diverted around the topography developing on the crest of fault 22 (Figure 5-10b) and avoid the central portion of the fault where strain rates are up to 4-5%/Ma (Figure 5-11b). However, these channels could not be traced further to the south.

Figure 5-9: A and B are the RMS amplitude extractions from two isoproportional slices within the 9.5 to 7.4 Ma interval. In C and D the resulting interpretation that shows the distribution and type of seismic facies present at each time.

Figure 5-10: – A) Facies interpretation shown in Figure 5-9c overlaid onto the isopach map of the interval shown in Figure 5-8a. B) facies interpretation shown in Figure 5-9d overlaid onto the isopach map of the interval shown in Figure 5-8a. Note the change in flow directions between the two times and that channels are present over thicker areas of the isopach. The dominant channel architecture is leveed-aggradational for both the inner and the outer domains.

Figure 5-11: A) Facies interpretation shown in Figure 5-9c overlaid onto the strain rate map of the interval shown in Figure 5-8c. B) Facies interpretation shown in Figure 5-9d overlaid onto the isopach map of the interval shown in Figure 5-8c. The dominant channel architecture is leveed-aggradational for both the inner and the outer domains.

128

5.2.4   Unit 3 (7.4 to 6.5 Ma)

5.2.4.1   Isopach and accumulation rate maps

The isopach map of this interval also shows that the distribution of sediment thicknesses significantly changes across the slope (Figure 5-12a). A large depocentre is found in area 1, inboard of fault 22, where depositional thicknesses reach a maximum of approximately 700 m (Figure 5-12a).

In the rest of the inboard domain (areas 1, 2 and 3) the isopach map shows north-west to south-east trending lineaments, where thickness minima (50 m or less) are developed on the anticlines of the thrusts-folds and are separated from thicker zones (350-400 m) with the same orientation on the hangingwall of the thrusts. These thickness trends clearly follow the strike orientation of the structures.

In area 4, a depocentre, 200-250 m thick, is present in the centre of the basin, while thickness minima (50-100 m or less) are only found at the north-west and south-east terminations along faults 12, 14 and 11. Despite these marked changes in isopach thicknesses, maximum sediment accumulation rates during this interval were the highest throughout the growth history of the fold belt. Rates were as high as 0.75 mm/yr in area 1, inboard of fault 22, as low as 0.05 to 0.1 mm/yr along the crests of the thrusts, and 0.25-0.30 mm/yr in the centre of area 4 (Figure 5-12b).

Figure 5-12: Characterization of unit 3. A) Isopach map. B) Sediment accumulation rate map. C) Distribution of strain rates between 7.4 and 6.5 Ma. D) Distribution of cumulative strain at 6.5 Ma.

5.2.4.2 Structural analysis

Unit 3 is bounded by the 7.4 Ma horizon and by the 6.5 Ma horizon at the top. This period records the moment of peak deformation throughout the growth history of the fold belt, particularly in the inner domain (areas 1, 2 and 3; Figure 5-12c). Here, faults 21, 20 and 19 achieved deformation rates higher than 7%/Ma along most of their strike length. The outer domain (area 4) also underwent higher deformation rates, yet lower than in the inner domain. Here faults 13 and 11 deformed at rates up to 6%/Ma, indicating that, in this interval, the

deformation front had propagated basinward and impacted the outer thrusts. However, as previously discussed, the strain rates between 7.4 and 6.5 Ma (se well as those between 6.5 and 5.5, and 5.5 and 3.7 Ma) were only measured in the inner domain along fault 22, 21, 20 and 19 due to the thicker stratigraphic intervals. In area 4 such further subdivision was not required, and strain rates were averaged over a longer time period (7.4 to 3.7 Ma). Therefore, in area 4, units 3, 2 and 1 exhibit the same strain rates between 7.4 and 3.7 Ma. By 6.5 Ma, all the faults in the study area had completely linked (Figure 5-12d). On average all the faults accumulated between 15 and 20% of shortening, except for faults 17 and 13, in the core of the fold belt, which achieved values between 26 and 35% of shortening.

5.2.4.3   <u>Seismic facies and structural impact</u>

Three attribute maps (Figure 5-13) show this interval to be initially dominated in the inner domain by lobes and, subsequently, by a series of mainly erosional channel complexes, or mixed aggradational-erosional systems. However, leveed-channels and low-relief channel levees are still observed in the outer domain (area 4).

This interval also records the maximum restriction on the areal distribution of the sedimentary systems. A comparison of the facies distribution with the isopach map (Figure 5-14) shows that tectonics exerted the strongest control on the location of deep-water facies. At first (time 3a; Figure 5-14a and Figure 5-15a) the large depocenter inboard of fault 22 was the locus of deposition for two lobes, that clearly onlap the back limb of fault 22 for strain rates up to 5%/Ma (Figure 5-15a; see also Figure 4-11) suggesting favourable conditions for ponding. I also believe that the up dip termination of the lobes reflects the location where the slope gradient was first affected by movement on fault 22, which can be up to 10-15 km up dip of the controlling fault (see chapter 7).

At the same time, two erosional channels (7-1, 7-7) were deflected to the lateral tips of fault 22 and channel 7-7 terminated with the deposition of a ponded lobe within the syncline formed between faults 22 and 21 (Figure 5-14a) after exploiting a zone of low strain rate on fault 22 (up to 2%/Ma; Figure 5-15a). Channel 7-1 could not be traced beyond fault 21, but it is likely the feeder system of a small-relief channel levee present in area 4 at the same stratigraphic level (Figure 5-14a and Figure 5-15a; see Figure 4-7).

Subsequently (time 3b; Figure 5-14b, Figure 5-15b), five erosional or mixed erosional-aggradational channels (7-3, 7-4, 7-5) and low-relief channel levees (7-0, 7-2), entered the study area from the north-east with an even spacing of approximately 10 km. The channels

were affected by fault 22 that directed their course towards different parts of the basin. The channels passed through four locations found at either the lateral tips of the fold (channels 7-2, 7-5) or the points of segment linkage along its strike (channels 7-3, 7-4; see section 5.3.2.1), generally avoiding the areas deforming at the greatest strain rates in the centre of fault 22 (Figure 5-15b). Additionally, channels 7-3 and 7-4 passed over the broad structural culmination of fault 22 (Figure 5-14b), likely in response to the filling of the accommodation space, following the deposition of the underlying ponded lobes.

Channel 7-2 was originally deflected into the syncline that formed between the footwall of fault 22 and the hangingwall of fault 21. Here it terminated into a ponded lobe elongated as the strike of the controlling faults (22 and 21). Subsequently the channel continued its course downslope through fault 21 but could not be traced further. Similarly, another channel (7-0), is probably the feeder system of the ponded lobe located up dip of fault 21 at its north-west end where strain rates were greater than 7%/Ma. The high strain rates later diverted the channel outside the study area. A zoom of the relationship between the low-relief channels and the lobes has been shown in Figure 4-5.

Channels 7-4 and 7-5 are two branches of the same channel that were deflected around one segment of fault 22. Subsequently, the two branches re-joined into a single erosional channel that continued downslope exploiting early zones of linkage between segments of faults 21 and 20 (see section 5.3.2.1). The same zone of linkage is also exploited by channel 7-3 (Figure 5-14b). It is also evident that both channel 7-3 and 7-4 exploited the locations of lower strain rate along the strike of each fault they crossed (Figure 5-15b), although, in absolute terms, strain rates were occasionally high, as on fault 21. These, in fact, are examples of channels forced to exploit high strain rate locations due to the diversions they took further up dip. Channels 7-3 and 7-4 could not be traced beyond fault 19, due to the large amount of deformation and erosion that this unit underwent in the core of the fold belt. However, it is evident that these channels entered area 4 (the outer domain) and altered their architecture into leveed-aggradational, however exploiting either fault tips (on fault 14) or central, along strike portions with relative low strain rates (on fault 11: Figure 5-14b and Figure 5-15b).

The uppermost interval (time 3c; Figure 5-14c, Figure 5-15c) shows a single mixed erosional-aggradational channel (7-6; see Figure 4-2) entering area 1 from the north-east and being diverted to the west following the strike of fault 22. The channel is then deflected south-west around the lateral termination of fold 22 before exploiting a passage through fault 21 at a location of minimum strain rate along its strike (Figure 5-15c). Channel 7-6 is probably the

feeder system of another aggradational leveed channel in area 4 at the same stratigraphic level (see Figure 4-3). In fact, the dominant architecture of channels in area 4 during this time interval is leveed-aggradational as opposed to the erosional channels of the inner domain.

This aggradational complex is also structurally diverted in the centre of area 4 by the growth of fault 14 and 11 (Figure 5-14c, Figure 5-15c).

These results show that none of the submarine channels in the area could keep pace with strain rates higher than 7%/Ma and that their location was structurally controlled: they cross active structures at zones of lower strain rates, relative to the surrounding segments along the strike of the same fault, regardless of the absolute magnitude of the strain rate.

The strain rate maps (Figure 5-15 a-c) show that a shortening rate as low as 1-2%/Ma is required to pond sediments; however, unlike submarine channels, ponded lobes are always located up dip of zones of greater strain rates, relative to the surrounding segments along the strike of the same fault.
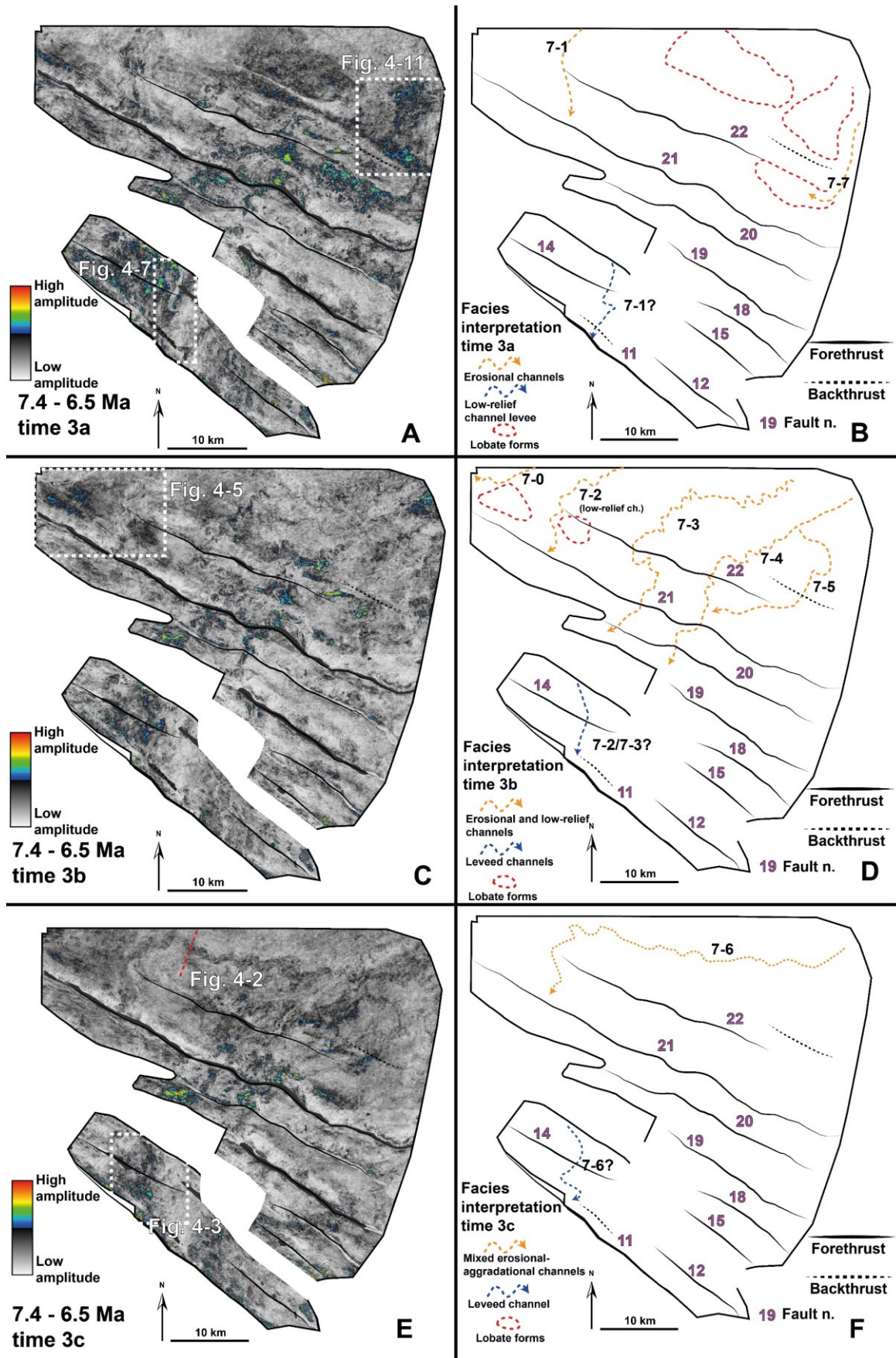
Figure 5-13: A, C and E are the RMS amplitude extractions from three isoproportional slices within the 7.4 to 6.5 Ma interval. In B, D and F the corresponding interpretation that shows the distribution and type of seismic facies present at each time.

134
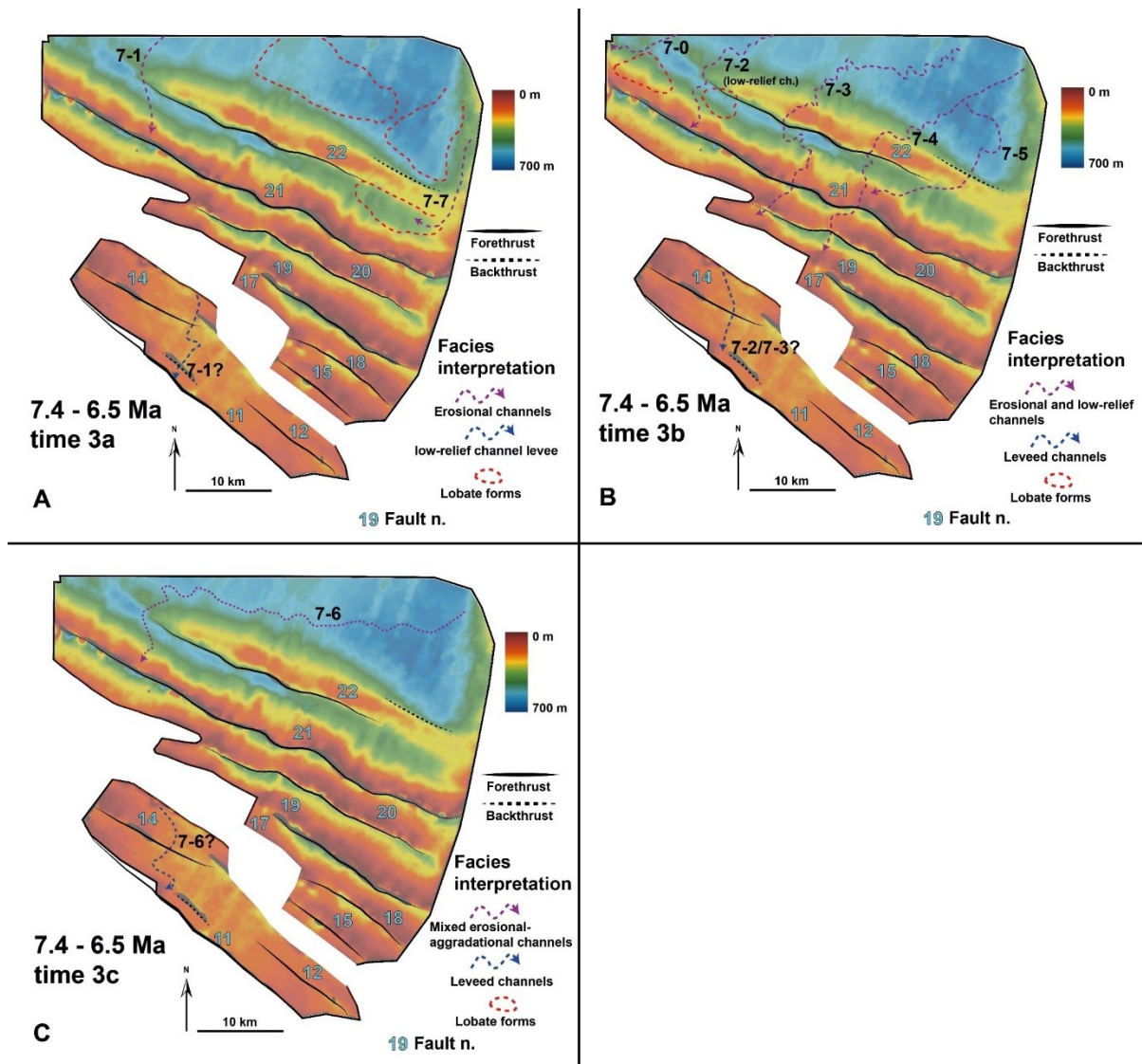
Figure 5-14: A) facies interpretation shown in Figure 5-13b overlaid onto the isopach map of the interval shown in Figure 5-12a. B) facies interpretation shown in Figure 5-13d overlaid onto the isopach map of the interval shown in Figure 5-12a. C) facies interpretation shown in Figure 5-13f overlaid onto the isopach map of the interval shown in Figure 5-12a. The dominant channel architecture is erosional in the inner domain where channel are forced to cut through the crest of growing folds and leveed-aggradational in the outer domain as channel can still exploit lateral tip points.
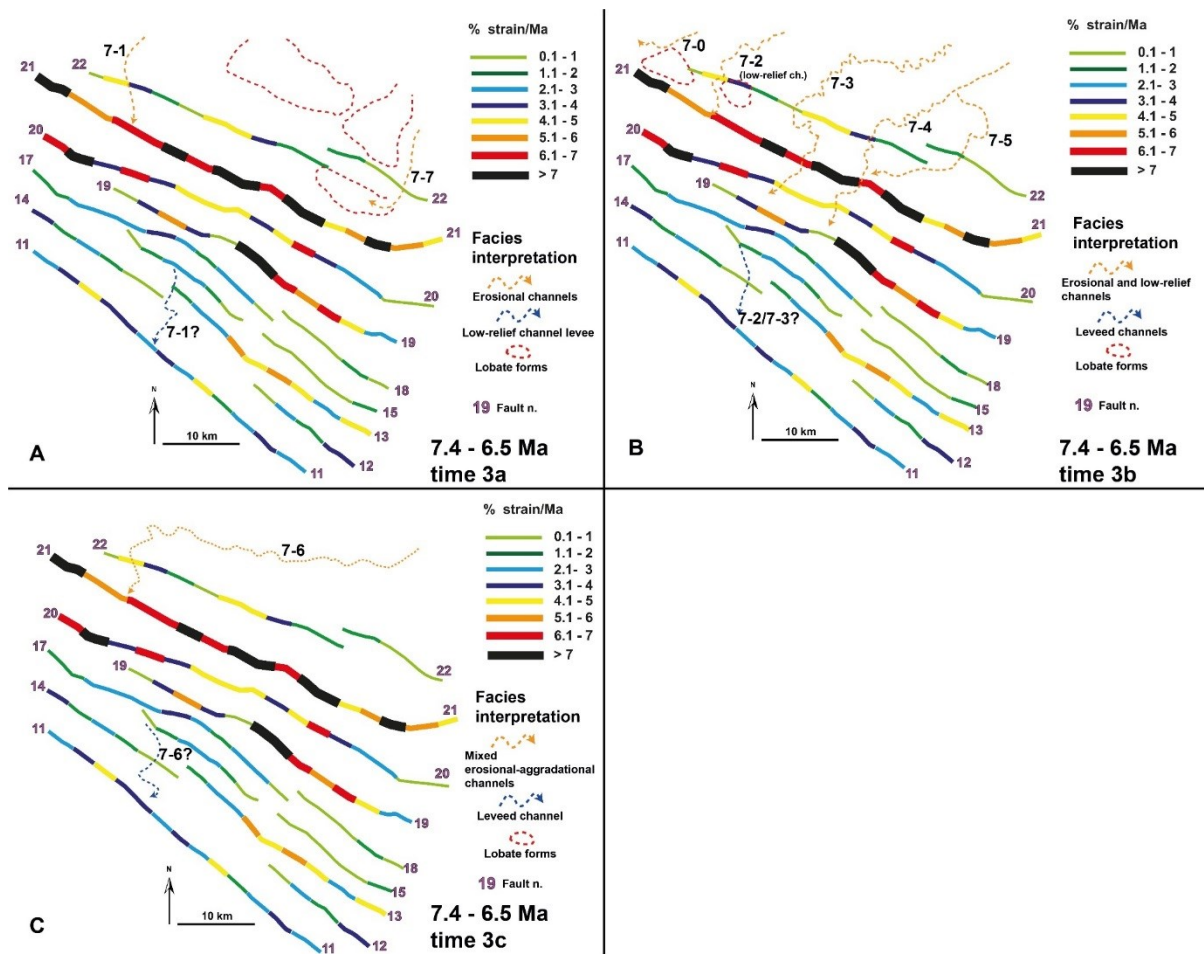
Figure 5-15: A) facies interpretation shown in Figure 5-13b overlaid onto the strain rate map of the interval shown in Figure 5-12c. B) facies interpretation shown in Figure 5-13d overlaid onto the strain rate map of the interval shown in Figure 5-12c. C) facies interpretation shown in Figure 5-13f overlaid onto the strain rate map of the interval shown in Figure 5-12c. The dominant channel architecture is erosional in the inner domain where channel are forced to cut through the crest of growing folds and/or explloit higher strain rates, and leveed-aggradational in the outer domain as channel can still exploit lateral tip points.

5.2.5 Unit 2 (6.5 to 5.5 Ma)

5.2.5.1 Isopach and accumulation rate maps

The isopach map of this interval (Figure 5-16a) shows a similar distribution of sediment thickness to the underlying unit, with the most notable change occurring in area 1. Here a thickness maximum of 400-450 m is present as a north-east to south-west trending depocenter in the centre of the basin which separate two areas of decreased thickness (Figure 5-16a). To the north-west and south-east of the depocenter the thickness decreases to 350 m and 250 m respectively. The minimum of 250 m is on the hangingwall of fault 22, however, it is only present along the southern half of the fold.

As for the underlying unit, in the rest of the inboard domain (areas 1, 2 and 3) the distribution of sediment thickness creates north-west to south-east trending lineaments, where thickness

136

minima (50 m or less) lie in the hangingwall of the fold-thrust structures (Figure 5-16a). Sediment accumulation rates during this interval decrease to an average 0.4-0.5 mm/yr in area 1, with minima of 0.25-0.3 mm/yr along fault 22. Elsewhere, accumulation rates were as low as 0.1-0.2 mm/yr along the strike of the thrust-folds, and 0.2 mm/yr in the centre of area 4 (Figure 5-16b).
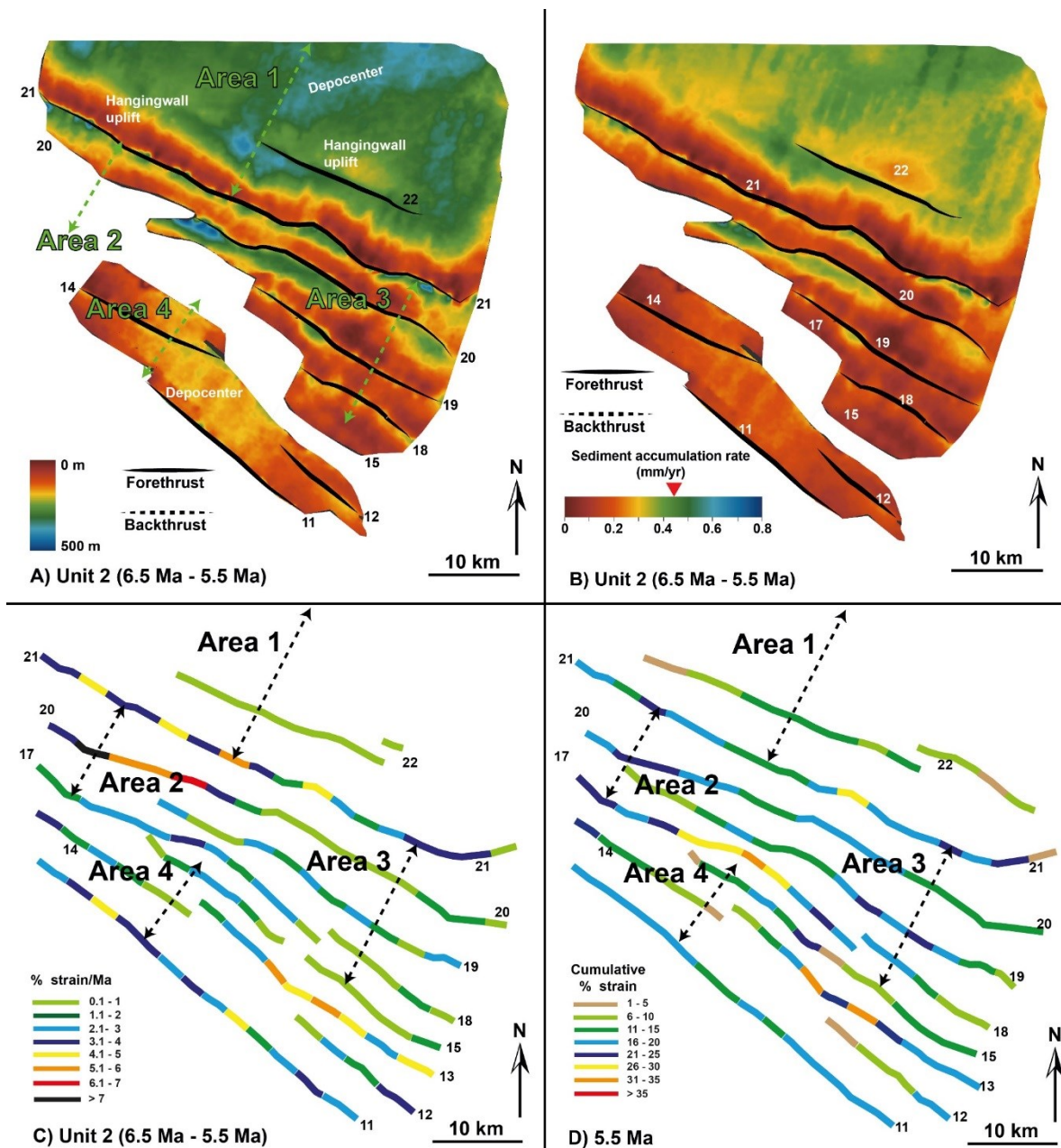
Figure 5-16: Characterization of unit 2. A) Isopach map. B) Sediment accumulation rate map. C) Distribution of strain rates between 6.5 and 5.5 Ma. D) Distribution of cumulative strain at 5.5 Ma.

5.2.5.2   Structural analysis

Unit 2 is bounded by the 6.5 Ma horizon and by the 5.5 Ma horizon at the top. This unit records a period of decreasing strain rates, particularly in the inner domain (Figure 5-16c). At this time, only the central segment of fault 22 was still deforming, but at rates as low as 1%/Ma. Along fault 21, rates decreased to 4 to 5%/Ma on its norther half, and to 2 to 4%/Ma on its southern part. Fault 20 was clearly divided into two parts, where, in the northern half, strain rates remained as high as 6-7%/Ma or more, whereas, in its southern half rates reduced to 1-2%/Ma. Along fault 19, strain rates were consistently between 1-3%/Ma.

As for unit 3, in area 4 strain rates are averaged over the same longer time period (7.4 to 3.7 Ma). By 5.5 Ma, deformation was distributed in a similar pattern to 6.5 Ma (Figure 5-16d). However, along the strike of faults 21, 20 and 19 more segments accumulated up to 25 % of shortening with a maximum of nearly 30% in the centre of fault 21.

5.2.5.3   Seismic facies and structural impact

Three attribute maps within this interval show great variability in the type and architecture of seismic facies. These range from high amplitude sheets and ponded lobes to erosional and mixed erosional-aggradational channels, low relief channel levees, highly aggradational channel levees and mud-dominated sequences (Figure 5-17).

The lowermost interval (Figure 5-17a-b; Figure 5-18a), taken at the 6.5 Ma horizon, shows several mixed erosional-aggradational (6-3) and low relief channel levees (6-1, 6-2, 6-4) sourced from the north and north-east of area 1, which broadly converge towards the centre of fault 21. At this location fault 21 displays the lowest strain rates along its strike (up to 2%/Ma; Figure 5-19a) which also coincides with the location of earlier fault linkage (see section 5.3.2.1). Channels exploit this central zone and avoid the higher strain rates developed to the north-west and sounth-east.

It is also evident that these channels were able to exploit a strain rate of 1%/Ma that was uniformly distributed along fault 22. However, the isopach map (Figure 5-18a) shows a thickness minimum of the crest of fault 22 which could be interpreted as the result on ongoing deformation, liable for the deflection of the channels around it.

Additionally, a high amplitude sheet-like reflection/lobe is found to the north-west of area 1, up dip of zones of greater strain rate developed along fault 21 (Figure 5-19a); this agrees with previous observations that lobes are generally linked to relative higher strain rates.

Almost coevally, another deeply erosional channel complex (channel 6-5; see also Figure 4-4) enters the study area from the east (area 3; Figure 5-17a-b, Figure 5-16a, Figure 5-18a), after bypassing the tip of fault 21. This erosional channel follows a sinuous route through faults 20, 19, 18, 15 and 13 to reach to exit point to the outer domain (area 4) of the fold belt, by exploiting the locations of minimum strain rate along the strike of each fault as well as their relay zones and oversteps (Figure 5-19a). Although the high level of erosion in the core of the fold belt makes it impossible to directly trace this complex across to the outer domain, it likely sourced the leveed channel complex observed in area 4 at the same stratigraphic level (Figure 5-17a-b, Figure 5-18a, Figure 5-19a).

After a period dominated by a muddy sequence (see Figure 4-13), the following interval (Figure 5-17c, d and Figure 5-18b) shows the presence of a sub-circular lobe restricted in the north-west of area 1 against the higher strain rates of fault 21 (Figure 5-19b). Again, this agrees with previous observations on the distribution of lobes.

To the south-east of area 1 another erosional channel (6-10; see Figure 4-4) flows towards the south-west cutting through fault 21 at a location of relative strain rate minimum (Figure 5-19b). The channel then follows a similar route to that of the earlier channel 6-5 towards the outer domain, exploiting locations of low strain rates along faults 20 and 19 and relay zones between faults 18, 17, 15, 13. This channel is probably correlated to the erosional channels found in the centre of area 4 (Figure 5-18b, Figure 5-19b). Notably, this time marks the first occurrence of erosional channels in area 4, the outer domain.

The uppermost interval, along the 5.5 Ma horizon (Figure 5-17e, f and Figure 5-18c), shows the presence of a low-amplitude, meandering channel belt (5-1; see fig Figure 4-12) developed within the north-east to south-west trending thick depocenter in the centre of area 1 (Figure 5-18c). The channel belt can be classified as a low-relief channel levee (see chapter 4). At first, this channel is structurally controlled by fault 22 as it is deflected towards the northern tip of the fault (Figure 5-18c, Figure 5-19c). As the channel approaches fault 21, it is deflected into a trough of local minimum strain rate along its strike (Figure 5-19c), a location that directly overlays the stratigraphically older lobe (Figure 5-19b). This channel could not be traced beyond fault 21. This unit ends with the deposition of a large mass-transport complex (MTD) in the centre of area 1 (over the top of fault 22), compensationally stacked to the south of channel 5-1 (Figure 5-18c; see Figure 4-12). The grooves formed by its basal erosional surface indicate that the MTD is deflected into the area of lowest strain rate in the centre of fault 21 and 20 (Figure 5-19c). The deposition of the MTD cause the complete healing of the relief created by fault 22. The results presented above suggest that channels are always located at

zones of relative lower strain rate with respect to the adjacent fault segments, but were clearly dependent upon the diversions and avulsions that took further up dip. Erosional channels are able to cut through structures with strain rates of 2-4%/Ma, and lobes are located up dip of zones above 4%/Ma.
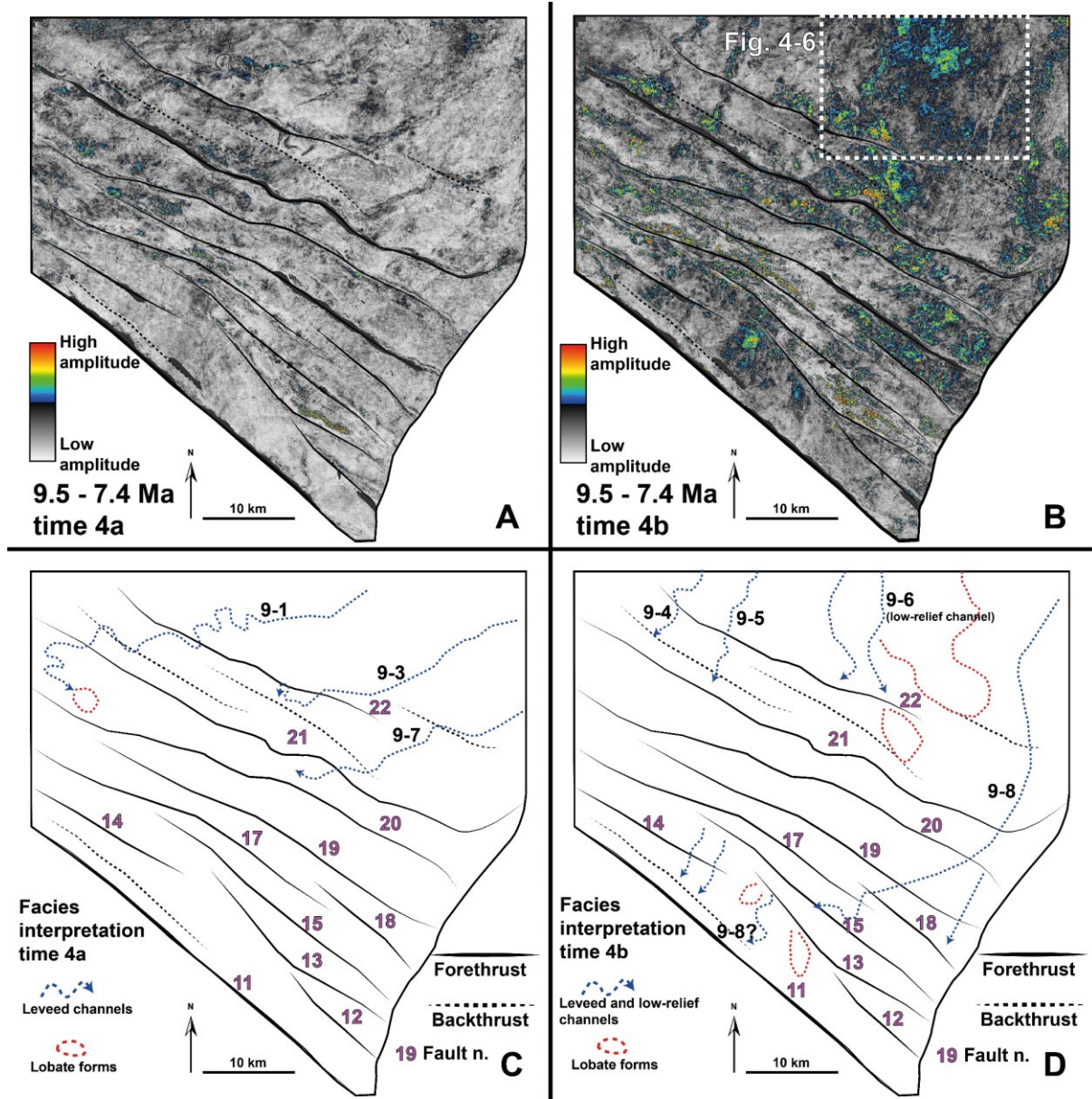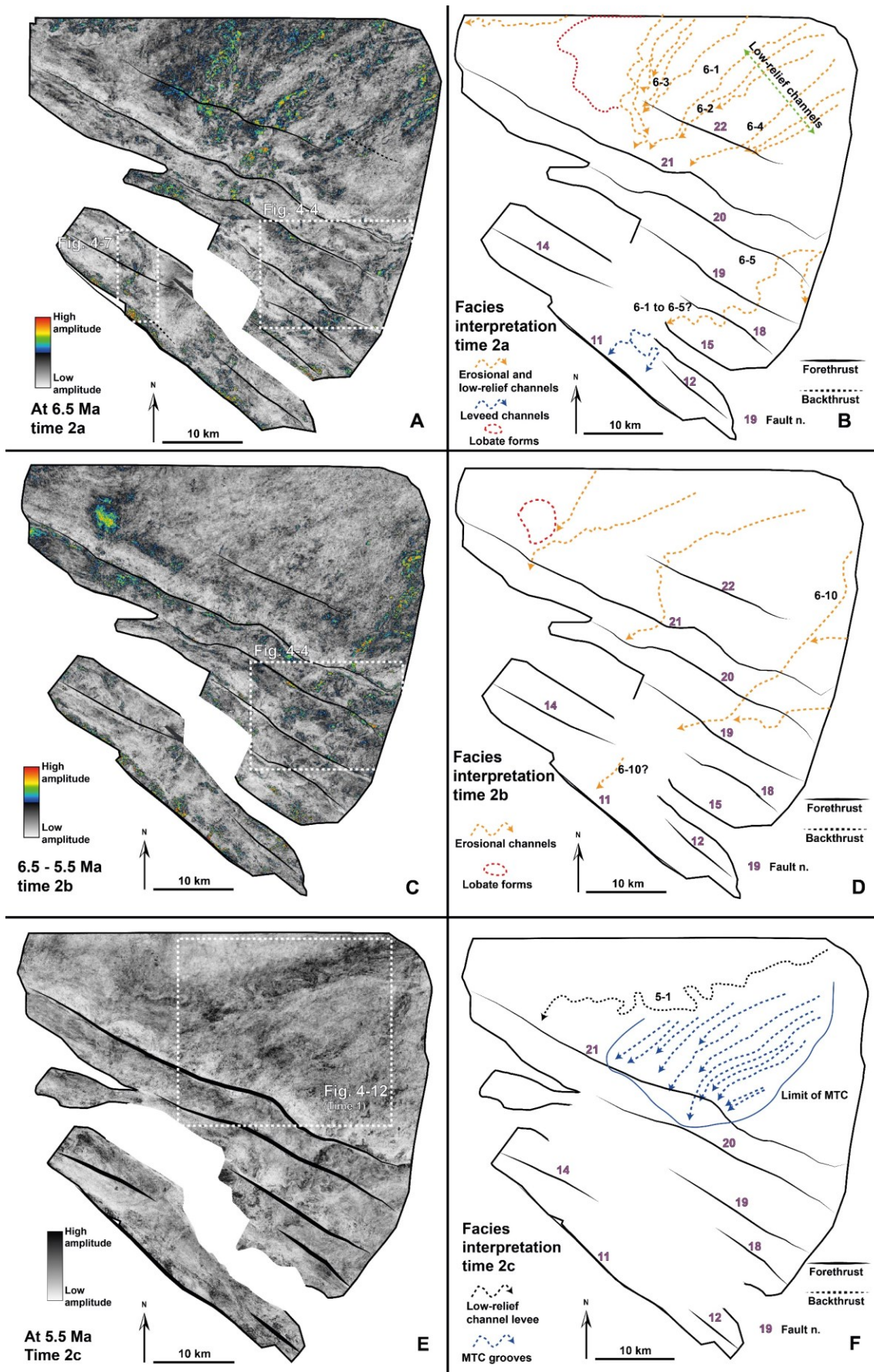
Figure 5-17: - A, C and E are the RMS amplitude extractions from three isoproportional slices within the 6.5 to 5.5 Ma interval. In B, D and F the corresponding interpretation that shows the distribution and type of seismic facies present at each time.
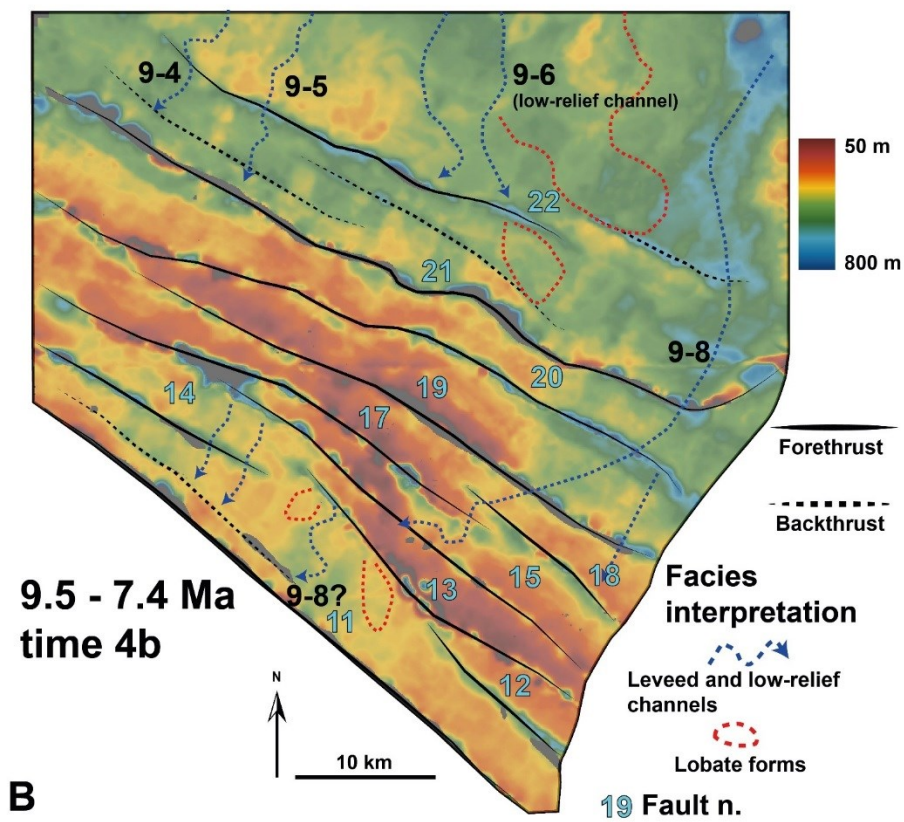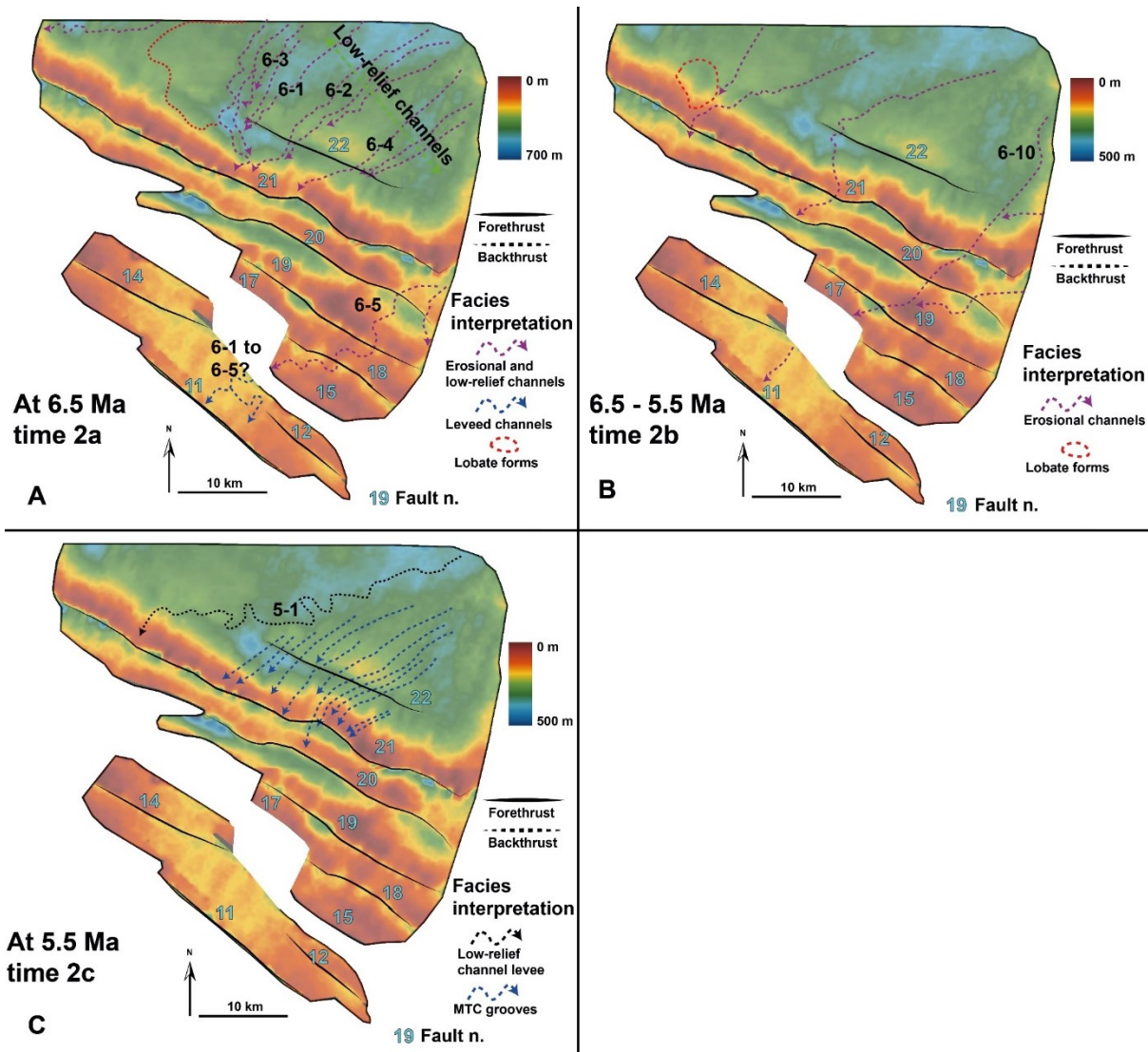
Figure 5-18: A) facies interpretation shown in Figure 5-17b overlaid onto the isopach map of the interval shown in Figure 5-16a. B) facies interpretation shown in Figure 5-17d overlaid onto the isopach map of the interval shown in Figure 5-16a. C) facies interpretation shown in Figure 5-17f overlaid onto the isopach map of the interval shown in Figure 5-16a. In the inner domain the dominant facies is represented by mixed erosional and small-relief channel levees, interbedded with MTDs. In the outer domain channels alter their architecture from leveed-aggradational (in A) to erosional (in B).
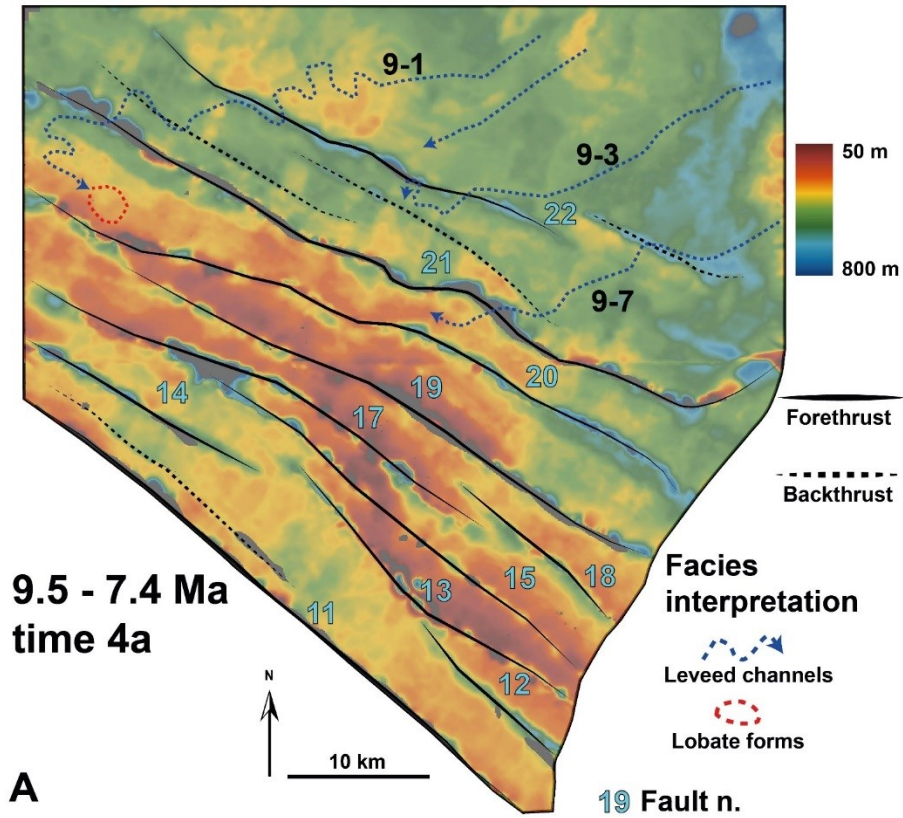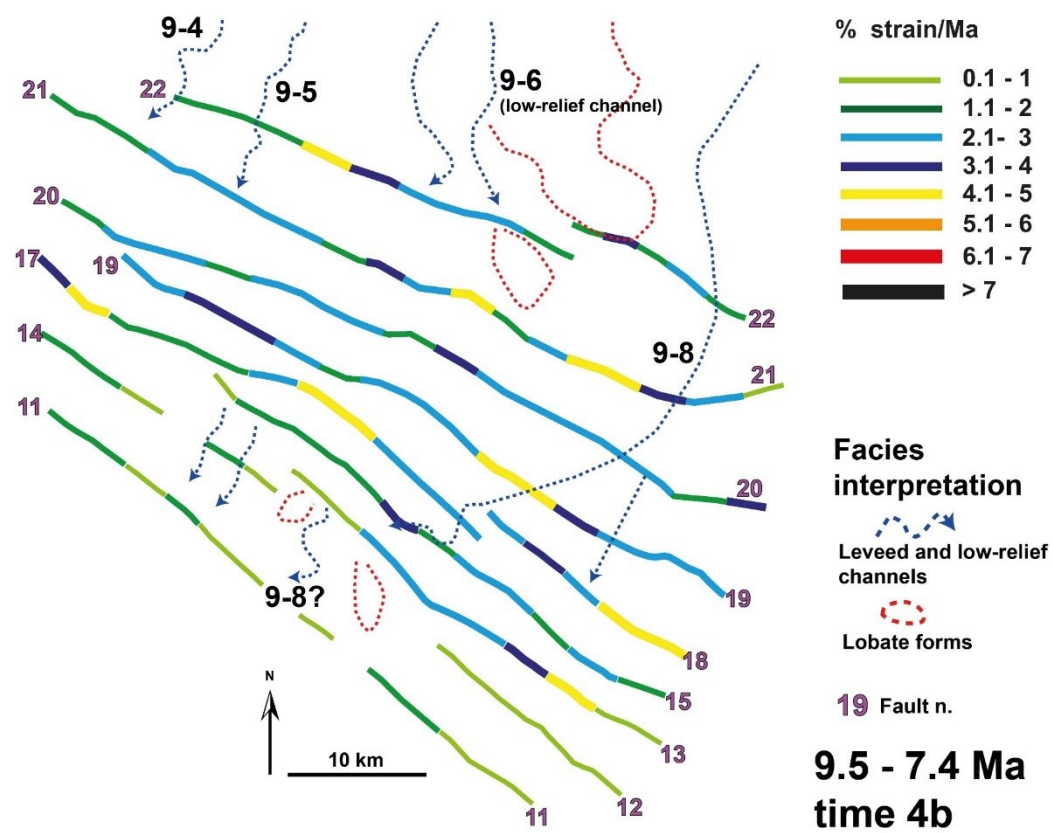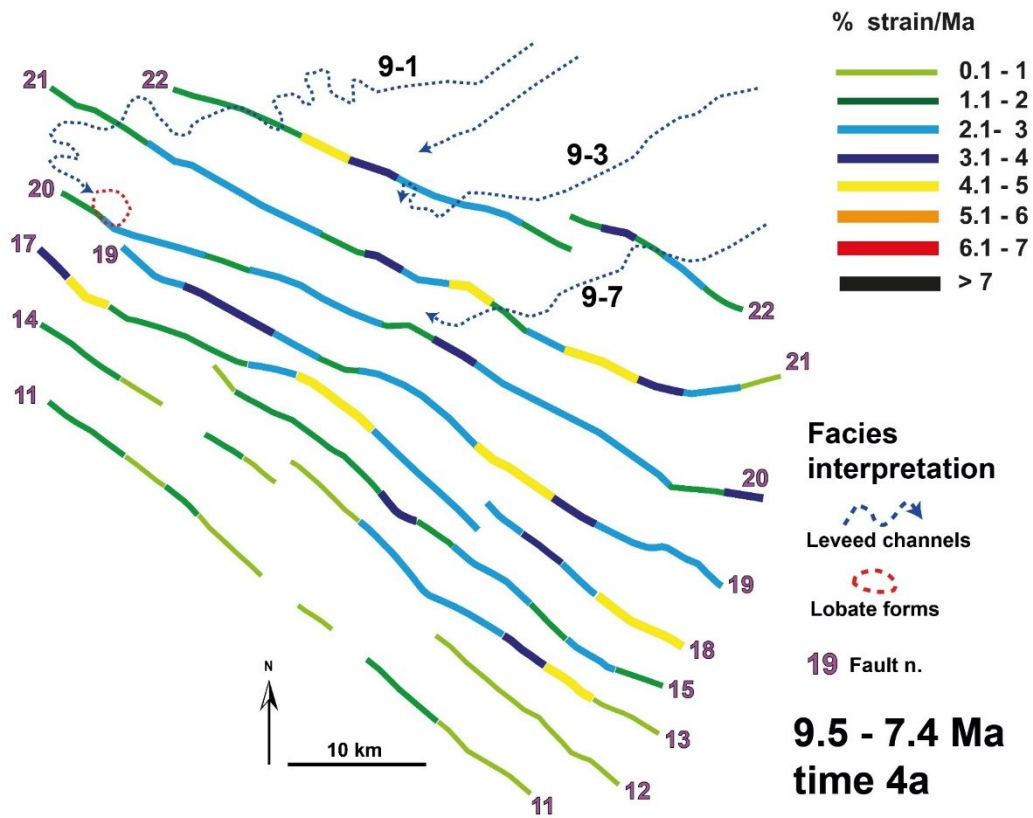
142
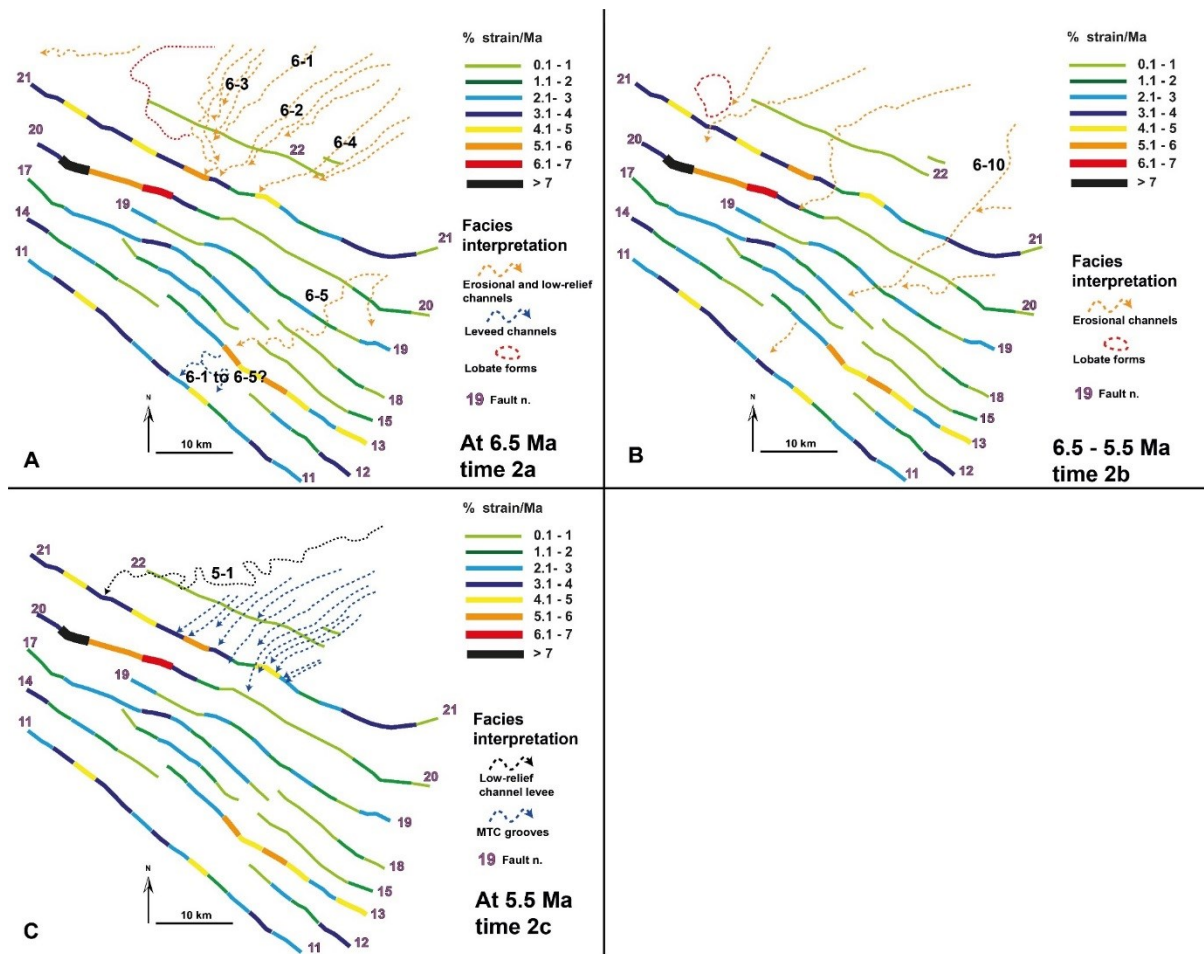
Figure 5-19: A) facies interpretation shown in Figure 5-17b overlaid onto the strain rate map of the interval shown in Figure 5-16c. B) facies interpretation shown in Figure 5-17d overlaid onto the strain rate map of the interval shown in Figure 5-16c. C) facies interpretation shown in Figure 5-17f overlaid onto the strain rate map of the interval shown in Figure 5-16c. In the inner domain the dominant facies is represented by mixed erosional and small-relief channel levees, interbedded with MTDs. In the outer domain channels alter their architecture from leveed-aggradational (in A) to erosional (in B).

5.2.6   Unit 1 (5.5 to 3.7 Ma)

5.2.6.1   Isopach and accumulation rate maps

The isopach map of this interval (Figure 5-20a) shows a clear change in sediment thickness distribution with respect to the underlying unit. In area 1 a large depocenter is present inboard of fault 21 reaching a maximum thickness of 450 m. The depocenter is oriented parallel to the strike of fault 21, and the crest of fault 21 is still an area of minimum thickness (50-100 m). Area 3 has also become a large depocenter up to 450 m thick with the only exception of a thickness minimum (100-150 m) along the southern part of fault 19 (Figure 5-20a). Other thickness minima (50-100 m) are present throughout the core of the fold belt and on the north-western part of fault 20. A third depocenter with a sediment thickness of up to 450 m is present

in the centre of area 4, elongated along the strike of fault 11. The crests of fault 11 and 14 are, in contrast, areas of thickness minima (50-100 m).

Sediment accumulation rates during this interval continued to decrease to values of 0.2-0.25 mm/yr within the depocenters and to less than 0.1 mm/yr along the crests of the thrust-folds (Figure 5-20b).
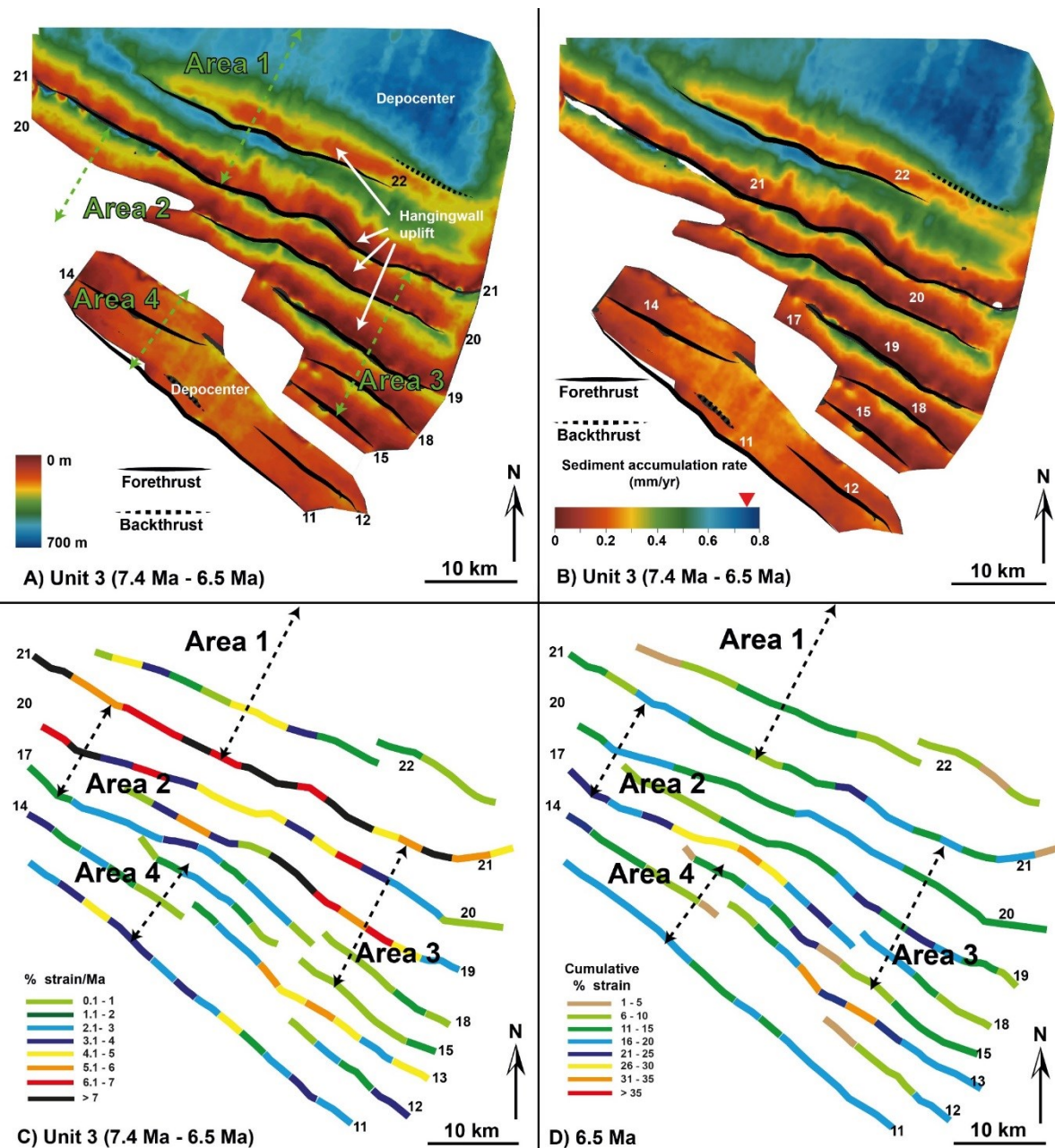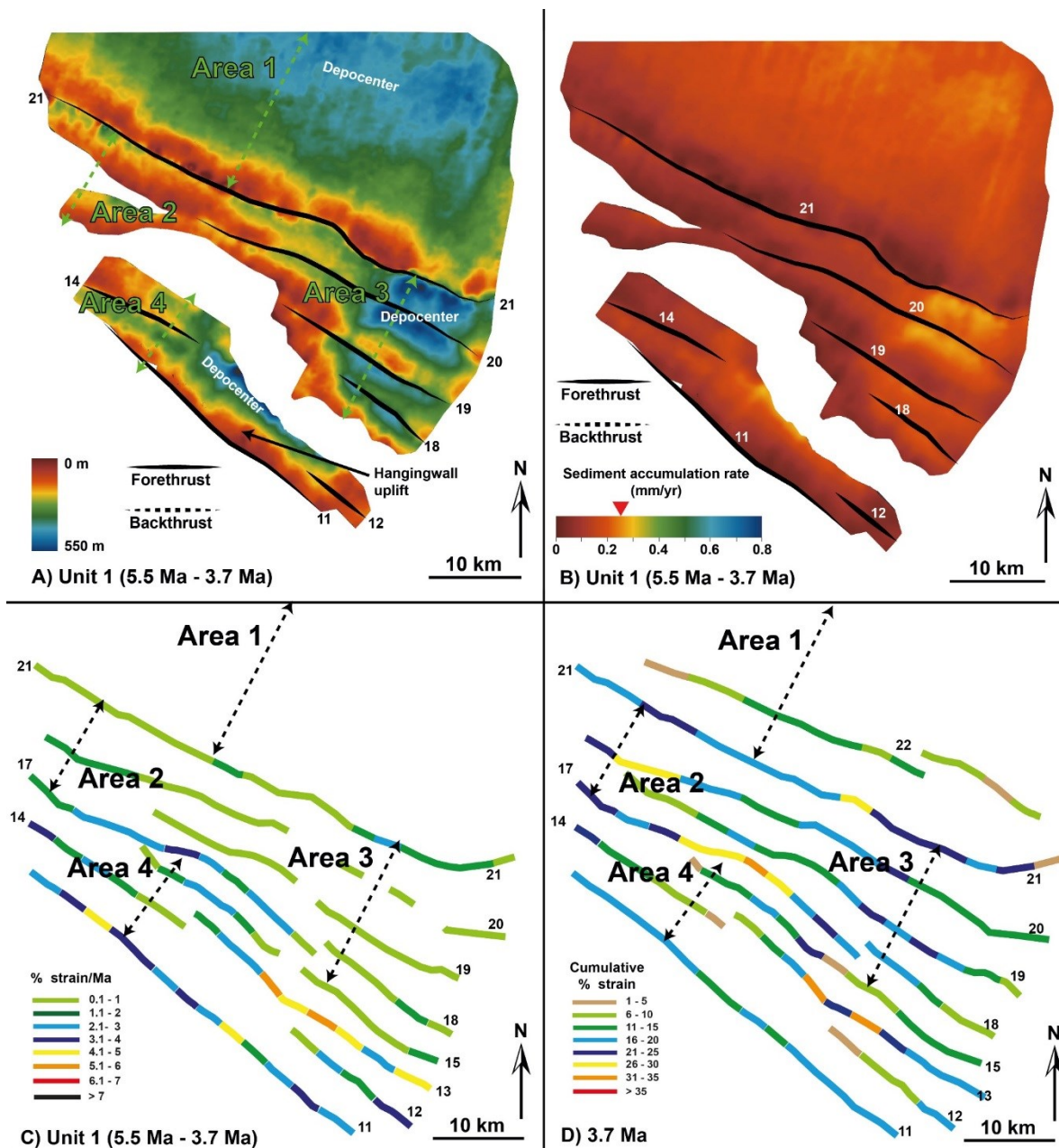

Figure 5-20: Characterization of unit 1. A) Isopach map. B) Sediment accumulation rate map. C) Distribution of strain rates between 5.5 and 3.7 Ma. D) Distribution of cumulative strain at 3.7 Ma.

5.2.6.2 Structural analysis

Unit 1 is bounded by the 5.5 Ma horizon and by the 3.7 Ma horizon at the top. During the deposition of this unit, the deformation front continued to propagate seaward and, as a result, strain rates decreased in the inner domain, while higher strain rates were still present in the outer domain (Figure 5-20c). In particular, fault 22 completely stopped growing and fault 21 slowed down to values of 1%/Ma in the northern half and 2%/Ma in the southern half. Only a few segments along faults 20 and 19 were still active with strain rates of 1%/Ma. In area 4 strain rates are the same as for units 2 and 3 as they are averaged over a longer time period (7.4 to 3.7 Ma). By 3.7 Ma, only faults 21 and 20 had accommodated deformation where, locally, the total strain increased by an additional 5% points (Figure 5-20d).

5.2.6.3 Seismic facies and structural impact

This unit is floored by the mass-transport complex shown in Figure 5-18c and Figure 5-19c. Subsequently, three attribute maps (Figure 5-21a, b, c) show that this interval is dominated, in the inboard domain, by channelized sheets, low-relief channel levees and mass-transport complexes (MTDs), while MTDs and erosional channels are present in the outboard domain (area 4; Figure 5-21d). Evidence of structural control on facies distribution is widely observed. The three RMS amplitude extractions show numerous channelized sheets and low-relief channel levees whose distribution is controlled by both structural interaction with fault 21 and autocyclic processes. There is, in fact, evidence for compensational stacking between the channelized facies and the interbedded MTDs as discussed in chapter 4 (Figure 5-22a; see Figure 4-9 and Figure 4-12). The channelized facies are widespread throughout areas 1 and 3 and flow in a north-east to south-west direction. These facies can be grouped into three main sets, each consisting of 3 to 6 individual channels. The channels cross fault 21 at a number of locations, each marked by small notches or troughs on the isopach map along the strike of the fault (Figure 5-22a). The channels are also seen to diverge upon entering area 1 from the north-east to then converge towards the crossing points along fault 21 (and 19) (Figure 5-22). Upon entering the core of the fold belt (areas 2 and 3), the channelized facies form two main sets that are largely diverted to the north-west and south-east of faults 19, 17, 15, which are responsible for a broad uplifted region at this time (Figure 5-22a).

The continuity of these systems is interrupted in the core of the fold belt due to high level of cumulative deformation and erosion. In the outer domain, a series of erosional channels (Figure 5-22a) are present in the centre of area 4 following the location of the depocenter.

The overlay of the channels location with the interval strain rate map (Figure 5-22b) makes clear that the channelized sheets were largely able to keep pace with strain rates up to 1-2%/Ma, as documented along the strike of fault 21. Additionally, I suggest that widespread low strain rates across the inner domain (Figure 5-22b) could be associated with (or favour) a wider spatial distribution of the channels. This was also observed for both units 5 and 6.

As observed for previous intervals, Figure 5-22b shows that channels continued to be located at fault crossing points with lower strain rates, relatively to the surrounding segments along the strike of the same fault. For example, along the southern part of fault 20, channels were deflected by segments deforming at only 1%/Ma thus passing through the inactive segments of the fault (Figure 5-22b).

Figure 5-22b also suggests that strain rates above 2%/Ma, as those developed in the core of the fold belt and in the outer domain, restricted and constrained the spatial distribution of the channelized facies. This was consistently observed since unit 4.

In the outer domain (area 4), however, both the channel architecture and the strain rates are different. Erosional channels are observed to exploit areas with strain rates up to 3-4%/Ma in the centre of fault 11, which still represents the region deforming at the lowest rates along the strike of the fault.
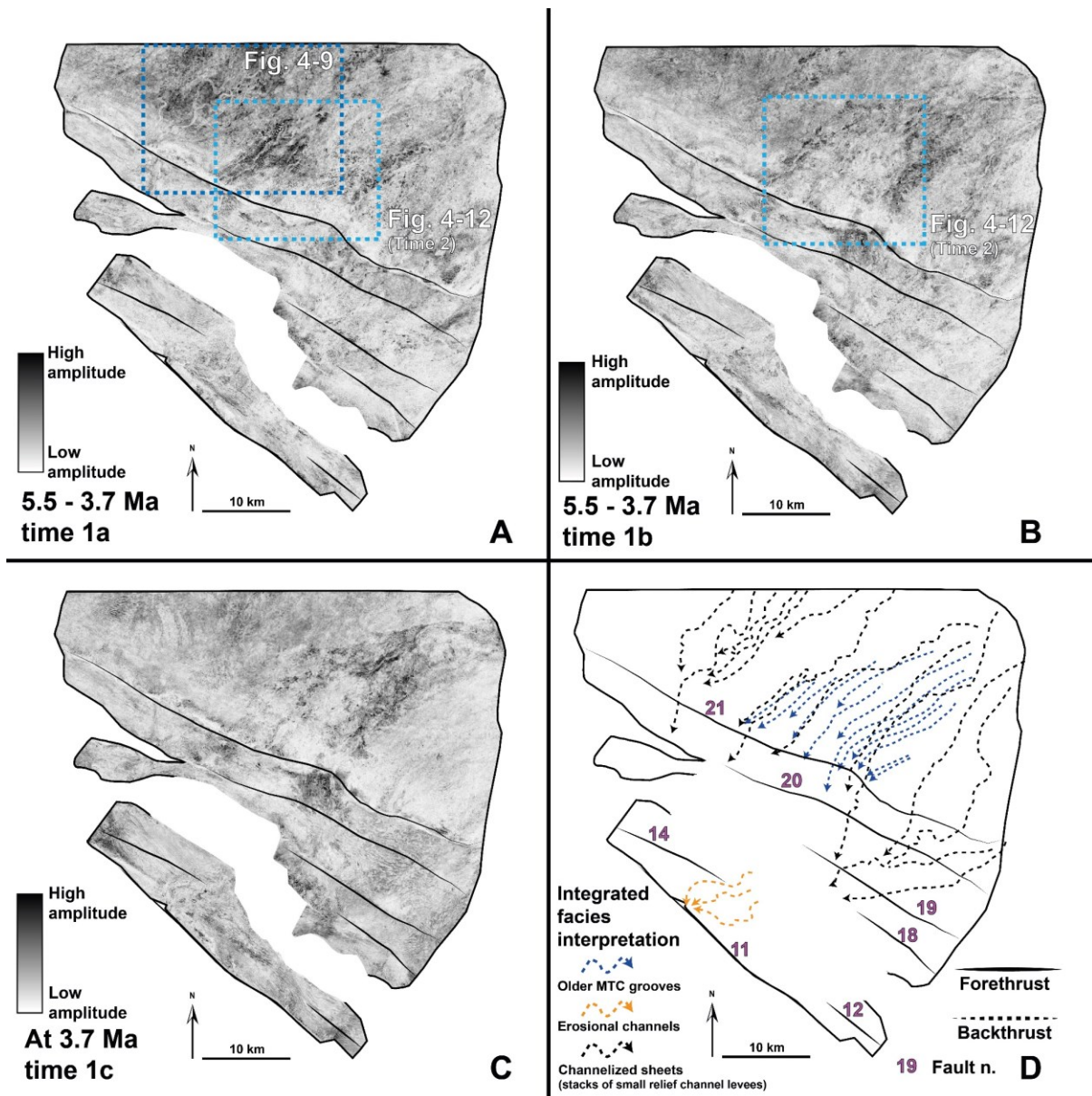
Figure 5-21: A, B and C are the RMS amplitude extractions from three isoproportional slices within the 5.5 to 3.7 Ma interval. In D the integrated interpretation that shows the distribution and type of seismic facies present at this time.
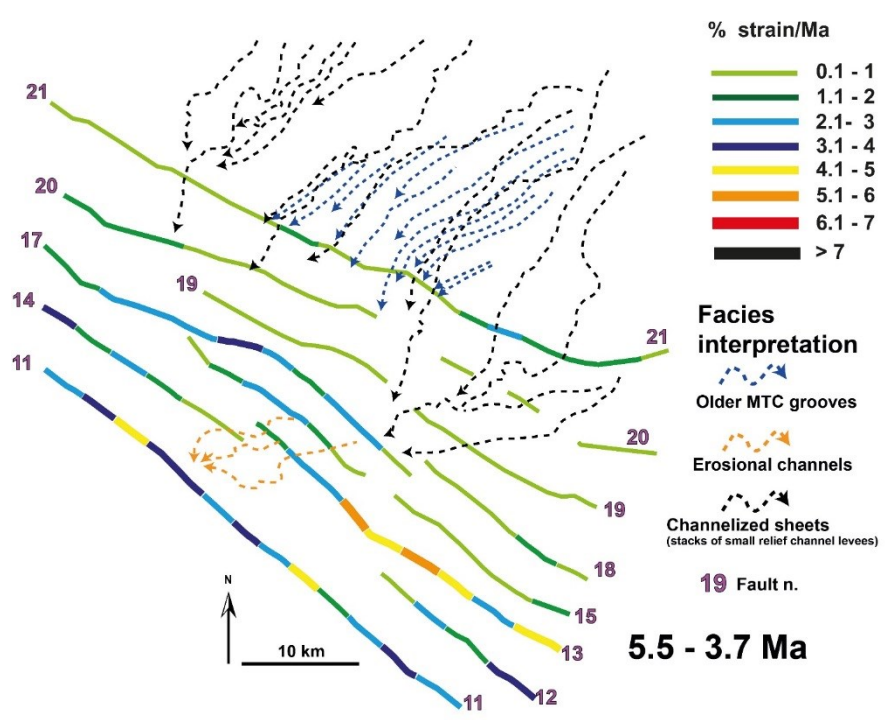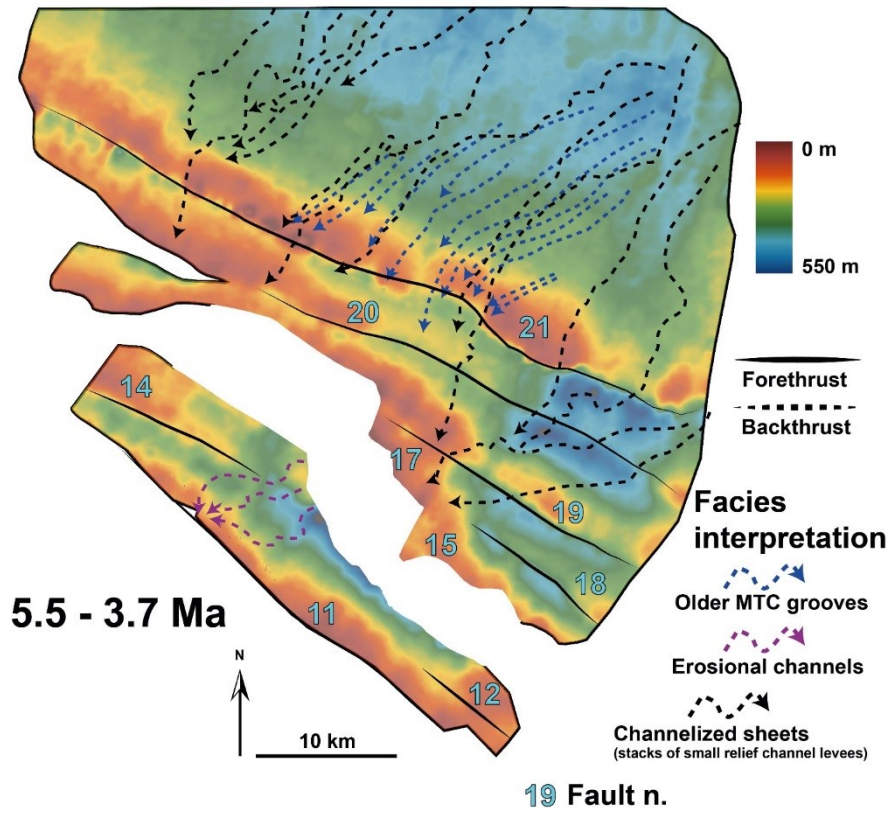
Figure 5-22: A) facies interpretation shown in Figure 5-21d overlaid onto the isopach map of the interval shown in Figure 5-20a. B) facies interpretation shown in Figure 5-21d overlaid onto the strain rate map of the interval shown in Figure 5-20c. the inner domain is dominated by small-relief channel levees and channelized sheets, interbedded with MTDs. In the outer domain channel architecture is erosional.

5.3 Discussion and summary

5.3.1 Evolution of basin configuration

The results presented in this chapter, integrated with the structural analysis conducted in chapter 3, confirm a complex, multi-phase evolution of the lower slope. While the evolution of fold and thrust belts, and more generally thrust-faults, is often tracked by the identification of sedimentary growth packages (Suppe et al., 1992), the complete growth history of such belts, including their evolving rates of deformation and the 3D interaction and linkage between fault segments, is not often studied in detail (Bergen and Shaw, 2010; Jolly et al., 2016; Totake et al., 2018; Don et al., 2019). As a result, relatively simple tectono-stratigraphic models whereby 1) a thick and tabular sequence of pre-kinematic strata is clearly separated from 2) a syn-kinematic sequence, showing abrupt thickness changes from fold limbs to crests, which may or may not be capped by 3) a final tabular sequence of post-kinematic strata are commonly invoked (Suppe et al., 1992; Shaw et al., 2004; Cartwright et al., 2012; Hughes and Shaw, 2014 and 2015; Eichelberger et al., 2015; Don et al., 2019). However, the results presented here show that an understanding of the growth and interaction of the fault array in time and space significantly influenced sedimentation throughout the study area. The data presented here show that both the "pre-kinematic" and syn-kinematic sequences can be divided, at least, into six units (U1 to U6) which describe specific evolutionary stages, each closely related to the rates of deformation occurring along and across the strike of the thrust-folds and to the degree of linkage and interactions between faults.

Despite the difficulties in mapping the deeper sequences (see section 5.1.1), it's clear that U6 and U5 (the oldest units in this study) were deposited during times of active deformation on the lower slope and do not form part of a pre-kinematic sequence. This is contrary to models that only use of the occurrence of visible growth packages to identify the start of deformation (Krueger and Grant, 2011). The evidence for this mostly derives from the structural analysis (chapter 3) but is also confirmed by RMS amplitude extractions showing sedimentary systems interacting with slowly-deforming fault segments (Figure 5-6 and Figure 5-8). Indeed, the complexity originates from the fact that faults (and folds), at this time, only existed as disconnected segments, shortening at low strain rates (up to 1-2%/Ma; 140 m/Ma). We hypothesise that this likely resulted in the creation of very subtle topography on the seabed, enough to have an impact on the distribution of sedimentary systems, but not to create large, visible growth sequences. The small amounts of deformation occurring at these times (<500 m

of cumulative shortening on individual structures) only caused subtle thickness changes from fold limb to crest in the order of 50-100 m.

In the time period between 9.5 and 7.4 Ma (U4), increased regional strain rates (locally up to 335 m/Ma; 5%/Ma) impacted the inner domain and accelerated the development of the thrust-folds in this region. In particular, linkage and imbrication of the thrusts in the core of the fold belt facilitated strain accommodation and resulted in a clear uplift of the region between thrusts 20 and 13 (Figure 5-8a). This uplift produced thickness changes by up to 200 m from the limb to the crest of folds. However, large portions of areas 1, 3 and 4, experienced less deformation and formed areas of lower topography around the uplifted core of the fold belt (Figure 5-8a).

In the time period between 7.4 and 6.5 Ma (U3) the lower slope region underwent the highest deformation rates (locally > 7%/Ma; >480 m/Ma). It is during this time that all the faults in the study area propagated laterally and fully linked along and across strike through the underlying detachment (chapter 3), thus reaching the final strike-length observed at present (Figure 5-12a). As a result, the basin configuration drastically changed as the inner domain became segmented in a series of piggy-back basins bounded by eight sub-parallel thrusts, trending from north-west to south-east. At this time the thrusts reached the maximum topographic expression, creating strike-oriented ridges where thickness changed up to 400 m from fold limb to crest over short distances (70 m/km). Variations in thickness along the crest of the thrust-folds coincide with the locations of earlier sites of segment linkage. This is firstly interpreted from the observation that, in many instances, channels crossed faults exploiting small notches along strike where a subtle thickness increase occurred (Figure 5-22a.; further discussed in section 5.3.2.1). While deformation was at its peak in the inner domain, faults in the outer domain had not reached yet the maximum topographic expression. It is, therefore, evident that deformation in the outer domain was delayed with respect to the inner domain, likely in response to the transient propagation of the deformation front as discussed in chapter 3.

While units 6 to 3 recorded the start of the deformation and its gradual increase that culminated with the 7.4-6.5 Ma interval, the two subsequent units (U2 and U1) record the start of decreasing rates of deformation and the progressive burial of the thrust-folds in the inner domain (Figure 5-18a, Figure 5-20a). As the deformation front continued to propagate basinward along with a regional decrease in strain rates, deformation concentrated on fewer, more distant and longer-lived structures (see chapter 3). In particular, the large basin inboard of fault 21 (area 1) changed configuration as strain rates decreased on fault 22 and the fold was gradually buried by sediments (6.5-5.5 Ma interval). By 3.7 Ma fault 22 had completely lost topographic expression and area 1 became a broad basin elongated along the strike of fault 21

that was shortening at rates up to 150m/Ma (1-2%/Ma; Figure 5-20). The isopach map of this interval shows that the rate of thickness change from the centre of area 1 to the crest of fault 21 is gradual (18 m/km), suggesting conditions of moderate relief which could have caused shallow ponding of sediments. Similarly, faults in area 3 (20 to 15) slowed down to strain rates of 1%/Ma (<100 m/Ma) and were gradually buried by sediments until they underwent a complete loss of topographic expression. This resulted in the development of another depocenter, only interrupted by some relief occurring on fault 19 (Figure 5-20a).

While the thrust-folds in the inner domain underwent substantial burial, it is in the intervals between 6.5 and 3.7 Ma that faults in the outer domain continued to grow at higher strain rates, reaching the maximum topographic expression in the 5.5 to 3.7 Ma interval (Figure 5-20). This is reflected in the isopach map that shows the formation of a ridge of consistent low thickness along fault 11. This suggests that, by this time, fault 11 behaved as a longer, fully linked structure. Nevertheless, fault 11 shows a local increase in hanging wall thickness in its centre that, as discussed above (and section 5.3.2.1), indicate the presence of inherited strain deficit at the location of earlier segment linkage. These observations confirm the diachronous structural development between the inner and outer domains in response to the progressive basinward migration of the deformation front. In absolute terms, however, the degree of deformation in the outer domain was never as high as that experienced by the inner domain, which indicate that regional strain rates were substantially lower by the time the outer domain was affected by the deformation front.

5.3.2   Distribution and architecture of deep-water facies

In chapter 4 the vertical evolution and change in seismic facies was originally presented, and I suggested that the observed change in architecture was driven (fully or partly) by tectonic processes. This interpretation derived from the observation that the occurrence and change between different seismic facies coincided with the timings of the major thrusting events in the area (Figure 4-16). It was also shown that the change between seismic facies was diachronous between the 4 areas as it followed the basinward propagation of the deformation front (discussed in chapter 3).

In support of this interpretation, in this chapter multiple RMS amplitude maps extracted from each interval (U1 to U6) allow a reconstruction of how sediment routing across the fold-thrust belt changed through time in response to the evolving basin configuration, by mapping the distribution and the type of the deep-water facies. The interpreted palaeogeographic maps have

been overlaid onto the strain and isopach maps of the relative units to provide a forensic understanding of the coupling between structural growth and sedimentation in this region. The results of this analysis are summarized in Figure 5-23.

The initial two stratigraphic intervals (U6 - 15 to 12.8 Ma; U5 - 12.8 to 9.5 Ma) are dominated by linear channels and leveed-channels and, to a minor extent, lobate forms either unconfined or ponded, and crevasse splays (Figure 5-23a). Evidence for structural impact is discussed in sections 5.2.1.3 and 5.2.2.3. Importantly, the channels are evenly distributed across the lower slope as they interact with subtle topography created by numerous incipient, highly segmented thrusts. These thrust segments deform at strain rates of 1 to 2 %/Ma which appears enough to deflect the channels towards the inactive zones along their strike. Leveed channels continue to be the dominant architectural style through to unit 4 (9.5 to 7.4 Ma), however, at this time channels interact with fault segments that have propagated laterally and linked (in the inner domain), forming continuous thrusts that deform at faster strain rates along most of their strike length (up to 5%/Ma). This results in the channels becoming more spatially restricted, away from the faster growing folds, and locally larger in dimensions (Figure 5-23b). I suggest that this is a result of the fact that channels are forced to exploit the same pathways for long periods of time, resulting in the stacking and aggradation of multiple flows (highly aggradational channel levee; Figure 4-3). Linear and leveed channels are, therefore, characteristic of the initial stages of deformation when the thrusts in the lower slope had accumulated no more than one third of the total shortening (10-15 %), strain rates were low, and folds only created subtle topography. At this time, the segmentation of the thrusts allows the channels to avoid structural culminations and exploit undeformed areas between fault segments (Figure 5-23a, b).

Soon after 7.4 Ma, until 6.5 Ma, the inner domain undergoes the highest recorded deformation rates (up to 7%/Ma and more) that cause a major change in the basin geometry and folds achieve their maximum topographic expression, as discussed in section 5.2.4.1.At this time, while the distribution of the channels is continuously dictated and restricted by the location of strain deficits and relative lower stain rates along the strike of faults, the sedimentary systems are occasionally forced (by the up dip diversions) to exploit the structural culminations (as seen on isopach maps) and/or zones of absolute higher strain rates, and alter their architecture into more erosional forms to keep pace with the relief created. In fact, the amount of incision reflects the topography created at those locations which results from the contribution of both the cumulative strain and the strain rate (Figure 5-23c; see chapter 7 for further detail).
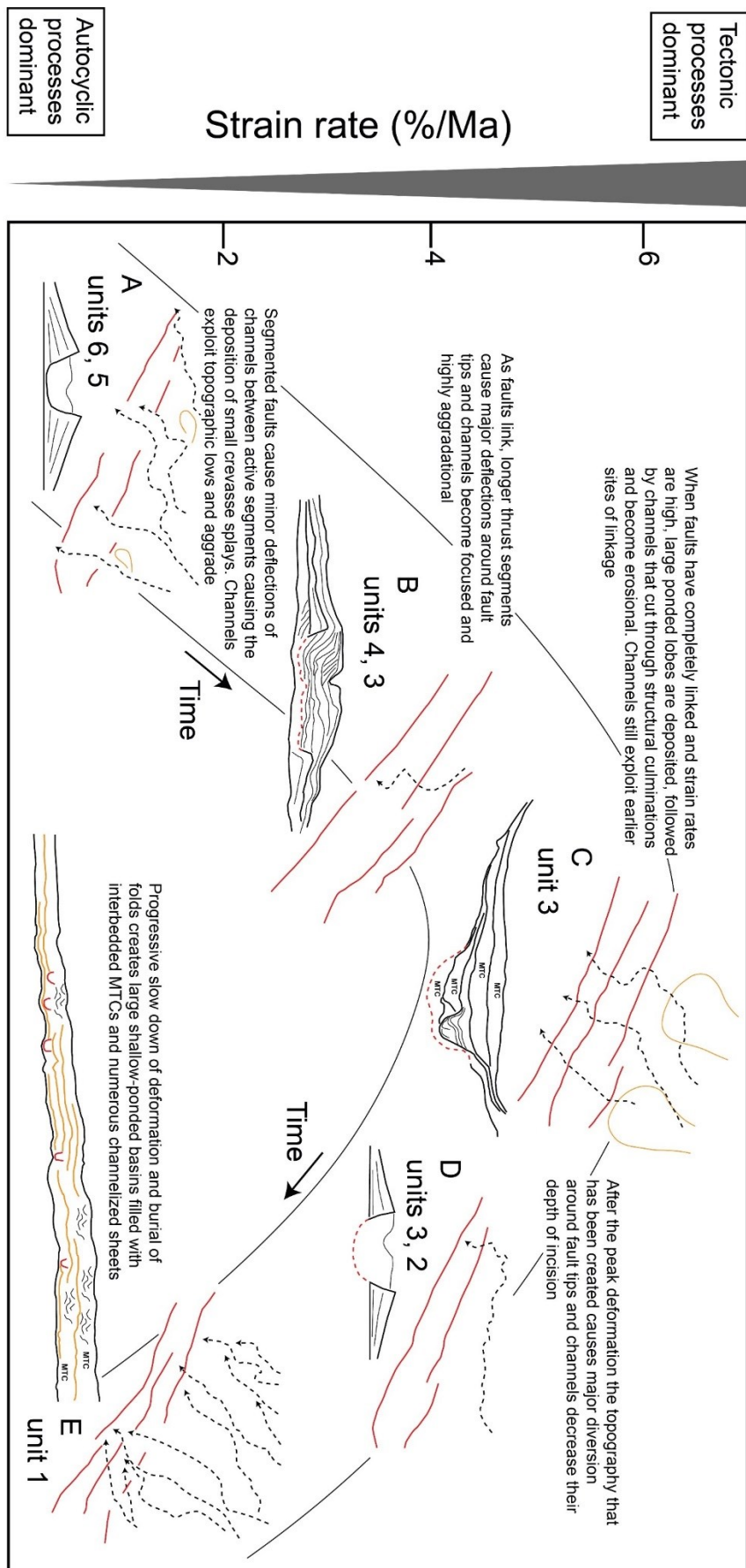
Figure 5-23: Summary diagram of the main architectural styles and facies distribution in response to variable strain rates, degree of fault linkage, cumulative strain, and likely resulting seabed topography.

153

This conclusion agrees with the observation that channel 7-6 (Figure 4-2) has a mixed erosional-aggradational architecture as it is able to exploit the lateral tip point of fault 22, avoiding its crest (Figure 5-23d).

Therefore, erosional channels are characteristic of strain rates in excess of 3%/Ma and high degree of fault linkage when the lower slope is highly segmented into discrete piggy-back basins, folds have high topographic expression and channels cannot exploit lateral tips (Figure 5-23c, d).

Additionally, while the deformation front reached the outer domain after 7.4 Ma, this region was significantly less deformed than the inner domain and thrusts 12 and 14 tip out in the centre, such that a depocenter formed in area 4 in front of the core of the fold belt (Figure 5-12a and Figure 5-16a). Upon exiting the inner domain, sedimentary systems were deflected around the lateral tip points of fault 14 and 13 into this depocenter in the form of highly aggradational channel levee complexes (Figure 5-14c, Figure 5-18a and Figure 4-3). This is again in response to the fact that channels are forced to exploit the same pathways for long periods of time, resulting in the stacking and aggradation of multiple flows (Figure 5-23b). The presence of these large aggradational complexes is in agreement with the conclusion that architectural styles change depending on where, along the strike, submarine channels cross a thrust-fold (e.g. crest vs lateral tip point). Therefore, the degree of fault linkage, both and along and across strike, directly impact the ability or inability of channels to exploit lateral tip points. These results also highlight that different architectures can be simultaneously present across the lower slope, because of different amount of deformation ongoing between sub-basins.

In the interval between 6.5 and 3.7 Ma strain rates in the inner domain progressively decreased to background values of 1-2%/Ma and eventually resulted in the development of large "shallow-ponded" basins in areas 1 and 3 (5.5 to 3.7 Ma; Figure 5-23e). The dominant seismic facies within the fill of these basins are channelized sheets interbedded with MTDs. The wider spatial distribution of the channels reaffirms that, for strain rates of 1-2%/Ma, sedimentary systems can be present throughout the basin, as it was observed for the systems in the 15-9.5 Ma intervals. It is additionally noted that for strain rates in excess of 2-3%/Ma, in the core of the fold belt, the channels are deflected and restricted to the side of it, as observed for the 9.5 to 7.4 Ma interval. Nevertheless, for similar strain rates as those in the 15-9.5 Ma interval, the depositional style is different (e.g. channelized sheets vs leveed-channels). This is likely the result of a different basin geometry (compare Figure 5-2a with Figure 5-20a) where

channelized sheets are deposited in response to a pre-existing topography that is almost, but not completely healed and, therefore, still able to confine the incoming flows (Figure 5-23e). In the outer domain, however, faults had fully linked and continued to grow at higher strain rates (up to 5%/Ma on fault 11), such that area 4 reached its maximum topographic expression. Within this structural setting erosional channels were the dominant architecture, highly restricted in the centre of area 4 and fault 11 (Figure 5-22). These observations demonstrate that for strain rates in excess 2-3%/Ma channels alter their architecture into erosional forms as well as being spatially restricted. It also confirmed that contrasting depositional styles may exist coevally across the lower slope. In conclusion, during the development of a deep-water fold and thrust belt, the progressive basinward migration of the deformation front inevitably results in the simultaneous occurrence of different seismic facies from proximal to distal locations.

5.3.2.1 Structural inheritance on the distribution of deep-water systems

The results presented above have demonstrated the importance of reconstructing how the interval strain rates changed across and along the strike of structures. However, while it is certain that submarine channels continuously exploited the locations of relative/local strain rate minima along each thrust-fold (during each period), their spatial distribution was also controlled by the location of earlier sites of fault linkage. This is shown in Figure 5-24 where the distribution of the sedimentary systems at various intervals is overlaid onto the cumulative strain map at 15 Ma. There it can be observed that the locations where the slope channels crossed the fault array coincide with the zones of strain deficits and linkage that existed between active fault segments when the fold belt had just started to develop. This proves that even 10-11 Myr after the start of deformation and nearly 3.5 km of deposited syn-kinematic sediments, the earliest structural framework, consisting of a distribution of sparse individual segments (separated by tectonically inactive zones), imparted a strong footprint on all the subsequent locations where channels crossed the structures, throughout the entire growth history of the fold belt. Effectively, even when fold-thrust structures appear to be fully covered by sediments they still control how sedimentary systems are distributed. This likely results from the fact that the locations of early linkage are later preserved as persistent zones of strain deficit and low cumulative strain in the strain-distance plots (chapter 3) and the sedimentation is never able to completely blanket them. The specific distribution of sedimentary systems within a unit is then controlled by the interval strain rates of that unit and, lastly, by autocyclic processes when the rates of sedimentation largely outpace those of deformation.
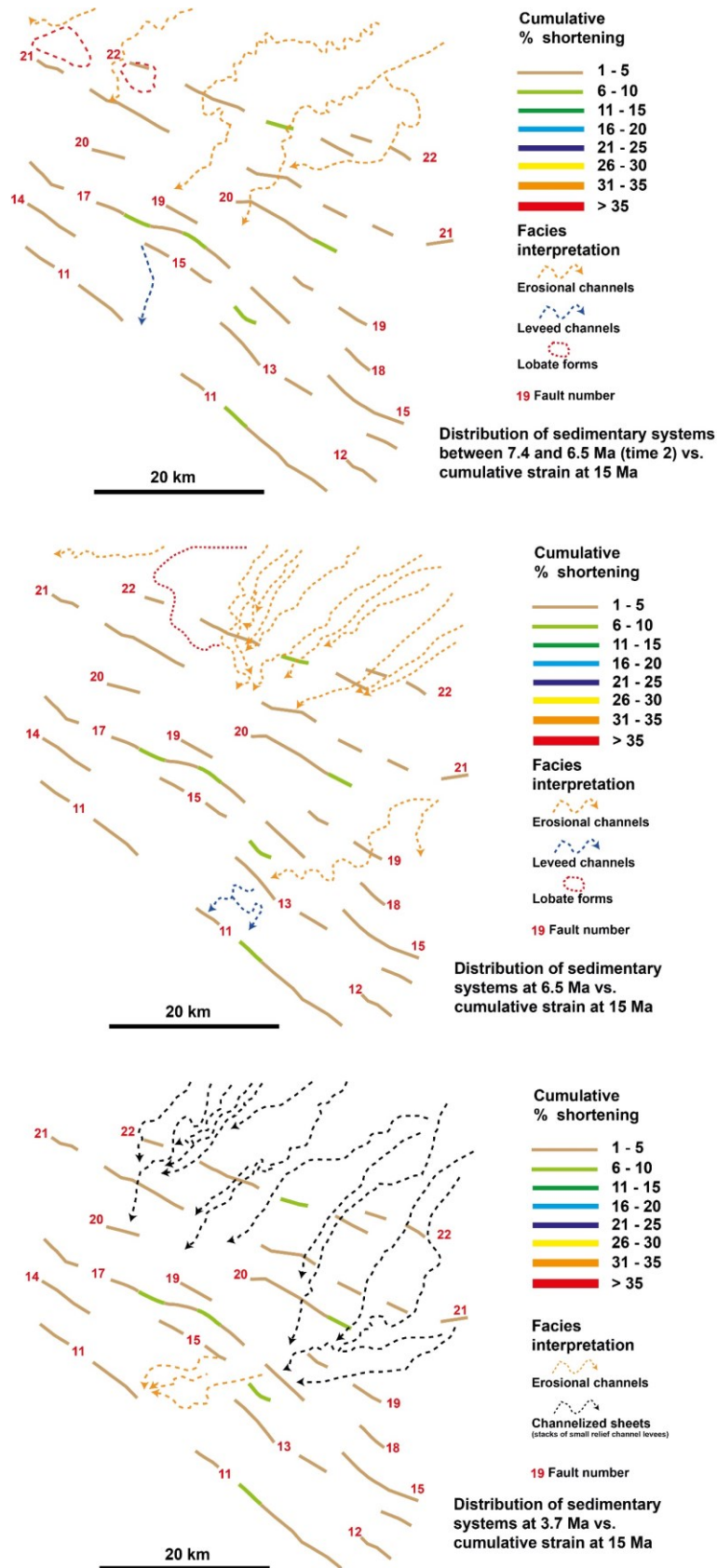
Figure 5-24: Distribution of sedimentary systems plotted against the cumulative strain map at the start of deformation (15 Ma). It can be noted that slope channels always crossed faults in correspondence of earlier sites of linkage between active fault segments.

5.3.3 Link between sediment supply and deformation

The results presented in this chapter suggest a link between changing strain rates over time and sediment supply. It is known that the amount of deformation on the toe-thrusts of gravity-driven systems compensate the extension occurring on the shelf and upper slope, which is, in turn, driven by the sediment supply to the delta top (Rowan et al 2004). Because this study does not address how the sediment provenance and routing changed over time from the shelf to the deep-water, it is not possible to demonstrate that the sediments accumulated on the lower slope, in absolute terms, equal the sediments delivered from the delta top. Nonetheless, a change in sediment accumulation rate (that we observe; Figure 5-1) on the lower slope must reflect, at least partially, a signal of changing sediment supply from the delta top to the lower slope and, therefore, is representative of changing supply rates to the delta top. However, here we are mostly concerned with the relative variations in accumulation rates, rather than the absolute magnitude. In fact, although the isopach maps presented here have not been corrected for compaction (see section 5.1.2), when divided by the time, they indicate a pattern of increasing-decreasing accumulation rates, which is still observed even when sediments are decompacted (Figure 5-1). This pattern matches the variation in regional strain rates discussed in chapter 3 (and presented here) where a relative increase in accumulation rate is matched by an increase in regional strain rates and vice versa. This evidence is particularly insightful when it is integrated with the observation that thrust-folds in the study area become eventually inactive (or slow down) and are buried by sediments; this can only occur when sediment accumulation rates outpace uplift rates (sedimentation/deformation > 1; Burbank and Verges 1994). In fact, it is evident that, after 6.5 Ma, folds in the inner domain were progressively buried (Figure 5-16a, Figure 5-20a). Because the burial of folds occurred simultaneously to a decrease in accumulation rates, it implies that, as accumulation rates decreased, deformation decreased at a faster rate in order to satisfy the condition where sedimentation/deformation > 1. On the other hand, our results show that the growth of thrusts is never outpaced when sedimentation rates are very high as we observe that under this conditions also strain rates increase, as for the 7.4 to 6.5 Ma interval, causing the ponding of sediments. Our results seem to confirm that the causes why thrusts stop growing or slow down must be sought in the way strain is partitioned and transferred between structures, along and across strike, in a system where the deformation front migrates basinward and the inner structures are gradually abandoned, as shown in chapter 3. This conclusion, derived by the analysis of isopach and accumulation rate maps alone, is consistent with the result of structural analysis that indicates that changing sediment supply to the delta top can impact the critical taper geometry, and, in

turn, this impacts the deformation history of the fold structures. This can explain why inner structures as fault 21 can be reactivated at later stages, after a period of quiescence and substantial sediment burial (Figure 3-5).

5.4 Conclusions

The results presented in this chapter demonstrate the close link between structural deformation and depositional style where for a given set of strain rates and for a given basin configuration (related to the cumulative strain and the degree of fault linkage) only one dominant seismic facies tend to develop.

The main results on the distribution of sedimentary systems are summarized below:

1. The distribution of the earliest active fault segments (the earliest structural framework) affects the location of the sedimentary systems throughout the growth history of the fold belt.

2. Sedimentary systems are widely distributed across the lower slope and along the strike of structures for strain rates up 2%/Ma, but they become highly restricted at greater strain rates.

3. At each time, submarine channels mostly exploit areas of relative lower strain rate along the strike of each fault to cross it.

4. Deflection of channels can occur for strain rates as low as 1%/Ma (<90 m/Ma).

The main results on the architecture of sedimentary systems are:

5. Linear and leveed channels are characteristic of strain rates < 2-3%/Ma when thrusts are highly segmented, and the channels are able to avoid structural culminations, passing between thrust segments.

6. Erosional channels are characteristic of strain rates > 2-3%/Ma and a high degree of fault linkage, when the lower slope is deformed into discrete piggy-back basins and channels are forced to go over structural culminations.

7. Channelized sheets are associated with strain rates between 1-2%/Ma during the late stages of deformation when the topography that has been previously created is progressively healed. They are characteristic of moderate topography on the seabed.

Deposition of lobes can also occur for strain rates as low as 1-2%/Ma, but more typically they occur for strain rates in excess of 4%/Ma. However, as opposed to channels, lobes occur up dip of the zones of greatest strain rate along the strike of faults. Deposition of lobes can occur 10-15 km up dip of the controlling faults.

6. Statistical quantification and validation of the structural impact on the distribution of deep-water systems

This chapter is presented in paper form – due to be submitted to *Geology*

6.1 Introduction

Submarine channel systems are recognized in many deep-water fans and play a crucial role in governing the routing and delivery of sediments from the shelf edge to deep water (Normark, 1970; Mutti and Ricci Lucchi, 1972; Walker, 1978; Ghosh and Lowe, 1993; Babonneau et al., 2002; Sweet and Blum, 2016; Jolly et al., 2017 amongst others). Understanding their distribution in space and time is important to constrain the locus and magnitude of deep-water sedimentation, and to predict stratigraphic architectures and reservoir facies (Mayall et al., 2006, 2010; Sømme et al. 2009; Stevenson et al., 2015). Submarine channels are often found on passive margins that deform under the effect of gravity tectonics (e.g. Niger Delta; Damuth 1994; Cohen and McClay 1996; Morley and Guerin 1996; Wu and Bally 2000; Corredor et al 2005; Jolly et al., 2016, 2017; Don et al., 2019), causing the growth of contractional folds and thrusts. The growth of these structures is expressed by the creation of seabed topography that modifies the slope gradient and creates tortuous corridors, which can be exploited by submarine channels (Smith, 2004; Callec et al., 2010; Bourget et al., 2011; Howlett et al., 2019). It is often argued that submarine channels, particularly those active coevally to deformation, are sensitive to gradient changes driven by deformation (Pirmez et al., 2000; Ferry et al., 2005). Several studies have suggested a close link between increased slope/structural uplift, greater channel incision, and a reduction in sinuosity (Pirmez et al., 2000; Ferry et al., 2005; Huyghe, 2004; Clark and Cartwright, 2009, 2012a, b; Mayall et al., 2010; Deptuck et al., 2012; Jolly et al., 2016). Analysis of stratal relationships and isopach maps has also indicated that the locations where channels cross growing structures may be dependent upon along-strike structural variations of thrust-folds and the relative rates of uplift and sediment accumulation (Clark and Cartwright 2012a, b, Jolly et al., 2017). However, this issue has often been addressed on a "case study" basis where examples of individual channels are shown to be diverted around structures, whose deformation rate may (or may not) have been quantified (Clark and Cartwright, 2009, 2012a, b; Jolly et al., 2016). To date, no work has attempted a statistical analysis of a large number of submarine channel-structure crossings in time and space, where the deformation rates are measured independently. This paper addresses that challenge.

Here, using 3D industry seismic data covering the southern lobe of the Niger Delta, we determined the frequency distribution of several Miocene to Pliocene channel complexes where they crossed gravity-driven fold-thrusts, at 173 locations, for which the temporal and spatial evolution of strain and strain rate have been recently constrained (chapters 3, 5). We used a comprehensive statistical approach to quantify what strain and shortening rates (see chapter 2 for conversion between strain and shortening) are documented where channels cross structures, compared to the fault array as a whole, throughout the growth history of the fold and thrust belt over 11 Myr. Our data set therefore allows us to test statistically the hypothesis that submarine channels are sensitive to on-going deformation at or near the sea bed.

6.2 Structural setting and evolution

The Niger Delta (Figure 6-1a) is a major Tertiary delta with a total area of 75000 km^2 and 12 km of deposited sediments since the Early Eocene (Damuth, 1994; Reijers et al., 1997). The fast advance of the delta front above the basinal, slope and pro-delta shale units caused the formation of elevated pore pressures due to rapid burial (Cohen and McClay, 1996; Morgan, 2003; Bilotti and Shaw, 2005; Briggs et al, 2006; Cobbold et al., 2009), which facilitated the gravitational collapse of the system since the Miocene. The gravity failure was accommodated by extensional tectonics on landward up-dip areas of the delta and thrusting and folding towards the delta toe (Evamy et al., 1978; Knox and Omatsola, 1989; Doust and Omatsola, 1990; Damuth, 1994).

Using 3D seismic reflection data supplied by PGS with a resolution ranging from 30 to 18 m from the Miocene to the Quaternary stratigraphic intervals, recent work has constrained the structural evolution of eleven thrust-folds on the lower slope of the southern lobe of the Niger Delta (thrusts labelled 11 to 22 in Figure 6-1b; chapters 3, 5; Jolly et al., 2016). Temporal and spatial evolution of strain rates have been quantified using line length balancing techniques (Dahlstrom, 1969). This work has revealed that deformation on the lower slope started at 15 Ma and the development of the fold and thrust belt until 3.7 Ma can be described by six evolutionary stages (chapter 5). In the interval between 15 and 12.8 Ma all the 11 thrusts in the area started to form coevally. The thrusts were highly segmented with an average strain rate up to 1%/Ma. Between 12.8 and 9.5 Ma, the thrusts segments started to propagate laterally and link into longer segments, however, the average strain rates were still in the order of 1%/Ma. In the interval between 9.5 and 7.4 Ma strain rates increased on the inboard structures to an average value of 3-4%/Ma and the thrusts fully linked along strike. However, the outboard

thrusts were still partially segmented and deformed at no more than 1-2%/Ma. Between 7.4 and 6.5 Ma all the 11 thrusts completely linked in 3D and strain rates reached maximum values of more than 7%/Ma. In the two subsequent intervals (6.5 to 5.5 and 5.5 to 3.7 Ma) strain rates progressively decreased on the inboard faults as a result of the basinward migration of the deformation front while the outboard faults maintained greater strain rates. Moreover, some of the inboard faults stopped growing or became partly inactive. In chapters 3 and 5 maps of strain rate along strike for each fault in the area have been provided. An example is given for the time interval from 5.5 to 3.7 Ma in Figure 6-1c.
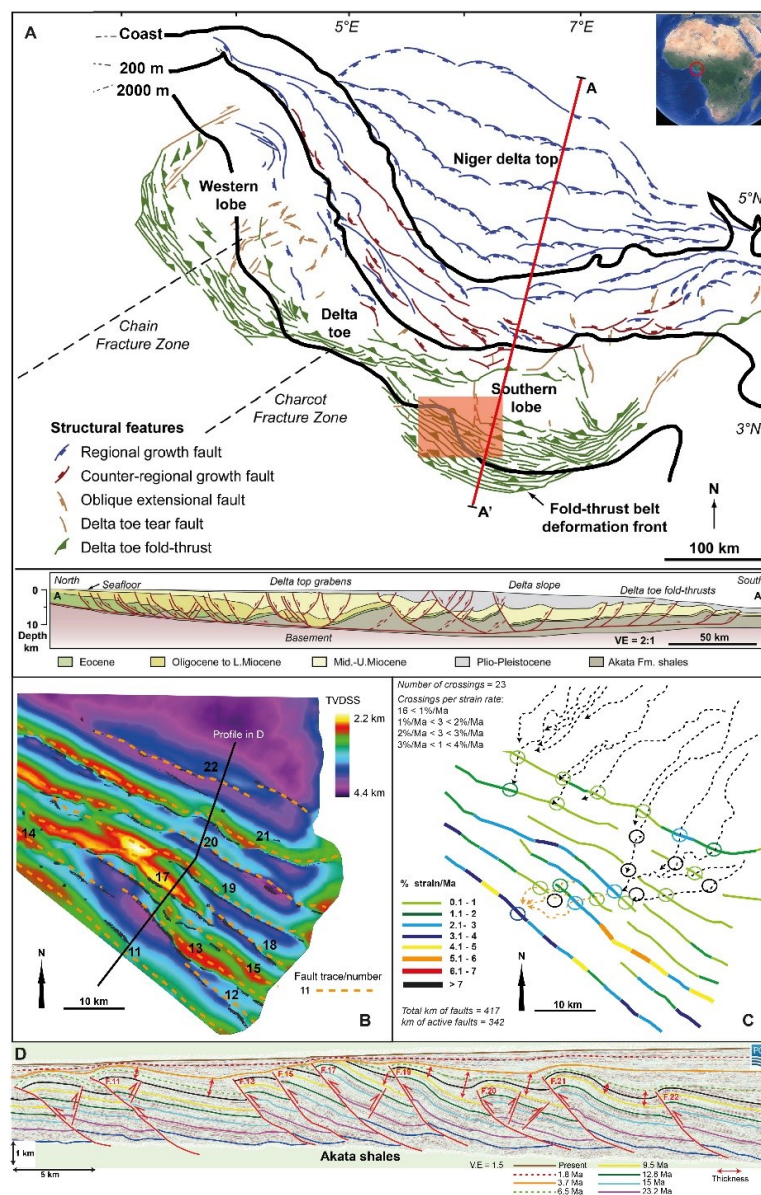
Figure 6-1: – A) Structural setting of the Niger Delta and location of the study area (orange box) on the toe-thrusts (modified from Wu et al., 2015). B) Depth-structure map of the 9.5 Ma horizon showing the 11 thrusts segmenting the lower slope. C) Example of strain rate map for the 5.5-3.7 Ma interval, showing several channels crossing the faults at specific locations. The total number of crossings (in each of the 6 units) and associated strain rate (circles) is recorded to compare it with the mean strain rate of the fault array during each interval.

6.3 Methodology

Deep-water slope channels were identified within each of the six units described in chapter 5, using standard seismic stratigraphic techniques (chapter 5). These interacted with, and crossed, coeval active fault segments. For each interval, the channel courses were mapped and overlaid onto the corresponding strain rate map in order to record the value of strain rate at each intersection between an active fault segment and a channel – as shown in Figure 6-1c for the time interval 5.5 to 3.7 Ma. This screening yielded 173 channel crossings in the period between 15 and 3.7 Ma (note that a single channel may cross multiple structures; Figure 6-2). Histograms were derived (Figure 6-3a, b) of the magnitude of strain rate recorded at each channel-fault intersection for each of the six time slices described above, and for the entire period of activity from 15 Ma to 3.7 Ma. The mean strain rate for a channel-fault intersection in each time interval was recorded. Analogous distributions of the total length of active fault segments, deforming at a given strain rate, were also compiled for each time slice and for the entire period of study. The maximum length of all the faults in the array for any one time interval was 417 km. The results from each unit were subsequently summed and normalized to derive three cumulative distribution functions (Figure 6-3c); one of the number of channel crossing points, and two depicting cumulative distribution of fault segments as a function of strain rate, with and without segments of zero strain which were subsequently or previously active. We compared these distributions to test the hypothesis that the channel crossing points preferentially exploited locations of lower strain rate in the evolving fault array. However, to confirm that the distribution of submarine channel crossing points observed is significantly different from the distribution of fault strain rates in the array (i.e. it is not random), it must be proved statistically that the two distributions could not be drawn from the same underlying distribution (the null hypothesis), given we have not sampled all possible channels on the Niger Delta as a whole. To determine this, a standard two sample Kolmogorov-Smirnov test (K-S test) was used to evaluate whether the distributions were different (Figure 6-2 and Table 6-1). The null hypothesis (i.e. that the distribution of strain rates at channel crossing points is the same as the distribution of fault segment strain rates) was rejected at the 95% confidence interval. In this case, channel crossing points would be therefore sensitive to deformation rates.
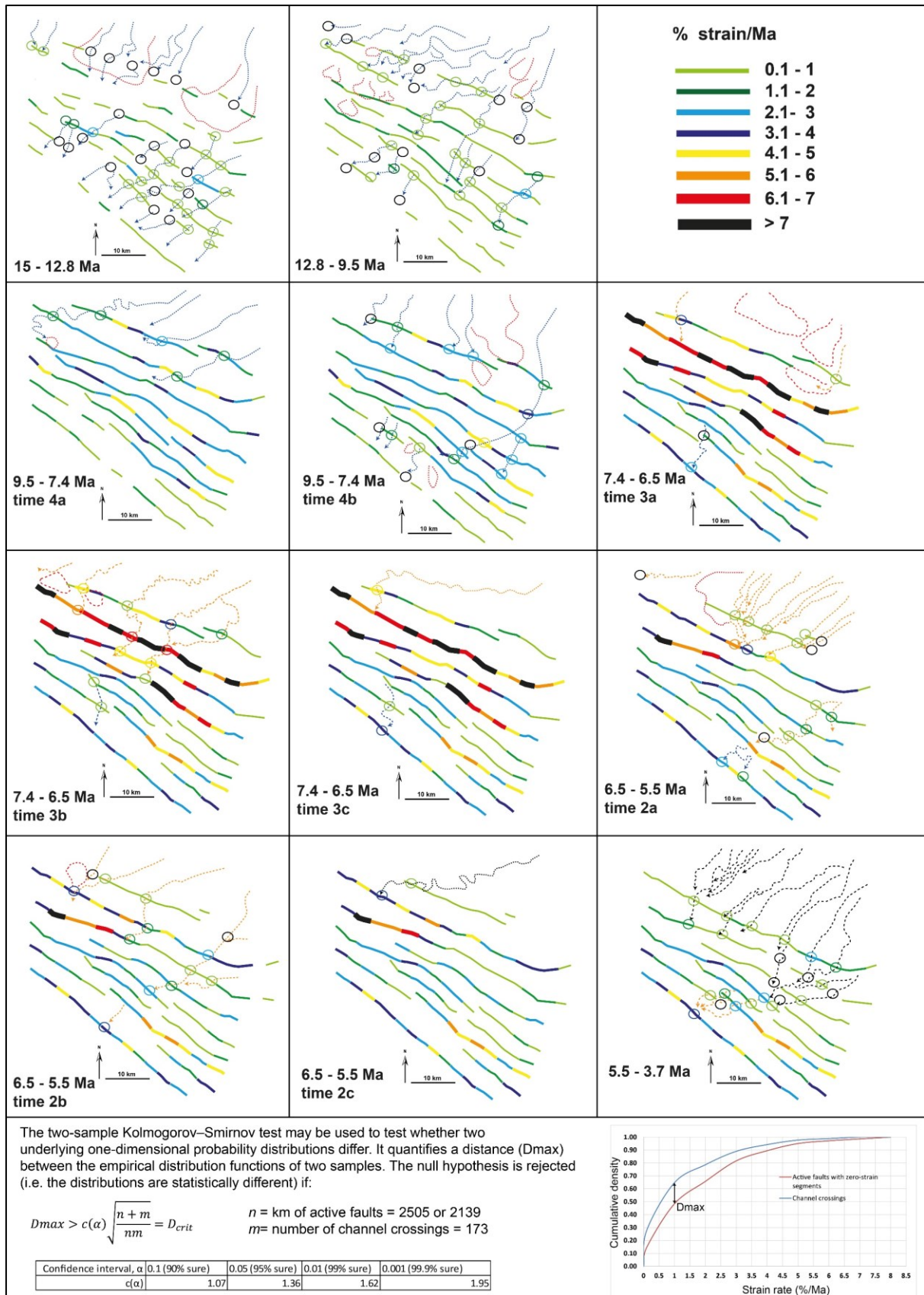
Figure 6-2: Distribution of channel crossing points for all the time intervals analysed and their internal subdivisions. Equation for the calculation of critical distance (Dcrit) during K-S test is also shown. Dmax between our empirical distribution is > Dcrit, therefore, the null hypothesis is rejected, and the distributions are statistically different.

Table 6-1: List of statistical parameters used to construct the cumulative distribution functions and validation with the Kolmogorov-Smirnov test.

Strain rate category (%/Ma)	Channel crossings (n)	Faults (km)	Cumulative strain rate (%/Ma)	Column A	Column B	Column C	Absolute difference between columns A-B (Normalized)	Absolute difference between columns A-C (Normalized)
				Cumulative channel crossings (normalized)	Cumulative km Faults with zero strain segments (normalized)	Cumulative km Faults without zero strain segments (normalized)		
0	48	366 (0)	0	0 (0)	0 (0)	0 (0)	0	0
0-1	64	847	0.1	48 (0.28)	366 (0.15)	0 (0)	0.13	**0.28**
1-2	24	434	1	112 (065)	1212 (0.48)	847 (0.40)	**0.16**	0.25
2-3	18	398	2	136 (0.79)	1647 (0.66)	1281 (0.60)	0.13	0.19
3-4	9	197	3	154 (0.89)	2044 (0.82)	1679 (0.78)	0.07	0.11
4-5	6	139	4	163 (0.94)	2241 (0.89)	1876 (0.88)	0.05	0.06
5-6	2	53	5	169 (0.98)	2380 (0.95)	2015 (0.94)	0.03	0.04
6-7	2	36	6	171 (0.99)	2433 (0.97)	2068 (0.97)	0.02	0.02
>7	0	35	7	173 (1)	2470 (0.99)	2104 (0.98)	0.01	0.02
Total	173	2505 (2139)	>7 (8)	173 (1)	2505 (1)	2139 (1)	0	0
			Max absolute difference (*Dmax*)				0.16	0.28
			Critical distance (*Dcrit*) for α = 0.05, and c(α) = 1.36 (95% confidence)				0.11	0.11
			Critical distance (*Dcrit*) for α = 0.001, and c(α) = 1.95 (99.9% confidence)				0.15	0.15
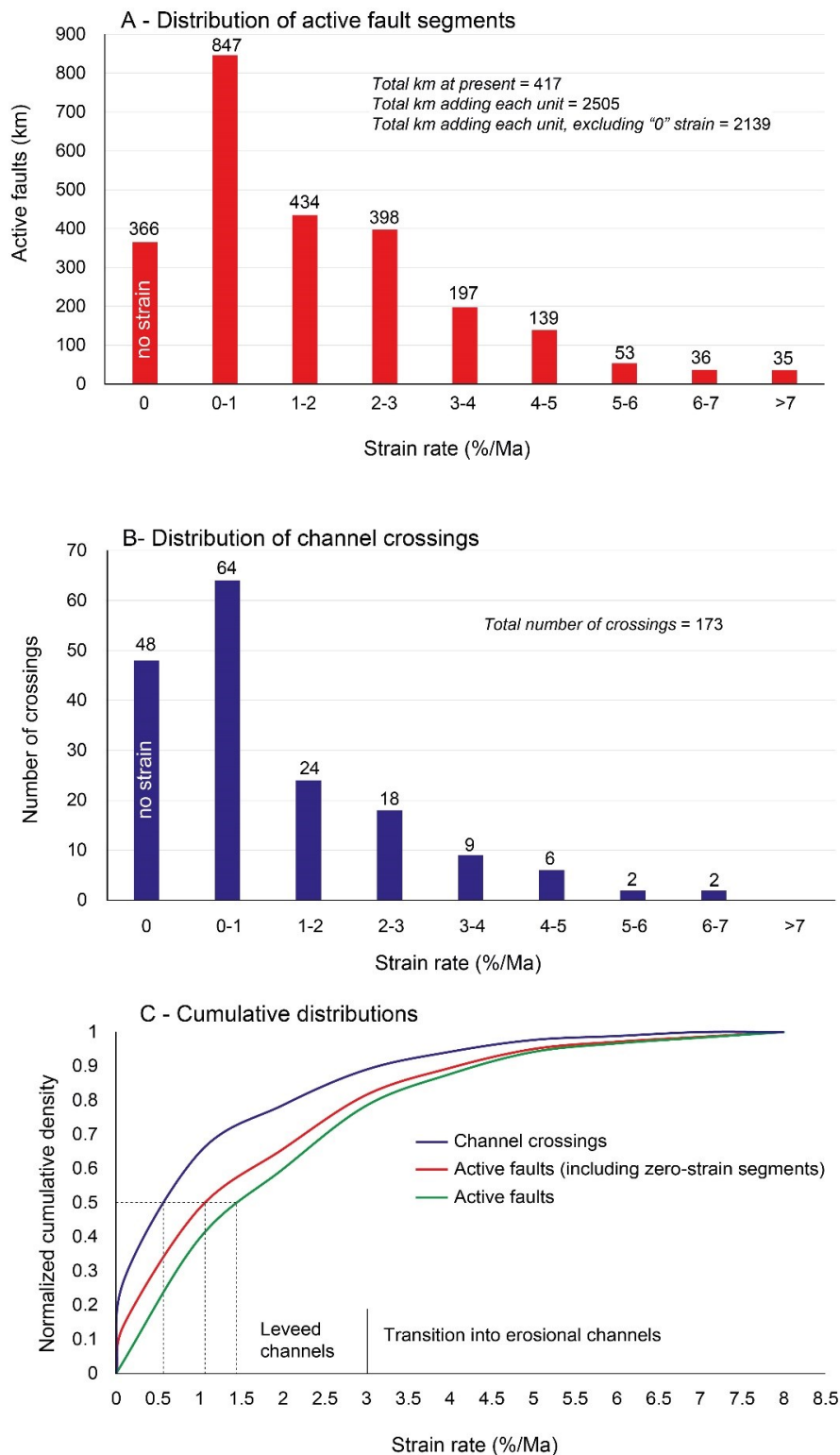
Figure 6-3: A) Total km of active fault segments for a given range of strain rate over 11 Myr. Most of the faults were active in 0-1 %/Ma range. B) Total number of channel crossings for a given range of strain rate over 11 Myr. Most of the crossings occurred over locations deforming within the 0-1 %/Ma range. C) Cumulative distributions derived from the histograms in A and B. The distributions of channels and faults are statistically different. Note that 50% of channels exploited strain rates <0.6%/Ma, while 50% of faults deformed up to 1.5%/Ma, indicating that channels seek the locations of lower strain rate along the strike of faults.

6.4 Results

6.4.1   Distribution of strain rates across the thrust-folds

The present-day total length of the 11 thrusts is approximately 417 km, however, they were not always active along their total strike length, reflecting their segmented nature. All mapped segments were active in the interval between 7.4 and 6.5 Ma; while in the early and late intervals thrust segments were mostly or partly inactive. By measuring the kilometres of active fault segments during each of the 6 intervals we obtained that a cumulative 2505 km of fault segments have been active in the period between 15 Ma to 3.7 Ma (Figure 6-3a). Integrated over this time period, the majority of fault segments (847 km) had strain rates up to 1 %/Ma (shortening rate < 0.08 mm/yr; conversion between strain and shortening is shown in chapter 2), and progressively fewer for higher strain rates. A more conservative approach, which excludes zero-strain rate segments for any time interval, yields a cumulative 2139 km of active fault segments in the period between 15 Ma and 3.7 Ma. When presented as normalized cumulative distributions (Figure 6-3c), the results show that 50% of the fault segments were active at less than either 1.5%/Ma or 1.1%/Ma (green and red curves excluding and including zero strain rate fault segments respectively) in the period between 15 Ma and 3.7 Ma.

6.4.2   Distribution of submarine channels

The results for the channel crossings (Figure 6-3b) show a broadly similar histogram distribution to that of the active fault segments. In other words, the majority of the channels crossings, in the period 15 Ma to 3.7 Ma, occurred for strain rates up to 1%/Ma (64) and an additional 48 crossings occurred over the inactive segments along the strike of faults, while progressively fewer crossings are recorded at higher strain rates. Only 4 channels are documented to cross structures with strain rates > 5%/Ma, and none are documented for strain rates > 7%/Ma, although these higher strain rates are found in <2% of all fault segments during the evolution of the fault array. Significantly, the normalized cumulative distribution (Figure 6-3c) shows that 50% of the crossings occurred for strain rates smaller than 0.6%/Ma (-0.006/Ma), a value markedly smaller than that recorded by median of the active fault segments (1.5%/Ma). The results presented above show that the distributions of channels is more skewed towards small values of strain rate than that of the cumulative distribution of the fault segment lengths as a function of strain rate. A K-S test at the 95% confidence interval confirms that we can reject the null hypothesis that the two observed distributions are drawn from a similar underlying distribution (Table 6-1). Indeed, our results show that we can reject the null

hypothesis even at the 99.9% confidence interval (Table 6-1). In other words, for the first time, our data allow us to prove that the cumulative distributions of channels and faults (with and without zero-strain-rate segments) are, indeed, statistically different, and this allows us to unambiguously show that slope channels preferentially exploited locations of lower strain rate to cross the developing fault array.

6.4.3 Temporal evolution of strain rates and channel crossings

Our data allow us to compare how the mean strain rate has evolved over time, for both the fault array and the channel crossings. As shown in Figure 6-4a, the evolution of the mean strain rate, recorded by the fault array within each time interval, produces a pattern of first increasing deformation rate until approximately 7 Ma, followed by decreasing strain rate thereafter. This broad evolution has been linked to a change in sediment supply to the delta top (chapter 5; Rouby et al., 2011; Jolly et al., 2016). The faults deformed at an average rate of 0.5 %/Ma from 15 to 9.5 Ma, reached a peak of 3.3%Ma in the 7.4 to 6.5 Ma interval, and decreased subsequently to background values of < 1.4%/Ma. The evolution of the mean strain rates recorded at the channel crossings (Figure 6-4a) follows a similar pattern. However, while originally they were the same as those for the fault array, suggesting that channels crossed structures randomly, they progressively diverged with time, with channel crossings persistently occurring at lower values of strain rate. The number of channel crossings also progressively decreases from 15 Ma to the 7.4-6.5 Ma interval and then increases thereafter (Figure 6-4b). However, the curve is asymmetric such that a slow decrease in the number of channel crossings is then followed by a fast increase when strain rates decrease.

The observation that when deformation slows after 7 Ma, the mean strain rate of channel crossings remains suppressed relative to the mean strain rate in the fault array (Figure 6-4a) indicates a fast response of the slope channel systems to changing boundary conditions, with new channels locating themselves in areas of low strain rate and shortening.
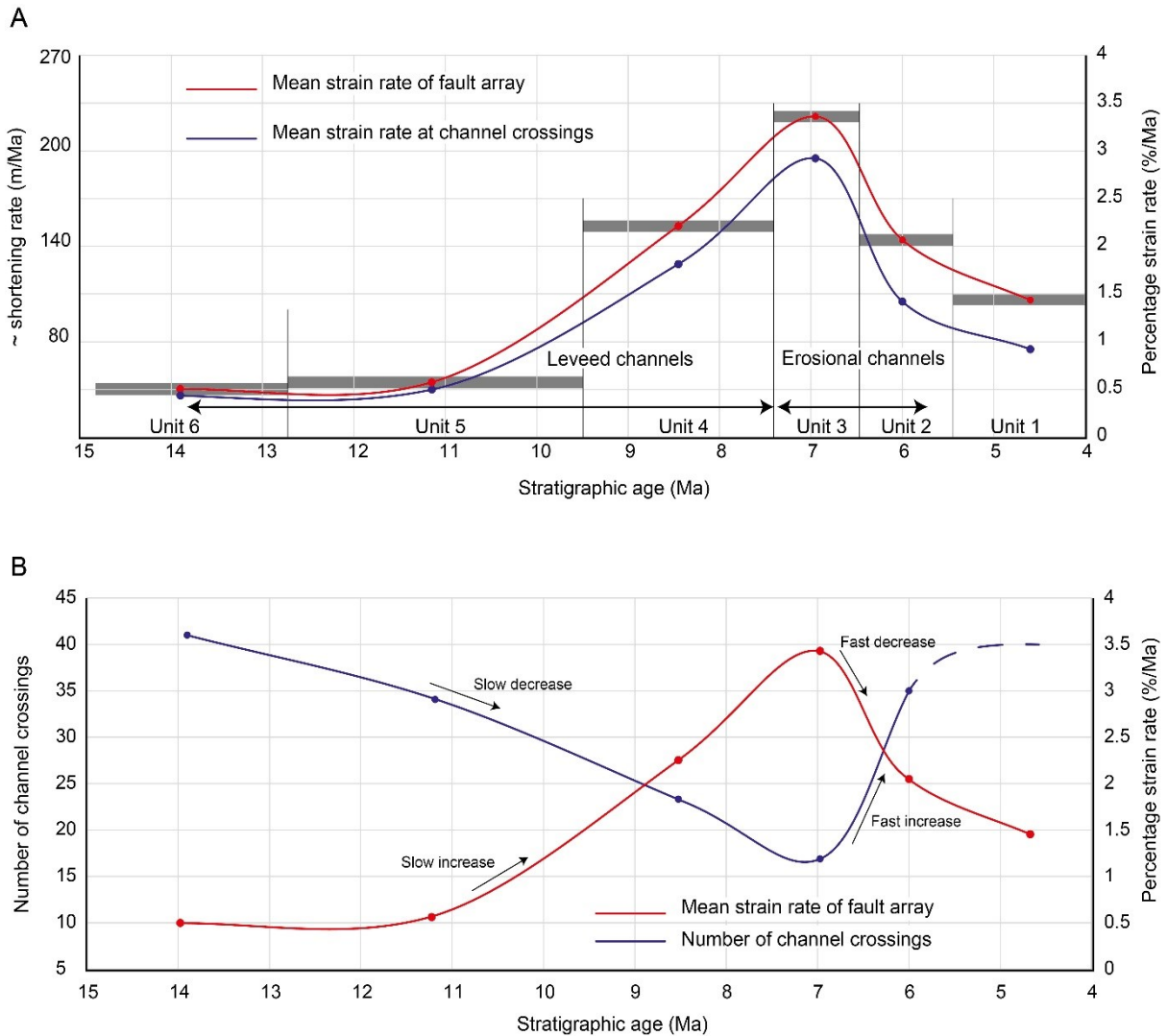
Figure 6-4: A) Strain and shortening rates (y axis) are plotted against time (x axis) to compare the evolution of mean strain rate of the fold belt vs. that recorded at the channel crossings. Both the curves show an increasing-decreasing pattern, but the channel crossings occur at persistently lower values of strain rate. B) Number of channel crossings (left y axis) are plotted against time (x axis) to compare it with the evolution of mean strain rate of the fold belt as in A. When strain rates are high slope channels are restricted on fewer locations as a result of topographic changes. This also contributes to the modification of their architecture into erosional forms. Note that the slopes of the two curves are inversely related, indicating that channels respond to the rate of change (acceleration/deceleration) of the strain rate through time.

6.5 Discussion

Previous authors (Mayall et al., 2010; Clark and Cartwright, 2012; Jolly et al., 2016) suggested that the irregular distribution of uplift and deformation along the strike of structures influences the positioning of the submarine channels by causing avulsions, diversions and deflections and, even under conditions of "little relief" (i.e. overlapping growth sequence), submarine channel morphology can be affected (Clark and Cartwright, 2012; Jolly et al., 2016). Our results demonstrate that two-thirds of all the channel crossings over a period of ca. 11 Myr have occurred at strain rates lower than 1%/Ma (Figure 6-3c). In fact, the evolution of strain rates (at the channel crossings) mirrors, but is persistently lower than that of the fault array (Figure

6-4a). Our K-S analysis shows that this observation is not coincidence or the result of incomplete sampling. Because the distributions of channel crossings, and lengths of active faults as a function of strain rate are statistically different, we determine that while the evolution of the channel crossings is forced to follow the tectonic history of the area, we argue that the channels, during each time interval, are actively driven to the locations of lowest/lower strain rate, along the strike of each thrust-fold, in order to cross these structures.

The results also demonstrate the broader importance of the tectonic forcing on the spatial distribution of submarine channels. For example, the fact that the number of channel crossings decreases for greater values of strain rates and increases when strain rates are low (Figure 6-4b), implies that the channels are widely distributed across the study area, being able to exploit various locations along the strike of structures at times of slow deformation, and are restricted at times of peak deformation. Likely, this reflects the reduced number of possible pathways that channels can exploit to reach the more distal areas during times of intense structural deformation. This, in turn, results from the occurrence of topographic changes when the faults link through the detachment and start to transfer strain across strike more efficiently (see chapter 7). Therefore, not only can channels be deflected around structures that deform at very low strain rates, but also the overall density of the channel network is highly reduced when deformation rates are high. In these circumstances subsequent flows are forced to persistently exploit the same crossing points. Because in chapter 4 I have documented that channel architectures change from constructional, leveed-confined, to erosional forms on or after 7.4 Ma (Figure 6-5), I suggest that this modification of the overall channel cut and fill architectures is partially due to sustained bypass of flows, when strain rates are greater than approximately 3%/Ma (0.2 mm/yr) and only limited pathways exist to cross a structure, enabling the channels to keep pace with on-going deformation (Jolly et al., 2016, 2017).

Finally, it is significant that after the time of peak deformation, the mean strain rates of both the fault array and the channel crossings decline, however, the two curves continue to diverge as the channel crossings decrease at a faster rate and establish their positions at low values of deformation rate (Figure 6-4a). In part, this results from the fact that the number of channel crossings rapidly increases after ca. 7 Ma (Figure 6-4b), implying that sedimentation is outpacing deformation as the channels again become widely distributed across the region. In this scenario progressively more crossing points become available to be exploited, enhancing the probability that channels "find" more crossings with lower strain/shortening rates. We also hypothesise that the variation in number of channel crossings through time is related to the rate at which the strain rate changes. For instance, a fast decrease in strain rate after 7 Ma is

accompanied by a fast increase in the number of channels flowing through the study area. In summary, our results demonstrate the importance of reconstructing and quantifying the evolution of deformation rates as a tool to understand and predict the temporal and spatial distribution of submarine channels and their evolving architecture in response to structurally-driven topography.
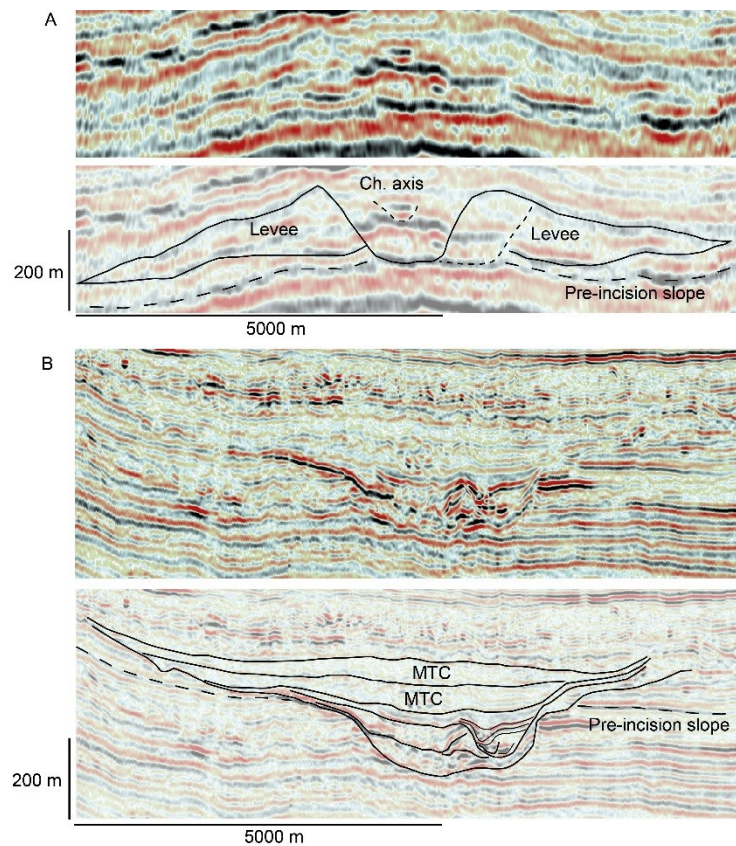
Figure 6-5: Examples of typical leveed channels (A) and erosional channels (B). The leveed channels dominate in the 12.8 to 7.4 Ma interval, while the erosional channels dominate in the 7.4 to 5.5 Ma interval.

6.6 Conclusions

Using a comprehensive statistical approach of 173 submarine channel crossings of faults and a cumulative 2505 km of faulting for which strain rates have been calculated over an 11 Myr history, this analysis shows that:

1. The distributions of strain rates of the outer fold and thrust belt of the Niger Delta and those recorded at the channel crossing points are statistically different at the 95% confidence interval using a two-sample K-S test;

2. Submarine channels strongly tend to exploit the available zones of lower/lowest strain rate along the strike of faults, although the mean strain rates recorded at the crossing points mirror the deformation history of the area;

3. The density of the channel network (crossing points) progressively reduces for greater rates of deformation and is related to the rate at which the strain rate changes through time;

4. When channels are spatially restricted, subsequent flows exploit the same locations, which contributes to the modification of the overall channel architecture into erosional forms;

As soon as the deformation rates drop, submarine channels quickly spread across the region and start to heal the topography, with new channels entering the area locating themselves in areas of low strain rate and shortening.

7. Discussion

7.1 Introduction and overview

This study has addressed the final goal of quantifying the structural influence on the distribution and architecture of deep-water systems interacting with the growth of gravity-driven fold and thrust belts. In chapter 3 a first detailed strain analysis reconstructed the individual growth history of each of the thrust-folds in the study area. This work created the background structural framework for the subsequent stratigraphic analysis as it showed how cumulative strains and strain rates varied along and across strike, and through time. One of the key findings of chapter 3 was the identification of the 7.4 Ma horizon as the most critical boundary in the growth history of the fold belt; this marked the time of complete linkage of all the structures in three dimensions, along the common underlying detachment. In fact, more generally after this time strain rates increased (also shown in chapter 5) and the thrust-folds changed their mode of growth, from lateral propagation (15 to 7.4 Ma) to accumulation of strain and shortening at nearly constant strike lengths (7.4 Ma to present). The structural information has been integrated with a detailed seismic-stratigraphic and facies analysis (chapters 4, 5 and 6).

The results presented in chapter 4 demonstrated that during the evolution of the outer fold and thrust belt of the Niger Delta, the architecture of the dominant seismic facies changed vertically upward from lobe complexes in the oldest strata (15 to 12.8 Ma) to leveed and linear channels (12.8 to 7.4 Ma) to ponded lobes followed by more erosional channels (7.4 to 5.5 Ma), finally capped by interbedded channelized sheets and MTDs (5.5 to 3.7 Ma). It has been also shown that, between the four individual areas that constitute the deep-water fold and thrust belt, this transition was not synchronous, but occurred at earlier times in the proximal inboard zones (areas 1, 2 and 3) and later in the outboard domain (area 4). Moreover, this transition followed the main tectonic phases and the observed basinward propagation of the deformation front that occurred at 7.4 Ma. This suggests a structural control on the type and architecture of deep-water sedimentary systems that developed during each time interval.

Further analysis conducted in chapter 5, by the integration of isopach and amplitude extraction maps with strain rate maps, revealed that not only the architecture but also the distribution of sedimentary facies was controlled by the structural development of the slope: submarine channels, during each time interval, crossed structures exploiting locations of lower strain rate

available along the strike of thrust-folds and, in many cases, these locations coincided with the earliest sites of fault linkage. The distribution of the channel crossing points was then statistically analysed in chapter 6. The results showed that, although the thrust-folds deformed at a median strain rate value of approximately 1.5% per Myr over 11 Myr, the channel crossings (of all the 6 units) were located at a median value of 0.6% per Myr, indicating that channels actively sought the locations of lower strain rate to cross structures. It was also proved that this result is statistically significant by using the Kolmogorov-Smirnov test. This analysis additionally demonstrated that determining how strain rates are distributed during each time interval would help in predicting where channels would cross faults and how many crossing points to expect at each time and, therefore, how widely distributed sedimentary systems are across the region.

I have shown that the architecture of the sedimentary facies is linked to a set of parameters that continuously evolve during the growth of the fold and thrust belt and that result in the occurrence of specific facies types. These include the degree of fault linkage, the cumulative strain, the interval strain rates and the basin geometry (as deduced from the isopach maps). The results of these analysis prove that early stages of deformation (low strain rate, low cumulative strain and segmented fault array) link to the development of leveed channels, whereas times of peak deformation (linked structures and high strain rates) favour the development of more erosional channel forms and ponded lobes. However, four main discussion points remain to be understood and answered:

1) To what extent the structural measurements indicate seabed topography?

2) Is it possible to predict how and why, in a mechanistic sense, channels alter their architecture from leveed into erosional in response to growing structure and/or seabed topography?

3) Likewise, can we predict the location, interval of occurrence and areal extent of ponded lobes?

4) If we can understand the mechanisms that govern these changes, how can we apply this knowledge to oil and gas exploration?

While it is well established that positive seabed topography causes channels to increase their incision (Pirmez 2000; Ferry 2005), as deduced in chapter 5 for the occurrence of erosional channels (Figure 5-23), it is also well known, and documented in this study, that even subtle seabed topography or minor deformation cause channels to divert away from the growing structures (Mayall et al, 2010; Jolly et al., 2016). Therefore, what causes the channels to cut through and incise into a growing structure? The answer to this question firstly relies on the

reconstruction of how deformation is distributed in 3D and how structures interact and transfer strain across-strike. This information, coupled with the sedimentary response, could be then used as an indication of seabed topography.

7.1.1   Methods for the estimation of surface topography

Surface topography, at any given time, is a function of three parameters: structural growth, sediment accumulation rate and erosion, hence, whether the structure is buried by sediments or emergent. In older, deformed stratigraphic sequences in both terrestrial and marine environments estimates of fold crestal uplift (and likely surface expression) have been usually made by the detailed analysis of growth sequences and stratigraphic relationships such as onlap, overlap and offlap that develop on the limb of growing folds as they provide information about the relative rates of sedimentation and uplift (Burbank and Verges, 1994; Cartwright, 1989; Suppe et al., 1992; Masaferro et al. 1999; Poblet et al. 2004). Generally, in the case of an overlapping growth sequence (sedimentation>uplift) the fold is buried by the sediments that only thin over its crest, and the thickness difference from limb to crest is interpreted to represent the cumulative fold uplift that occurred during the deposition of the interval analysed.

In the case of an onlap relationship (sedimentation<uplift), the crestal uplift is interpreted at least as the entire thickness of the (ponded) growth sequence. However, the amount of information that we obtain from this analysis is limited by the following factors:

1. The measured cumulative uplifts may be in the order of several hundred metres, however, this was never the actual relief on the seabed or at land surface at any time, which gives no indication of how channels responded to topography;

2. In the case of overlapping growth sequences, it is implied that no seabed relief is developed on the fold crest. This assumption is often wrong, not least due to the differential compaction occurring between limbs and crest;

3. The analysis of visible growth sequences, in seismic based studies, only gives information about seabed topography created during times of high strain rates after faults link (see chapter 3). The early stages of deformation are not analysed.

4. This method does not account for the seabed topography caused by the combined effect of the multiple, imbricated and interacting thrusts.

In the present study I have tried to overcome these issues by measuring (through line-length balancing) the strain and shortening that thrusts folds have accumulated along strike and

through time and have been able to quantify how strain and shortening rates have evolved in 4D without relying on kinematic assumptions or on visible thickness variations. The results have provided considerable insight on the structural evolution of thrust-folds (both isolated and as an interacting array) and are a reliable tool to predict how deformation is distributed by reconstructing the strain-distance plots through time of each structure. Simultaneously, the interval strain rates provide useful information on what structures were mostly active (creating more topography) at any time. Jolly et al 2016, 2017, who first adopted this methodology, attempted to convert their shortening values into crestal uplift using the method proposed by Hardy and Poblet (2005), although acknowledging the limitations of a kinematic approach (simple-step, flexural-slip fault-propagation folds and constant ramp dip). Nonetheless, the conversion between shortening and shortening rate into uplift and uplift rate produced similar absolute values. In effect, the estimated structural uplift does not equal seabed relief as it does not account for the coeval sedimentation, which leads to the same issues encountered for the stratigraphic approach; i.e. the measured uplifts were never the actual relief on the seabed at any time.

This study does not attempt to quantify or estimate structural uplift and/or seabed topography as it argues that an accurate prediction of the distribution and architecture of sedimentary systems through time can be obtained with the use of the strain and shortening measurements alone as presented here. On the other hand, the integration of the structural parameters with the sedimentary responses could be used as proxies to infer what the seabed topography would have been (at a given time) by quantifying the underlying structural control.

In particular, this work has documented and highlighted that a fundamental aspect of the growth of structures is that they interact in a 3D space and I argue that the main challenge to achieve an accurate prediction is reconstructing the complex morphology deriving from the contribution of multiple folds across strike. This discussion focuses on this specific issue and in the next sections a new mechanism is proposed that aims to recreate the plausible combined topographic expression of multiple interacting folds and how that controlled the change in architectural style (as well as location) of the slope facies. The applicability of this model to the oil and gas exploration relies on its ability to fully predict and understand the mechanisms that cause the variations in the stratigraphic architecture.

To achieve this, here I synthetize the results of the structural analysis (chapter 3) with the evolving stratigraphic architecture (chapters 4 and 5) to further investigate the effect that the structural evolution has had on seafloor bathymetry; this is done using the strain-distance plots of the eleven thrust-folds originally presented in chapter 3 (Figure 3-9). I will then first discuss

to what extent strain-distance plots can be used as proxies for (paleo)topography (section 7.2) and subsequently show how they can be used to assess and explain the distribution and architecture of both channels and lobes (sections 7.3 and 7.4). These findings are synthetized in a predictive facies model presented and discussed in section 7.5. The integration of the structural analysis with the architectural and stratigraphic findings will be further discussed in terms of implications for oil and gas exploration (section 7.6).

7.2 Strain-distance plots as proxies to topography

Strain-distance plots can represent the actual morphology of the seabed only if:

1. Thrust-folds are isolated (Higgins et al., 2009) and if no syn-kinematic sedimentation take place;

2. If syn-kinematic sedimentation takes place they can still approximate the seabed morphology as long as folds are not entirely buried.

Effectively, in deep-water areas the second case is more likely to happen because of net deposition through time. However, strain-distance plots can give an indication of topography on the (past) seabed because they directly allow us to visualise how deformation is distributed along the strike of the structures responsible for the topography on the overlying seabed. Therefore, although the final topographic expression of a given structure will result from the relative amounts of deformation vs. depositional and erosional processes (that smooth the topography; Clark and Cartwright, 2012a; Deptuck et al., 2012; Jolly et al., 2016), knowing the location of maximum strain or displacement along-strike gives a reliable indication that the seabed, at that location, may be more uplifted compared to the surrounding areas. Moreover, although both sedimentation and erosion smooth the structurally-driven topography, in strain-distance plots the shape of the present-day profile broadly mirror the current morphology of the pre-kinematic sequence (15 Ma horizon). This is indeed observed (Figure 7-1) and, additionally, I note that this assumption is valid for the strata up to the 7.4 Ma horizon too, therefore, for the entire early syn-kinematic sequence (15 to 7.4 Ma), likely because of low strain rates and the segmented state of faults.

It follows that the shape/geometry of the reconstructed strain-distance plots in the past, could be a valid representation of what the morphology of the pre-kinematic and early syn-kinematic horizons (15-7.4 Ma) would have looked like at the time. This is an invaluable tool to reconstruct the shape of the receiving basins (not seabed topography), at least, until 7.4 or 6.5

Ma because after that time, sedimentation rates outpaced deformation and eventually thrust-folds were buried by sediments.

In fold and thrust belts (as in this study), however, it is common to find multiple imbricated thrust sheets (Elliot 1976; Boyer and Elliot 1982; Butler 1982, 1987; Shaw et al., 1999; Corredor et al., 2005) which are often vertically stacked such to cause an enhanced topographic expression. In this case the resulting topography (or relief) on the seabed would be controlled by sum of the relative uplift of each of the thrust-folds involved in the thrust-stack. An example of this effect is shown in Figure 7-2 where the location of highest structural relief in the centre of the study area is clearly the result of the stacking of faults 15, 17 and 19. When this complication occurs, then the strain-distance plots of the single faults cannot be used as a proxy for seabed morphology because more structures are involved in the deformation process. This problem can be overcome by adding together the strain-distance plots of all the faults involved in the thrust-stack. In this study this effect is particularly evident in the core of fold belt (areas 2 and 3) where five faults (20, 19, 18, 17, and 15) are closely spaced and their joint effect makes the seabed topography very complex. By adding together their strain-distance plots, the aggregate profile of the 5 faults provides a higher-fidelity representation of the present-day shape of the "pre-kinematic horizons" (15-7.4 Ma; Figure 7-3) in the core of the fold belt. Clearly the aggregate profile constructed in this way has to be considered an "average" across the area examined but it is powerful as not only it shows the topographic effect of multiple interacting faults, but it can also show it through time, as previously discussed. In summary, strain-distance plots, as reconstructed in this study, can be used as per the following:

1. The present-day strain profiles mirror the geometry of the current pre-kinematic and early syn-kinematic horizons, therefore, the geometry of the receiving basins.
2. The reconstructed profiles in the past tell us how the geometry of the receiving basins changed over time.

If thrust-folds are not isolated (i.e. imbricated thrusts sheets) the strain distance plots of all the faults involved in the thrust-stack can be summed to obtain and reconstruct the geometry of the receiving basin, although averaged.
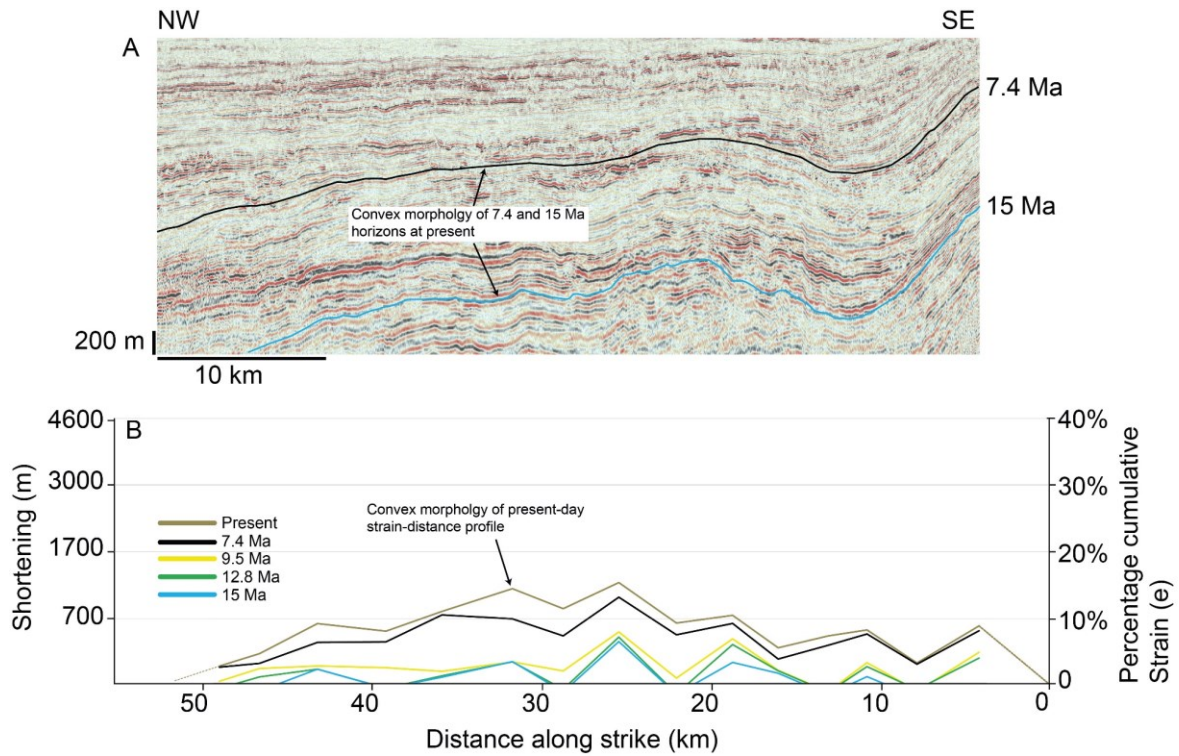
Figure 7-1: A) seismic section "b" (location in Figure 7-2) passing through the crest of fault 22 compared with its strain-distance plot trough time (B). 15 Ma represents the start of deformation, however, until 7.4 Ma the stratigraphic section can be approximated as "pre-kinematic" (see text for explanation), thus showing similar present-day depth structure. Note that the present-day strain profile of the fault in (B) mirrors the shape of both the 15 and 7.4 Ma horizons. This suggests that the reconstructed strain profiles at different times represent the shape of the "pre-kinematic" horizons (15 to 7.4 Ma) prior to fault linkage. Note that A and B are shown at same horizontal scale and exact along-strike distance.
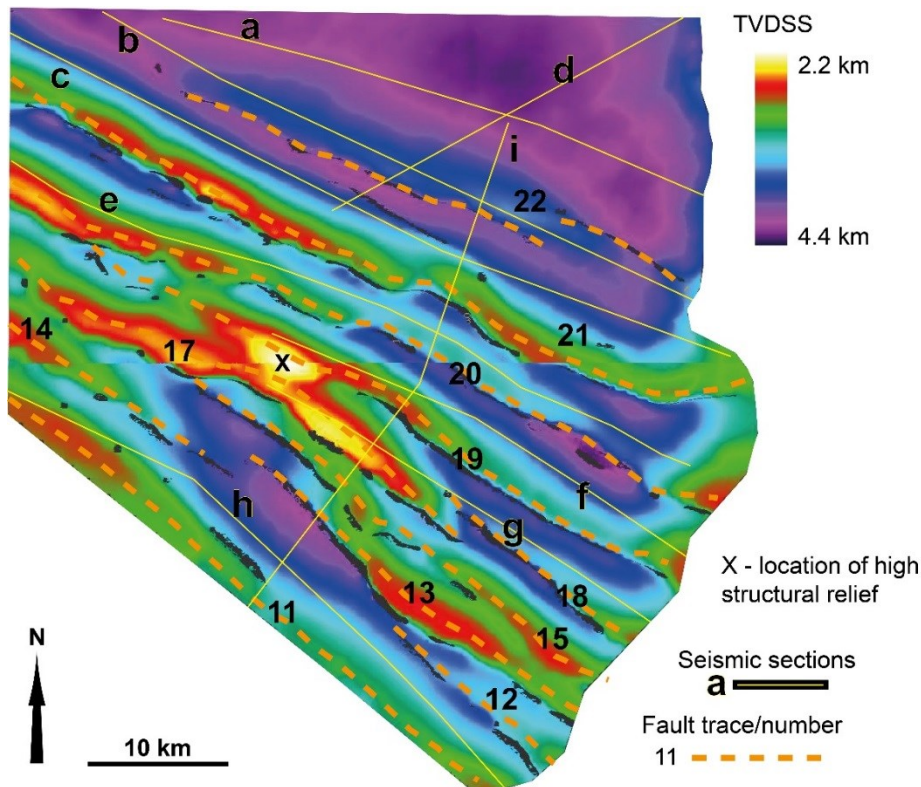
Figure 7-2: Depth structure map of the 9.5 Ma horizons. The locations of all the seismic sections used in this chapter are also shown.
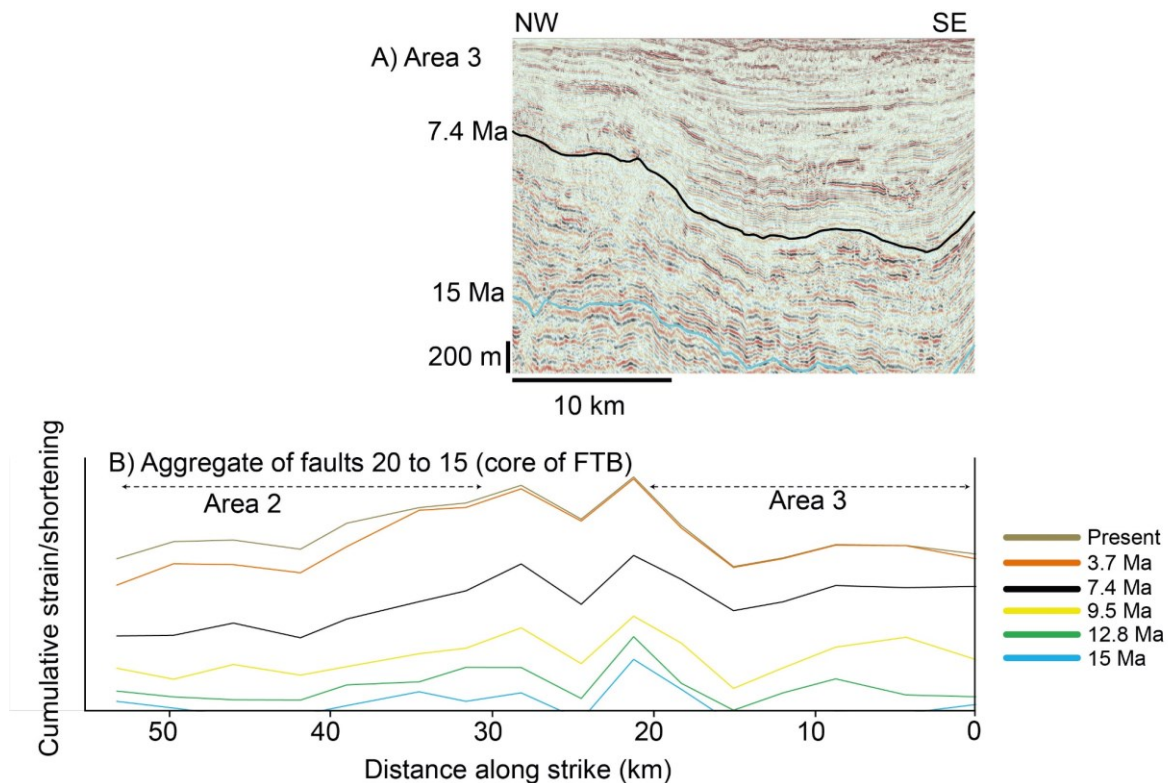
Figure 7-3: A) seismic section "f" (location in Figure 7-2) passing through the centre area 3, inboard of fault 19. In (B) the strain distance plots of all the faults in the core of the fold belt (20 to 15) are summed together. The aggregate profile in area 3 mirrors the concave shapes of the 15 and 7.4 Ma horizons in the centre. This indicates that summing together the strain profiles of multiple faults involved a thrust stack allows their combined topographic effect to be reconstructed. Note that A and B are shown at same horizontal scale and exact along-strike distance.

7.3 Location and architecture of deep-water facies interacting with growing structures

I now examine the relationships between the location and architecture of the sedimentary systems against the evolving geometry of the strain-distance plots of the structures (Figure 7-2). These will be shown per area of interest (1 to 4), from proximal to distal, and, therefore, highlight the evolution of the architectural style along-strike and through time as opposed to the map-views presented in chapter 5.

7.3.1   Area 1

The stratigraphic evolution in area 1, the most inboard part of the fold belt, is well-represented by three seismic sections (Figure 7-4, Figure 7-5, Figure 7-6). Four broad facies associations are observable in area 1:

1.   Unconfined lobes between 15 to 12.8 Ma;

2.   Linear and leveed channels, low-relief channel levees and sheets between 12.8 to 7.4 Ma;

180

3. Ponded lobes, erosional and low-relief channels between 7.4 and 5.5 Ma;

4. Channelized sheets, low-relief channel levees and MTDs between 5.5 to 3.7 Ma.

Further detail on understanding the vertical evolution in architectural style derives from plotting the location of the slope channels along the strain-distance plot of the faults they interact with, at the relevant time interval.

In terms of spatial distribution of the sedimentary systems, Figure 7-7a shows that the slope channels interacting with fault 22 form a distribution that mirrors that of the strain profile of the fault. In other words, the early slope channels (12.8 to 9.5 Ma; dark blue dots) were distributed along the entire strike-length of the fault (and beyond) and, as the fault grew, slope channels became progressively restricted in space. At the end of the peak deformation (7.4 to 6.5 Ma; see chapter 5) the channels were exclusively present on the crest of fault 22 (orange dots; Figure 7-7a). The implication of this in terms of depositional style is that channel architectures are inevitably linked to where along-strike they cross the fault and what was the geometry of the strain profile at the time they crossed it. For example, the early slope channels (12.8 to 7.4 Ma; dark and light blue dots) interacted with a number of unlinked fault segments that likely created only subtle topography, therefore, the channels were able to exploit topographic lows between the active segments and developed an aggradational architecture. The occurrence of erosional channel forms (red and orange dots; Figure 7-7a) instead relates to the time of complete fault linkage along strike at 7.4 Ma, when (a) the fault strain profile approached its present-day shape and (b) there was high cumulative strain in the centre of the fault that progressively decreased towards the lateral tips.

The channels that crossed the structure on its central crest (7-3, 6-3; Figure 7-5; Figure 7-7a) were more erosional than those diverted to the lateral tips (7-6; Figure 7-5; Figure 7-7a). This confirms that strain-distance plots can be used as proxies for topography where larger cumulative strain in the central portion of a fault should translate to more seabed topography promoting deeper channel incision.

The occurrence of ponded lobes (after 7.4 Ma) is restricted to the south-eastern half of fault 22 (Figure 7-7a), which coincides with a concave shape of the cumulative strain profile on and after 7.4 Ma, effectively representing a broad area of strain deficit. Therefore, I interpret that at the time of complete linkage, 7.4 Ma, the morphology of the seabed resembled that of an enclosed basin able to pond incoming flows. This is consistent with the onlap relationships shown in Figure 7-8.

Along fault 21 (Figure 7-7b), early slope channels (dark and light blue dots; 12.8 to 7.4 Ma) also interacted with a segmented fault array that allowed these systems to be widely distributed and aggradational (see above). In the same way as fault 22, the subsequent channels (7.4 to 6.5 Ma; red and orange dots) became spatially restricted and erosional. These channels were concentrated within the large zone of strain deficit along fault 21, suggesting the presence of a topographic low that captured the flows. Subsequently (6.5 to 3.7 Ma; purple and black dots), slope systems became more widely distributed as a direct result of decreasing strain rates that was translated into decreased topographic confinement. Finally, the distribution of ponded lobes is related to areas of greater structural growth that likely represented topographic highs (Figure 7-7b; see section 7.4).

However, the interactions between slope systems and structures cannot be fully understood without interpreting them in light of the mutual structural interactions occurring between across-strike faults (see chapter 3). In fact, why were channels at 6.5 Ma (orange dots in Figure 7-7a) only located on the crest on fault 22 and not diverted around it? As already discussed, 6.5 Ma represents the end of the period of maximum strain rates across the region. Because of the way strain has been measured in this study, high strain rates implicitly mean that clear growth sequences are present on both the limbs of a given fold, hence, indicate that topography has been created on the seabed during that interval (Suppe et al., 1992; Burbank and Verges, 1994; Burbank et al., 1996; Verges et al., 1996; Shaw et al., 2004; Clark and Cartwright, 2012a, b). As also discussed in chapter 5, the condition when folds are buried by sediments does not occur when sedimentation rates are high, because this leads to increased deformation rates too, but when sedimentation rates decrease. This confirms that periods of high strain rates must result is some topographic expression, which I am unable to quantify, and is out of the scope of this work. However, the fact that the channels at 6.5 Ma are able to cross the crest of fault 22 also implicitly means that sedimentation rates have started to outpace the growth of the structure, most likely in response to a relative decrease in growth rate. Nonetheless, one would expect that, if the structure was completely covered by sediments, slope channels could be present through the entire strike length of the thrust-fold if it does not have any seabed relief; yet they only occur on its crest, which is the least probable location.

Therefore, the answer most likely reflects how structural deformation is partitioned between structures across-strike.

For instance, it is evident that the area of maximum strain in the centre of fault 22 balances the zone of strain deficit at the same strike distance on fault 21 (particularly after 9.4 and 7.4 Ma; Figure 7-7). Similarly, the decreased strain at the lateral terminations of fault 22 is balanced by

increased strain along fault 21 (Figure 7-7). Nonetheless, between the two faults (22 and 21), fault 21 was the largest and exerted the strongest control on the structural and stratigraphic evolution of area 1. Until 9.5 Ma the two faults were mostly segmented, with leveed channels widely distributed along both faults, but after 9.5 and 7.4 Ma the greater development of fault 21 at the south-east and north-west portions forced the incoming flows towards its less-deformed centre. However, in order to achieve this, slope channels were forced to erode through the crest of fault 22 updip. This explains why channels at 6.5 Ma (orange dots) are only present at that specific location as well as their erosional character. Similarly, the concave shape on the southern half of fault 22 (Figure 7-7a), where ponded lobes occur, was directly induced by strain being accommodated by fault 21. The distribution of the ponded lobes along fault 21 (Figure 7-7b) also reflects flows being diverted to the south-east and north-west of the crest of fault 22 and blocked by the structural highs along fault 21. Therefore, while the sedimentary architecture depends on the specific location along-strike, this is ultimately controlled by structural interactions between faults across-strike.
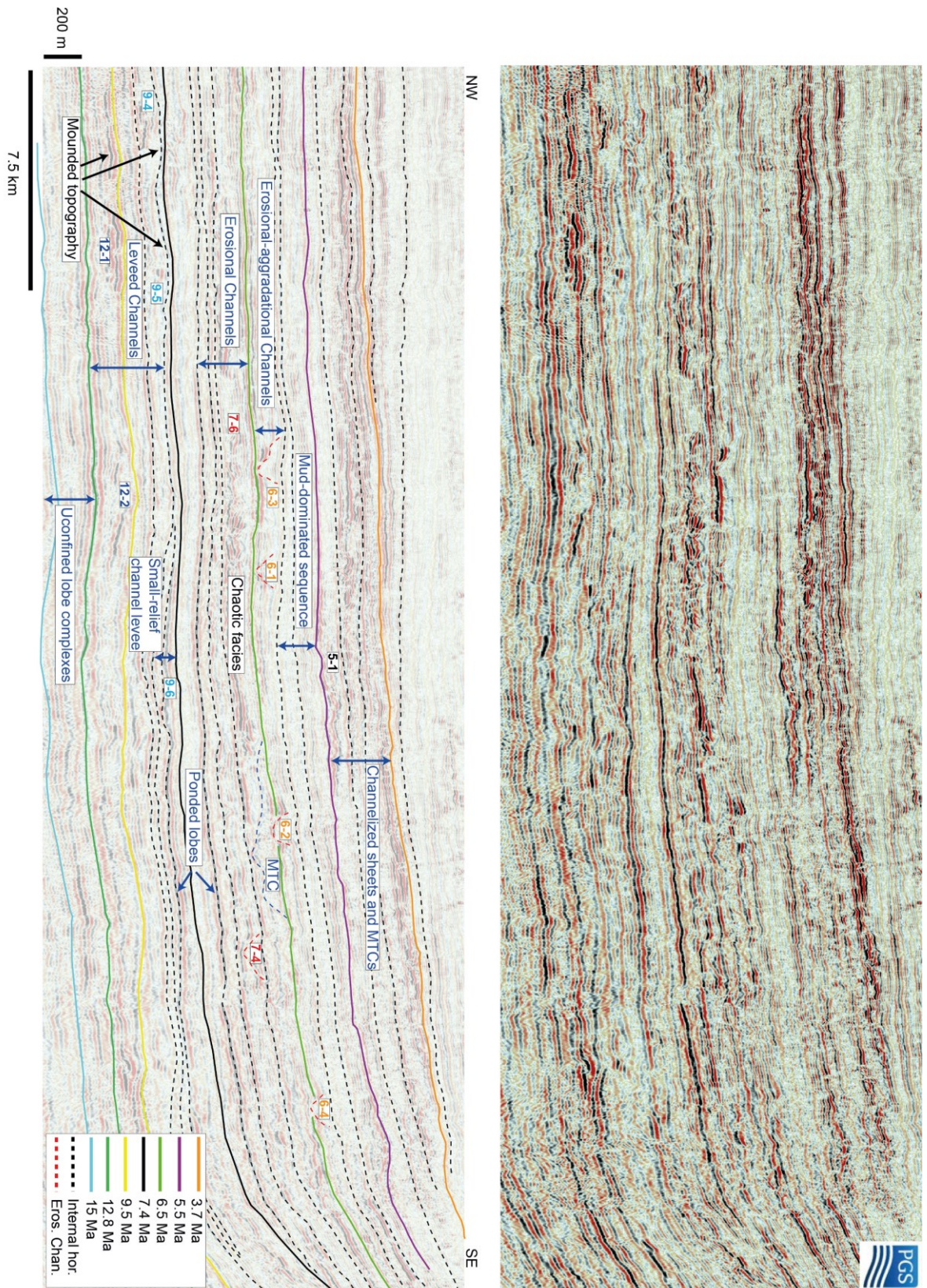
Figure 7-4: Seismic section "a" and interpretation (location in Figure 7-2). Note the mainly leveed channels until 7.4 Ma, followed by ponded lobes and erosional channels between 7.4 and 6.5 Ma. Channelized sheets and MTDs are dominant between 5.5 and 3.7 Ma. The numbered channels are specific examples shown in Figure 7-7 and the same as those shown in chapter 5.
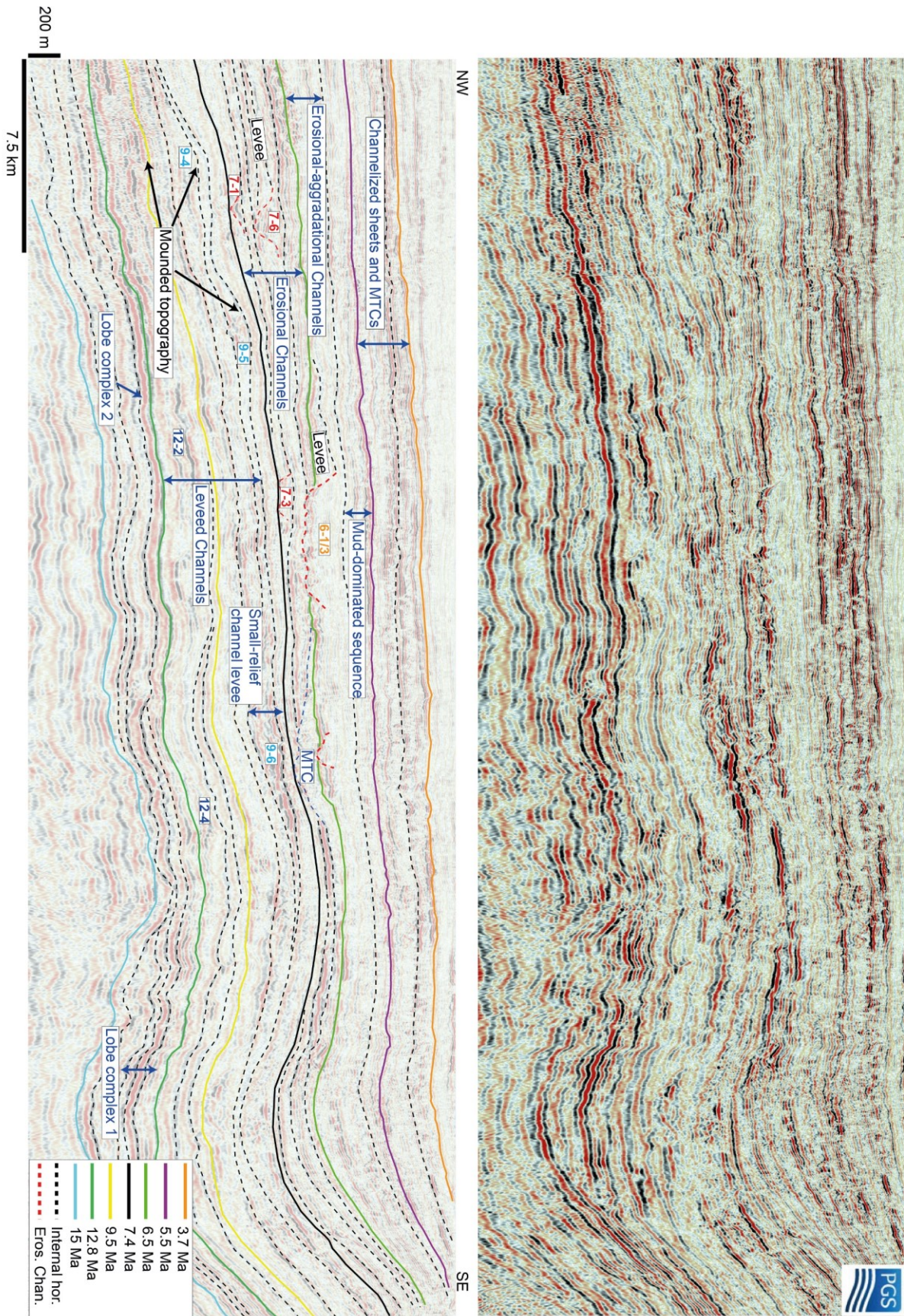
Figure 7-5: Seismic section "b" and interpretation (location in Figure 7-2). Note the mainly leveed channels until 7.4 Ma, followed by ponded lobes and erosional channels between 7.4 and 6.5 Ma. Channelized sheets and MTDs are dominant between 5.5 and 3.7 Ma. The numbered channels are specific examples shown in Figure 7-7 and the same as those shown in chapter 5.

185
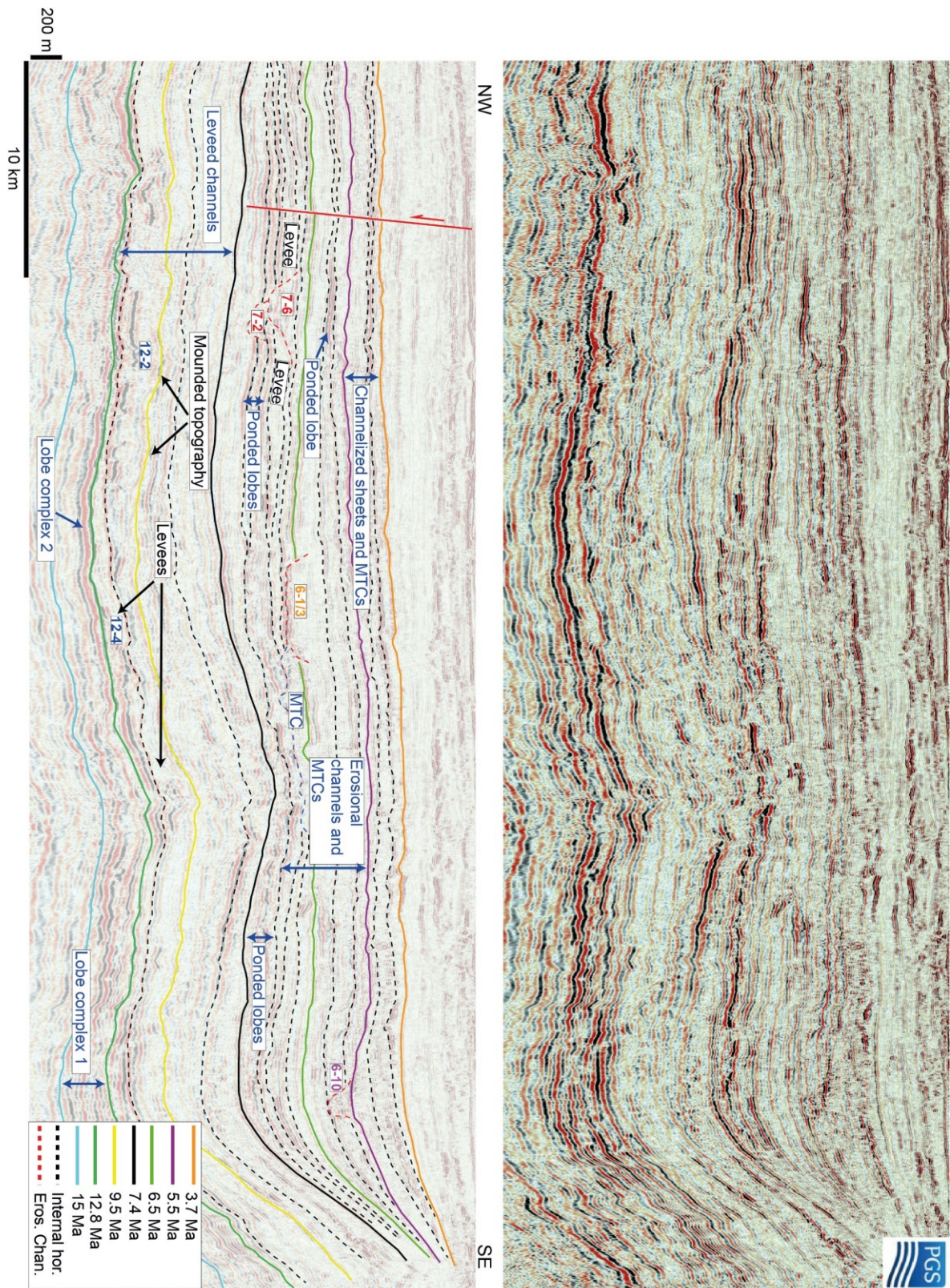
Figure 7-6: Seismic section "c" and interpretation (location in Figure 7-2). Note the mainly leveed channels until 7.4 Ma, followed by ponded lobes and erosional channels between 7.4 and 6.5 Ma. Channelized sheets and MTDs are dominant between 5.5 and 3.7 Ma. The numbered channels are specific examples shown in Figure 7-7 and the same as those shown in chapter 5.
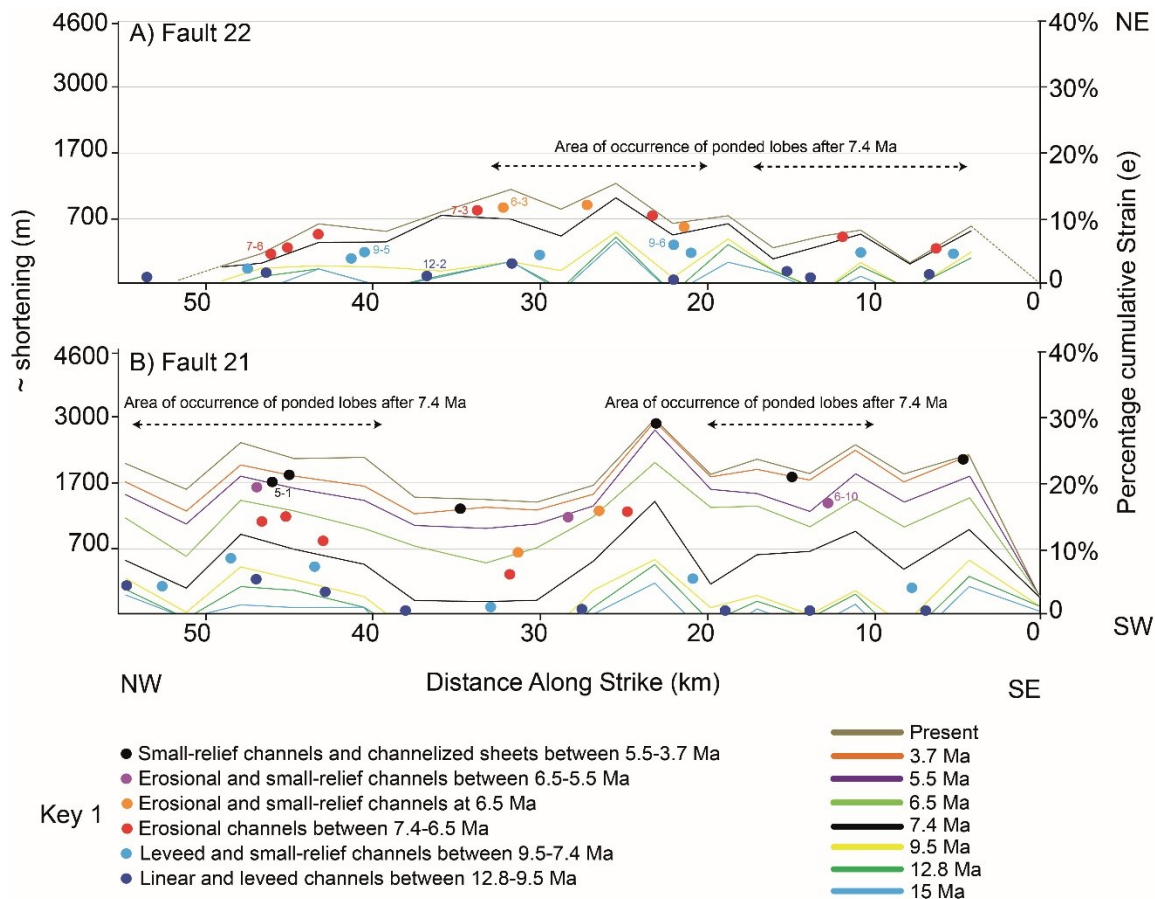
Figure 7-7: Strain-distance plots through time for fault 22 (A) and 21 (B). Fault 22 reached its max cumulative strain at 6.5 Ma and stopped growing thereafter, therefore, the present strain profile also coincides with the 3.7, 5.5, and 6.5 Ma profiles. The distance along strike and architectures of the various slope channels (shown in sections a, b and c) is also shown. Channels are plotted according to their interval of occurrence. To note the wide distribution of the leveed channels between early fault segments and the progressive spatial restriction as the faults grow as well as the transition into erosional forms. Erosional channels occur at 8 to 10 % of cumulative strain.
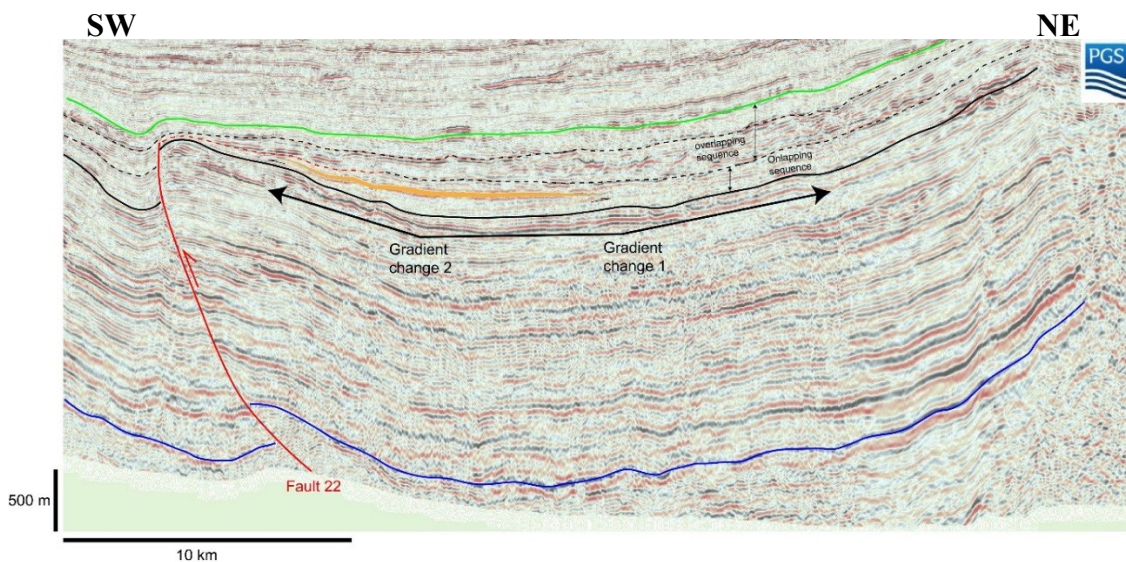
Figure 7-8: Seismic section "d" (location in Figure 7-2). A lobe (yellow shape) is ponded inboard of fault 22 after the 7.4 Ma horizon (black). Although the present-day structure of the 7.4 Ma horizon has been modified/exaggerated by subsequent deformation, it shows two main gradient changes that coincide with the areal distribution of the ponded lobe. This suggests that the gradient changes were originally present, therefore, the deposition of the ponded lobe started 10-15 km up dip of the controlling structure. Blue horizons represent the base of Agbada Formation.

187

7.3.2   Core of the FTB (areas 2 and 3)

The stratigraphic evolution in the core of the fold belt is well-represented by three seismic sections (Figure 7-9, Figure 7-10, Figure 7-11), and the discussion will focus on area 3.

This central zone is part of the inner domain of the fold belt and the vertical change in architectural style follows the same chronology observed in area 1. Because of its more distal location the core of the fold belt features overall fewer slope channels, however, these are bigger in dimension and their architecture much more well-defined. Four broad facies associations are observable in area 3:

1. Unconfined lobes between 15 to 12.8 Ma;
2. Linear and leveed channels, minor MTDs and low-relief channel levees between 12.8 to 7.4 Ma;
3. Erosional channels between 7.4 and 5.5 Ma;
4. Channelized sheets, low-relief channel levees and MTDs between 5.5 to 3.7 Ma.

As discussed previously, deformation in the core of the fold belt results from five faults (20, 19, 18, 17 and 15) and can be approximated by their aggregate profile (Figure 7-3 and Figure 7-12d). This helps us to assess the architectural evolution of the area. As for area 1, leveed channels (9-8) developed when the fault system was immature with unlinked segments, exploiting zones of low cumulative strain, which favoured an aggradational style (Figure 7-12a, b). Subsequently, erosional channels (7-3, 7-4, 6-5 and 6-10) developed during times of complete fault linkage (along and across-strike), increased strain rates and strong interactions between faults, as they often exploited the zones of greater structural development (Figure 7-12a, b). Again, understanding how cumulative strains and strain rates evolved through time, and the identification of the most deformed zones along the strike of faults versus the relative positions of the slope channels, allow prediction of their resulting architecture. However, the ability to predict these relative locations where channels cross individual folds derives from the identification of:

1. The largest structures in an array with dominant topographic effect.
2. Their combined "topographic" effect across strike (e.g. Figure 7-12d).
3. The strain profile of the most up dip structure responsible for the earliest diversion of sedimentary systems (Figure 7-12a).
4. The distribution of interval strain rates along the strike of each fault.

For example, two sets of erosional channels (7-3, 7-4 and 6-5, 6-10) were originally diverted to the north-west and south-east of fault 20 (most inboard fault) to avoid the area of greater

structural development in its centre (Figure 7-12a). However, channels 6-5 and 6-10 subsequently exploited the crest of fault 19 (Figure 7-12b) because the overall topographic effect of the five faults across strike created a depression in area 3 (Figure 7-12d).
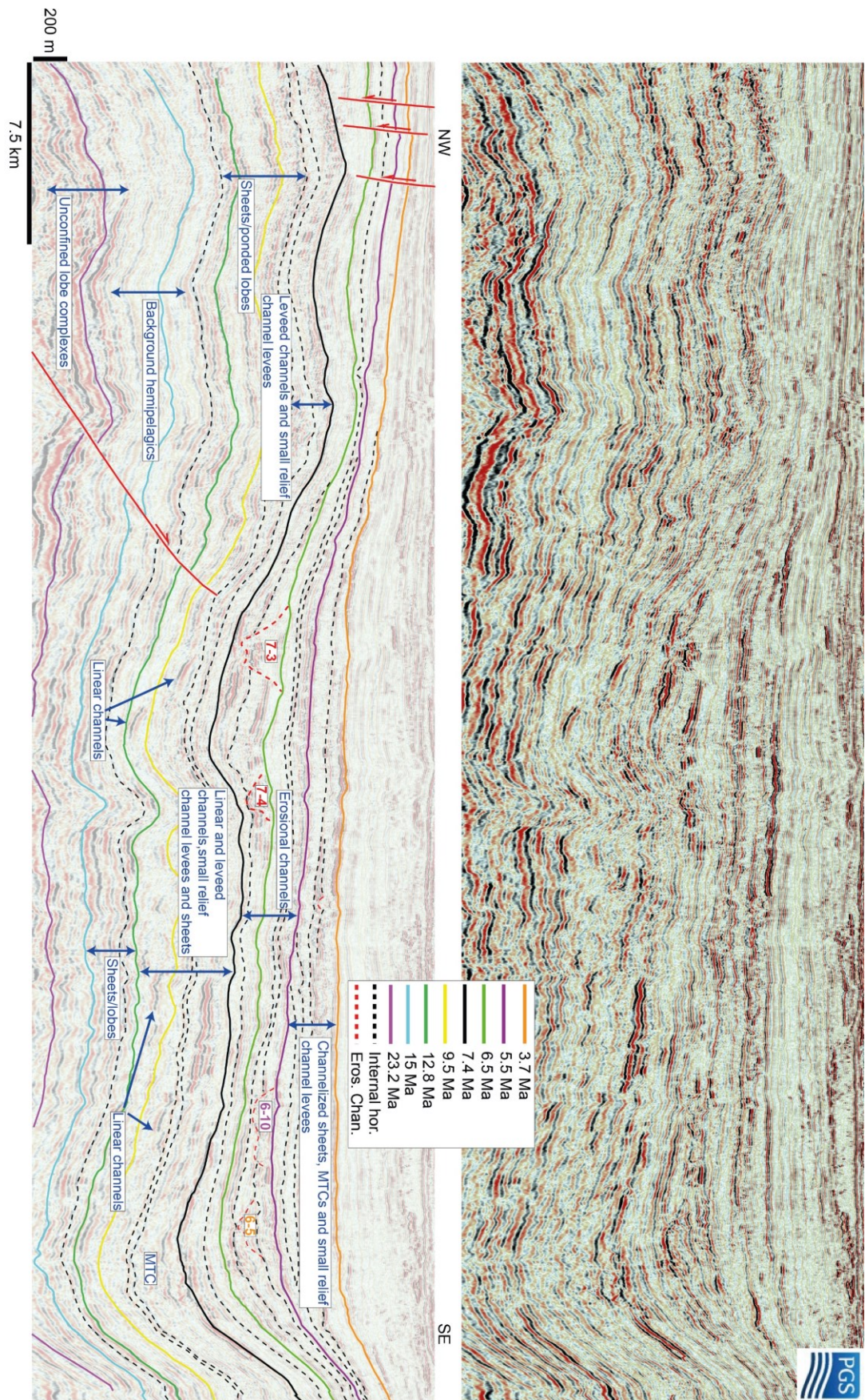
Figure 7-9: Seismic section "e" and interpretation (location in Figure 7-2). Note the mainly leveed channels until 7.4 Ma, followed by the large erosional channels between 7.4 and 5.5 Ma. Channelized sheets and MTDs are dominant between 5.5 and 3.7 Ma. The numbered channels are specific examples shown in Figure 7-12 and the same as those shown in chapter 5.
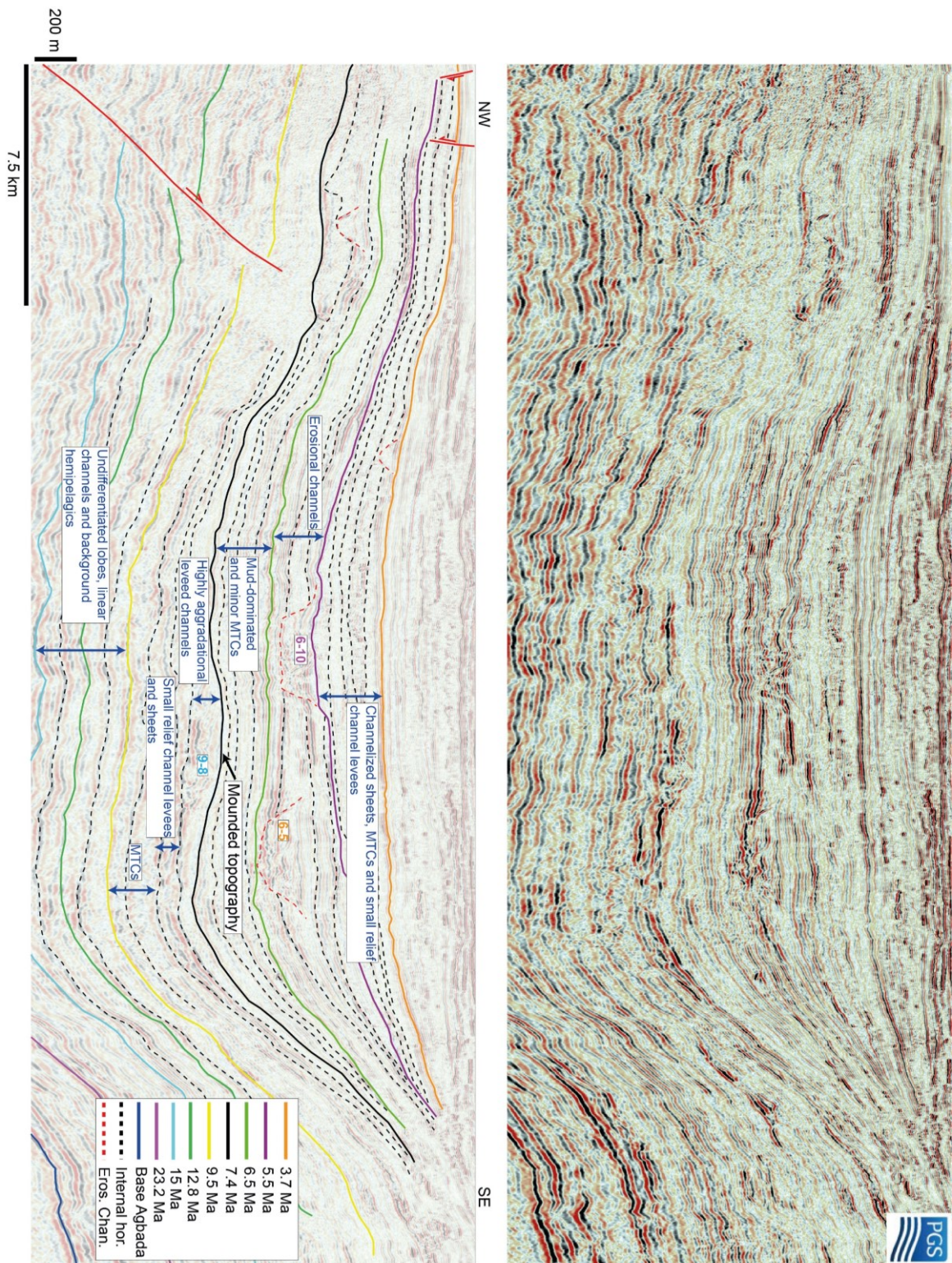
Figure 7-10: Seismic section "f" and interpretation (location in Figure 7-2). Note the mainly leveed channels until 7.4 Ma, followed by the large erosional channels between 7.4 and 5.5 Ma. Channelized sheets and MTDs are dominant between 5.5 and 3.7 Ma. Note how channels 6-5 and 6-10 compensate the topography created by channel 9-8. The numbered channels are specific examples shown in Figure 7-12 and the same as those shown in chapter 5.

191
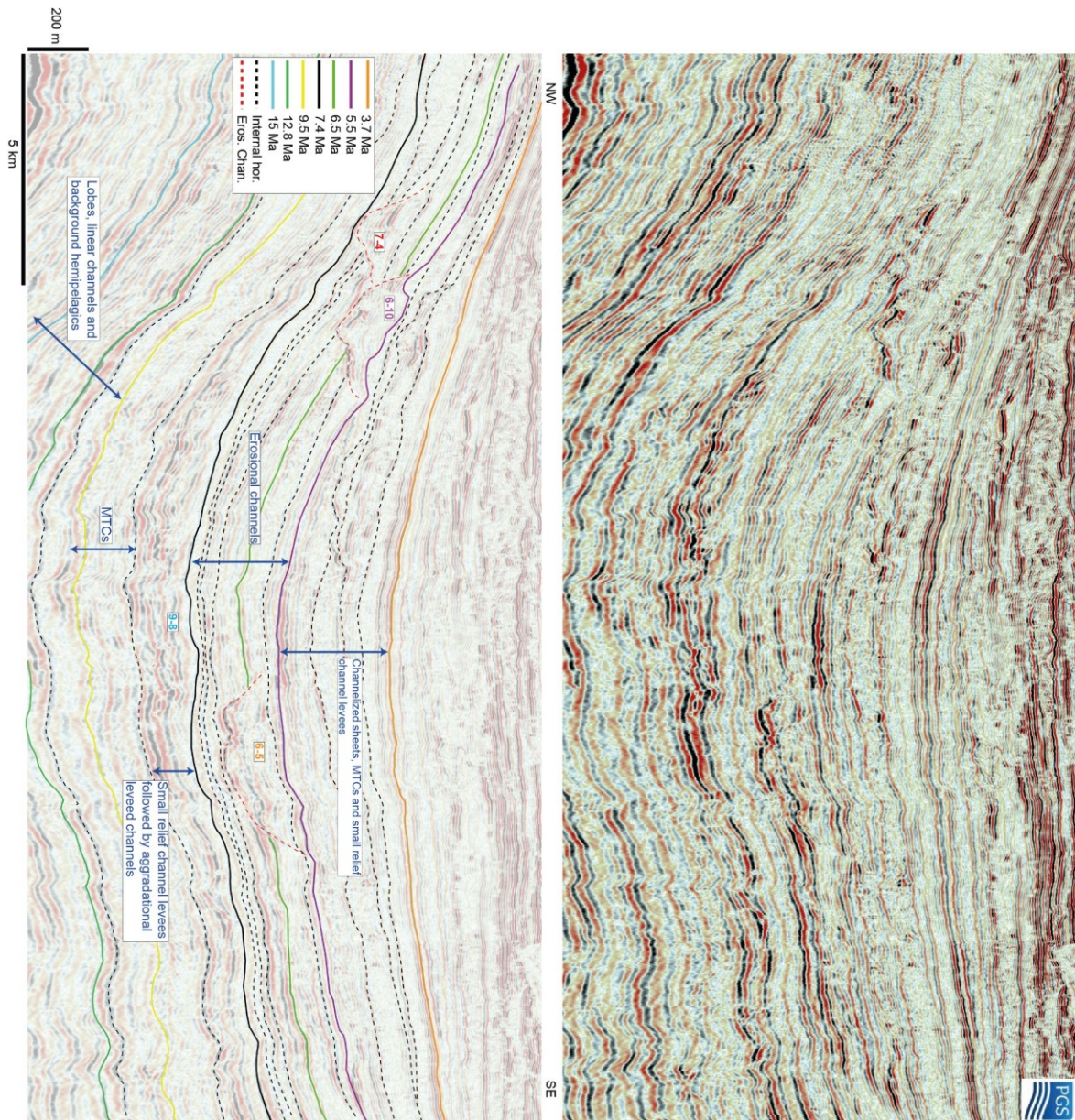
Figure 7-11: Seismic section "g" and interpretation (location in Figure 7-2). Note the mainly leveed channels until 7.4 Ma, followed by the large erosional channels between 7.4 and 5.5 Ma. Channelized sheets and MTDs are dominant between 5.5 and 3.7 Ma. The numbered channels are specific examples shown in Figure 7-12 and the same as those shown in chapter 5.

192

Figure 7-12: Strain-distance plots through time for fault 20 (A), 19 (B), 18 (C). The aggregate profile in (D) is constructed with the contribution of two more faults not shown here. The distance along strike and architectures of the various slope channels (shown in sections e, f and g) is also shown. Channels are plotted according to their interval of occurrence. To note the leveed channels (9-8) between early fault segments and the erosional character of channels 6-5 and 6-10 as they are forced to erode into the crest of fault 19 by the 3D topographic effect of multiple faults. Erosional channels occur at 8 to 10 % of cumulative strain.
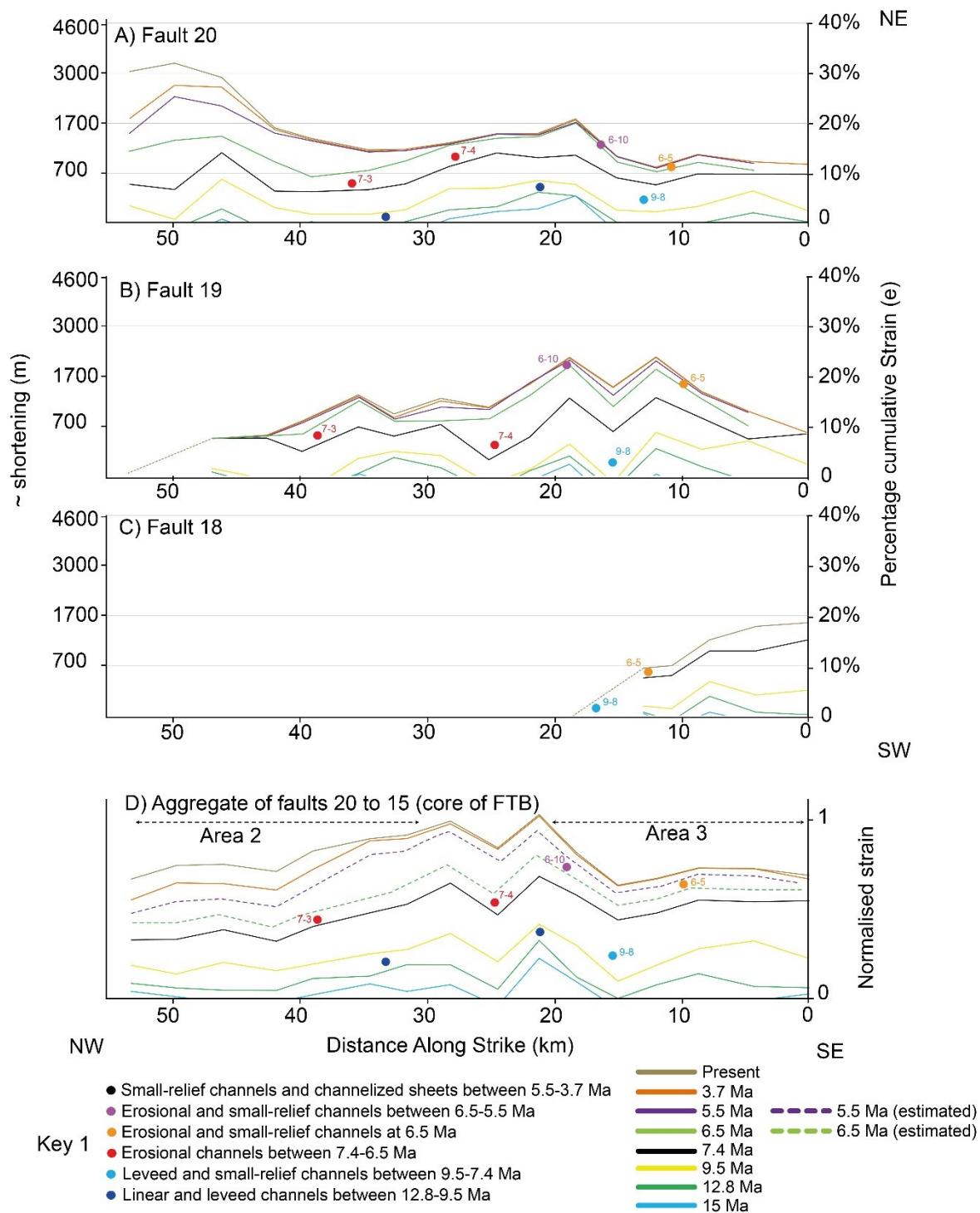
7.3.3 Area 4

The evolution of the stratigraphic architecture of area 4 (outer domain) is shown in Figure 7-13 and is characterized by the succession of three main facies associations:

1. Background hemipelagic sediments interbedded with linear channels and minor sheets between 15 and 9.5 Ma;

2. Minor MTDs followed by mostly leveed channels between 9.5 and 6.5 Ma (and slightly beyond, ca 6 Ma);

3. Erosional channels and MTDs between 6 and 3.7 Ma.

The vertical changes in architectural style in area 4 occurred later with respect to the inner domain, reflecting the basinward migration of the deformation front. In effect, in area 4, leveed channels have been the dominant style for a longer time interval, and this resulted in the simultaneous occurrence of contrasting depositional styles across the slope (e.g. erosional inboard vs leveed outboard). To understand the reasons behind the diachronous development of the channel architectures, it is important to assess how structures grew in area 4 with respect to the inner domain. Area 4 comprises three faults (11, 12, 14; Figure 7-14) and fault 11 is the largest and dominant. Faults 12 and 14 are only partially present in the area and both die out in the centre (Figure 7-14a). Fault 11, which covers the entire strike length of area 4, also shows a persistent location of strain deficit in the centre (Figure 7-14b) and when the three faults are summed together, this is even more accentuated (Figure 7-14c). Even at 7.4 Ma, fault 11 was partially unlinked in its centre and the subsequent phase of faster growth (from 7.4 to 3.7 Ma) was still concentrated to the edges of the area, resulting in a v-shaped strain profile. This structural evolution is closely linked to the growth history of the more proximal structures. In fact, the large zone of strain deficit in the centre of area 4 results from most of the strain being accommodated by the core of the fold belt which lies directly up dip (Figure 7-14c). The slope channels were, therefore, continuously deflected towards this central area of low topography and were leveed-confined. In effect, the evolution of area 4 confirms that independently from the timing of the main structural growth, channels will have an aggradational architecture as long as they are able to exploit early sites of fault linkage between segmented faults that have not yet accumulated substantial strain (blue, red and orange dots in Figure 7-14). Slope channels will continue to have an aggradational architecture until the time of complete linkage, which is then followed by an increase in strain rates which, in turn, leads to the accommodation of larger cumulative strains. When substantial strain eventually occurs, which for fault 11 happens after ca. 6 Ma, slope channels alter their architecture and are erosional (purple and

black dots in Figure 7-14). However, because of the absence of a structural culmination (as in the centre of area 4) the erosional channels tend to stack vertically rather that laterally.
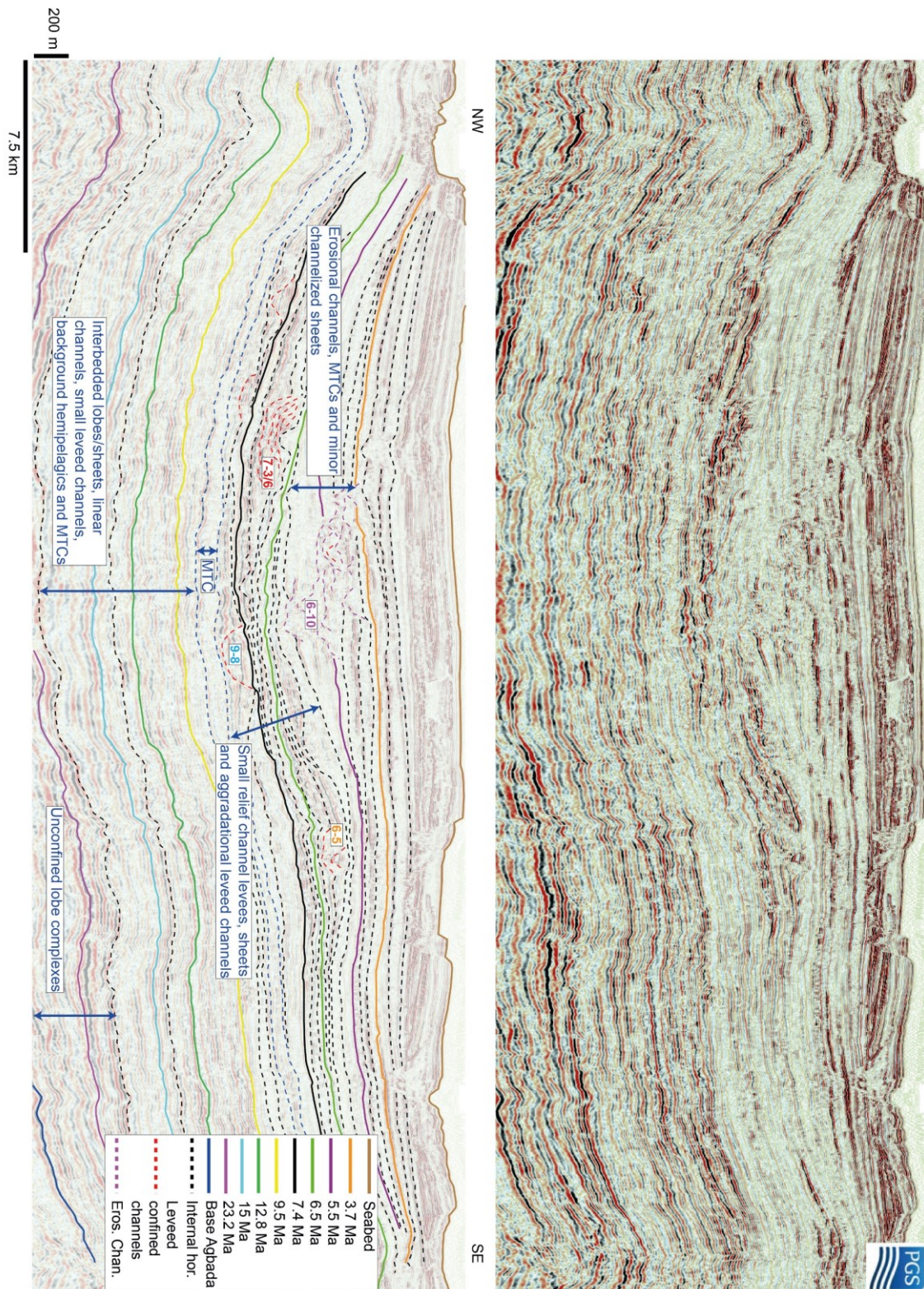
Figure 7-13: Seismic section "h" (through the outer domain) and relative interpretation (location in Figure 7-2). Note the mainly leveed channels until 6.5 Ma and slight after (delayed respect to the inner domain), followed by the large v-shaped and vertically stacked erosional channels between 6 and 3.7 Ma. The numbered channels are specific examples shown in Figure 7-14 and the same as those shown in chapter 5.
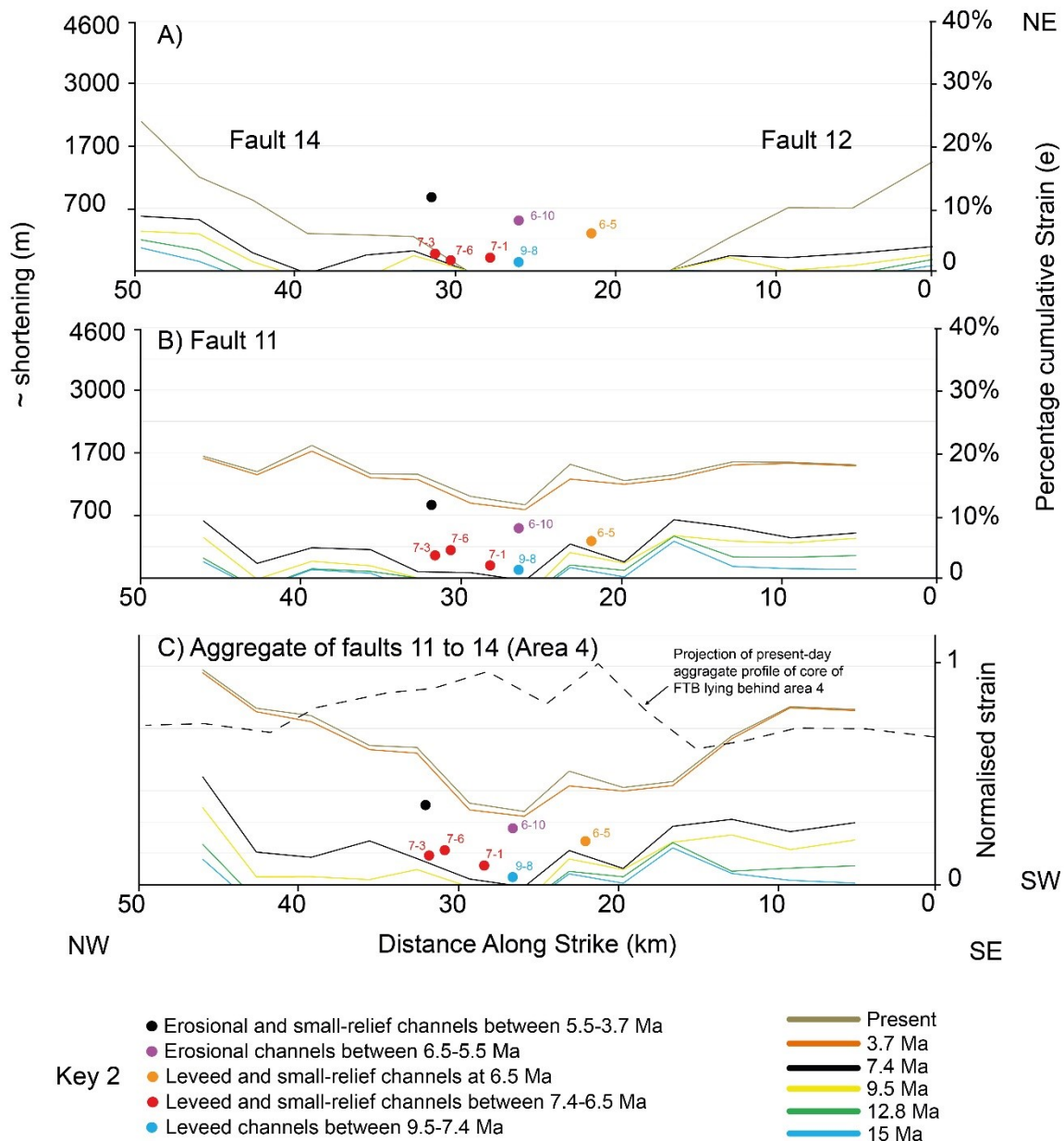
Figure 7-14: Strain-distance plots through time for fault 14 and 12 (A), 11 (B), and their aggregate profile in (c). The distance along strike and architectures of the various slope channels (shown in sections h) is also shown. Channels are plotted according to their interval of occurrence. All channels are deflected towards the less-deformed centre of area 4 and only become erosional after 6.5 Ma when fault 11 has accumulated 8 to 10 % of cumulative strain. The steep lateral gradients have a secondary effect on the channels' architectures by focusing the flows in the centre.

7.4 Ponded lobes

Although channel forms have been the dominant architectural style throughout the deformation history of this part of the Niger Delta, ponded lobes characterize the lower part of unit 3 in area 1 (7.4 to 6.5 Ma) and dominate the depositional style for approximately 300 ka. As for channels, the distribution of the ponded lobes can be carefully understood by analysing the strain profiles of the structures that constrain the area where ponding occurs. The concept of ponding itself (Van Andel and Komar, 1969; Pickering and Hiscott, 1985; Lomas and Joseph, 2004) requires

196

the simultaneous occurrence of a negative topography to capture the flows and a positive topography to block them. However, under what circumstances does this condition occur? In chapter 5 it has been shown that, as opposed to channels, ponded lobes occur up dip of the zones of relative greater strain rate along the strike of faults, therefore, where topography is being created. However, in order to capture the flows towards those locations, a depression must have been originally present otherwise flows would be simply diverted away from the growing topography.

The results presented here complete the picture and show that ponded lobes occur in areas of lows of the strain profiles where the seabed morphology would have been that of an enclosed basin (Figure 7-7). This is represented by lobes occurring above the 7.4 Ma horizon in Figure 7-6 where the horizon has a concave shape.

This condition occurred in the study area, soon after 7.4 Ma, when faults linked along and across strike and strain rates reached the greatest. In effect, ponded lobes occur at the very beginning of periods of high strain rates which occur after faults have completely linked and have an inherited asymmetry in the strain-distance profiles that shows the most significant lateral gradient changes (Figure 7-7). It is this asymmetry that creates topographic depressions able to capture the flows.

It is important to note, however, that the asymmetry of the strain-distance profiles is caused by a series of strain transfer mechanisms to adjacent folds across strike as described in chapter 3. This is, in fact, observed in area 1 where the zone of occurrence of lobes behind fault 22 is caused by fault 21 that accommodates most of the strain (Figure 7-7). It follows that the distribution of ponded deposits has also to be interpreted in the light of mutual interaction between folds across strike.

With time, these depressions are progressively filled, and the topography smoothed, as well as the strain-distance profile. As a result, channels can then overcome the obstacle and erode into the crest of folds (chapter 5). This sequence of events (lobes followed by channels) has been previously reported (Fonnesu, 2003: Hay, 2012; Prather et al., 1998, 2012) and is recorded stratigraphically by two onlapping-overlapping sub-units, both within unit 3 (Figure 7-8). This also suggests that, although the strain rates have been averaged between 7.4 and 6.5 Ma, the relative rates of deformation and sedimentation changed within the unit. While it is generally proposed that sedimentation (and erosion) are responsible for smoothing a "static" topography in order to produce a lobe-channel sequence (Prather et al., 1998, 2012; Deptuck et al., 2012; Hay, 2012), we interpret this in terms of dynamic interactions between deformation and

sedimentation where the eventual overlap of the sediment (and bypass of flows) is actually caused by a relative decrease in strain rates.

This work has demonstrated that high strain rates developed on a fold limit the down-dip extent of ponded lobes and the presence of strain minima on the strain-distance profiles limits their lateral extent. However, structures also limit the up-dip extent of the lobes as they affect seabed gradients up to 10-15 km up dip of the fold axis. This is shown in Figure 7-8 where a lobe is ponded inboard of fault 22, soon after 7.4 Ma, as it onlaps the depression both up and down dip. Although the present day structure of the 7.4 Ma does not reflect the seabed morphology at the time of deposition, it does show two main gradient changes along it that appear to govern the location of the lobe deposit. The up dip pinch out of the lobe corresponds to the first gradient change and, after thickening in the centre of the depression, the lobe starts to thin in correspondence of the second gradient change until its down dip pinch out. The magnitude of the gradient changes has been enhanced by ongoing folding, however the geometry of the deposit suggests that structurally-driven seabed gradients were present at 7.4 Ma. I suggest that the up dip termination of the lobe reflects the position where the seabed was first impacted by motion on fault 22 and where incoming flows changed from being channel-confined to unconfined.

7.5 Towards a predictive facies model

The results presented above and in the previous chapters demonstrate that predictions on the spatial distribution and architecture of sedimentary systems that interact with growing thrust-folds are dependent upon simultaneously analysing the effect of multiple structures across strike. In other words, to understand how sedimentary systems respond to growing seabed deformation, structures cannot simply be analysed in isolation.

Consequently, this thesis argues that quantification and reconstruction of how deformation was accommodated along and across-strike, as well as through time, is required. Quantifying the growth history of all the structures within an array gives direct knowledge of the following:

1. The earliest structural framework (i.e. distribution of early fault segments and linkage zones);
2. Timing of complete linkage along and across strike;
3. Timing of the increase in strain rates in different parts of the basin;
4. Quantification of the size of the structures and their evolution through time;
5. Identification of strain deficits and maxima in the strain-distance plots;

6. Identification of the largest and longest-lived structures in an area with dominant effect on the creation of seabed topography;

7. The ability to recreate the geometry of the receiving basins (i.e. pre and early growth sequences) by determining the contributions of all the faults involved.

Unravelling all the above variables is crucial for the development of a predictive facies model applicable to other deep-water fold and thrust belts. My results clearly indicate that when faults are segmented (both along and across strike; 15 to 9.5 Ma) slope channels can be widely distributed across the basin as they exploit multiple linkage zones along the strike of faults. The channels may follow a tortuous route through a population of incipient folds and their overall distribution can be partially dictated by compensation of the topography created by the previous systems. In fact, because they largely avoid the crests of the incipient folds, they aggrade with time and develop levees. This is also promoted by the fact that faults at this time grow primarily by accruing lateral extent rather than strain and uplift (chapter 3), therefore, not favouring channel incision. Most importantly, at the early stages of deformation, none of the faults has yet a dominant effect on the creation of topography and/or on how strain is accumulated on the neighbouring faults across strike as they are not yet linked through the common detachment and are, therefore, equally developed.

However, when faults completely link (7.4 Ma), particularly across-strike through detachment linkage, the resulting increased strain rates are directly translated into accumulation of strain (and uplift) at nearly constant strike length. When detachment linkage occurs, faults start to efficiently transfer strain across strike in a complex 3D interaction that creates highly asymmetric strain-distance profiles that likely cause topographic changes on the seabed, and which can be approximated by the aggregate strain profiles of multiple faults (Figure 7-12d). At this time, some of the faults become larger and dominant, in respect to the surrounding faults in the area, having seabed expression and therefore exert stronger controls on the distribution of channels. In this scenario, the location of channels and the channel architecture is entirely dependent on the relative size and spatial arrangement of the other structures across strike. In fact, the results of this study have highlighted that at least two end-member cases may simultaneously exist across the slope, which are illustrated in Figure 7-15. In the first case, a small thrust-fold (A) is up dip and there is a linked strain deficit in the centre of a larger down dip structure (B) in the foot-wall. As the small fold (A) dies out laterally, the large structure (B) shows two corresponding strain maxima (B1 and B2). Because the strain maxima on B have greater topographic expression than the crest of A, slope channels will respond to fault B

199

and will be deflected towards the centre of B, where a strain deficit (a depression) is present. However, by doing so, channels are forced to cross A on its crest, hence, eroding into it. This type of fold interaction has been dominant in the inner domain of the fold belt and is shown by fault 22 and 21 in area 1 (Figure 7-7) and by the faults in area 3 (Figure 7-12).

The second type of fold interaction (Figure 7-15) shows an opposite scenario where a very large fold (C) is present up dip of two (or three) smaller structures (D, E) in its foot-wall. The large amount of strain accommodated by C leaves a large undeformed area in the foot-wall where D and E tip out. Therefore, slope channels are diverted around C and subsequently deflected towards the undeformed foot-wall. However, their course is also confined by the topography of folds D and E that focus the channels around their lateral tip points. This causes the channels to develop a highly aggradational architecture as subsequent flows are persistently focused on the same location (Figure 7-15). This mode of interaction has been dominant in area 4 (outer domain; Figure 7-14). During the time of peak deformation (7.4 and 6.5 Ma) these two modes coexisted in the study area and resulted in the simultaneous occurrence of different architectural style across the slope.

As previously suggested, the transition from leveed into erosional forms is predicted to occur when the structures have both linked and attained a substantial amount of deformation, in addition to where the structure is crossed. Our data indicate that, along faults 22, 21, 20, 19 and 11 (Figure 7-7, Figure 7-12, Figure 7-14), erosional forms consistently appear only when faults have accumulated between 8 to 10 % of cumulative strain (550 to 700 m of shortening), with the most erosional forms (6-5, 6-10; Figure 7-12b) occurring at cumulative strains of 15-20% (1150-1700 m of shortening). However, whether these large cumulative strains are developed on the crest of a fault (as for fault 22; Figure 7-7a) or in a zone of relative strain deficit (as for fault 11; Figure 7-14b, c), has an impact on the way erosional channels stack as well as on their external geometry. This is synthetized in Figure 7-15 where the channels exploiting the crest of fold A are laterally offset/stacked as they also respond to its subtle seabed topography and have a flat base, whereas those flowing between folds (B1) and (B2) will stack vertically and have an external "V" shape.

With the progressive basinward migration of the deformation front, the most inboard structures will be eventually abandoned, and fold A will be completely buried, while strain rates decrease on folds B1 and B2 and their topography is smoothed by the coeval deposition of MTDs and widespread channelized sheets within a large, newly-formed, shallow-ponded basin.

However, as the migrating deformation front reaches the outer structures, folds D and E will eventually merge, and the newly-linked structure will experience increased strain rates which

will develop larger cumulative strain (Figure 7-15). As a result, channel styles will also become erosional, however, with a delay of approximately 1 Myr respect to the inner, up dip structures. Of course, the delay in the occurrence of erosional forms between the inner and outer structures will depend on the rate of frontal migration of the deformation front.

In summary, in deep-water fold and thrust belt, an accurate prediction of channel distribution and architecture requires a careful assessment of both cumulative strains and strain rates; i.e. the topography that has been created plus that being created. While the absolute value of cumulative strain and the degree of fault linkage dictate the overall architecture of submarine channels, the specific position of the crossing points will depend on:

1. how strain rates are distributed along the strike of a structure, where channels preferentially exploit locations of low strain rate (chapters 5 and 6)

2. the location of strain deficits in the strain-distance plots, which often coincide with the earliest sites of fault linkage (chapters 3 and 5)

3. the 3D spatial arrangement of multiple folds of variable size (see above).

However, during periods of intense deformation, variable strain rates along-strike can cause steep lateral gradient changes that have a secondary control on channel architectures by favouring channel incision. This is observed along fault 11 where steep lateral gradients have contributed to cause the channels to be stacked vertically and v-shaped (Figure 7-14, Figure 7-15).

Figure 7-15: Schematic model for the development of synchronous and different architectures based on the degree of fault linkage, size and spatial arrangement of multiple fault/folds in 3D.

7.6 Implications for oil and gas exploration

Understanding and reconstructing the tectono-stratigraphic evolution of deep-water fold and thrust belts is particularly important for the oil industry as commonly hydrocarbons are structurally trapped within hangingwall anticlines so that reconstructing the timing of trap formation with respect to oil or gas generation, migration and charging becomes critical. Understanding the along-strike evolution of thrust-faults is also very important for hydrocarbon exploration as it will dictate the geometry and size of anticlinal traps. Moreover, the identification of thrust reactivation or episodic growth patterns is critical to mitigate the risk associated with leakage through faults which are later reactivated. Finally, as deep-water sedimentation occurs at the same time as the growth of fold belts, understanding and quantifying the tectonic forcing on sedimentation is necessary to predict the distribution and architecture of the main reservoir facies and to assess the potential for combined structural and stratigraphic traps.

7.6.1 Characterization of the main phases of slope development

7.6.1.1 Stratal geometries and associated facies

The analysis conducted in chapters 3, 4 and 5 has identified three main phases of development of the Niger Delta slope, which are summarized in (Figure 7-16) and characterized by specific stratal geometries and slope facies architectures. A (1) pre-kinematic section is present from the base of the Agbada Formation until 15 Ma. This sequence is characterized by sub-parallel reflectors across the slope comprising facies dominated by base of slope lobe complexes and multiple small slope channels. The (2) syn-kinematic section starts at 15 Ma and is divided into three sub-phases. The early syn-kinematic (2a; 15 to 7.4 Ma) is also identified by sub-parallel reflectors comprising larger channel levee complexes deflected by the early growth of individual thrust segments. Locally growth stratigraphy can be seen on individual folds. The main syn-kinematic section (2b; 7.4 to 6.5 Ma) is characterized by thickening-thinning of the stratigraphy on all the thrust-folds of the inner domain, however, sub-parallel reflectors are still present on the outboard structures. Facies are dominated by sheets sands that onlap the inboard structures followed by erosional channels that cut through and/or deflect around the inboard structures. Simultaneously, large leeved channels deflect around the tips of the outboard structures.
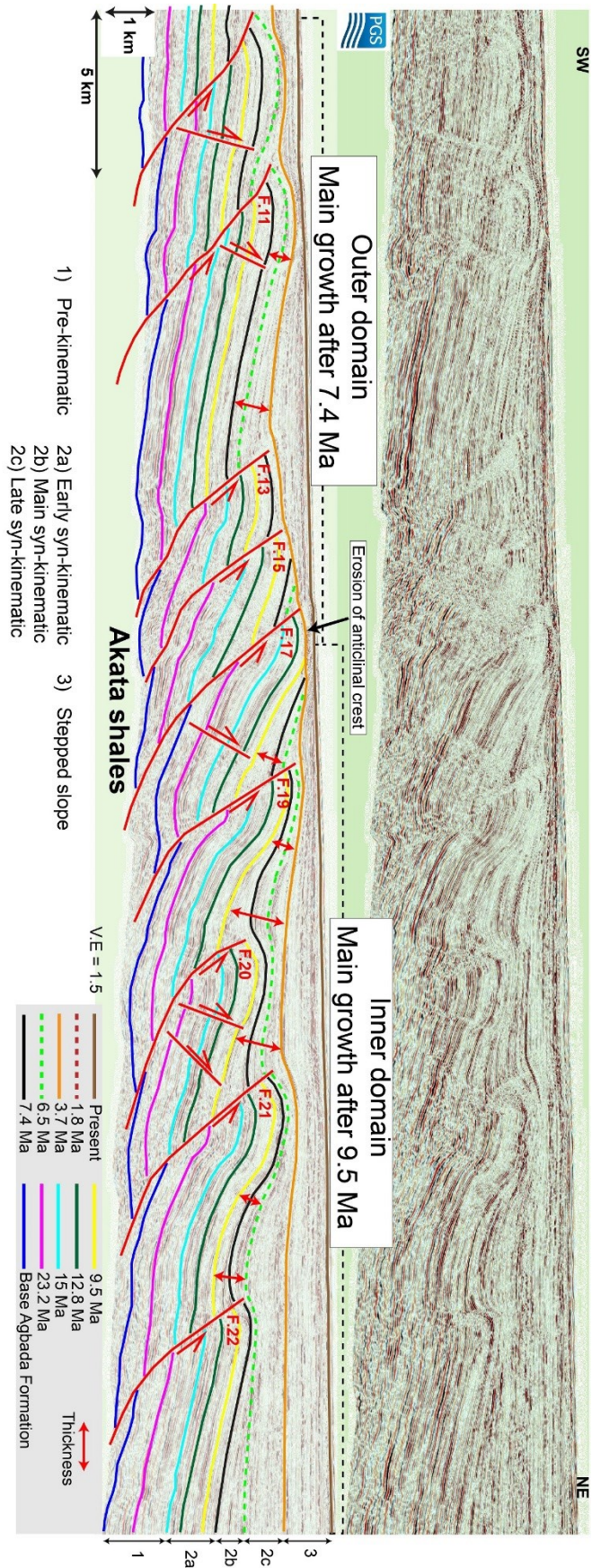
Figure 7-16: Seismic section "i" and relative interpretation (location in Figure 7-2). The section highlights the stratal geometries associated with different phases of slope development.

The late syn-kinematic section (2c; 6.5 to 3.7 Ma) is dominated by moderate thickening-thinning of stratigraphy across the entire slope testifying the basinward migration of the deformation front and the decreasing strain rates. Facies are dominated by MTDs and channelized sheets in the inner domain and erosional channels in the outer domain. During the last phase (3; 3.7 Ma to present) the slope progressively acquires its present, stepped configuration. Facies are dominated by MTDs and very large leveed channels that exhibit variable degree of incision, however, these are not the focus of this study and will not be discussed further.

7.6.1.2   Evolution of thrust folds and anticlinal traps

This work has demonstrated that all thrusts on the lower slope started at about the same time (15 Ma; chapter 3) and developed in a non-piggy back fashion apart from a wave of deformation that propagated basinward at 7.4 Ma. This also means that all the thrusts in the belt could have provided a migration focus since 15 Ma. Our data indicate that, at least, until 9.5 Ma the thrusts were highly segmented and the related folds (potential traps) small and disconnected. However, between 9.5 and 6.5 Ma (depending on the specific structure) the thrust-folds progressively linked along and across strike through the detachment and this moment marks the time when:

1. The thrusts connected to the basal detachment and likely provided potential migration pathways;
2. The strain-distance profile of each thrust took a similar shape to the present day and so did the related anticlines;
3. Strain rate increased by accumulation of displacement/uplift and folds amplified increasing their potential trapping capacity.

The results also show that the inboard structures grew rapidly, forming larger traps, between 9.5 and 5.5 Ma, whereas the growth of the outboard thrusts was delayed from 7.4 to 3.7 Ma. Moreover, episodic reactivation events have been identified on inboard structures (fault 21) at times when the deformation was concentrated further outboard (after 3.7 Ma), which could increase the risk of trap leakage on the inboard structures.

7.6.2   Type and occurrence of reservoir facies and trapping mechanisms

A significant aspect of the research findings is that what would be generally considered the top of the pre-kinematic section (or start of deformation; 9.5 Ma horizon; Wiener et al., 2010; Kreuger and Grant, 2011) based on the occurrence of visible growth strata is, in reality, the moment when thrusts-folds, for the first time, took on a similar shape to the present day as a result of progressive linkage that completed with detachment linkage at 7.4 Ma, and this marks the most important boundary impacting on the type of reservoir facies and trapping mechanisms (Figure 7-17). After 7.4 Ma strain rates increased markedly causing visible growth strata along the strike of linked structures, however, deformation was ongoing since 15 Ma and slope facies interacted with these early growing folds. It follows the both the pre-kinematic (1) and the early syn-kinematic (2a) sections are today incorporated within the hangingwall and footwall sides of the mature thrust-folds. Therefore, the basal lobe complexes, linear channels, and the leveed-channels with associated frontal and crevasse splays can all be found (today) folded into anticlinal traps or in footwall synclines as well as tilted on the back limbs of folds and/or faulted. As the channels flowed into the strain minima of structures that continued to grow by lateral propagation and subsequent uplift, they developed 2-way dip (along the axis of the channels) and 2-way lateral stratigraphic traps at the channel edges. However, while the linear channels flowed almost parallel to the slope, the leveed channels underwent larger deflections between the disconnected early structures and are today obliquely folded into the mature structures. Additionally, it is likely that none of these channels developed an early trapping geometry.

Because the development of the outer domain (area 4) was delayed by the propagating deformation front, fault 11 only reached a fully connected state at (or slightly after) 6.5 Ma. Therefore, in addition to the above mentioned facies, in area 4 also the highly aggradational leveed channels (see chapter 5) can be found incorporated within the mature thrust-folds. These highly aggradational complexes could have, instead, developed an early 3-way dip and up dip lateral stratigraphic traps as they were deflected around the tips of the growing folds, hence, being tilted to one side since their deposition.

Erosional channels and ponded lobes only occurred after faults linked and accommodated enough cumulative strain (after 7.4 Ma in the inner domain and 6.5 Ma in the outer domain). In fact, their occurrence is a direct result of the faster growth of mature, linked structures.

In terms of stratal geometries, both the erosional channels and ponded lobes are contained within the clear growth sequences developed between 7.4 and 3.7 Ma. The erosional channels cut almost perpendicularly through the crests of the growing folds and likely did not develop

an early trapping geometry as they kept pace with the uplift by incising more. However, once abandoned, continued deformation could have folded parts of the channel courses over broad anticlinal structures. These channels, as the earlier leveed channels, would develop 2-way dip (along the axis of the channels) and 2-way lateral stratigraphic traps at the channel edge. The main difference is that, because of continued erosion and bypass on the fold crest, the reservoir connectivity within the channel fill may be lost thus producing two separate sand bodies on the back and front limbs (Clark and Cartwright, 2012); this process did not occur with the deposition of the earlier leveed channels.

Ponded lobes as well as the later channelized sheets represent typical good quality reservoirs. Their trapping mechanism would be purely through stratigraphic pinch-out either on the back limb of folds or within the synclines formed between two thrusts, thus developing 3-way stratigraphic traps and 1-way dip or even 4-way stratigraphic traps. They are also generally encased within hemipelagic, mud-dominated sequences or other non-reservoir facies, such as the MTDs, thus providing good seals. The only risk associated with them is posed by the potential erosion of the subsequent channels that could either remove substantial parts of the reservoir and/or compartmentalize it. The latter is particularly associated with channelized sheets which are evidently cut by a dense network of small, mud-filled channels that could create baffles to flow.

Age (Myr)	Inner domain (areas 1, 2 and 3)		outer domain (area 4)		Age (Myr)
	Reservoir facies	Description	Reservoir facies	Description	

Inner domain (areas 1, 2 and 3)

Growth stratigraphy

5.5 — Channelized sheets (up to 250 m, 10s of km)
- **Stratal geometry**: incorporated within the growth packages.
- **Trap**: have developed 3-way stratigraphic traps and 1-way dip or 4-way stratigraphic traps.
- **Risk**: subsequent erosion by MTCs and connectivity due to mud-filled channels.

6.5 — Erosional channels (up to 250 m, 3 to 5 km)
- **Stratal geometry**: channels incorporated within the growth packages. Folded subsequently to deposition, but rarely faulted.
- **Architecture**: repeated cutting and filling. lateral stacking and lateral offset of channel complexes.
- **Trap**: have developed 2-way dip (along the axis of the channels) and 2-way lateral stratigraphic traps at the channel edges. Likely not early trapping geometry.
- **Risk**: reservoir discontinuity on fold crest.

Ponded lobes (up to 10 or 20 km, up to 100 m thick)
- **Stratal geometry**: lobes incorporated within the growth packages.
- **Trap**: have developed 3-way stratigraphic traps and 1-way dip or 4-way stratigraphic traps.
- **Risk**: erosion by later channels.

7.4 — Detachment linkage — Leveed channels (up to 10 km, up to 2 km, up to 200 m)
- **Architecture**: No signs of lateral migration or stacking. No direct observation of repeated erosion.
- **Stratal geometry**: channels incorporated within the limbs of the mature thrusts. Can be obliquely folded and faulted.
- **Trap**: have developed 2-way dip (along the axis of the channels) and 2-way lateral stratigraphic traps at the channel edges. Likely not early trapping geometry.
- **Risk**: internal architecture largely unknown.

15 — Start of deformation — Sub-parallel reflectors — Unconfined lobe complexes (up to 10 or 20 km, up to 250 m thick)
- **Stratal geometry**: lobe complexes folded into anticlinal traps or in footwall synclines as well as tilted on the back limbs of folds.
- **Trap**: may have developed 4-way dip closures.
- **Risk**: faulted by multiple thrusts due to large areal extent.

outer domain (area 4)

Growth stratigraphy

6 — Erosional channels (1 to 2 km, up to 400 m)
- **Stratal geometry**: channels incorporated within the growth packages. Folded subsequently to deposition, but rarely faulted.
- **Architecture**: vertical to lateral stacking of v-shaped channels. Internal chaotic fills.
- **Trap**: have developed 2-way dip (along the axis of the channels) and 2-way lateral stratigraphic traps at the channel edges. Likely not early trapping geometry.
- **Risk**: reservoir discontinuity due to extensive erosion.

6.5 — Highly aggradational leveed channel complexes (up to 350 m, up to 8 km)
- **Stratal geometry**: channels incorporated within the limbs of the mature thrusts. Can be faulted.
- **Architecture**: vertical stacking of leveed channels. Internal lateral accretion and repeated cut and fills.
- **Trap**: have developed 3-way dip and up dip lateral stratigraphic traps being tilted to one side since their deposition. Likely have early trapping geometry.
- **Risk**: Unknown lithology at base of single infills, possible barrier within the larger reservoir.

7.4 — Detachment linkage — Leveed channels (up to 10 km, up to 2 km, up to 200 m)
- **Architecture**: No signs of lateral migration or stacking. No direct observation of repeated erosion.
- **Stratal geometry**: channels incorporated within the limbs of the mature thrusts. Can be obliquely folded and faulted.
- **Trap**: have developed 3-way dip and up dip lateral stratigraphic traps being tilted to one side since their deposition. Likely have early trapping geometry.
- **Risk**: internal architecture largely unknown.

15 — Start of deformation — Sub-parallel reflectors — Unconfined lobe complexes (up to 10 or 20 km)
- **Stratal geometry**: lobe complexes folded into anticlinal traps or in footwall synclines as well as tilted on the back limbs of folds.
- **Trap**: may have developed 4-way dip closures.
- **Risk**: faulted by multiple thrusts due to large areal extent.

Figure 7-17: Summary diagram of the different reservoir facies and their evolution in both in inner and outer domains. Note that at 7.4 Ma the stratigraphic architectures take separate paths.

208

7.6.3   Summary

The variation in the rate of growth of the structures and phases of progressive fault linkage has been clearly linked to changes in facies through time, along strike and across strike, particularly reservoir development across the slope. The model predicts that the vertical change in overall architectural style (leveed channels to erosional to channelized sheets) occurs in response to evolving basin configuration, timing of fault linkage and increasing to decreasing strain rates. This is also linked to variable size of channels in response to the evolutionary stage. The model also predicts the downslope change in architectural style, depending on where the main wave of deformation is at any time. For example, faster growing inboard structures cause ponding and erosional channels while leveed channels still exist downslope as structures deform slower and are not fully linked. Therefore, it allows the correlation of channels of different nature in downslope direction even when a direct connection is not visible. Finally, it predicts the lateral change in architecture along the same fault (leveed channels towards lateral tip points vs. erosional forms towards the centre of the structures). By understanding the mechanisms that cause these changes, it gives greater confidence to interpret facies seen on amplitude maps or in poorly imaged regions of the slope.

8. Conclusions

8.1 Key conclusions

Using line-length balancing, cumulative strains and strain rates have been measured and quantified along the strike of eleven thrust-folds that form the outer fold and thrust belt of the southern lobe of the Niger Delta, over an area of 4500 km^2. This has enabled me to reconstruct, for the first time, the 4D growth history of a thrust array to investigate the relationships and interactions between structural deformation (and likely seabed topography) and the distribution and architecture of deep-water sedimentary systems active coevally to deformation, over a period of ca. 15 Ma. Principally, this work has documented and highlighted that, in order to understand these relationships, one needs first to quantify and reconstruct deformation and carefully assess how structures interact in 3D. Using this structural frame, a predictive model has been derived for the distribution and architecture of slope channels and lobes through time. The main findings of this PhD work are summarized below:

1. Growth history of the thrust array

All the thrusts in the region started to nucleate coevally (at ≈ 15 Ma) and progressively grew with time through segment linkage. For the first ≈ half of their history, the thrusts grew by lateral propagation and subsequently by accommodation of strain and shortening at nearly constant strike length. The switch in the mode of growth occurred when the thrusts linked across strike through the detachment which resulted in the efficient transfer of strain between across strike structures. The manifestation of this process is recorded by the highly asymmetric strain-distance plots of the individual structures where strain minima on a thrust are balanced by strain maxima on the adjacent fold down or up dip. Additionally, this is confirmed by the smooth aggregate strain profile of the fold belt, which suggests that the structures behave as a linked, coherent system. The strain rates in the region have evolved from an initial period of slow deformation (15-9.5 Ma; average of 1.2%/Ma ≈ 100 m/Ma), followed by a marked increase (9.5 to 6.5 Ma; up to 7%/Ma ≈ 480 m/Ma) and a subsequent decrease (6.5 Ma to present; average of 2%/Ma ≈ 150 m/Ma). All the structures show this broad pattern, which is believed to have been driven by changes in the sediment supply rate from the delta top. However, the distribution of strain rates along the strike of structures, through time, shows high variability which reflects the way thrusts interact across-strike. Finally, the inboard thrusts grew rapidly earlier than the outboard thrusts,

which reflects the basinward migration of the deformation front. This is the result of massive shelf progradation which caused increased wedge surface slopes and induced thrusting at the toe.

2. Classification and evolution of depositional elements

The evolution of the sedimentary architecture shows a characteristic change in the occurrence of seismic facies and interpreted depositional elements. Unconfined lobe complexes are present in the older strata before the start of deformation (15 Ma) and partially until 12.8 Ma. These are followed by linear and leveed-channels between 12.8 Ma and 7.4 Ma (6.5 Ma in the outboard thrusts). Between 7.4 and 5.5 Ma, ponded lobes are first deposited and then followed by erosional channels. In the 5.5 to 3.7 Ma interval, interbedded channelized sheets and MTDs become dominant. The timing in the change between different facies is diachronous in the down slope direction, suggesting a link with the transient basinward migration of the deformation front.

3. Link between depositional elements and structural evolution

The integration of the strain data with isopach maps and the mapping of the channel drainage systems through time has demonstrated that leveed channels occur when they are able to exploit the (early) sites of linkage that exist at the early stages of structural evolution, when the fault array is immature and segmented. However, leveed-channels continue to occur as long as they can exploit the lateral tips of growing folds. Ponded lobes and erosional channels occur when the fault array has linked in 3D, strain rates increase and lead to high cumulative strains, which likely translate into more seabed topography. Channelized sheets dominate when strain rates across the fold belt decrease, structures start to be buried by sediments and the basin geometry is that of a shallow-ponded basin.

4. Temporal distribution of slope channels

Throughout the history of deformation slope channels are continuously driven to the sites of relative lower or lowest strain rate along the strike of each fault in order to cross it (the channel crossing points), where strain rates of 1%/Ma (< 90 m/Ma) developed on a fault segment are sufficient to deflect channel courses. However, while channels are widespread across the region when the fault array is immature, they become highly restricted when faults link in 3D. This likely results in more topographic confinement that forces the channels to consistently exploit fewer pathways to cross the structures, although relatively at the locations of lower strain rate. However, these locations can have locally strain rates

up to 6%/Ma (≈ 400 m/Ma), which contributes to alter the channel architectures into erosional forms. When strain rates decline and sedimentation starts to outpace deformation, the channels become again widely distributed across the region as they quickly re-occupy the locations of strain deficit present along the strike of structures. This indicates that, along with the temporal distribution of strain rates, the earliest structural deformation (i.e. the early sites of fault linkage) dictates the spatial distribution of sedimentary systems throughout the entire growth history. The rate of change in the number of channel crossings present at each time interval is related to the rate at which strain rates change over time (i.e. the acceleration/deceleration).

5. The mechanism that make channels alter their architecture

The change from leveed-channels into erosional forms occurs as a direct result of how structures are arranged in 3D and their relative size. The larger/largest structures in area can have a dominant effect in the creation of seabed topography such that channels primarily respond to these large folds. Because structures transfer strain efficiently across strike once they link through the detachment, channels may be directed towards the strain deficits present along the large structures, however, being forced to erode into the corresponding strain maxima on the smaller up dip folds. Conversely, if the large folds are present up dip, they will leave a wide undeformed area in their footwall, such that channels will become aggradational as they enter this zone of low cumulative strains (and likely low topography).

6. Down slope diachronous development of architectural styles

The two types of channel-structure interactions can be simultaneously present across the slope, which leads to the coeval development of erosional channels up dip and leveed-channels further outboard. However, as the deformation front migrates basinward, the inboard structures become progressively abandoned and will develop a shallow-ponded configuration dominated by channelized sheets. As deformation concentrates on the outboard structures, these completely link and start to deform at high strain rates, which causes the development of erosional forms in the outboard domain; a process that leads to the diachronous development of the architectural styles.

7. Where and when do ponded lobes occur?

When faults first link in 3D they inherit highly asymmetric strain-distance profiles, as strain is transferred between across-strike faults, and are under displaced with respect to the length

of the new linked structures. This asymmetry likely causes topographic changes where flows are directed towards the zones of strain deficits, which also correspond to the zones that subsequently undergo higher strain rates as faults grow by accumulation of strain at constant lengths. Ponded lobes are predicted to occur within the strain deficits present along the strike of faults once they have linked in 3D. They also occur up dip of the zones of greater/greatest strain rate and at the beginning of the interval. Structures also control their up dip termination as they can affect the seafloor several km up slope.

8. Stratal geometries associated with slope development

The Niger Delta slope is divided into three main phases of structural development. The pre-kinematic (before 15 Ma) and early syn-kinematic phase (15 to 7.4 Ma) are both characterized by sub-parallel reflectors and comprise lobe complexes and leveed channel diverted by early growing structures. The main syn-kinematic phase (7.4 to 5.5 Ma) shows clear growth strata comprising ponded lobes and erosional channels. The late syn-kinematic phase (5.5 to 3.7 Ma) shows moderate thickening-thinning of stratigraphy and comprise channelized sheets and MTDs. The onset of detachment linkage (7.4 Ma) marks the change in the observed stratal geometries and the differentiation of architectural styles across the slope.

8.2 Future work and open questions

The results of this study should be tested elsewhere in the Niger Delta (e.g. western lobe) or on other gravity-driven fold belt generally found along the African margin to validate the predictions (or understand the differences) of both the facies and structural growth models. Given the common occurrence of deep-water fold and thrust belts and the typical presence of shale detachments (Morley et al., 2011), the results of this study should be also tested in other tectonic regimes for progressively more contribution of far-field stresses. For example, it would be interesting to know if both the mode of thrusts growth and the resulting facies changes through time are confirmed in areas where deformation is driven by a combination of gravity gliding/spreading and plate convergence (e.g. north-west Borneo) or in subduction zones where deformation is entirely driven by lithospheric stresses and the extensional-compressional domains are weakly linked (e.g. Barbados accretionary prims; Morley et al., 2011). Should the predictions be confirmed, then they would be applicable at global scale.

Measuring strain and shortening rates in different tectonic settings would also help bridge the gap between strain rate and seabed relief/topography. In chapter 3 it was shown that, at present,

the distribution of the few active fault segments that deform at low strain rates (1 to 5%/Ma) closely mirrors the seabed topography created by uplift on those same fault segments. It follows that a correlation could be made directly between strain rates and actual seabed relief. Future research should aim to integrate and calibrate the structural measurements with high quality bathymetric data in order to overcome the issue of calculating uplift via a kinematic model. Detailed analysis of how strain rates change along the strike of structures could be linked to the variation in seabed relief extracted from DEMs to find a best-fit correlation. The same approach could be tested in different tectonic regimes where deformation rates are currently high (e.g. Borneo) in order to produce a calibration for a wide range of strain rates. If a robust correlation exists, then it could enable reconstruction of past seabed relief using our reconstructed cumulative strains through time.

Related to this topic is that slope channels always exploited the locations of lowest strain rate to cross structures and, often, these coincided with early sites of fault linkage. Therefore, it would be interesting to know how long it would take for the channels to "forget" the early structural framework and whether this condition would ever be achieved.

This work has, for the first time, recognised the occurrence, at specific intervals, of a range of sediment architectures as a result of, and controlled by, the growth of a deep-water fold and thrust belt. This has been a semi regional-scale exercise that aimed to document and explain the evolution of the stratigraphic architecture in response to structural controls. The study has produced a robust model to predict the occurrence of particular sedimentary styles down the slope profile, along strike and through time through the quantification of deformation. However, during the analysis a number of observations have been made that would need to be investigated with further research. The natural continuation of this work would include a more in-depth analysis of the change in internal architecture of the different sedimentary facies as they approach the growing structures. This should be done by mapping the individual third-order channel forms and, where possible, the internal stacking of the single channel fills and amalgamation surfaces to understand how these change in response to the measured deformation rates. Mapping of the internal architectures should be then integrated with outcrop analogues in order to create more robust predictive models which could be used to aid field development.

It would be also interesting to further investigate the leveed channels of the 12.8 to 9.5 Ma interval. These are purely aggradational forms that developed in the lows between early incipient folds at times of very low strain rates. Even compared with the systems today active

on the seabed, at comparable strain rates, they seem to be very different forms both in terms of internal architecture and type of sinuosity. Therefore, could the old systems reoccur today or were they indicative of boundary conditions that cannot be reproduced today?

The same approach is to be used with the lobate forms, by mapping the top and base of the individual lobes and sheets in order to characterize their stacking and geometry. For example, channelized sheets are strongly interbedded with MTDs and together they create sequences a few hundred meters thick. Their internal relationships should be unravelled by the detailed deconvolution of the stratigraphy. Moreover, channelized sheets seem to result from the lateral and vertical stacking of numerous low-relief channel levees into pseudo sheet-like reflections. Therefore, more attention should be given to understanding the internal architectures and stacking of these systems given their proven hydrocarbon potential. Lastly, they are observed to occur at the beginning and at the end of periods of very high strain rates (at the inflection points), therefore they seem to be characteristic of shallow ponding or weak topographic confinement; additional work should aim to further characterize these transitional periods to confirm the predictions made on their occurrence.

Similarly, the deeper and older unconfined lobe complexes are well imaged in the dataset and characterize the oldest strata prior to the start of deformation at 15 Ma. These deposits cover very large portion of the dataset; therefore, it would be interesting to map them in detail aiming to reconstruct their depositional characteristic and the geometry of the environment of deposition, which most likely occurred in a distal basin floor setting.

9. References

Abreu, V., Sullivan, M., Pirmez, C., & Mohrig, D. (2003). Lateral accretion packages (LAPs): an important reservoir element in deep water sinuous channels. Marine and Petroleum Geology, 20(6-8), 631-648.

Adeogba, A. A., McHargue, T. R., & Graham, S. A. (2005). Transient fan architecture and depositional controls from near-surface 3-D seismic data, Niger Delta continental slope. AAPG bulletin, 89(5), 627-643.

Alpak, F. O., Barton, M. D., & Naruk, S. J. (2013). The impact of fine-scale turbidite channel architecture on deep-water reservoir performance. AAPG bulletin, 97(2), 251-284.

Amos, C.B., Burbank, D.W. and Read, S.A., 2010. Along-strike growth of the Ostler fault, New Zealand: Consequences for drainage deflection above active thrusts. Tectonics, 29(4).

Babonneau, N., Savoye, B., Cremer, M., & Klein, B. (2002). Morphology and architecture of the present canyon and channel system of the Zaire deep-sea fan. Marine and Petroleum Geology, 19(4), 445-467.

Bally, A.W., Gordy, P.L. and Stewart, G.A., 1966. Structure, seismic data, and orogenic evolution of southern Canadian Rocky Mountains. Bulletin of Canadian Petroleum Geology, 14(3), pp.337-381.

Beaubouef, R. T. (2004). Deep-water leveed-channel complexes of the Cerro Toro Formation, Upper Cretaceous, southern Chile. AAPG bulletin, 88(11), 1471-1500.

Bergen, K.J. and Shaw, J.H., 2010. Displacement profiles and displacement-length scaling relationships of thrust faults constrained by seismic-reflection data. Geologica Society of America Bulletin, 122(7-8), pp.1209-1219.

Bilotti, F. and Shaw, J.H., 2005. Deep-water Niger Delta fold and thrust belt modeled as a critical-taper wedge: The influence of elevated basal fluid pressure on structural styles. AAPG Bulletin, 89(11), pp.1475-1491.

Booth, J. R., Dean, M. C., DuVernay III, A. E., & Styzen, M. J. (2003). Paleo-bathymetric controls on the stratigraphic architecture and reservoir development of confined fans in the Auger Basin: central Gulf of Mexico slope. Marine and Petroleum Geology, 20(6-8), 563-586.

Bouma, A. H. 1962. Sedimentology of Some Flysch Deposits. A Graphic Approach to Facies interpretation. Elsevier Publishing Company, Amsterdam.

Bouma, A. H. (2004). Key controls on the characteristics of turbidite systems. Geological Society, London, Special Publications, 222(1), 9-22.

Bourget, J., Zaragosi, S., Ellouz-zimmermann, N., Mouchot, N., Garlan, T., Schneider, J.L., Lanfumey, V. and Lallemant, S., 2011. Turbidite system architecture and sedimentary processes along topographically complex slopes: the Makran convergent margin. Sedimentology, 58(2), pp.376-406.

Boyer, S.E. and Elliot, D., 1982. Thrust systems: Bulletin American Association of Petroleum Geologists, v. 66, pp.1196-1230.

Boyer, S.E., 1992. Geometric evidence for synchronous thrusting in the southern Alberta and northwest Montana thrust belts. In Thrust tectonics (pp. 377-390). Springer, Dordrecht.

Briggs, S.E., Davies, R.J., Cartwright, J.A. and Morgan, R., 2006. Multiple detachment levels and their control on fold styles in the compressional domain of the deepwater west Niger Delta. Basin Research, 18(4), pp.435-450.

Broucke, O., Temple, F., Rouby, D., Robin, C., Calassou, S., Nalpas, T., & Guillocheau, F. (2004). The role of deformation processes on the geometry of mud-dominated turbiditic systems, Oligocene and Lower–Middle Miocene of the Lower Congo basin (West African Margin). Marine and Petroleum Geology, 21(3), 327-348.

Buiter, S.J., Babeyko, A.Y., Ellis, S., Gerya, T.V., Kaus, B.J., Kellner, A., Schreurs, G. and Yamada, Y., 2006. The numerical sandbox: comparison of model results for a shortening and an extension experiment. Geological Society, London, Special Publications, 253(1), pp.29-64.

Burbank, D. W., & Vergés, J. (1994). Reconstruction of topography and related depositional systems during active thrusting. Journal of Geophysical Research: Solid Earth, 99(B10), 20281-20297.

Burbank, D., Meigs, A., & Brozović, N. (1996). Interactions of growing folds and coeval depositional systems. Basin Research, 8(3), 199-223.

Burbidge, D.R. and Braun, J., 2002. Numerical models of the evolution of accretionary wedges and fold-and-thrust belts using the distinct-element method. Geophysical Journal International, 148(3), pp.542-561.

Burgess, P. M., Masiero, I., Toby, S. C., & Duller, R. A. (2019). A Big Fan of Signals? Exploring Autogenic and Allogenic Process and Product In a Numerical Stratigraphic Forward Model of Submarine-Fan Development. Journal of Sedimentary Research, 89(1), 1-12.

Burgreen, B., & Graham, S. (2014). Evolution of a deep-water lobe system in the Neogene trench-slope setting of the East Coast Basin, New Zealand: Lobe stratigraphy and architecture in a weakly confined basin configuration. Marine and Petroleum Geology, 54, 1-22.

Butler, R.W., 1982. The terminology of structures in thrust belts. Journal of structural Geology, 4(3), pp.239-245.

Butler, R.W.H., 1987. Thrust sequences. Journal of the Geological Society, 144(4), pp.619-634.

Callec, Y., Deville, E., Desaubliaux, G., Griboulard, R., Huyghe, P., Mascle, A., Mascle, G., Noble, M., Padron de Carillo, C. and Schmitz, J., 2010. The Orinoco turbidite system: Tectonic controls on sea-floor morphology and sedimentation. AAPG bulletin, 94(6), pp.869-887.

Cartwright, J.A., Trudgill, B.D. and Mansfield, C.S., 1995. Fault growth by segment linkage: an explanation for scatter in maximum displacement and trace length data from the Canyonlands Grabens of SE Utah. Journal of Structural Geology, 17(9), pp.1319-1326.

Cartwright, J., & Huuse, M. (2005). 3D seismic technology: the geological 'Hubble'. Basin Research, 17(1), 1-20.

Cartwright, J. A. (1989). The kinematics of inversion in the Danish Central Graben. Geological Society, London, Special Publications, 44(1), 153-175.

Catterall, V., Redfern, J., Gawthorpe, R., Hansen, D., & Thomas, M. (2010). Architectural style and quantification of a submarine channel–levee system located in a structurally complex area: offshore Nile Delta. Journal of Sedimentary Research, 80(11), 991-1017.

Chamberlin, R.T., 1910. The Appalachian folds of central Pennsylvania. The Journal of Geology, 18(3), pp.228-251.

Chapin, M., Swinburn, P., van der Weiden, R., Skaloud, D., Adesanya, S., Stevens, D., ... & Blaauw, M. (2002). Integrated seismic and subsurface characterization of Bonga Field, offshore Nigeria. The Leading Edge, 21(11), 1125-1131.

Clark, J. D., Kenyon, N. H., & Pickering, K. T. (1992). Quantitative analysis of the geometry of submarine channels: implications for the classification of submarine fans. Geology, 20(7), 633-636.

Clark, I. R., & Cartwright, J. A. (2009). Interactions between submarine channel systems and deformation in deepwater fold belts: Examples from the Levant Basin, Eastern Mediterranean sea. Marine and Petroleum Geology, 26(8), 1465-1482.

Clark, I. R., & Cartwright, J. A. (2011). Key controls on submarine channel development in structurally active settings. Marine and Petroleum Geology, 28(7), 1333-1349.

Clark, I. R., Cartwright, J. A. (2012). Interactions between coeval sedimentation and deformation from the Niger delta deepwater fold belt. Application of the Principles of Seismic Geomorphology to Continental Slope and Base-of-Slope Systems: Case Studies from Seafloor and Near-Seafloor Analogues: SEPM, Special Publication, 99, 243-267.

Clark, Ian R., and Joseph A. Cartwright, 2012, A case study of three-dimensional fold and growth sequence development and the link to submarine channel-structure interactions in deep-water fold belts, in D. Gao, ed., Tectonics and sedimentation: Implications for petroleum systems: AAPG Memoir 100, p. 315–335.

Cobbold, P.R., Clarke, B.J. and Løseth, H., 2009. Structural consequences of fluid overpressure and seepage forces in the outer thrust belt of the Niger Delta. Petroleum Geoscience, 15(1), pp.3-15.

Cohen, H.A. and McClay, K., 1996. Sedimentation and shale tectonics of the northwestern Niger Delta front. Marine and Petroleum Geology, 13(3), pp.313-328.

Colletta, B., Letouzey, J., Pinedo, R., Ballard, J.F., Balé P. 1991. Computerized X-ray tomography analysis of sandbox models: Examples of thin-skinned thrust systems. Geology, 19, 1063-1067.

Corredor, F., Shaw, J.H. and Bilotti, F., 2005. Structural styles in the deep-water fold and thrust belts of the Niger Delta. AAPG Bulletin, 89(6), pp.753-780.

Costa, E, and Vendeville, B. 2002 . Experimental Insigths on the geometry and kinematics of fold-and-thrust belts above weak, viscous, evaporitic décollement. J. Struct. Geology, 24, 1729-1739.

Cowie, P.A. and Scholz, C.H., 1992. Displacement-length scaling relationship for faults: data synthesis and discussion. Journal of Structural Geology, 14(10), pp.1149-1156.

Cowie, P.A., 1998. A healing–reloading feedback control on the growth rate of seismogenic faults. Journal of Structural Geology, 20(8), pp.1075-1087.

Cowie, P.A. and Roberts, G.P., 2001. Constraining slip rates and spacings for active normal faults. Journal of Structural Geology, 23(12), pp.1901-1915.

Cross, N. E., Cunningham, A., Cook, R. J., Taha, A., Esmaie, E., & El Swidan, N. (2009). Three-dimensional seismic geomorphology of a deep-water slope-channel system: The Sequoia field, offshore west Nile Delta, Egypt. AAPG bulletin, 93(8), 1063-1086.

Cruciani, F., Barchi, M.R., Koyi, H.A. and Porreca, M., 2017. Kinematic evolution of a regional-scale gravity-driven deepwater fold-and-thrust belt: The Lamu Basin case-history (East Africa). Tectonophysics, 712, pp.30-44.

Cullis, S., Colombera, L., Patacci, M., & McCaffrey, W. D. (2018). Hierarchical classifications of the sedimentary architecture of deep-marine depositional systems. Earth-Science Reviews, 179, 38-71.

Daëron, M., Avouac, J.P. and Charreau, J., 2007. Modeling the shortening history of a fault tip fold using structural and geomorphic records of deformation. Journal of Geophysical Research: Solid Earth, 112(B3).

Dahlstrom, C.D.A., 1969. Balanced cross sections. Canadian Journal of Earth Sciences, 6(4), pp.743-757.

Dahlstrom, C.D., 1970. Structural geology in the eastern margin of the Canadian Rocky Mountains. Bulletin of Canadian Petroleum Geology, 18(3), pp.332-406.

Damuth, J.E., 1994. Neogene gravity tectonics and depositional processes on the deep Niger Delta continental margin. Marine and Petroleum Geology, 11(3), pp.320-346.

Davis, K., Burbank, D.W., Fisher, D., Wallace, S. and Nobes, D., 2005. Thrust-fault growth and segment linkage in the active Ostler fault zone, New Zealand. Journal of Structural Geology, 27(8), pp.1528-1546.

Dawers, N.H. and Anders, M.H., 1995. Displacement-length scaling and fault linkage. Journal of Structural Geology, 17(5), pp.607-614.

Dean, S., Morgan, J. and Brandenburg, J.P., 2015. Influence of mobile shale on thrust faults: Insights from discrete element simulationsInfluence of Mobile Shale on Thrust Faults. AAPG Bulletin, 99(3), pp.403-432.

Delcaillau, B., B. Deffontaines, L. Floissac, J. Angelier, J. Deramond, P. Souquet, H. T. Chu, and J. F. Lee (1998), Morphotectonic evidence from lateral propagation of an active frontal fold: Pakuashan anticline, foothills of Taiwan, Geomorphology, 24(4), 263–290, doi:10.1016/S0169-555X(98)00020-8.

Deptuck, M. E., Steffens, G. S., Barton, M., & Pirmez, C. (2003). Architecture and evolution of upper fan channel-belts on the Niger Delta slope and in the Arabian Sea. Marine and Petroleum Geology, 20(6-8), 649-676.

Deptuck, M. E., Sylvester, Z., Pirmez, C., & O'Byrne, C. (2007). Migration–aggradation history and 3-D seismic geomorphology of submarine channels in the Pleistocene Benin-major Canyon, western Niger Delta slope. Marine and Petroleum Geology, 24(6-9), 406-433.

Deptuck, M. E., Piper, D. J., Savoye, B., & Gervais, A. (2008). Dimensions and architecture of late Pleistocene submarine lobes off the northern margin of East Corsica. Sedimentology, 55(4), 869-898.

Deptuck, M. E., Sylvester, Z., & O'Byrne, C. (2012). Pleistocene seascape evolution above a "simple" stepped slope, western Niger Delta. Application of the principles of seismic geomorphology to continental slope and base-of-slope systems: Case studies from sea floor and near–sea floor analog: SEPM Special Publication, 99, 199-222.

Deptuck, M. E., & Sylvester, Z. (2018). Submarine fans and their channels, levees, and lobes. In Submarine Geomorphology (pp. 273-299). Springer, Cham.

Diegel, F.A., 1986. Topological constraints on imbricate thrust networks, examples from the Mountain City window, Tennessee, USA. Journal of Structural Geology, 8(3-4), pp.269-279.

Dingle, R. V. (1982). Continental margin subsidence: a comparison between the east and west coasts of Africa. In Dynamics of Passive Margins (Vol. 6, pp. 59-71). American Geophysical Union (AGU).

Doughty-Jones, G., Mayall, M., & Lonergan, L. (2017). Stratigraphy, facies, and evolution of deep-water lobe complexes within a salt-controlled intraslope minibasin. AAPG Bulletin, 101(11), 1879-1904.

Doust, H., Omatsola, E., 1990. Niger Delta. In: Edwards, J.D., Santogrossi, P.A. (Eds.), Divergent/passive Margin Basins. AAPG Memoir, 48, pp. 201-238.

Don, J., Shaw, J. H., Plesch, A., Bridgwater, D. D., & Lufadeju, G. (2019). Characterizing the growth of structures in three dimensions using patterns of deep-water fan and channel systems. AAPG Bulletin, (20,190,506).

Eichelberger, N.W., Hughes, A.N. and Nunns, A.G., 2015. Combining multiple quantitative structural analysis techniques to create robust structural interpretations. Interpretation, 3(4), pp.SAA89-SAA104.

Elliott, D. (1976), Energy-balance and deformation mechanisms of thrust sheets, Philos. Trans. R. Soc. London, A, 283(1312), 289–312.

Emery, K. O., Uchupi, E., Phillips, J., Bowin, C., & Mascle, J. (1975). Continental margin off western Africa: Angola to Sierra Leone. AAPG Bulletin, 59(12), 2209-2265.

Epard, J.L. and Groshong Jr, R.H., 1993. Excess area and depth to detachment. AAPG bulletin, 77(8), pp.1291-1302.

Evamy, B.D., Haremboure, J., Kamerling, P., Knaap, W.A., Molloy, F.A. and Rowlands, P.H., 1978. Hydrocarbon habitat of Tertiary Niger delta. AAPG bulletin, 62(1), pp.1-39.

Fermor, P., 1999. Aspects of the three-dimensional structure of the Alberta Foothills and Front Ranges. GSA bulletin, 111(3), pp.317-346.

Ferry, J. N., Mulder, T., Parize, O., & Raillard, S. (2005). Concept of equilibrium profile in deep-water turbidite system: effects of local physiographic changes on the nature of sedimentary process and the geometries of deposits. Geological Society, London, Special Publications, 244(1), 181-193.

Fildani, A., Normark, W. R., Kostic, S., & Parker, G. (2006). Channel formation by flow stripping: Large-scale scour features along the Monterey East Channel and their relation to sediment waves. Sedimentology, 53(6), 1265-1287.

Fildani, A., Hubbard, S. M., Covault, J. A., Maier, K. L., Romans, B. W., Traer, M., & Rowland, J. C. (2013). Erosion at inception of deep-sea channels. Marine and Petroleum Geology, 41, 48-61.

Fillon, C., Huismans, R.S. and van der Beek, P., 2013. Syntectonic sedimentation effects on the growth of fold-and-thrust belts. Geology, 41(1), pp.83-86.

Fonnesu, F. (2003). 3D seismic images of a low-sinuosity slope channel and related depositional lobe (West Africa deep-offshore). Marine and Petroleum Geology, 20(6-8), 615-629.

Ford, M., Williams, E.A., Artoni, A., Vergés, J. and Hardy, S., 1997. Progressive evolution of a fault-related fold pair from growth strata geometries, Sant Llorenc de Morunys, SE Pyrenees. Journal of structural Geology, 19(3-4), pp.413-441.

Gamboa, D., & Alves, T. M. (2015). Spatial and dimensional relationships of submarine slope architectural elements: a seismic-scale analysis from the Espírito Santo Basin (SE Brazil). Marine and Petroleum Geology, 64, 43-57.

Gardner, D.A.C. and Spang, J.H., 1973. Model studies of the displacement transfer associated with overthrust faulting. Bulletin of Canadian Petroleum Geology, 21(4), pp.534-552.

Gardner, M. H., Borer, J. M., Melick, J. J., Mavilla, N., Dechesne, M., & Wagerle, R. N. (2003). Stratigraphic process-response model for submarine channels and related features from studies of Permian Brushy Canyon outcrops, West Texas. Marine and Petroleum Geology, 20(6-8), 757-787.

Ge, Z., Nemec, W., Gawthorpe, R. L., & Hansen, E. W. (2017). Response of unconfined turbidity current to normal-fault topography. Sedimentology, 64(4), 932-959.

Ge, Z., Nemec, W., Gawthorpe, R. L., Rotevatn, A., & Hansen, E. W. (2018). Response of unconfined turbidity current to relay-ramp topography: insights from process-based numerical modelling. Basin Research, 30(2), 321-343.

Gee, M. J. R., & Gawthorpe, R. L. (2006). Submarine channels controlled by salt tectonics: Examples from 3D seismic data offshore Angola. Marine and Petroleum Geology, 23(4), 443-458.

Gee, M. J. R., Gawthorpe, R. L., Bakke, K., & Friedmann, S. J. (2007a). Seismic geomorphology and evolution of submarine channels from the Angolan continental margin. Journal of Sedimentary Research, 77(5), 433-446.

Gee, M. J. R., & Gawthorpe, R. L. (2007b). Early evolution of submarine channels offshore Angola revealed by three-dimensional seismic data. Geological Society, London, Special Publications, 277(1), 223-235.

Georgiopoulou, A., & Cartwright, J. A. (2013). A critical test of the concept of submarine equilibrium profile. Marine and Petroleum Geology, 41, 35-47.

Gervais, A., Mulder, T., Savoye, B., & Gonthier, E. (2006). Sediment distribution and evolution of sedimentary processes in a small sandy turbidite system (Golo system, Mediterranean Sea): implications for various geometries based on core framework. Geo-Marine Letters, 26(6), 373.

Gervais, A., Savoye, B., Mulder, T., & Gonthier, E. (2006). Sandy modern turbidite lobes: a new insight from high resolution seismic data. Marine and Petroleum Geology, 23(4), 485-502.

Ghibaudo, G. (1992). Subaqueous sediment gravity flow deposits: practical criteria for their field description and classification. Sedimentology, 39(3), 423-454.

Gonzalez-Mieres, R. and Suppe, J., 2006. Relief and shortening in detachment folds. Journal of Structural Geology, 28(10), pp.1785-1807.

Ghosh, B., and D. R. Lowe, 1993, The architecture of deep water channel complexes, Cretaceous Venado Sandstone member, Sacramento Valley, California, in S. Graham and D. R. Lowe, eds., Advances in the sedimentary geology of the Great Valley Group, Sacramento Valley, California: guidebook for Pacific Section SEPM 1993 Fall Field Trip: Los Angeles, California, Pacific Section SEPM, p. 51–65.

Haack, R.C., Sundararaman, P., Diedjomahor, J.O., Xiao, H., Gant, N.J., May, E.D. & Kelsch, K. 2000. Niger Delta petroleum systems, Nigeria. In: Mello, M.R. & Katz, B.J. (eds) Petroleum Systems of South Atlantic Margins. American Association of Petroleum Geologists Memoirs, 73, 213–231.

Hampton, B. D., T. V. Wilson, and R. Crookbain, 2006, From euphoria to reality: One perator's experience with reservoir performance in the deep-water Gulf ofMexico: AAPG Annual Convention Abstracts, v. 15, p. 42.

Hansen, L., Janocko, M., Kane, I., & Kneller, B. (2017). Submarine channel evolution, terrace development, and preservation of intra-channel thin-bedded turbidites: Mahin and Avon channels, offshore Nigeria. Marine Geology, 383, 146-167.

Hardy, S., & Poblet, J. (2005). A method for relating fault geometry, slip rate and uplift data above fault-propagation folds. Basin Research, 17(3), 417-424.

Hardy, S., McClay, K. and Muñoz, J.A., 2009. Deformation and fault activity in space and time in high-resolution numerical models of doubly vergent thrust wedges. Marine and Petroluem Geology 26, 232-248

Hatcher, R. D. Jr., 2004, Properties of thrusts and upper bounds for the size of thrust sheets, in K. R. McClay, ed., Thrust tectonics and hydrocarbon systems: AAPG Memoir 82, p. 18– 29.

Hay, D. C., (2012). Stratigraphic evolution of a tortuous corridor from the stepped slope of Angola. Application of the principles of seismic geomorphology to continental slope and base-of-slope systems: Case studies from sea floor and near–sea floor analogs: SEPM Special Publication, 99, 163-180.

Haughton, P., Davis, C., McCaffrey, W., & Barker, S. (2009). Hybrid sediment gravity flow deposits–classification, origin and significance. Marine and Petroleum Geology, 26(10), 1900-1918.

Haughton, P. D. (2000). Evolving turbidite systems on a deforming basin floor, Tabernas, SE Spain. Sedimentology, 47(3), 497-518.

Heiniö, P., & Davies, R. J. (2007). Knickpoint migration in submarine channels in response to fold growth, western Niger Delta. Marine and Petroleum Geology, 24(6-9), 434-449.

Higgins, S., Clarke, B., Davies, R.J. and Cartwright, J., 2009. Internal geometry and growth history of a thrust-related anticline in a deep water fold belt. Journal of Structural Geology, 31(12), pp.1597-1611.

Hiscott, R. N., Hall, F. R., & Pirmez, C. (1997). Turbidity-current overspill from the Amazon Channel: texture of the silt/sand load, paleoflow from anisotropy of magnetic susceptibility, and implications for flow processes. In Proceedings-Ocean Drilling Program Scientific Results (pp. 53-78). NATIONAL SCIENCE FOUNDATION.

Hodgson, D. M., & Haughton, P. D. (2004). Impact of syndepositional faulting on gravity current behaviour and deep-water stratigraphy: Tabernas-Sorbas Basin, SE Spain. Geological Society, London, Special Publications, 222(1), 135-158.

Hooper, R.J., Fitzsimmons, R.J., Grant, N. and Vendeville, B.C., 2002. The role of deformation in controlling depositional patterns in the south-central Niger Delta, West Africa. Journal of Structural Geology, 24(4), pp.847-859.

Hoth, S., Adam, J., Kukowski, N. and Oncken, O., 2006. Influence of erosion on the kinematics of bivergent orogens: results from scaled sandbox simulations. Tectonics, Climate, and Landscape Evolution, 398, p.201.

Howlett, D.M., Ge, Z., Nemec, W., Gawthorpe, R.L., Rotevatn, A. and Jackson, C.A.-L. (2019), Response of unconfined turbidity current to deep-water fold and thrust belt topography: Orthogonal incidence on solitary and segmented folds. Sedimentology, 66: 2425-2454.

Hughes, A. N., & Shaw, J. H. (2014). Fault displacement-distance relationships as indicators of contractional fault-related folding styleDisplacement Variations and Folding Styles. AAPG bulletin, 98(2), 227-251.

Hughes, A.N. and Shaw, J.H., 2015. Insights into the mechanics of fault-propagation folding styles. GSA Bulletin, 127(11-12), pp.1752-1765.

Hughes, A., Rood, D. H., Whittaker, A. C., Bell, R. E., Rockwell, T. K., Levy, Y., Wilcken, K. M., Corbett, L. B., Bierman, P. R., Devecchio, D. E., Marshall, S. T., Gurrola, L. D., & Nicholson, C., 2018. Geomorphic evidence for the geometry and slip rate of a young, low-angle thrust fault: Implications for hazard assessment and fault interaction in complex tectonic environments. Earth and Planetary Science Letters, 504, 198– 210.

Huyghe, P., Foata, M., Deville, E., Mascle, G., & Group, C. W. (2004). Channel profiles through the active thrust front of the southern Barbados prism. Geology, 32(5), 429-432.

Ingram, G. M., Chisholm, T. J., Grant, C. J., Hedlund, C. A., Stuart-Smith, P., & Teasdale, J. (2004). Deepwater North West Borneo: hydrocarbon accumulation in an active fold and thrust belt. Marine and Petroleum Geology, 21(7), 879-887.

Jackson, J., Norris, R. and Youngson, J., 1996. The structural evolution of active fault and fold systems in central Otago, New Zealand: evidence revealed by drainage patterns. Journal of Structural Geology, 18(2-3), pp.217-234.

Janocko, M., Nemec, W., Henriksen, S., & Warchoł, M. (2013). The diversity of deep-water sinuous channel belts and slope valley-fill complexes. Marine and Petroleum Geology, 41, 7-34.

Jermannaud, P., Rouby, D., Robin, C., Nalpas, T., Guillocheau, F. and Raillard, S., 2010. Plio-Pleistocene sequence stratigraphic architecture of the eastern Niger Delta: A record of eustasy and aridification of Africa. Marine and Petroleum Geology, 27(4), pp.810-821.

Jobe, Z. R., Howes, N. C., & Auchter, N. C. (2016). Comparing submarine and fluvial channel kinematics: Implications for stratigraphic architecture. Geology, 44(11), 931-934.

Jobe, Z. R., Sylvester, Z., Howes, N., Pirmez, C., Parker, A., Cantelli, A., ... & Prather, B. (2017). High-resolution, millennial-scale patterns of bed compensation on a sand-rich intraslope submarine fan, western Niger Delta slope. GSA Bulletin, 129(1-2), 23-37.

Jolly, B.A., Lonergan, L. and Whittaker, A.C., 2016. Growth history of fault-related folds and interaction with seabed channels in the toe-thrust region of the deep-water Niger delta. Marine and Petroleum Geology, 70, pp.58-76.

Jolly, B.A., Whittaker, A.C. and Lonergan, L., 2017. Quantifying the geomorphic response of modern submarine channels to actively growing folds and thrusts, deep-water Niger Delta. Geological Society of America Bulletin, 129(9-10), pp.1123-1139.

Jones, G., Mayall, M., and Lonergan, L., 2012, Contrasting depositional styles on a slope system and their control by salt tectonics: through-going channels, ponded fans, and mass transport complexes, in, Rosen, N.C. Weimer, P., dos Anjos, S.M.C., Henrickson, S., Marques, E., Mayall, M., Fillon, R, D'Agostino, T, Saller, A., Campion, K., Huang, T., Sarg, R. and Schroeder, F., eds, New Understanding of the Petroleum Systems of Continental Margins of the World, 32nd Annual GCSSEPM Foundation Bob. F. Perkins Conference, p. 503-533.

Keller, E.A., Gurrola, L. and Tierney, T.E., 1999. Geomorphic criteria to determine direction of lateral propagation of reverse faulting and folding. Geology, 27(6), pp.515-518.

Kim, Y.S. and Sanderson, D.J., 2005. The relationship between displacement and length of faults: a review. Earth-Science Reviews, 68(3-4), pp.317-334.

King, G. and Yielding, G., 1984. The evolution of a thrust fault system: processes of rupture initiation, propagation and termination in the 1980 El Asnam (Algeria) earthquake. Geophysical Journal International, 77(3), pp.915-933.

Kneller, B., & Buckee, C. (2000). The structure and fluid mechanics of turbidity currents: a review of some recent studies and their geological implications. Sedimentology, 47, 62-94.

Knox, G.J., Omatsola, E.M., 1989. Development of the Cenozoic Niger Delta in terms of the 'escalator regression' model and impact on hydrocarbon distribution. In: Van Der Linden, W.J.M., Cloetingh, S.A.P.L., Kaasscheiter, J.P.K., Van Ger Graaf, W.J.E., Vandenberglie, J., Van Der Gun, J.A.M. (Eds.), Proceedings of the KNGMG Symposium Coastal Lowlands. Geology and Geotechnology, pp. 181e202.

Kolla, V. (2007). A review of sinuous channel avulsion patterns in some major deep-sea fans and factors controlling them. Marine and Petroleum Geology, 24(6-9), 450-469.

Krueger, S. W., and N. T. Grant, 2011, The growth history of toe thrusts of the Niger Delta and the role of pore pressure, in K. McClay, J. Shaw, and J. Suppe, eds., Thrust fault-related folding: AAPG Memoir 94, pp. 357–390.

Lavé, J. and Avouac, J.P., 2000. Active folding of fluvial terraces across the Siwaliks Hills, Himalayas of central Nepal. Journal of Geophysical Research: Solid Earth, 105(B3), pp.5735-5770.

Li, T., J. Chen, J. A. Thompson, D. W. Burbank, and X. Yang (2013), Quantification of three-dimensional folding using fluvial terraces: A case study from the Mushi anticline, northern margin of the Chinese Pamir, J. Geophys. Res. Solid Earth, 118, 4628–4647, doi:10.1002/jgrb.50316

Liu, S. and Dixon, J.M., 1991, November. Centrifuge modelling of thrust faulting: structural variation along strike in fold-thrust belts: Tectonophysics V188, N1/2, March 1991, P39–62. In International Journal of Rock Mechanics and Mining Sciences & Geomechanics Abstracts (Vol. 28, No. 6, p. A334). Pergamon.

Lomas, S. A., & Joseph, P. (2004). Confined turbidite systems. Geological Society, London, Special Publications, 222(1), 1-7.

Lowe, D. R., (1979b). Sediment gravity flows: their classification and some problems of application to natural flows and deposits: Soc. Econ. Paleontologists Mineralogists Spec. Pub. 27, p. 75-82.

Lowe, D. R. (1982). Sediment gravity flows; II, Depositional models with special reference to the deposits of high-density turbidity currents. Journal of sedimentary research, 52(1), 279-297.

Maier, K. L., Fildani, A., McHargue, T. R., Paull, C. K., Graham, S. A., & Caress, D. W. (2012). Punctuated deep-water channel migration: high-resolution subsurface data from the Lucia Chica channel system, offshore California, USA. Journal of Sedimentary Research, 82(1), 1-8.

Mayall, M. and Stewart I, 'The Architecture of Turbidite Slope Channels' in Deep-Water Reservoirs of the World, GCSSEPM, Dec 3-6th. Ed. P. Weimer, RM Slatt, J. oleman, NC Rosen, H Nelson, AH Bouma, MJ Styzen, DT Lawrence. 2000 p. 37.

Mayall, M., & O'Byrne, C. (2002, January). Reservoir prediction and development challenges in turbidite slope channels. In Offshore Technology Conference. Offshore Technology Conference.

Mayall, M., Jones, E., & Casey, M. (2006). Turbidite channel reservoirs—Key elements in facies prediction and effective development. Marine and Petroleum Geology, 23(8), 821-841.

Mayall, M., Lonergan, L., Bowman, A., James, S., Mills, K., Primmer, T., ... & Skeene, R. (2010). The response of turbidite slope channels to growth-induced seabed topography. AAPG bulletin, 94(7), 1011-1030.

Marsden, D., 1992. V 0—K method of depth conversion. The Leading Edge, 11(8), pp.53-54.

Marshak, S., Haq, S.S.B., & Sen, P. 2019. Ramp initiation in fold-thrust belts: Insight from PIV analysis of sandbox models. J. Struct. Geol. 118, 308-323.

Masaferro, J. L., Poblet, J., Bulnes, M., Eberli, G. P., Dixon, T. H., & McCLAY, K. E. N. (1999). Palaeogene-Neogene/present day (?) growth folding in the Bahamian foreland of the Cuban fold and thrust belt. Journal of the Geological Society, 156(3), 617-631.

Mazzoli, S., Pierantoni, P.P., Borraccini, F., Paltrinieri, W. and Deiana, G., 2005. Geometry, segmentation pattern and displacement variations along a major Apennine thrust zone, central Italy. Journal of Structural Geology, 27(11), pp.1940-1953.

McHargue, T., Pyrcz, M. J., Sullivan, M. D., Clark, J. D., Fildani, A., Romans, B. W., ... & Drinkwater, N. J. (2011). Architecture of turbidite channel systems on the continental slope: patterns and predictions. Marine and Petroleum Geology, 28(3), 728-743.

Middleton, G.V., Hampton, M.A., 1973. Sediment gravity flows: mechanics of flow and deposition. In: Middleton, G.V., Bouma, A.H., (Eds.), Turbidites and Deep-water Sedimentation. Los Angeles, CA: Society of Economic Paleontologists and Mineralogists, 1-38.

Milici, R.C., 1975. Structural patterns in the southern Appalachians: Evidence for a gravity slide mechanism for Alleghanian deformation. Geological Society of America Bulletin, 86(9), pp.1316-1320.

Mitchum Jr, R. M., Vail, P. R., & Thompson III, S. (1977). Seismic stratigraphy and global changes of sea level: Part 2. The depositional sequence as a basic unit for stratigraphic analysis: Section 2. Application of seismic reflection configuration to stratigraphic interpretation.

Moody, J. D., Pyles, D. R., Clark, J., & Bouroullec, R. (2012). Quantitative outcrop characterization of an analog to weakly confined submarine channel systems: Morillo 1 member, Ainsa Basin, Spain. AAPG bulletin, 96(10), 1813-1841.

Morgan, R., 2003. Prospectivity in ultradeep water: the case for petroleum generation and migration within the outer parts of the Niger Delta apron. Geological Society, London, Special Publications, 207(1), pp.151-164.

Morgan, R., 2004, Structural controls on the positioning ofsubmarine channels on the lower slopes of the NigerDelta, in R. J. Davies, J. A. Cartwright, S. A. Stewart,M. Lappin, and J. R. Underhill, eds., 3-D seismic technology: Application to the exploration of sedimentary basins: Geological Society (London) Memoirs 29, p. 45–51.

Morley, C.K. and Guerin, G., 1996. Comparison of gravity-driven deformation styles and behavior associated with mobile shales and salt. Tectonics, 15(6), pp.1154-1170.

Morley, C.K., 1988. Out-of-sequence thrusts. Tectonics, 7(3), pp.539-561.

Morley, C. K., & Leong, L. C. (2008). Evolution of deep-water synkinematic sedimentation in a piggyback basin, determined from three-dimensional seismic reflection data. Geosphere, 4(6), 939-962.

Morley, C.K., 2007. Interaction between critical wedge geometry and sediment supply in a deep-water fold belt. Geology, 35(2), pp.139-142.

Morley, C.K., 2009. Growth of folds in a deep-water setting. Geosphere, 5(2), pp.59-89.

Morley, C.K., King, R., Hillis, R., Tingay, M. and Backe, G., 2011. Deepwater fold and thrust belt classification, tectonics, structure and hydrocarbon prospectivity: A review. Earth-Science Reviews, 104(1-3), pp.41-91.

Mulder, T., & Alexander, J. (2001). The physical character of subaqueous sedimentary density flows and their deposits. Sedimentology, 48(2), 269-299.

Mutti, E., & Ricci Lucchi, F. (1972). Le torbiditi dell'Appennino Settentrionale: Introduzione all'analisi di facies: Memoria Società Geologica Italiana, v. 11.

Mutti, E., & Normark, W. R. (1987). Comparing examples of modern and ancient turbidite systems: problems and concepts. In Marine clastic sedimentology (pp. 1-38). Springer, Dordrecht.

Mutti, E., & Normark, W. R. (1991). An integrated approach to the study of turbidite systems. In Seismic facies and sedimentary processes of submarine fans and turbidite systems (pp. 75-106). Springer, New York, NY.

Muraoka, H. and Kamata, H., 1983. Displacement distribution along minor fault traces. Journal of Structural Geology, 5(5), pp.483-495.

Navarre, J. C., Claude, D., Liberelle, E., Safa, P., Vallon, G., & Keskes, N. (2002). Deepwater turbidite system analysis, West Africa: Sedimentary model and implications for reservoir model construction. The Leading Edge, 21(11), 1132-1139.

Nemec, W. (1990). Aspects of sediment movement on steep delta slopes. In Coarse-grained deltas (Vol. 10, pp. 29-73).

Nicol, A., Gillespie, P.A., Childs, C. and Walsh, J.J., 2002. Relay zones between mesoscopic thrust faults in layered sedimentary sequences. Journal of Structural Geology, 24(4), pp.709-727.

Nicol, A., Walsh, J., Berryman, K. and Nodder, S. 2005. Growth of a normal fault by the accumulation of slip over millions of years. Journal of Structural Geology, 27, 327-342.

Niyazi, Y., Eruteya, O. E., Harishidayat, D., Johansen, S. E., & Waldmann, N. (2018). Seismic geomorphology of submarine channel-belt complexes in the Pliocene of the Levant Basin, offshore central Israel. Marine Geology, 403, 123-138.

Normark, W. R. (1970). Growth patterns of deep-sea fans. AAPG bulletin, 54(11), 2170-2195.

Nunns, A. G. (1991). Structural Restoration of Seismic and Geologic Sections in Extensional Regimes (1). AAPG Bulletin, 75(2), 278-297.

O' Byrne, C.J., Prather, B.E., Steffens, G.S., and Pirmez, C., 2004, Reservoir architectural styles across stepped slope profiles: Implications for exploration, appraisal and development (abstract): American Association of Petroleum Geologists, International Conference Abstract, Cancun, Mexico.

Oluboyo, A. P., Gawthorpe, R. L., Bakke, K., & Hadler-Jacobsen, F. (2014). Salt tectonic controls on deep-water turbidite depositional systems: Miocene, southwestern Lower Congo Basin, offshore Angola. Basin Research, 26(4), 597-620.

Ori, G.G. and Friend, P.F., 1984. Sedimentary basins formed and carried piggyback on active thrust sheets. Geology, 12(8), pp.475-478.

Peach, B.N., Horne, J., Gunn, W., Clough, C.T., Teall, J.J.H. and Hinxman, L.W., 1907. The geological structure of the North-West Highlands of Scotland. HM Stationery Office.

Peacock, D.C.P. and Sanderson, D.J., 1991. Displacements, segment linkage and relay ramps in normal fault zones. Journal of Structural Geology, 13(6), pp.721-733.

Peacock, D.C.P. and Sanderson, D.J., 1994. Geometry and development of relay ramps in normal fault systems. AAPG bulletin, 78(2), pp.147-165.

Peacock, D.C.P. and Sanderson, D.J., 1996. Effects of propagation rate on displacement variations along faults. Journal of Structural Geology, 18(2-3), pp.311-320.

Peacock, D.C.P., 2002. Propagation, interaction and linkage in normal fault systems. Earth-Science Reviews, 58(1-2), pp.121-142.

Peakall, J., & Sumner, E. J. (2015). Submarine channel flow processes and deposits: A process-product perspective. Geomorphology, 244, 95-120.

Peel, F. J. (2014). The engines of gravity-driven movement on passive margins: Quantifying the relative contribution of spreading vs. gravity sliding mechanisms. Tectonophysics, 633, 126-142.

Pemberton, E. A., Hubbard, S. M., Fildani, A., Romans, B., & Stright, L. (2016). The stratigraphic expression of decreasing confinement along a deep-water sediment routing system: Outcrop example from southern Chile. Geosphere, 12(1), 114-134.

Pickering, K. T., & Hiscott, R. N. (1985). Contained (reflected) turbidity currents from the Middle Ordovician Cloridorme Formation, Quebec, Canada: an alternative to the antidune hypothesis. Sedimentology, 32(3), 373-394.

Pickering, K., Stow, D., Watson, M., & Hiscott, R. (1986). Deep-water facies, processes and models: a review and classification scheme for modern and ancient sediments. Earth-Science Reviews, 23(2), 75-174.

Piper, D. J., & Normark, W. R. (2001). Sandy fans-from Amazon to Hueneme and beyond. AAPG bulletin, 85(8), 1407-1438.

Pirmez C, Hiscott R, Kronen J (1997) Sandy turbidite successions at the base of channel-levee systems of the Amazon Fan revealed by FMS logs and cores: unraveling the facies architecture of large submarine fans. In: Flood RD, Piper DJW, Klaus A et al (eds) Proceedings of the ocean drilling program, Scientific Results Leg 155, pp 7–33.

Pirmez, C., Beaubouef, R. T., Friedmann, S. J., Mohrig, D. C., & Weimer, P. (2000, December). Equilibrium profile and baselevel in submarine channels: examples from Late Pleistocene systems and implications for the architecture of deepwater reservoirs. In Global deep-water reservoirs: Gulf Coast Section SEPM Foundation 20th Annual Bob F. Perkins Research Conference(pp. 782-805).

Pirmez, C., & Imran, J. (2003). Reconstruction of turbidity currents in Amazon Channel. Marine and petroleum geology, 20(6-8), 823-849.

Poblet, J. and Stuart, H., 1995. Reverse modelling of detachment folds; application to the Pico del Aguila anticline in the South Central Pyrenees (Spain). Journal of Structural Geology, 17(12), pp.1707-1724.

Poblet, J., Bulnes, M., McClay, K. and Hardy, S., 2004. Plots of crestal structural relief and fold area versus shortening—A graphical technique to unravel the kinematics of thrust-related folds.

Porter, M. L., A. R. G. Sprague, M. D. Sullivan, D. C. Jennette, R. T. Beaubouef, T. R. Garfield, C. Rossen, D. K. Sickafoose, G. N. Jensen, S. J. Friedmann, and D. C. Mohrig, 2006, Stratigraphic organization and predictability of mixed coarse- and fine-grained lithofacies successions in a lower Miocene deep-water slope-channel system, Angola Block 15, in P. M. Harris and L. J. Weber, eds., Giant hydrocarbon reservoirs of the

world: From Rocks to reservoir characterization and modeling: AAPG Memoir 88/SEPM Special Publication, p. 281-305.

Posamentier, H. W., & Kolla, V. (2003). Seismic geomorphology and stratigraphy of depositional elements in deep-water settings. Journal of sedimentary research, 73(3), 367-388.

Prather, B. E., Booth, J. R., Steffens, G. S., & Craig, P. A. (1998). Classification, lithologic calibration, and stratigraphic succession of seismic facies of intraslope basins, deep-water Gulf of Mexico. AAPG bulletin, 82(5), 701-728.

Prather, B. E., Pirmez, C., Sylvester, Z., Prather, D. S., Deptuck, M. E., Mohrig, D., ... & Wynn, R. (2012a). Stratigraphic response to evolving geomorphology in a submarine apron perched on the upper Niger Delta slope. Application of the principles of seismic geomorphology to continental-slope and base-of-slope systems: Case studies from seafloor and near-seafloor analogues: Society for Sedimentary Geology (SEPM) Special Publication 99, 145-161.

Prather, B. E., Pirmez, C. A. R. L. O. S., Winker, C. D., Deptuck, M. E., & Mohrig, D. (2012b). Stratigraphy of linked intraslope basins: Brazos-Trinity system western Gulf of Mexico. Application of the principles of seismic geomorphology to continental-slope and base-of-slope systems: Case studies from seafloor and near-seafloor analogues: SEPM, Special Publication, 99, 83-109.

Prather, B. E. (2000). Calibration and visualization of depositional process models for above-grade slopes: a case study from the Gulf of Mexico. Marine and Petroleum Geology, 17(5), 619-638.

Prather, B. E. (2003). Controls on reservoir distribution, architecture and stratigraphic trapping in slope settings. Marine and Petroleum Geology, 20(6-8), 529-545.

Prélat, A., Hodgson, D. M., & Flint, S. S. (2009). Evolution, architecture and hierarchy of distributary deep-water deposits: a high-resolution outcrop investigation from the Permian Karoo Basin, South Africa. Sedimentology, 56(7), 2132-2154.

Prelat, A., Covault, J. A., Hodgson, D. M., Fildani, A., & Flint, S. S. (2010). Intrinsic controls on the range of volumes, morphologies, and dimensions of submarine lobes. Sedimentary Geology, 232(1-2), 66-76.

Price, R.A. and Mountjoy, E.W., 1970. Geologic structure of the Canadian Rocky Mountains between Bow and Athabasca Rivers: A progress report. Geological Association of Canada Special Paper, 6, pp.7-25.

Reading, H. G., & Richards, M. (1994). Turbidite systems in deep-water basin margins classified by grain size and feeder system. AAPG bulletin, 78(5), 792-822.

Reijers, T. J. A., Petters, S. W., & Nwajide, C. S. (1997). The Niger delta basin. In Sedimentary basins of the world (Vol. 3, pp. 151-172). Elsevier.

Reijers, T. (2011). Stratigraphy and sedimentology of the Niger Delta. Geologos, 17(3), 133-162.

Romans, B. W., Fildani, A., Hubbard, S. M., Covault, J. A., Fosdick, J. C., & Graham, S. A. (2011). Evolution of deep-water stratigraphic architecture, Magallanes Basin, Chile. Marine and Petroleum Geology, 28(3), 612-628.

Rouby, D., Nalpas, T., Jermannaud, P., Robin, C., Guillocheau, F. and Raillard, S., 2011. Gravity driven deformation controlled by the migration of the delta front: the Plio-Pleistocene of the Eastern Niger Delta. Tectonophysics, 513(1-4), pp.54-67.

Rotevatn, A., Jackson, C.A-L., Tvedt, ABM, Bell, R.E. 2019, How do normal faults grow? Journal of Structural Geology 125, 174-184.

Rowan, M.G., Peel, F.J. and Vendeville, B.C., 2004. Gravity-driven fold belts on passive margins. AAPG Memoir, v.82, pp.157-182.

Rowan, M. G. (1997). Three-dimensional geometry and evolution of a segmented detachment fold, Mississippi Fan foldbelt, Gulf of Mexico. Journal of Structural Geology, 19(3-4), 463-480.

Saller, A., Werner, K., Sugiaman, F., Cebastiant, A., May, R., Glenn, D., & Barker, C. (2008). Characteristics of Pleistocene deep-water fan lobes and their application to an upper Miocene reservoir model, offshore East Kalimantan, Indonesia. AAPG bulletin, 92(7), 919-949.

Salvini, F., & Storti, F. (2002). Three-dimensional architecture of growth strata associated to fault-bend, fault-propagation, and décollement anticlines in non-erosional environments. Sedimentary Geology, 146(1-2), 57-73.

Savoye, B., Babonneau, N., Dennielou, B., & Bez, M. (2009). Geological overview of the Angola–Congo margin, the Congo deep-sea fan and its submarine valleys. Deep Sea Research Part II: Topical Studies in Oceanography, 56(23), 2169-2182.

Scholz, C.H., 1982. Scaling laws for large earthquakes: consequences for physical models. Bulletin of the Seismological Society of America, 72(1), pp.1-14.

Sclater, J.G. and Christie, P.A., 1980. Continental stretching: An explanation of the post-Mid-Cretaceous subsidence of the central North Sea Basin. Journal of Geophysical Research: Solid Earth, 85(B7), pp.3711-3739.

Searle, M.P., 1985. Sequence of thrusting and origin of culminations in the northern and central Oman Mountains. Journal of Structural Geology, 7(2), pp.129-143.

Shaw, J.H., Bilotti, F. and Brennan, P.A., 1999. Patterns of imbricate thrusting. Geological Society of America Bulletin, 111(8), pp.1140-1154.

Shaw, J. H., E. Novoa, and C. D. Connors, (2004), Structural controls on growth stratigraphy in contractional fault-related folds, in K. R. McClay, ed., Thrust tectonics and hydrocarbon systems: AAPG Memoir 82, p. 400–412.

Short, K.C. and Stauble, A.J., 1967. Outline of geology of Niger Delta. AAPG bulletin, 51(5), pp.761-779.

Simoes, M., Avouac, J.P. and Chen, Y.G., 2007. Slip rates on the Chelungpu and Chushiang thrust faults inferred from a deformed strath terrace along the Dungpuna river, west central Taiwan. Journal of Geophysical Research: Solid Earth, 112(B3).

Simpson, G.D., 2006. Modelling interactions between fold–thrust belt deformation, foreland flexure and surface mass transport. Basin Research, 18(2), pp.125-143.

Sinclair, H. D., & Tomasso, M. (2002). Depositional evolution of confined turbidite basins. Journal of Sedimentary Research, 72(4), 451-456.

Skene, K. I., Piper, D. J., & Hill, P. S. (2002). Quantitative analysis of variations in depositional sequence thickness from submarine channel levees. Sedimentology, 49(6), 1411-1430.

Smallwood, J. R. (2002). Use of V0-K depth conversion from shelf to deep-water: how deep is that brightspot?. First Break, 20(2).

Smith, R. U. (2004). Silled sub-basins to connected tortuous corridors: Sediment distribution systems on topographically complex sub-aqueous slopes. Geological Society, London, Special Publications, 222(1), 23-43.

Sømme, T. O., Helland-Hansen, W., Martinsen, O. J., & Thurmond, J. B. (2009). Relationships between morphological and sedimentological parameters in source-to-sink systems: a basis for predicting semi-quantitative characteristics in subsurface systems. Basin Research, 21(4), 361-387.

Spinewine, B., Sun, T., Babonneau, N., & Parker, G. (2011). Self-similar long profiles of aggrading submarine leveed channels: Analytical solution and its application to the Amazon channel. Journal of Geophysical Research: Earth Surface, 116(F3).

Sprague, A. R. G., Garfield, T. R., Goulding, F. J., Beaubouef, R. T., Sullivan, M. D., Rossen, C., ... & Jensen, G. N. (2005). Integrated slope channel depositional models: the key to successful prediction of reservoir presence and quality in offshore West Africa. CIPM, cuarto E-Exitep, 1e13.

Spychala, Y. T., Hodgson, D. M., Prélat, A., Kane, I. A., Flint, S. S., & Mountney, N. P. (2017). Frontal and lateral submarine lobe fringes: comparing sedimentary facies, architecture and flow processes. Journal of Sedimentary Research, 87(1), 75-96.

Stacher, P. (1995). Present understanding of the Niger Delta hydrocarbon habitat. Geology of Deltas: Rotterdam, AA Balkema, 257-267.

Steffens, G. S., Biegert, E. K., Sumner, H. S., & Bird, D. (2003). Quantitative bathymetric analyses of selected deepwater siliciclastic margins: receiving basin configurations for deepwater fan systems. Marine and Petroleum Geology, 20(6-8), 547-561.

Stevenson, C. J., Jackson, C. A. L., Hodgson, D. M., Hubbard, S. M., & Eggenhuisen, J. T. (2015). Deep-water sediment bypass. Journal of Sedimentary Research, 85(9), 1058-1081.

Stockmal, G.S., Beaumont, C., Nguyen, M. and Lee, B., 2007. Mechanics of thin-skinned fold-and-thrust belts: Insights from numerical models. Geological Society of America Special Papers, 433, pp.63-98.

Storti, F. and McClay, K., 1995. Influence of syntectonic sedimentation on thrust wedges in analogue models. Geology, 23(11), pp.999-1002.

Storti, F., Salvini, F. and McClay, K., 1997. Fault-related folding in sandbox analogue models of thrust wedges. Journal of Structural Geology, 19(3-4), pp.583-602.

Straub, K. M., Paola, C., Mohrig, D., Wolinsky, M. A., & George, T. (2009). Compensational stacking of channelized sedimentary deposits. Journal of Sedimentary Research, 79(9), 673-688.

Sullivan, M., Formeman, J.L., Jennette, D., Stern, D., Gerrick, N.J. and Goulding, F.J. (2004) An integrated approach to characterization and modeling deep-water reservoirs, Diana Field, Western Gulf of Mexico, an integration of outcrop and modern analogs in reservoirs modeling. AAPG Mem., 80, 215– 234.

Sun, Y. and Liu, L., 2018. Structural evolution of thrust-related folds and associated fault systems in the eastern portion of the deep-water Niger Delta. Marine and Petroleum Geology, 92, 285-307. https://doi.org/10.1016/j.marpetgeo.2017.12.012.

Suppe, J., Chou, G.T. and Hook, S.C., 1992. Rates of folding and faulting determined from growth strata. In Thrust tectonics (pp. 105-121). Springer, Dordrecht.

Sweet, M. L., & Blum, M. D. (2016). Connections between fluvial to shallow marine environments and submarine canyons: Implications for sediment transfer to deep water. Journal of Sedimentary Research, 86(10), 1147-1162.

Sylvester, Z., Pirmez, C., & Cantelli, A. (2011). A model of submarine channel-levee evolution based on channel trajectories: Implications for stratigraphic architecture. Marine and Petroleum Geology, 28(3), 716-727.

Sylvester, Z., & Covault, J. A. (2016). Development of cutoff-related knickpoints during early evolution of submarine channels. Geology, 44(10), 835-838.

Talling, P. J., Masson, D. G., Sumner, E. J., & Malgesini, G. (2012). Subaqueous sediment density flows: Depositional processes and deposit types. Sedimentology, 59(7), 1937-2003.

Taylor, S.K., Nicol, A. and Walsh, J.J., 2008. Displacement loss on growth faults due to sediment compaction. Journal of Structural Geology, 30(3), pp.394-405.

Torabi, A. and Berg, S.S., 2011. Scaling of fault attributes: A review. Marine and Petroleum Geology, 28(8), pp.1444-1460.

Totake, Y., Butler, R.W. and Bond, C.E., 2017. Structural validation as an input into seismic depth conversion to decrease assigned structural uncertainty. Journal of Structural Geology, 95, pp.32-47.

Totake, Y., Butler, R.W., Bond, C.E. and Aziz, A., 2018. Analyzing structural variations along strike in a deep-water thrust belt. Journal of Structural Geology, 108, pp.213-229.

Van Andel, T. H., & Komar, P. D. (1969). Ponded sediments of the Mid-Atlantic Ridge between 22 and 23 North latitude. Geological Society of America Bulletin, 80(7), 1163-1190.

Vergés, J., Burbank, D. W., & Meigs, A. (1996). Unfolding: An inverse approach to fold kinematics. Geology, 24(2), 175-178.

Walker, R. G. (1978). Deep-water sandstone facies and ancient submarine fans: models for exploration for stratigraphic traps. AAPG Bulletin, 62(6), 932-966.

Walsh, J.J. and Watterson, J., 1988. Analysis of the relationship between displacements and dimensions of faults. Journal of Structural geology, 10(3), pp.239-247.

Walsh, J.J., Nicol, A. and Childs, C., 2002. An alternative model for the growth of faults. Journal of Structural Geology, 24(11), pp.1669-1675.

Walsh, J.J., Bailey, W.R., Childs, C., Nicol, A. and Bonson, C.G., 2003. Formation of segmented normal faults: a 3-D perspective. Journal of Structural Geology, 25(8), pp.1251-1262.

Watkins, H., Butler, R.W. and Bond, C.E., 2017. Using laterally compatible cross sections to infer fault growth and linkage models in foreland thrust belts. Journal of Structural Geology, 96, pp.102-117.

Wiener, R. W., M. G. Mann, M. T. Angelich, and J. B. Molyneux, 2010, Mobile shale in the Niger Delta: Characteristics, structure, and evolution, in L. Wood, ed., Shale tectonics: AAPG Memoir, 93, p. 145–161.

Willemse, E.J., Pollard, D.D. and Aydin, A., 1996. Three-dimensional analyses of slip distributions on normal fault arrays with consequences for fault scaling. Journal of Structural Geology, 18(2-3), pp.295-309.

Winker, C. D. (1996, January). High-resolution seismic stratigraphy of a late Pleistocene submarine fan ponded by salt-withdrawal mini-basins on the Gulf of Mexico

continental slope. In Offshore Technology Conference. Offshore Technology Conference.

Wu, S. and Bally, A.W., 2000. Slope Tectonics-Comparisons and Contrasts of Structural Styles of Salt and Shale Tectonics of the Northern Gulf of Mexico with Shale Tectonics of Offshore Nigeria in Gulf of Guinea. Atlantic rifts and continental margins, pp.151-172.

Wu, J.E. and McClay, K.R., 2011. Two-dimensional analog modeling of fold and thrust belts: Dynamic interactions with syncontractional sedimentation and erosion. in K. McClay, J. Shaw, and J. Suppe, eds., Thrust fault-related folding: AAPG Memoir, v. 94, p. 301–333.

Wu, J. E., McClay, K., and Frankowicz, E., 2015, Niger Delta gravity-driven deformation above the relict Chain and Charcot oceanic fracture zones, Gulf of Guinea: Insights from analogue models: Marine and Petroleum Geology, v. 65, p. 43-62.

Wynn, R. B., Cronin, B. T., & Peakall, J. (2007). Sinuous deep-water channels: Genesis, geometry and architecture. Marine and Petroleum Geology, 24(6-9), 341-387.

Yamada, Y., Baba, K. and Matsuoka, T., 2006. Analogue and numerical modelling of accretionary prisms with a decollement in sediments. Geological Society, London, Special Publications, 253(1), pp.169-183.

Yarbuh, I., González-Fernández, A., Spelz-Madero, R.M., Negrete-Aranda, R. and Contreras, J., 2018. Development of Detachment Folds in the Mexican Ridges Foldbelt, Western Gulf of Mexico Basin. Tectonics, 37(7), pp.2013-2028.

Zhang, J., Wu, S., Hu, G., Fan, T. E., Yu, B., Lin, P., & Jiang, S. (2018). Sea-level control on the submarine fan architecture in a deepwater sequence of the Niger Delta Basin. Marine and Petroleum Geology, 94, 179-197.

Zhao, X., Qi, K., Patacci, M., Tan, C., & Xie, T. (2019). Submarine channel network evolution above an extensive mass-transport complex: A 3D seismic case study from the Niger delta continental slope. Marine and Petroleum Geology, 104, 231-248.